

**Studies on electrical and optical properties of p-type  
porous silicon (PS) and its hybrid structures**



**Samarjit Sarmah**

Department of Physics  
Gauhati University

This thesis is submitted to  
Gauhati University as requirement for the degree of  
*Doctor of Philosophy*

*Dedicated to my beloved parents*

**Mr. Nripen Sarmah and Mrs. Arpana Devi**

*Without their love, trust and sacrifices, success would*

*have been a dream for me*

## **Declaration**

I hereby declare that the thesis entitled “**Studies on electrical and optical properties of p-type porous silicon (PS) and its hybrid structures**” is the result of my own research work which has been carried out under the guidance of Prof. Deepali Sarkar of Dept. of Physics, Gauhati University. I further declare that this thesis as a whole or any part thereof has not been submitted to any university (or institute) for the award of any degree or diploma.

The thesis contains less than 90,000 (ninety thousand) words excluding bibliography and captions.

*Samarjit Sarmah.*

**Samarjit Sarmah**

**Research Scholar**


**Dept. of Physics, GU**

**August 2021**

## Certificate


This is to certify that the thesis entitled “**Studies on electrical and optical properties of p-type porous silicon (PS) and its hybrid structures**” is the result of research work of **Samarjit Sarmah**, carried out under my supervision, submitted to **Gauhati University** for the award of the degree of **Doctor of Philosophy in Physics**. The results embodied in this thesis have not been submitted to any other University or Institute for the award of any degree or diploma.

This thesis conforms to the standard of PhD Thesis under Gauhati University including the standard related to plagiarism and has a similarity index not more than 10 % (ten percent), excluding the bibliography.

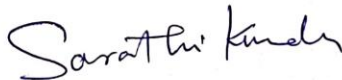
  
Prof. Deepali Sarkar, Supervisor  
Professor  
Department of Physics, GU  
Gauhati University  
August 2021

Members of the Research Advisory Committee:

Prof Anurup Gohain Barua, Department of Physics, GU

  
09/08/2021  
Anurup Gohain Barua  
Professor, Department of Physics  
Gauhati University, Assam

Dr Sarathi Kundu, Physical Sciences Division, IASST

  
Dr. Sarathi Kundu  
Associate Professor  
Physical Science Division  
Institute of Advanced Study in Science and Technology,  
Paschim Boraigaon, Guwahati-35, Assam, India

## Acknowledgements

First of all, I would like to express my deepest gratitude to my supervisor Prof. Deepali Sarkar, Department of Physics, Gauhati University for her appreciable guidance, valuable suggestions and support throughout the tenure of my Ph. D. work. Her friendly nature and freedom provided in research works inspired me to continue my works with dedication.

I convey my sincere thanks and regards to Prof. Buddhadeb Bhattacharjee, Head of the Department of Physics, Gauhati University, for his compliments to my works and giving me the necessary official permissions to carry out the research works.

I acknowledge CSIR, DST, DST FIST and UGC for providing various instrumental facility and financial support. I am also grateful to CIF-GU, SAIF-GU and CIF-IIT Guwahati for providing different characterisation facilities.

I am thankful to Prof. Anurup Gohain Barua of this department and Dr. Sarathi Kundu of IASST, Guwahati for their help and fruitful suggestions. I am also thankful to Dr. B.K. Sarma and Dr. M. P. C. Kalita of this department for providing some fabrication and characterisation facilities related to my thesis works. I also appreciate their valuable suggestions to improve my research works.

My grateful appreciation is owed to all the faculty members, non-academic staff members, canteen and security staff of the department for extending their help in different ways during my research works.

My special thanks to Dr. Mintu Das, who actually acted as an unofficial co-guide to help and motivate me during my research tenure. I also want to express thanks to my present lab mates Ali Akbar, Pranjal Nath, Jonmani Rabha, Saponjit Bora and Rahul Thakuria and my ex-lab mate Dr. Mausumi Das Kakati for their help and constructive discussions together throughout my research work. I am grateful to all other research scholars of the department who made the research period interesting and enjoyable.

Specially, I would also like to thank my colleagues of Kamrup Polytechnic and G.L.C. College for their help and inspirations.

Great thanks are owed to most important persons in my life, Maa (Arpana Devi), Deuta (Nripen Sarmah), Bhaity (Nitul Sarmah) and all my family members for their whole-hearted support, encouragement and care during this period.

*Samarjit Sarmah.*  
(Samarjit Sarmah)

## Abstract

The present dissertation work deals with the studies on optical and electrical properties of porous silicon (PS) and its hybrid structures with different semiconductor materials such as CdS, ZnS and ZnO. The effects of ageing and the effects of annealing treatment to improve photo sensing performances of the aged PS:p-Si structure based photodiode (PD) are studied. Additionally, photo sensing performances of annealed ZnO-PS:p-Si heterostructure based PDs are also studied in details. The work comprised of seven chapters and an appendix.

**Chapter 1** gives general introduction to the present work, giving literature survey on the topic and also motivation which leads to the present work.

**Chapter 2** gives idea about materials and methods involved in the present work. It particularly deals with the materials required for the fabrication and also the experimental methods which are involved to carry out the present investigation.

In **Chapter 3**, UV-visible light sensing property of metal-semiconductor-metal (MSM) device based on nanostructured CdS-PS:p-Si heterostructure has been studied. Porous silicon is prepared on p-Si wafer using electrochemical anodization method by alternate variation of etching current density within the limit of 17.2-22.1 mAcm<sup>-2</sup>. Nanostructured CdS layer is deposited on PS substrate by thermal evaporation method. To achieve MSM configuration, interdigitated Al electrodes of 6 x 6 mm dimension are deposited on top of the heterostructure. FESEM and EDX analyses confirm growth of hierarchical flower like CdS nanostructures on PS substrate. Band gap energy of nanostructured CdS from UV-vis absorption spectra is found to be 2.6 eV. Photoluminescence study of the heterostructure reveals presence of various defect dominated luminescence bands peaked at ~450, 460, 468 and 482 nm along with PS characteristic peak at 590 nm. The heterostructure shows low leakage current of ~32 nA at -2 V with ideality factor ( $n$ ) and reverse saturation current ( $I_s$ ) values of 1.57 and 0.2 nA respectively. Spectral response of the heterostructure is found to be maximum under irradiation wavelength of 400 nm with responsivity ( $R_\lambda$ ) value of ~0.6 AW<sup>-1</sup> and

external quantum efficiency of ~180 % at -2 V bias. Response and recovery times of the device are ~160 and ~350 ms respectively. These electrical parameters of the device have been compared with other silicon based optoelectronic switching devices to find a suitable alternate choice.

In **Chapter 4**, distinct and enhanced UV-visible light sensing property of ZnS-PS:p-Si heterostructure based MSM device has been demonstrated. ZnS (99.99 % purity) powder is deposited on PS surface via thermal evaporation technique to fabricate ZnS-PS:p-Si heterostructure. Al+Au electrodes are coated on top of the heterostructure to achieve Schottky contact. FESEM analyses confirm formation of single layer ZnS particles over PS surface with uniform interface. Cross sectional EDX analyses indicate diffusion of ZnS particles into PS layer. Optical analysis observed via UV-visible spectroscopy gives bandgap of bare ZnS film to be 3.4 eV with 70-95 % transparency in near UV to visible region (380-700 nm). Optical reflectance spectra of the heterostructure shows decreased reflectivity compared to that of bare PS:p-Si structure which is itself 20-30 % less compared to bulk silicon. Spectral response measured for the wavelength range of 200-500 nm gives distinct and enhanced responsivity peak values of ~0.95 and ~1.13  $\text{AW}^{-1}$  at 365 nm (UV) and 400 nm (visible) compared to ~0.59  $\text{AW}^{-1}$  at 400 nm for bare PS:p-Si based device under -4 V bias. The response and recovery times of the heterostructure for UV illumination are found to be  $0.54 \pm (4.3 \times 10^{-4})$  s and  $0.38 \pm 9.5 \times 10^{-5}$  s respectively, similarly for visible light these are  $0.50 \pm 2.8 \times 10^{-4}$  s and  $0.35 \pm 6.5 \times 10^{-5}$  s respectively.

**Chapter 5** deals with fabricating UV-visible radiation sensing photodetectors by architecting planar (PD1) and sandwich (PD2) electrode configurations on ZnO-PS:p-Si heterostructure. Thin ZnO layer of ~160 nm is deposited on PS:p-Si substrate by pulsed DC magnetron sputtering technique. Gold (Au) is combined with Aluminium (Al) to provide rectifying Schottky contacts to the devices. To study the effect of post annealing treatment on photo sensing property of the heterostructure, it is annealed at the temperature range of 200-500  $^{\circ}\text{C}$ . FESEM analyses confirm uniform deposition of spherical ZnO grains with mean grain size of ~35 nm, which increases to ~50 nm when annealed at 500  $^{\circ}\text{C}$  due to agglomeration. Cross-sectional EDX analyses confirm diffusion of ZnO grains into pores of PS layer. UV-vis absorption spectrum shows

bandgap energy of untreated ZnO to decrease from 3.30 eV to 3.23 eV upon annealing. ZnO film remains highly transparent (65-78 %) in the visible-NIR range even after annealing. Photoluminescence study reveals quenching of ZnO band edge related luminescence peaks and complete disappearance of PS characteristic peak at 590 nm. PD1 and PD2 show UV-visible photoresponse with maximum responsivity of 2.6 and 68  $\text{AW}^{-1}$  respectively under 400 nm illumination at -2 V bias. PD1 annealed at 200  $^{\circ}\text{C}$ , exhibits rise in responsivity upto 30  $\text{AW}^{-1}$ . It shows dominance of pyroelectric effect over photo sensing performances when annealed at 300-500  $^{\circ}\text{C}$  and responsivity drops to 0.5  $\text{AW}^{-1}$ . Response times for annealed PD1 (200  $^{\circ}\text{C}$ ) at 375 and 400 nm are found to be relatively faster (0.6, 0.8 s) compared to the untreated one (2.1, 1.1 s).

In **Chapter 6**, Al/PS: p-Si planar Schottky UV-vis photodetector has been successfully designed. The photoresponsivity of the aged device shows enhancement upon thermal annealing treatment. FESEM analyses confirm formation of mesopores on p-Si surface with uniform PS: p-Si interface. Elemental EDX analyses endorse development of silicon suboxide ( $\text{SiO}_x$ ,  $x \leq 2$ ) layers on PS: p-Si surface for aged and annealed structure. Photoluminescence spectra of as-prepared and aged structure show strong characteristic peak at 590 nm along with some weak emission peaks at 470 and 500 nm related to defect levels of  $\text{SiO}_x$  layers developed on PS surface. The silicon suboxide related peaks gradually dominate over PS characteristic peak upon annealing and suppress this peak completely when annealed at 400  $^{\circ}\text{C}$ . Defect enriched aged device show increase of  $I_{ph}$  for higher voltage region, subsequently responsivity and EQE values enhances upto 0.47  $\text{AW}^{-1}$  and 145 % respectively. However,  $R_{\lambda}$  and EQE values drop by 20-fold after 90 days, due to device degradation with grow of high interfacial defects. The device exhibits best multiband UV-visible photoresponse when annealed at 400  $^{\circ}\text{C}$  with  $R_{\lambda}$  values of 50 and 25  $\text{AW}^{-1}$  at 365 and 400 nm illumination respectively for -2V bias. Response and recovery times of the as-prepared device are found to be 0.16 and 0.24 s respectively, which remain constant with ageing of the device. However, some pyro-spikes are observed when the device is annealed in the temperature range of 200 to 400  $^{\circ}\text{C}$ . These spikes are completely eliminated when annealed at 500  $^{\circ}\text{C}$ . So as to say, annealing of the naturally oxidized Al/PS: p-Si Schottky device at an appropriate temperature (400  $^{\circ}\text{C}$ ) minimizes interfacial defects, which consequently enhances its UV-visible photoresponse.



**Chapter 7** gives overall summary and future prospects of the entire thesis work. This will give an idea about the whole dissertation work in a concise manner. Also, the future prospects that can be carried out based on the present work also have been specified in this chapter.

Finally, there is an **Appendix** added at the end, which gives the list of publications in referred journals and conference proceedings arising out of this dissertation work. The conferences/seminars/workshops attended by the author during the period of the entire work also have been listed.

## Table of contents

<b>List of figures</b>	<b>ix</b>
<b>List of tables</b>	<b>xv</b>
<b>Chapter 1 Introduction</b>	<b>1</b>
1.1 Background and motivation.....	1
1.2 Synthesis methods of porous silicon (PS).....	9
1.2.1 Electrochemical etching or anodization method.....	10
1.2.1.1 Chemical factors controlling anodization.....	11
1.2.1.2 Physical factors controlling anodization.....	12
1.2.2 Metal assisted chemical etching.....	12
1.2.3 Template assisted approach.....	14
1.3 Synthesis methods of hybrid structures from PS.....	15
1.4 Objectives of the thesis works.....	20
1.5 Outline of the thesis.....	20
<b>Chapter 2 Materials and methods</b>	<b>22</b>
2.1 Materials used.....	22
2.2 Methods of preparations.....	24
2.2.1 Cutting, cleaning and anodization of silicon wafers.....	24
2.2.2 Deposition of CdS and ZnS powders and metal electrodes.....	26
2.2.3 Preparation of CdS nanoparticles.....	26
2.2.4 Deposition of nanostructured ZnO.....	27
2.2.5 Annealing of bulk ZnS powder and Schottky devices.....	28
2.3 Characterisation techniques.....	29
2.3.1 Field emission scanning electron microscopy (FESEM).....	29

2.3.2 Energy dispersive X-ray spectroscopy (EDX).....	30
2.3.3 Field emission transmission electron microscopy (FETEM).....	31
2.3.4 X-ray diffraction (XRD).....	33
2.3.5 Raman spectroscopy.....	34
2.3.6 UV-Visible spectroscopy.....	36
2.3.7 Photoluminescence spectroscopy (PL).....	37
2.3.8 Dark and photo current measurement.....	39
<b>Chapter 3 Optical and electrical properties of nanostructured CdS-PS: p-Si</b>	
<b>heterostructure</b>	<b>41</b>
3.1 Introduction .....	41
3.2 Experimental.....	46
3.2.1 Preparation of Al/nano CdS-PS:p-Si MSM heterostructure.....	46
3.3 Results and discussion.....	43
3.3.1 Morphological analysis.....	43
3.3.2 Optical studies.....	44
3.3.3 Electrical and photo response studies.....	47
3.3.4 Conclusion .....	51
<b>Chapter 4 Optical and electrical properties of ZnS-PS: p-Si heterostructure</b>	<b>53</b>
4.1 Introduction .....	53
4.2 Experimental.....	54
4.2.1 Preparation of Al + Au/ZnS-PS: p-Si MSM heterostructure.....	54
4.3 Results and discussion.....	54
4.3.1 Morphological analysis.....	54
4.3.2 Optical analysis.....	56

4.3.3 Electrical and photo response analysis.....	57
4.4 Conclusion.....	61
<b>Chapter 5 Optical and electrical properties of as-prepared and annealed ZnO-PS:</b>	
<b>p-Si heterostructure</b>	<b>63</b>
5.1 Introduction.....	63
5.2 Experimental.....	64
5.2.1 Preparation of ZnO-PS:p-Si heterostructure.....	64
5.2.2 Preparation of MSM hybrid structures.....	64
<b>5.3 Results and discussion: Part A: Optical and electrical properties of as-</b>	
<b>    prepared ZnO-PS: p-Si heterostructure</b>	<b>65</b>
5.3.1 Morphological analysis.....	65
5.3.2 Optical analysis.....	67
5.3.3 Electrical and photo response analysis.....	70
<b>5.4 Results and discussion: Part B: Optical and electrical properties of annealed</b>	
<b>    ZnO-PS: p-Si heterostructure</b>	<b>77</b>
5.4.1 Microstructural and optical studies.....	77
5.4.2 Electrical and photo sensing studies.....	81
5.5 Conclusion.....	85
<b>Chapter 6 Optical and electrical properties of aged PS: p-Si structure</b>	<b>87</b>
6.1 Introduction.....	87
6.2 Experimental details.....	88
6.2.1 Preparation of Al/PS: p-Si MSM structure.....	88
<b>6.3 Results and discussion: Part A: Optical and electrical properties of aged PS:</b>	
<b>    p-Si structure</b>	<b>89</b>

6.3.1 Microstructural and optical studies.....	89
6.3.2 Electrical and photo response studies.....	93
<b>6.4 Results and discussion: Part B: Optical and electrical properties of annealed PS: p-Si structure</b>	<b>101</b>
6.4.1 Morphological and optical analysis.....	101
6.4.2 Electrical and photo response analysis.....	103
6.5 Conclusion.....	109
<b>Chapter 7 Overall summary and future prospects</b>	<b>111</b>
7.1 Overall summary.....	111
7.2 Future prospects.....	114
<b>References</b>	<b>116</b>
<b>Appendix</b>	<b>125</b>

## List of figures

<b>Fig. 1.1</b> PS fabricated with different pore sizes exhibiting different luminescence.....	9
<b>Fig. 1.2</b> Schematic for top-down and bottom-up approaches for synthesis of PS.....	10
<b>Fig.1.3</b> Mechanism for electrochemical etching of Si in HF solution.....	11
<b>Fig. 1.4</b> Cross-sectional SEM images of Si nanowires synthesised by metal-assisted stain etching of (100) p-type Si. ....	13
<b>Fig. 1.5</b> Tilted view SEM images of (a and e) nanopillars, (b and f) nanorods, (c and g) nanopencils, and (d and h) nanocones arrays synthesised by Ag-assisted MACE method.....	13
<b>Fig. 1.6</b> (a) Silica diatom frustule template. (b) Si replica after magnesiothermic reduction, (c) Schematic diagram of the magnesiothermic reduction of SBA-15 mesoporous silica template. (d) TEM image and (e) SEM image of a mesoporous Si particle replica, (f-h) SEM image of macroporous Si from different size templates of pre-sintered silica microspheres by CVD method.....	14
<b>Fig. 1.7</b> Tilted view FESEM images and EDX spectra of (a-b) Si-NWs and (c-d) CdS: Si NWs respectively, (e) schematic of Si: CdS heterojunction device, spectral responsivity of the device.....	16
<b>Fig. 1.8</b> Schematic of fabrication process of Si-NPA: MAPbI <sub>3</sub> : ZnO heterojunction PD.....	17
<b>Fig. 1.9</b> Tilted view FESEM image of (a) Si-NPA and (b) Si-NPA: MAPbI <sub>3</sub> : ZnO heterostructure, (c-d) planar & cross sectional FESEM image of ZnO thin film on glass and (e) n-ZnO: p-Si, planar FESEM image of (f) ZnO NWs-Si and (g-h) PS & ZnO: PS heterostructure.....	18
<b>Fig. 1.10</b> FESEM images of (a) ZnS nanowire and (b) ZnO branched ZnS NWs, (c) Si NWs fabricated by MACE, (d) Si NWs after KOH treatment, (e) fabricated well-separated radial heterojunction arrays by depositing ZnS and AZO, (f) cross sectional image of Si core and ZnS shell, (g) bottom part showing AZO: ZnS layer, tilted view FESEM image of (h) Si-NPA, (i) ZnS: Si-NPA.....	19

<b>Fig. 2.1</b> Schematic of [(100), (111)] oriented p-type and n-type Si-wafers.....	23
<b>Fig. 2.2</b> Hot probe measurement of conductivity type.....	24
<b>Fig. 2.3</b> Experimental setup for electrochemical etching.....	25
<b>Fig. 2.4</b> Schematic for thermal evaporation method using vacuum coating unit.....	26
<b>Fig. 2.5</b> Schematic for wet chemical synthesis of CdS nanopowder.....	27
<b>Fig. 2.6</b> Schematic for pulsed DC magnetron sputtering of ZnO nanoparticles.....	28
<b>Fig. 2.7</b> Schematic diagram of high temperature horizontal tube furnace.....	29
<b>Fig. 2.8</b> Schematic for FESEM imaging and EDX analysis.....	31
<b>Fig. 2.9</b> Schematic for FETEM imaging process.....	32
<b>Fig. 2.10</b> Schematic for (a) Bragg's diffraction law and (b) X-ray diffractometer setup.....	34
<b>Fig. 2.11(a)</b> Schematic for Raman spectroscopy analysis.....	35
<b>Fig. 2.11(b)</b> Energy level diagram of Raman spectroscopy.....	36
<b>Fig. 2.12</b> Schematic for UV-visible spectrophotometer.....	37
<b>Fig. 2.13 (a)</b> Schematic for photoluminescence process using spectro fluorometer setup.....	38
<b>Fig. 2.13 (b)</b> Schematic for energy level diagram of photoluminescence process.....	38
<b>Fig. 2.14</b> Schematic for experimental setup for device dark and photo current analysis.....	39
<b>Fig. 3.1</b> Schematic of Al: CdS-PS: p-Si MSM heterostructure PD.....	42
<b>Fig. 3.2 (a)</b> FESEM and (b) FETEM micrographs of CdS nanopowder, insets show particle size histograms.....	43
<b>Fig. 3.3</b> FESEM micrograph of (a) PS surface, (b) CdS-PS surface, (c) CdS-PS:p-Si interface and EDX spectrum of (d) CdS-PS: p-Si heterostructure.....	44

<b>Fig. 3.4</b> (a) UV-vis absorbance spectra, (b) $(\alpha hv)^2$ vs. $hv$ plot of nanostructured CdS, (c) UV-vis reflectance spectra of PS:p-Si and CdS-PS:p-Si heterostructure.....	45
<b>Fig. 3.5</b> PL spectra of (a) CdS nanostructure, (b) PS:p-Si structure, (c) CdS-PS:p-Si heterostructure and (d) schematic of CdS nanostructure luminescence mechanism.....	46
<b>Fig. 3.6</b> (a) Forward biased semi-log dark $I-V$ plot, inset shows the plot under reverse bias, (b) plot of defect conduction model fitted forward $I-V$ curve for PS:p-Si and CdS-PS: p-Si heterostructure.....	48
<b>Fig. 3.7</b> plot of $R_\lambda$ and $EQE$ vs. $\lambda$ at -2V for both the heterostructure PDs, inset shows absorbance and $R_\lambda$ spectra of nanostructured CdS.....	49
<b>Fig. 3.8</b> (a) Linear $I-V$ plot under dark and illumination condition, (b) intensity dependent $I_{ph}$ plot, (c) On-off kinetics under different intensity of 400 nm and (d) response and recovery time calculation for CdS PS:p-Si heterostructure PD at -2V.....	51
<b>Fig. 4.1</b> FESEM view of (a) PS:p-Si surface, (b) PS:p-Si interface, (c) ZnS-PS:p-Si surface (inset shows particle size histogram), (d) ZnS-PS:p-Si interfaces.....	55
<b>Fig. 4.2</b> (a) Selected areas for EDX analysis, EDX spectra for (b) ZnS region, (c) PS region and (d) p-Si region.....	55
<b>Fig. 4.3</b> (a) absorbance spectra of bare ZnS (inset shows transmittance spectra), (b) Tauc plot for ZnS, (c) UV-vis reflectance spectra of p-Si, bare ZnS, PS and ZnS-PS, (d) PL spectra of bare ZnS, PS and ZnS:PS heterostructure.....	57
<b>Fig. 4.4</b> (a) Forward biased semi-log dark $I-V$ plot (inset shows the plot for reverse bias) and (b) plot of defect conduction model fitted $I-V$ curve for PS and ZnS: PS devices...	58
<b>Fig. 4.5</b> (a) Schematic of ZnS-PS device, plot of (b) semi-log $I-V$ under dark and illumination condition, $R_\lambda$ vs. $\lambda$ (c) at -4V for ZnS-PS and PS devices, (d) at -3, -4 and -5V for ZnS-PS device.....	60
<b>Fig. 4.6</b> (a) Intensity dependent $I_{ph}$ plot, time response kinetics of ZnS-PS device under 365 and 400 nm at (b) 0V, (c) -4V, (d) response time calculations.....	61
<b>Fig. 5.1</b> Schematic of the devices (a) PD1, (b) PD2 (c) and bare ZnO.....	65



**Fig. 5.2** Planar FESEM images of (a) PS:p-Si, (b) bare ZnO on glass, (c) ZnO-PS:p-Si, (insets-particle size histograms), Cross sectional FESEM images of (d) PS:p-Si, (e) ZnO:glass and (f) ZnO-PS:p-Si interfaces.....66

**Fig. 5.3** (a) Selected areas for EDX analysis of ZnO-PS:p-Si interfaces, EDX spectra of (b) p-Si region, (c) PS region and (d) ZnO region.....67

**Fig. 5.4** (a) Absorbance spectra of bare ZnO inset shows its transmittance spectra, (b) Tauc plot for bare ZnO, (c) reflectance spectra of p-Si, ZnO, PS:p-Si, ZnO-PS:p-Si...68

**Fig. 5.5** PL spectra of (a) ZnO-PS:p-Si, (b) bare ZnO and (c) schematic of PL mechanism.....69

**Fig. 5.6** (a) Forward bias semi-log dark *I-V* plot (inset shows the plot under reverse bias condition), (b) plot of defect conduction model fitted *I-V* curve for PD1, PD2 and bare ZnO.....71

**Fig. 5.7** Plot of EQE and  $R_{\lambda}$  vs.  $\lambda$  for (a) PD1, (b) PD2 and (c) bare ZnO at -2V, inset shows similar plots at -0.5V.....72

**Fig. 5.8** Semi-log *I-V* plot under dark and illumination condition for (a) PD1, (b) PD2 and (c) bare ZnO, (d, e) energy band diagram for the respective PDs under reverse bias conditions.....74

**Fig. 5.9** On-off transient kinetics of (a) PD1, (b) PD2 and bare (c) ZnO at -2V bias condition.....75

**Fig. 5.10** Planar FESEM images of ZnO-PS:p-Si annealed at (a) 200 °C, (b) 300 °C, (c) 400 °C and (d) 500 °C, (Insets show cross sectional FESEM images), (e-h) particle size histograms for annealed samples (i) change of thickness with annealing conditions...77

**Fig. 5.11** (a) Selected area for EDX analysis of ZnO-PS:p-Si, EDX spectra of ZnO-PS:p-Si (b) untreated, annealed at (c) 200 °C, (d) 300 °C, (e) 400 °C and (f) 500 °C (Insets show elemental contents).....78

**Fig. 5.12** Selected area for EDX analysis of ZnO-PS:p-Si (a) untreated, (e) annealed at 500 °C, EDX spectra for untreated ZnO-PS:p-Si (b) p-Si region (c) PS region (d) ZnO region, annealed ZnO-PS:p-Si at 500 °C (f) p-Si region (g) PS region (h) ZnO region..79

<b>Fig. 5.13</b> (a) Absorbance spectra, (b) Tauc plot and (c) transmittance spectra for annealed bare ZnO, (d) reflectance spectra for annealed ZnO-PS:p-Si heterostructure.....	80
<b>Fig. 5.14</b> (a) PL spectra for untreated and annealed ZnO-PS:p-Si heterostructure, (b) zoomed view of PL spectra for annealed ZnO-PS:p-Si heterostructure.....	81
<b>Fig. 5.15</b> (a) semi log dark $I-V$ curve and (b) $\ln I-\ln V$ plot of forward dark current for annealed ZnO-PS:p-Si heterostructure device.....	82
<b>Fig. 5.16</b> (a-d) Responsivity plot at -2 V (Insets show plots at 0 V), PDCR plot under illumination of (e) 375 nm, (f) 400 nm for annealed ZnO-PS:p-Si heterostructure.....	83
<b>Fig. 5.17</b> Semi- log dark and photo $I-V$ plots for ZnO-PS:p-Si heterostructure device annealed at (a) 200 °C, (b) 300 °C, (c) 400 °C and (d) 500 °C.....	84
<b>Fig. 5.18</b> Time response kinetics for ZnO-PS:p-Si heterostructure device annealed at 200 °C, 300 °C, 400 °C and 500 °C for biasing of (a-d) -2V and (e-h) 0V.....	85
<b>Fig. 6.1</b> Planar FESEM micrographs of PS:p-Si (a) as-prepared, aged for (b) 18 days, (c) 36 days and (d) 60 days, [insets show cross-sectional FESEM micrographs], (e-h) pore size histograms.....	89
<b>Fig. 6.2</b> (a) Cross- sectional selected areas for EDX analysis, EDX spectra of (b) PS region (area 1), (c) p-Si region (area 2) and (d) RCA treated bare p-Si surface.....	90
<b>Fig. 6.3</b> (a) Planar selected area for EDX analysis, EDX spectra of PS:p-Si (b) as-prepared, (c) aged for 18 days, (d) 36 days, (e) 60 days and (f) plot of atomic percentage of O with ageing.....	91
<b>Fig. 6.4</b> (a) XRD patterns [inset shows enlarged view] and (b) Raman spectra of p-Si, as-prepared and aged PS:p-Si heterostructure, PL spectra of (c) as-prepared PS:p-Si for different $\lambda_{Exc.}$ and (d) as-prepared and aged PS:p-Si for $\lambda_{Exc.}$ of 275 nm [inset of (c) shows PLE spectra of as-prepared PS:p-Si].....	92
<b>Fig. 6.5</b> (a) Linear dark $I-V$ plot, [inset shows plot at reverse bias], (b) forward biased semi-log dark $I-V$ plot (c) defect conduction model fitted forward $I-V$ plot and (d) plot of variation of $\phi_b$ and $n$ with device ageing under dark and illumination condition.....	94

**Fig. 6.6** *Semi-log I-V* plot under dark and illumination condition for (a) as-prepared and (b-e) aged device and (f) comparative plots of *semi-log* photo *I-V* for fresh and 90 days aged device [inset shows plot under dark condition].....95

**Fig. 6.7** (a) Schematic of the prepared MSM device, energy band diagram for (b) as-prepared and (c) aged device under illumination, (d) plot of  $R_L$  and EQE vs.  $\lambda$ .....97

**Fig. 6.8** (a) light intensity dependent  $I_{ph}$ , on-off kinetics for (b) as-prepared, (c) 60 days and (d) 90 days aged device for different illumination wavelengths, (e) as-prepared and aged device plotted together and (f) calculation of response time for illumination of 400 nm at -3 V bias.....99

**Fig. 6.9** Planar FESEM micrographs of PS:p-Si annealed at (a) 200 °C (b) 300 °C, (c) 400 °C and (d) 500 °C, [insets show cross-sectional views], (e) pore size histogram, (f) change of pore size/thickness with annealing.....101

**Fig. 6.10** Selected area of annealed PS:p-Si for EDX analysis, EDX spectra of (b) untreated and annealed PS:p-Si at (c) 200 °C (d) 300 °C, (e) 400 °C and (f) 500 °C....102

**Fig. 6.11** (a) Reflectance spectra of bare p-Si and annealed PS:p-Si, (b) PL spectra of untreated and annealed PS:p-Si, (c) zoomed view of PL spectra for annealed PS:p-Si.....103

**Fig. 6.12** (a) Semi log dark *I-V* plot, (b) forward dark  $Ln I-Ln V$  plot, (c) variation of ideality factor and (d) barrier height for annealed PS:p-Si.....104

**Fig. 6.13** Responsivity plot for PS:p-Si annealed at (a) 200 °C, (b) 300 °C, (c) 400 °C and (d) 500 °C at -2V [Insets show plots at 0V], PDCR plots for annealed PS:p-Si under illumination of (e) 365 nm and (f) 400 nm.....106

**Fig. 6.14** Dark and photo semi log *I-V* plot for annealed PS:p-Si at (a) 200 °C, (b) 300 °C, (c) 400 °C and (d) 500 °C [inset of (d) show linear *I-V* plot].....107

**Fig. 6.15** (a-h) Time response plots for annealed PS:p-Si at 0V and -1V biasing under illumination of 365 and 400 nm, (i) different stages of pyroelectric effect, (j,k) fitted curves for calculation of response times.....108

## List of tables

<b>Table 3.1</b> Comparative performance analysis of Al: CdS- PS:p-Si heterostructure PD with some of the best reported Si-based PDs in the literature.....	52
<b>Table 5.1</b> Comparative performance analysis of PD 1, 2 with some of the best reported ZnO and Si-based PDs in literature.....	76
<b>Table 6.1</b> Comparative performance analysis of Al/PS: p-Si structure PD with some of the best reported Si-based PDs in the literature.....	100
<b>Table 6.2</b> Performance analysis of annealed Al/PS:p-Si MSM Schottky device.....	109
<b>Table 7.1</b> Summarized results of the whole dissertation work.....	115

# Chapter 1

## **Introduction**



## 1

**Introduction****1.1 Background and motivation**

Silicon is one of the most abundant element on the crust of Earth (27.2 % wt. %), which comes at second place after oxygen which has abundance of 45.5 wt. % [1]. Also, it's the widely used semiconductor material in the application of fabricating numerous electronic devices. Nonetheless, its applicability in optoelectronic field is constrained due to its narrow and indirect energy band gap property.

Porous silicon (PS), which was first accidentally discovered by Uhlir et al. [2] in the Bell laboratory, has broad and direct energy band gap due to quantum confinement effect [3] in silicon nanostructure. PS also shows strong visible luminescence at room temperature under UV light illumination as reported by Canham et al. [4] in 1990s. These basic advantageous characteristics of PS make it competent for employing in optoelectronic field. PS can be considered as a network of nano-sized silicon atoms surrounded by pores or void spaces on the surface of bulk c-Si. It also maintains same crystal structure as that of bulk c-Si, besides it shows unique character of large surface to volume ratio as that of a nanomaterial [5]. Additionally, it also has good mechanical strength and chemical stability, so it's widely applicable in various photo or gas sensors, solar cells, batteries and other optoelectronic devices [6]. Due to surface roughness, PS has lower refractive index compared to that of bulk Si, which subsequently reduces reflectance of incident light from its surface. Surface roughness also triggers trapping of incident light, which subsequently make it suitable for solar

cell applications [7]. To explore various properties and application potentials of PS, quite a number of works have been performed till now, some of these will be mentioned here. Works related to exploration of physical, optical and electrical properties of PS give basic idea about possibilities of its application areas. In this regard, one may mention a recent report by K. Kulathuraan et al. [8] on the influence of varying etching current density on morphological, optical and electrical properties of nanostructured PS:p-Si. They found that device ideality factor decreases with increase in etching current density and attributed this to decrease in interfacial roughness of the heterojunction. Another work by A.G. Roman et al. [9], reported development of graphene nanoflakes and carbon nanotubes passivated porous silicon heterostructures and achieved maximum current gain upto 40 under illumination condition. N. Naderi et al. [10] reported stabilisation of optical properties of porous silicon by deposition of reduced graphene oxide on it using electrophoretic deposition (EPD) method. However, from literature [11,12], it's quite clear that since the last two decades, PS and its hybrid heterostructures are taking attention of researchers' for utilising these in fabricating and analysing more specifically photodiodes (PDs) and solar cell devices.

UV-vis photodetectors (PDs) are most commonly used in astronomical detection, video recording system, memory storage, optoelectronic circuits etc., whereas, NIR PDs are basically used for medical imaging and diagnostics, surveillance, remote sensing etc. UV-vis-NIR range broadband PDs are widely used in various application fields as compared to that of narrow band traditional PDs operating in either UV, visible or NIR range of electromagnetic (EM) spectrum. This is the reason behind attraction of researcher's interest in developing and demonstrating such broadband PDs for wide application areas [13]. The band of UV light that reach the earths surface, can cause serious health hazards to human beings due to prolonged exposure to these radiations [14]. Also, these rays can't be detected by normal human eyes, due to which presence of these radiations in any region should be monitored with effective scientific ways. Many recent reports are available for developing UV PDs based on wide band gap semiconductor materials such as ZnO, ZnS, TiO<sub>2</sub> etc. [15]. Some of the recent reports in this direction are mentioned here for ready bibliography on the field. Many reserarch groups [16] most recently developed high responsive and ultrafast UV-vis PDs based on some inorganic perovskite nanomaterials. Among these, Tao Yang et al.



[16] recently reported highly stable ones based on CsPbI<sub>3</sub> nanorods with excellent responsivity of 3.0 kAW<sup>-1</sup> and ultrafast response time of 0.05 ms. It is evident from literature [17], that bare Si or PS based PDs are typically used for photo sensing purposes in visible to near infrared (NIR) range of EM spectrum, as Si and PS has low electrical band gap of ~1.1 and 2.1 eV respectively [18]. However, Si or PS based PDs may be modified to widen their effective wavelength range by incorporating wide band gap semiconductor materials to be operative in the range extending from UV to NIR. In this context, it's worthwhile to mention a recent study by Y. Cheng et al. [19], who developed deep UV to NIR range broadband photovoltaic PDs based on methylammonium lead iodide (MAPbI<sub>3</sub>) perovskites thin films grown on silicon nanoporous pillar arrays (Si-NPA) with maximum photoresponsivity of 8 mA W<sup>-1</sup> and response time of 250 μs. Here Si-NPA template is prepared by hydrothermal etching of heavily doped silicon wafer, whereas MAPbI<sub>3</sub> thin film is deposited on this template by one step spin coating method. Another work by U.M. Nayef et al. [20] reported porous silicon-based PDs which has photo sensing ability in the UV-visible range of 200- 900 nm, but with very low responsivity of 0.045 AW<sup>-1</sup>. However, the same group, later on in their another report [21], witnessed enhancement in photodetection property of PS:n-Si structure with maximum responsivity of 0.5 AW<sup>-1</sup> in the wavelength range of 400-900 nm after deposition of bismuth oxide (Bi<sub>2</sub>O<sub>3</sub>) nanoparticles on PS surface. In another recent study, N. Naderi et al. [22] reported highly sensitive porous silicon carbide based (SiC) UV sensors with sensitivity of 54.5. They adopted RF sputtering to deposit SiC of thickness 1 μm on n-type Si, then UV assisted electrochemical etching was carried out for fabrication of porous SiC thin films. N.A. Abdulkhaleq et al. [23] synthesized MgO nanoparticles via laser ablation technique and deposited these on PS to finally devise MgO NPs: PS based broadband photodetectors with maximum responsivity of 0.4 AW<sup>-1</sup>. U.M. Nayef et al. [20] prepared wideband gap (3.2 eV) TiO<sub>2</sub> nanoparticles by laser ablation technique to finally devise TiO<sub>2</sub>: PS based UV-vis photodetectors exhibiting maximum responsivity of ~0.05 AW<sup>-1</sup>.

Porous silicon can also be used as efficient photovoltaic devices because of its high surface to volume ratio, antireflective surface, adjustable energy band gap and high photo absorption across the solar irradiation range [24]. In this regard, S. Mahmoudi et al. [25] recently reported design of optimized porous silicon based solar cells by metal

assisted chemical etching (MACE) process which exhibited maximum efficiency upto 13.6%. D.H. Shin et al. [26] recently reported graphene: porous silicon based Schottky junction stable solar cells showing maximum power-conversion efficiency (PCE) of 4%. Fang et al. [27] reported high efficiency (~11.4%) silicon nanowire based solar cells and attributed their high efficiency to excellent anti-reflection property of the slatingly aligned silicon nanowire arrays.

Apart from optoelectronic applications for photodiode and solar cell devices, PS is also widely used as chemical or gas sensors for its stability and porous nature [28]. Highly reactive and sensitive surface of PS can adsorb different analytes on its surface. It can also record the subsequent changes in its key electrical properties such as conductance, capacitance etc. These key parameters can be utilized to employ PS for sensing different chemicals or gases. Here, one can mention a recent work by Mohd. Husairi et al., who developed ZnO: PS based high sensitive improvised ethanol gas sensors using electrochemical impedance technique [29]. F.A. Harraz et al. [30] fabricated meso-PS structures with top-Ag contacts for sensing different organic solvents such as ethanol, methanol, acetone, chloroform etc. at room temperature. The rapid change of surface charge density upon solvent infiltration into the mesoporous structure may be the reason for observed high sensitivity and response of the sensor. M. Li et al. [31] reported high response NH<sub>3</sub> and NO<sub>2</sub> gas sensors using PS with intermediate pore sizes of 100-200 nm. Pt thin film contacts deposited by RF magnetron sputtering on PS were used as electrodes and the sensor exhibited fast response-recovery characteristics and good reproducibility. In another work, A.M Alwan et al. [32] devised an efficient bimetallic nanoparticle embedded porous silicon carbon monoxide (CO) gas sensors, here gas molecule get adsorbed inside the porous substrate and metallic nanoparticles increase specific surface area of the sensor.

Many researchers had reported cadmium sulphide (CdS) nanostructure based optoelectronic devices by incorporating it with Si or PS substrates for devising UV-visible photodiodes. CdS is a II-VI group semiconductor material with bulk band gap of ~2.4 eV at room temperature. It has unique characteristic of light absorption in the visible range, which make it a potential candidate for visible light sensing device applications [33]. It can be synthesised and deposited on either PS or glass substrates

by using various techniques, viz. chemical bath deposition, SILAR (successive ionic layer adsorption and reaction), thermal evaporation, wet chemical synthesis process etc. [34-36]. To discuss more about recent progresses in this context, one can mention a work by R.A Ismail et al. [37], who fabricated CdS: PS heterojunction PDs by depositing CdS on PS substrate by spray pyrolysis technique with maximum responsivity of  $0.3 \text{ AW}^{-1}$  in the wavelength range of 300- 1100 nm. M. Moghaddam et al. [38] reported photosensing property of nanostructured CdS decorated ZnO heterostructure exhibiting responsivity upto  $0.62 \text{ AW}^{-1}$  for UV light illumination, which may be an evidence for incorporating these inorganic compounds on PS for broad range UV-visible photosensing purposes. However, devising high reponsive and efficient PDs or solar cells using CdS nanostructure is still a challenge for researchers [34-38]. For optimisation of the CdS nanostructure based devices, lots of works are yet to be done for in-depth exploration of its physical or chemical properties and their correlation.

Another II-VI semiconducting material, zinc oxide (ZnO), has also attracted intense attention of worldwide researchers due to its exclusive physical properties and application potential in solar cells, LEDs, photodiodes, gas sensors, transparent electrodes etc [39]. ZnO is a II-VI semiconductor material with a wide band gap of 3.37 eV with large excitonic binding energy of 60 meV at ambient temperature. Single crystalline p or n-type Si wafer is widely used as a reliable substrate in optoelectronics or IC technology. When ZnO thin film is directly grown or deposited on Si substrate, there is a large stress between these two due to mismatch in their lattice constants and thermal expansion coefficients [40]. However, PS substrates being an open and porous structure with adjustable roughness, good absorbability and large surface to volume ratio may act as suitable nucleation site for accomodating ZnO nanostructures on it and hence overcome the limitations of Si substrates. Additionally, nanostructured ZnO films show emission in the blue or green region of EM spectrum, so when it is combined with PS which usually emits light in the red or yellow region, it would be possible to devise white LEDs for various applications [41]. ZnO nanostructure has high absorption in the UV range, but has transparency in the Vis-NIR range of EM spectrum, on the other hand PS shows absorption in visible range, making PS: ZnO heterostructure suitable for UV-NIR wide band photo sensing PDs [42,43]. Excessive

intrinsic defect states or oxygen vacancy sites present in nanostructured ZnO make it exhibiting n-type semiconductor characters [44]. It also has high density of intrinsic trap or defect states, which further enhances photo responsivity and response time. High response time of ZnO PDs can also be ascribed to low transient time of charge carriers compared to the ones present in other nanomaterial based PDs. Researchers adopt numerous techniques viz. spray pyrolysis, wet chemical method, pulse laser deposition, metal organic chemical vapour deposition, RF and pulsed DC magnetron sputtering etc. for deposition of ZnO nanostructures on PS substrates [43]. Among these processes cost effective magnetron sputtering method provides uniform, highly adhesive and transparent ZnO thin film on the PS or glass substrates [45]. Lei Luo et al. [46] reported UV PDs based on n-ZnO:p-Si heterojunction, though the device exhibited very low responsivity of  $0.07 \text{ AW}^{-1}$  under high biasing voltage for UV light illumination. A.S. Ibraheem et al. [47] recently fabricated Al-doped zinc oxide: p-Si (AZO: p-Si) heterostructure based high responsive UV PDs. They used spray pyrolysis technique to develop AZO over p-Si substrate and studied UV sensing of the PD for different concentration of Al in the heterostructure. From literature, one can mention some other works (apart from PDs) related to ZnO: PS heterostructures for assembling various other devices, viz., solar cells chemical or gas sensor, optical waveguides, memristive devices, biosensors etc. [48]. M. Taherkhani et al. [49] studied solar cell application potential of ZnO nanoflowers decorated over porous silicon template. Chemical bath deposition technique was used to deposit ZnO nanoflowers on PS substrate taking zinc acetate dihydrate and ammonia as precursors. ZnO nanoflowers enhance surface roughness of PS substrate, which increase amount of incident light captured in the heterostructure and consequently make it suitable for photovoltaic device application. A.M. Alwan [32] in a recent study reported hazardous carbon monoxide (CO) gas sensors based on bimetallic (Au-Pd) nanoparticle embedded porous silicon heterostructure. They carried out ion reduction process for embedding Au-Pd alloy nanoparticles onto PS substrate. Due to increased surface area and higher barrier height of the prepared heterostructure, it shows improvements in sensitivity and temporal response as compared to that of bare p-Si. A recent work by T.V.K. Karthik et al. [50] reported CO<sub>2</sub> gas sensing properties of SnO<sub>2</sub>: PS and ZnO: PS heterostructures. SnO<sub>2</sub> and ZnO were deposited on macro porous silicon (PS) by CBD method taking tin

chloride, zinc carbonate and zinc acetate respectively as precursors. F.S. Husairi et al. [51] recently reported ZnO: PS heterostructure based ethanol solution sensors. ZnO nanostructure was deposited on PS by catalytic immersion technique using zinc nitrate hexahydrate as precursor and urea as stabilizer. In their study, they revealed that high concentration of deep-level defects and oxygen interstitials present in the heterostructure played a significant role in the sensing process. L. Haji et al. [52] reported anti resonant optical waveguide based on oxidised PS (SiO<sub>x</sub>: PS) for bio sensing applications. This planar optical waveguide prepared from PS by modulating refractive indices of the heterostructure are found to be more efficient as compared to that of conventional resonant waveguides. L. Martinez et al. [53] reported fabrication of ZnO: PS nanocomposites for memristive device applications. Mesoporous silicon (meso-PS) templates were first prepared by electrochemical etching of p<sup>++</sup>-type Si wafer, then ZnO thin films were deposited over it by sol-gel spin coating method, taking zinc acetate dehydrate, mono ethanolamine as precursors. Meso- PS substrate modifies the ZnO grain size and consequently enhances oxygen vacancies for efficient resistive switching performances. F. Miao et al. [54] reported ZnO-NW: Si-NW nanocomposites for immobilization of enzymes on a glucose biosensor. Si-NW arrays are fabricated by Ag-metal assisted electroless etching, further aqueous thermal decomposition method was used to synthesize ZnO nanowires on the walls of Si-NWs. Here, large specific surface area, abundant microspace and high isoelectric point (IEP) fracture of the nanocomposite allows effective fluid circulation for immobilization of enzymes.

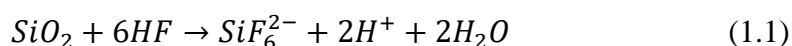
Another II-VI group semiconductor material, zinc sulphide (ZnS), is getting much attention among the researchers since last few decades due to its applicability in communication technology, optoelectronic devices such as solar cells, LEDs, lasers, PDs etc. [55]. It has wide band gap of ~3.7 eV, which is favourable for UV light sensing applications. Again being a non-toxic nanomaterial, it may act as a promising alternative to overcome the toxicity issues of Cd-buffer layer present in CdS nanostructures. ZnS thin films, when integrated with silicon or porous silicon substrates, may perform as broad band UV-Vis photo sensing PDs. These thin films can be prepared or deposited over silicon or PS substrates by numerous deposition techniques viz., chemical bath deposition, chemical vapour deposition, spray pyrolysis, thermal evaporation, pulsed laser deposition, DC or RF sputtering etc. [56,57]. U.M.

Nayef [56] recently reported UV PDs based on ZnS: c-Si and ZnS: PS heterostructures, but their PDs were limited to provide responsivity only upto  $\sim 0.07 \text{ AW}^{-1}$  for UV light illumination. In a recent work, Kai Zhang et al. [57] reported synthesis of ZnS:InP nanowire heterostructure based rigid flexible UV PDs by chemical vapour deposition process. These flexible PDs exhibited photoconductive gain upto  $\sim 1.1 \times 10^3$  with response time of  $\sim 0.5$  sec.

Apart from these potential application fields, mentioned above, PS and its hybrid heterostructures are widely studied for utilising their applicability in other areas too. In this regard, one can mention PS based microcavities developed for display technology, optical waveguides, Bragg gratings or reflectors used as optical sensors, LEDs, optical memory, anti reflection coating, biosensors etc. [58]. Refractive indices of PS, fabricated using electrochemical etching method is easily tunable, which evidently helps for developing optical waveguides [59]. PS also has key property of efficient electroluminescence, due to which it can be used for fabricating LEDs [60]. Non linear properties of PS make it suitable for employing in optical memory units [61]. PS has low refractive index as compared to that of bare Si, due to which it can be used as anti-reflection coating in constructing solar cells [62]. In addition to these properties, due to its large surface to volume ratio, PS also has capability for controlling fluid circulation, specially in enzyme immobilisation to be used in various biosensors [30].

## 1.2 Synthesis methods of porous silicon (PS)

Formation of porous silicon in presence of HF involves formation of various bonds viz., Si-Si, Si-H, Si-O, Si-F at the surface of silicon substrate. Among these bonds, F being a highly electronegative element makes the Si-F bond more polar, which in turn makes the silicon atom more vulnerable to nucleophilic attack. The Si-F bond enthalpy drives the main chemical dissolution reaction involved in the formation of porous silicon. In presence of HF solution, the insulating layer of silicon dioxide ( $\text{SiO}_2$ ) over silicon wafer can be removed and a stable dianion of silicon hexafluoride ( $\text{SiF}_6^{2-}$ ) gets dissolved in water, the overall reaction is given by,



Hence, HF becomes the most vital additive for the preparation of porous silicon which is free from insulating oxide layer for processing and developing microelectronic devices.

Based on IUPAC recommendations for the different categories of porous materials, PS can be classified in the following three categories:

1. Microporous (pore size < 2nm)
2. Mesoporous (pore size between 2-50 nm)
3. Macroporous (pore size > 50 nm)

Depending upon type of conductivity and dopant concentration of silicon wafers, porous silicon of different pore morphologies can be synthesized as per the scheme shown in fig 1.1. From p and n-type Si wafers micro and macroporous silicon can be obtained respectively, whereas, from  $p^+$ ,  $p^{++}$ ,  $n^+$  Si wafers mesoporous silicon can be obtained by electrochemical etching process.

Two broad approaches for fabrication of PS can be classified as: top down and bottom up approaches. In top down approach, two methods viz. electrochemical etching and electroless (metal assisted) etching are used, whereas, in bottom up approach, PS is fabricated by template assisted synthesis method. These methods are schematically presented in fig. 1.2 and briefly discussed in the following sub sections.

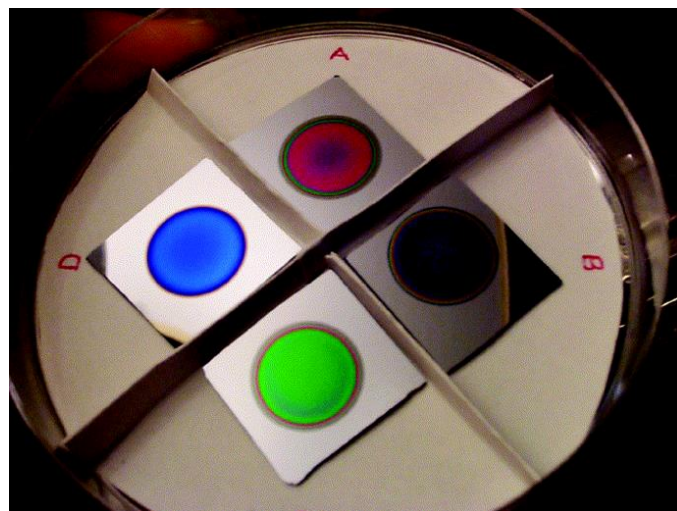


Fig. 1.1 PS fabricated with different pore sizes exhibiting different luminescence (Image courtesy-[63])

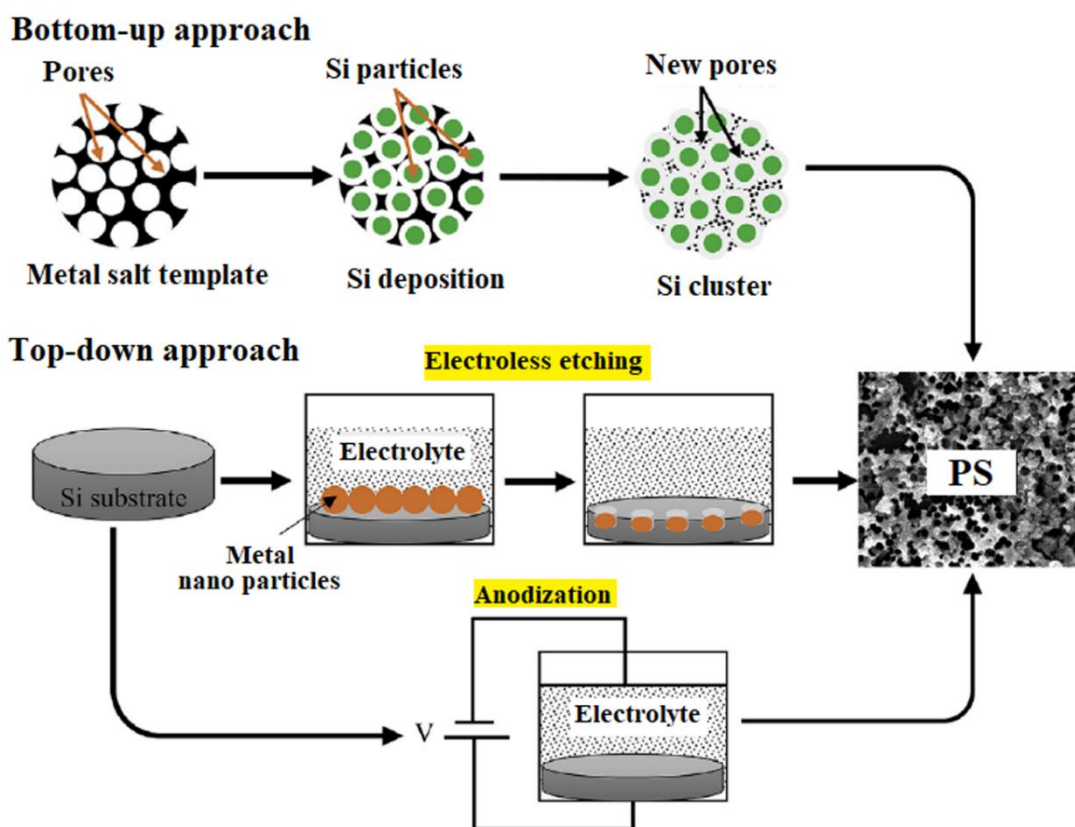


Fig. 1.2 Schematic for top-down and bottom-up approaches for synthesis of PS (Image courtesy- [64])

### 1.2.1 Electrochemical etching or anodization method

This method of PS preparation is the widely used technique which is highly reproducible and provides good control over porosity, pore size, thickness etc. [65]. The method involves etching of n or p-Si carried out in a non-reactive teflon cell, where aqueous hydrofluoric acid (HF) acts as electrolyte. Aluminium or copper in contact with silicon wafer acts as working electrode (anode) and a platinum wire dipped in the electrolyte acts as counter electrode (cathode). This etching process is in general performed in a constant current mode (galvanostatic) to achieve good control over reproducibility and various physical properties of PS. n-type Si wafer etching process requires external illumination for getting homogenous PS layer. Illumination generates electron-hole pairs and holes are the driving agents for pore formation. On the other hand, for p-type Si wafers, where holes are the majority carriers, external illumination is not essential [66]. The chemical and physical factors controlling the etching mechanism are briefly discussed in the section to follow.



### 1.2.1.1 Chemical factors controlling anodization

The holes in the valence band starts the process of oxidation by getting driven to the surface of Si atom due to application of electric field and the Si atom become susceptible to get attacked by nucleophiles ( $F^-$ ,  $H_2O$ ) in the electrolyte solution. Here a competition between F, O and H takes place to form chemical bonds such as Si-F, Si-O and Si-H at Si atom surface during electrochemical corrosion process. Among these bonds, Si-F bonds are highly polarized due to strong electronegativity of fluorine, and these bonds are more vulnerable to be attacked by nucleophiles than other Si-atom bonds. Therefore, if a Si atom is attached to a fluoride ion, that atom is rapidly attacked by additional  $F^-$  ions and gets removed from the wafer surface. Some Si-O bonds are also formed on the Si surface, but these bonds are significantly less in number as these bonds are chemically attacked by  $F^-$  ions. Thus,  $F^-$  ions also help in removing the insulating oxide layer present on the Si surface that terminates propagation of pores on the film. Further, holes in the valence band move towards the PS matrix to oxidize Si atoms that are accessible to the fluoride ions in the electrolyte solution, resulting in more thinning of the Si layer adjacent to the PS: c-Si interface. The surface Si atoms capped with weak Si-H bonds also get attacked by  $F^-$  ions and releases  $H_2$  gas from the electrolyte solution [65]. The schematic of the chemical reaction mechanism is shown in fig. 1.3.

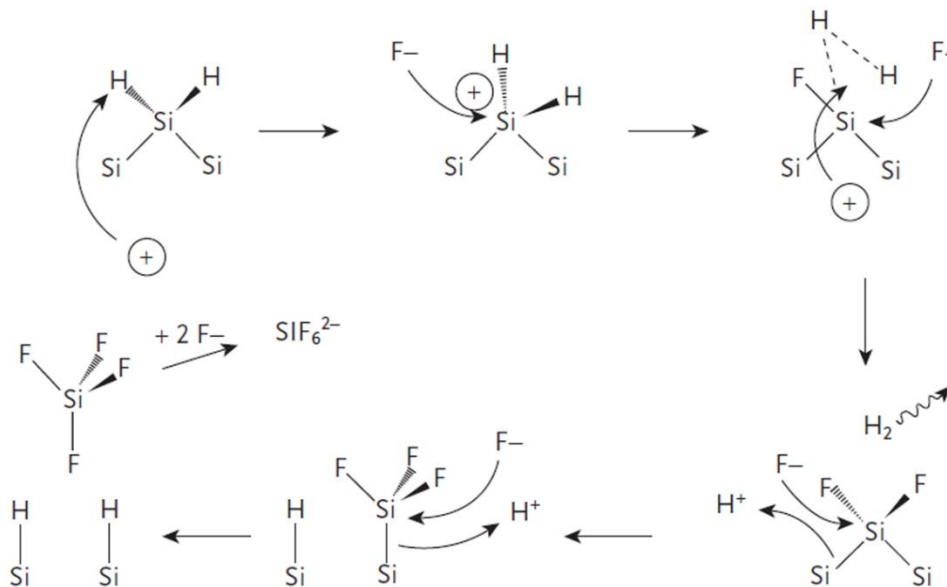


Fig.1.3 Mechanism for electrochemical etching of Si in HF solution (Image courtesy- [66])

### 1.2.1.2 Physical factors controlling anodization

The physical factors determining pore morphology of etched PS are primarily the conductivity type, concentration of the dopants and the band structure of bare c-Si. In particular, the most significant factor that plays a crucial role in pore formation is the availability of the holes in the valence band. Availability of these holes in Si wafer is mostly influenced by magnitude of the applied electric field, electrolyte HF concentration and illumination intensity. Pores formed and oriented perpendicular to the surface of the wafer are called “current line - oriented pores”, or “current pores”. These pores are formed at higher current densities and the reason behind this is that the equipotential surfaces are parallel to the wafer surface, resulting into a “path of least resistance” for the holes along the perpendicular direction of the wafer [66]. Similarly, we get branching of pores in PS when the “path of least resistance” for the holes is sideways through pore wall [66]. p-type Si has surplus of valence band holes, so the process of etching is not limited by their availability. However, for n-type Si, there is scarcity of holes, which in turn limit pore density in the exposed area of the wafer. Therefore, during etching process for n-type Si, usually light illumination is required depending upon the desired pore morphology for various applications.

### 1.2.2 Metal assisted chemical etching

Metal-assisted etching is an inexpensive and convenient method in comparison to other methods such as vapour-liquid-solid (VLS) growth etc. for preparation of silicon nanowires (Si-NW). This method of etching was discovered by Kelly et al. [67] in the 1990s and later a group led by Peng [68] practically implemented the method for fabrication of Si-NWs. Here, selective metal nanoparticles are deposited on a Si wafer surface as catalyst to perform the etching process. The noble metal is usually deposited on Si wafer by various methods of deposition viz., photo patterning, ion implantation or electro less deposition [69]. Hydrogen peroxide ( $H_2O_2$ ) used as oxidising agent in the reaction gets decompose on the metal surface and helps injecting the valence band holes into the Si substrate, causing formation of pores on the substrate. Further, the metal nanoparticles drill into the wafer surface, leaving behind an array of vertically aligned Si-NWs. Peng et al. [70] in 2005 first attempted fabrication of vertically aligned Si-NWs by electroless deposition of Ag nanoparticles on p and n-type Si wafers with

different resistivities as shown in fig. 1.4. They used a mixture of aqueous  $\text{H}_2\text{O}_2$ , HF and ethanol as electrolyte for the etching reaction. Recently, B. Moumni et al. [71] reported preparation of PS adopting metal assisted electroless etching process and its modification to Si-NWs by simply tuning the oxidant ( $\text{H}_2\text{O}_2$ ) to higher concentration values. J. M. Chen [72] recently reported metal assisted chemical etching (MACE) process for fabrication of porous silicon nanostructures from lightly doped p-type Si wafer using palladium metal. Fig. 1.5 shows tilted view SEM images of Si nanopillar, nanorods, nanopencil and nanocones fabricated by Ag-metal assisted etching of p-type Si for developing efficient photovoltaic devices [73].

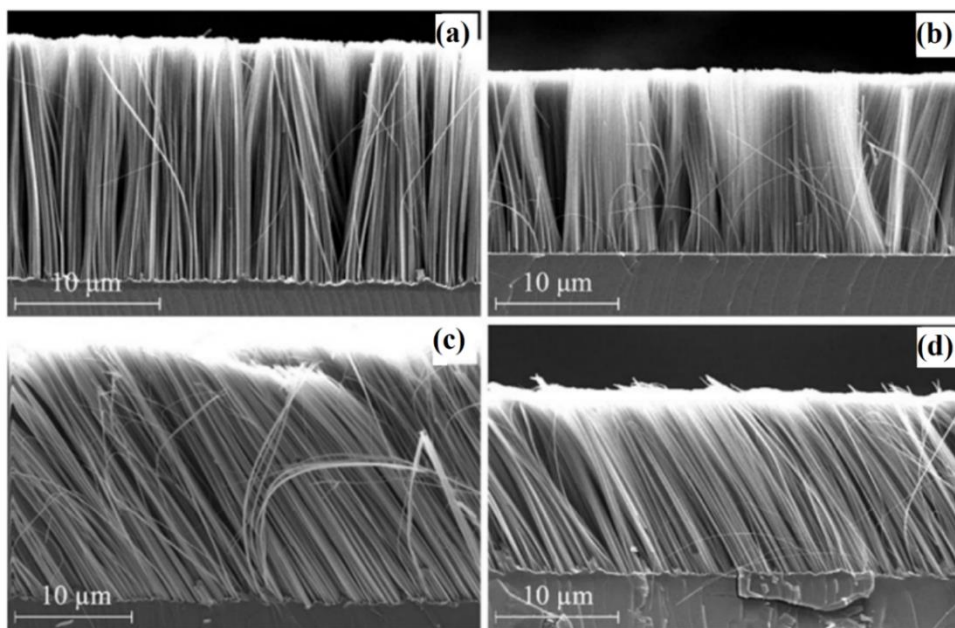


Fig. 1.4 Cross-sectional SEM images of Si nanowires synthesised by metal-assisted stain etching of (100) p-type Si. (Image courtesy: [66])

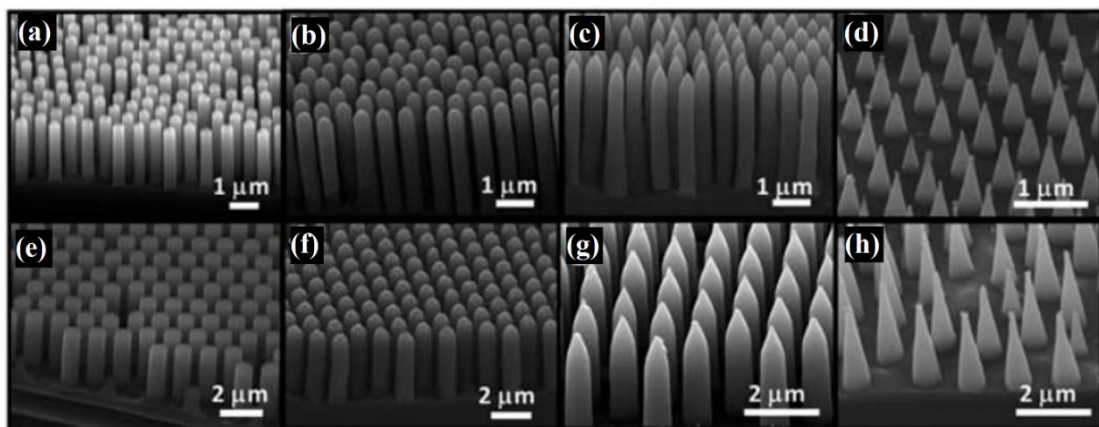


Fig. 1.5 Tilted view SEM images of (a and e) nanopillars, (b and f) nanorods, (c and g) nanopencils, and (d and h) nanocones arrays synthesised by Ag-assisted MACE method (Image courtesy: [73])

### 1.2.3 Template assisted approach

This method is a physio-chemical one, which uses nano porous structures as sacrificial templates to fabricate porous nanostructures. In general, various hard and soft materials such as silica spheres, alumina membrane, polycarbonate, gas bubble templates etc. are the typical templates used for this purpose. Researchers adopt numerous chemical electrodeposition methods to fabricate 1D porous nanostructures [74-76]. A. Esmanski et al. [74] reported fabrication of macroporous Si for application as negative electrodes for lithium ion batteries from silica microsphere templates. They prepared macroporous silicon from different sized templates of pre-sintered silica microspheres by CVD method. The SEM images for these are shown in fig. 1.6 (f-h) [74]. Another group led by Bao Z. H. [75] synthesised mesoporous silicon by magnesiothermic reduction of SBA-15 mesoporous silica template. Here, magnesium (Mg) is used to convert three-

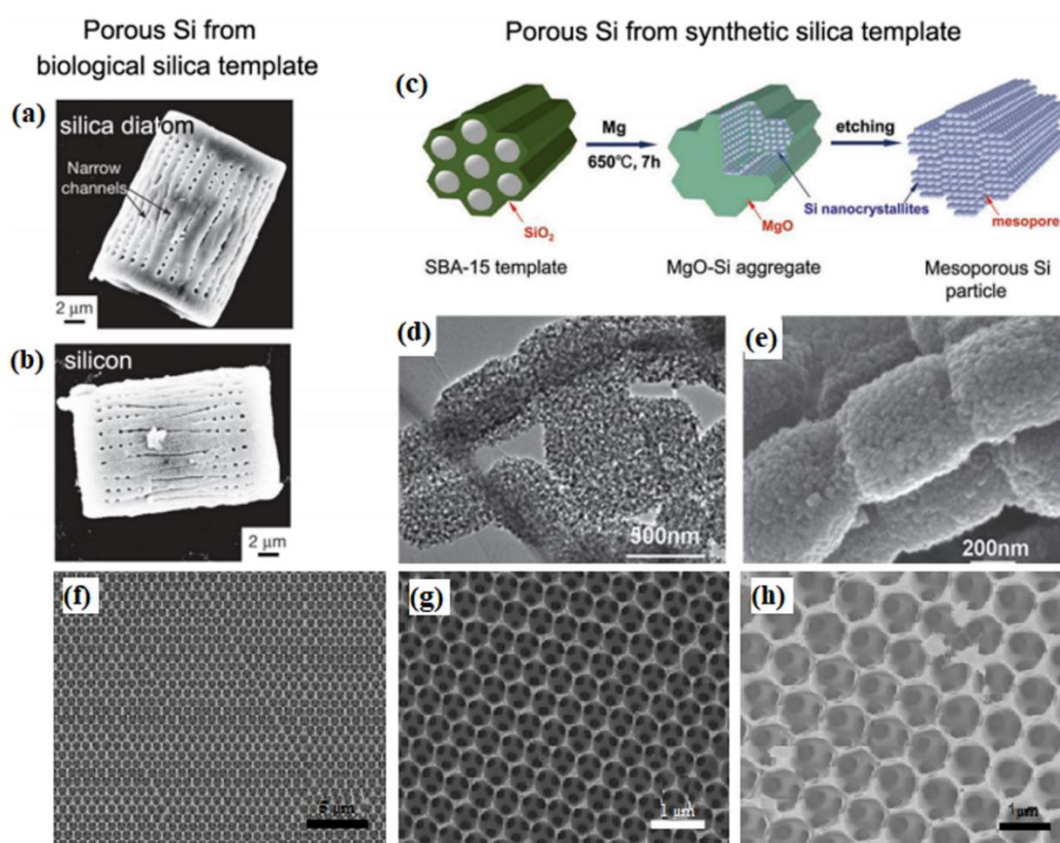


Fig. 1.6 (a) Silica diatom frustule template. (b) Si replica after magnesiothermic reduction, (c) Schematic diagram for magnesiothermic reduction of SBA-15 mesoporous silica template. (d) TEM and (e) SEM image of a mesoporous Si particle replica, (f-h) SEM image of macroporous Si from different size templates of pre-sintered silica microspheres by CVD method (Image courtesy: [74-76])

dimensional nanostructured silica templates into continuous Si nanocrystallites at temperature of  $\sim 650^{\circ}$  C, which on further etching gives mesoporous silicon as schematically illustrated in fig. 1.6 (a-c) [75]. Jia H. P. et al. [76] developed three-dimensional novel mesoporous Si from synthetic silica templates for application as anode material in high power lithium-ion batteries [Fig. 1.6 (d-e)]. However, nano structures prepared by this method suffers from poor quality and uncontrollable porosity, shape and size.

In present dissertation work, cost effective electrochemical anodization process has been adopted for fabrication of PS, which has high reproducibility and better control over porosity, size, thickness etc. of the nano porous structures.

### 1.3 Synthesis methods of hybrid structures from PS

Passivation of pores on the PS surface by some nanomaterials has proven further enhancement in its optical and electrical properties as mentioned in earlier studies by various research groups [77].

Many research groups have reported preparation of CdS nanostructures for diverse fields applications by various cost effective chemical or hydrothermal methods using different chemical reagents [77,78]. Further, the performance of CdS based optoelectronic device can be enhanced by incorporating it with Si or PS substrates. As mentioned earlier, CdS nanostructure can be incorporated on PS substrates by using numerous techniques, viz. wet chemical synthesis process, chemical bath deposition, SILAR (successive ionic layer adsorption and reaction), pulsed laser ablation, thermal evaporation etc. [34-38,78]. In a recent work, S. Manna et al. [78] designed p-Si:n- CdS radial nanowire based high efficiency PDs. The authors fabricated vertically aligned Si-NWs by Ag-metal assisted electroless etching of p-Si wafer and then deposited CdS on it by pulsed laser deposition from a CdS target. The PDs can function in the broad vis-NIR range of EM spectrum with maximum responsivity of  $\sim 1.4 \text{ AW}^{-1}$ . Fig. 1.7 (a-d) shows the tilted view FESEM images of the prepared bare Si-NWs and CdS: Si NWs core shell along with EDX spectrum, which further confirms formation of CdS:Si NWs junction arrays [78].

Motivated by these works and to explore further in depth in this field, the present work utilizes cost effective wet chemical synthesis process for synthesis of CdS

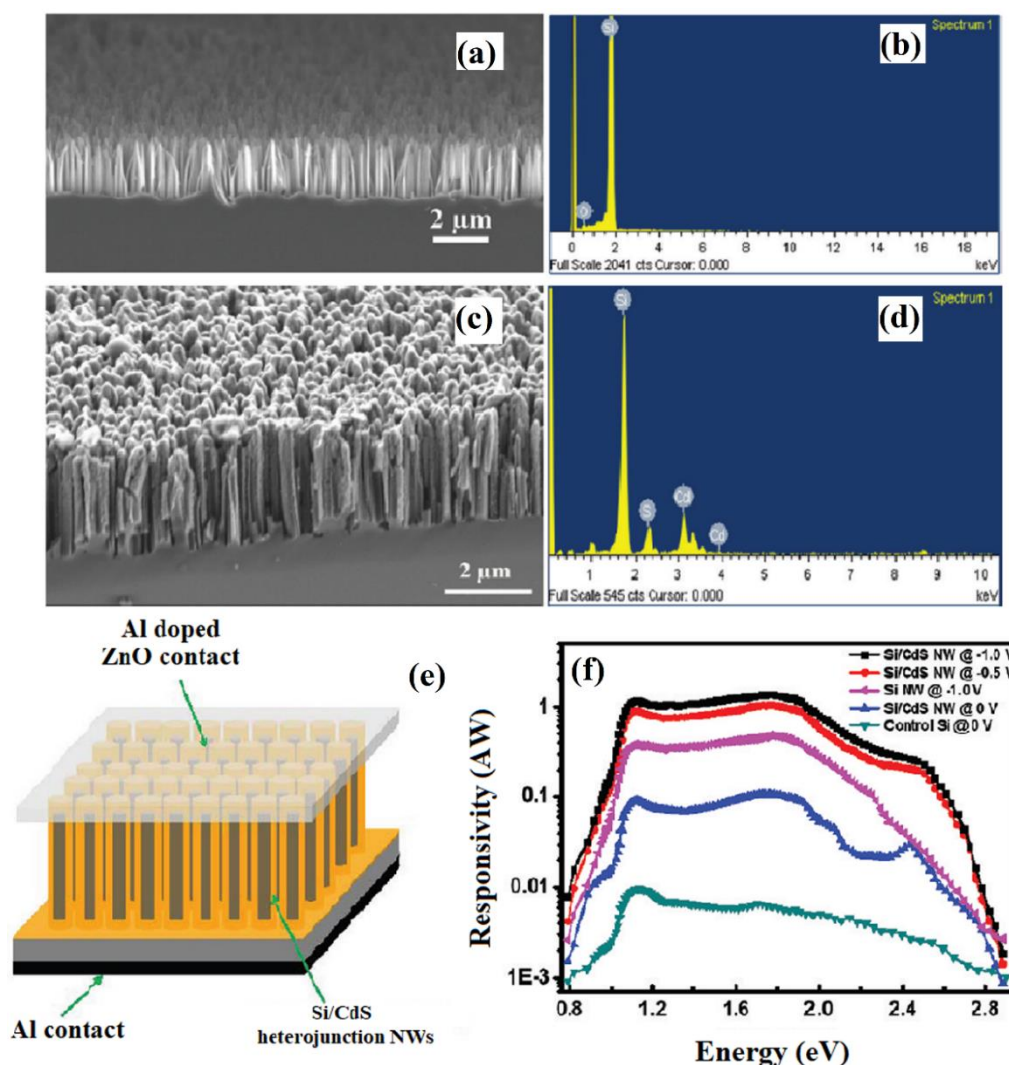


Fig. 1.7 Tilted view FESEM images and EDX spectra of (a-b) Si-NWs and (c-d) CdS: Si NWs respectively, (e) schematic of Si: CdS heterojunction device, spectral responsivity of the device (Image courtesy- [78])

nanostructures, were deposited on PS:p-Si substrates to fabricate CdS:PS:p-Si heterostructures by thermal evaporation method. The details of the experimental process is to be discussed in Chapter 2 to follow.

In recent works by worldwide researchers, it has been visualised that there is enhancement in optical and electrical properties of silicon or porous silicon due to incorporation of ZnO nanostructures on it [19,45,79-82]. For deposition of nanostructured ZnO on Si or PS substrates, researchers adopt numerous techniques viz. hydrothermal, spray pyrolysis, physical vapour deposition, pulse laser deposition, MOCVD, RF and pulsed DC magnetron sputtering etc. To mention few recent works, a group led by Y. Cheng [19] deposited nanostructured ZnO layer on MAPbI<sub>3</sub>-

perovskite film grown on Si- nano porous array (Si-NPA) template by RF magnetron sputtering to fabricate broadband PDs. They used a high purity (99.999%) ZnO: Al<sub>2</sub>O<sub>3</sub> ceramic target for sputter deposition of ZnO, which acts as a transparent electrode and an electron transport layer over the MAPbI<sub>3</sub> thin film. The details of the fabrication process of Si-NPA: MAPbI<sub>3</sub>: ZnO heterojunction PD is presented in the schematic of fig. 1.8. T. Yen et al. [79] reported fabrication of nanocrystalline ZnO:Si heterojunction MSM PDs with enhanced photo responsivity as compared to that of bare p or n-type Si. The authors used RF magnetron sputtering to deposit nanocrystalline ZnO on Si substrate. N.H. Hardan et al. [80] developed a wideband UV photodetector based on ZnO:p-Si heterostructure. They first deposited a uniformly distributed thin ZnO seed layer on p-Si substrate using a reactive DC sputtering process, then prepared ZnO nanorods over it by low-temperature hydrothermal process. R. K. Biroju et al. [81] reported growth of ZnO nanowires and nanorods (ZnO-NW/NRs) on Si or quartz substrates by using physical vapour deposition (PVD) method and studied their photoluminescence properties. They carried out growth of ZnO-NW/NRs using highly pure (99.99%) commercial zinc powder as source material placed in a quartz furnace chamber. Another group of researchers led by S. Sampath [82] studied photocatalytic and photoelectrocatalytic activity of ZnO:PS heterostructure. For this study, they

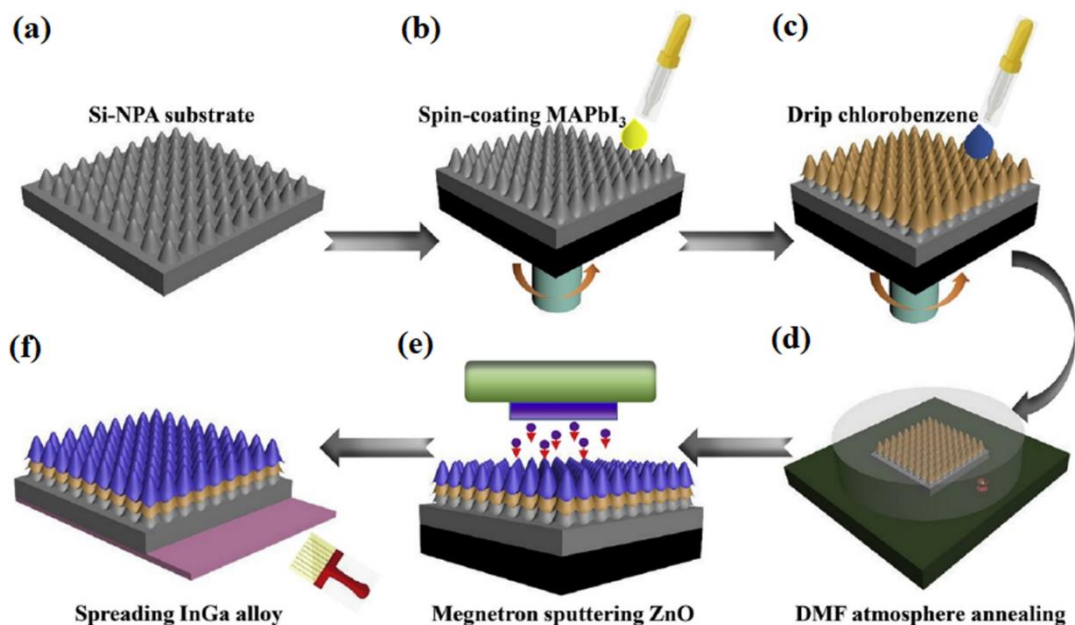


Fig. 1.8 Schematic of fabrication process of Si-NPA: MAPbI<sub>3</sub>: ZnO heterojunction PD (Image courtesy-[19])

deposited ZnO nanostructures on PS substrate by atomic layer deposition (ALD) method using water and diethyl zinc  $[(C_2H_5)_2Zn]$  as precursors. ZnO nanostructures thus formed are found to be larger than pore size of nanopores on PS substrate, as there is disappearance of porous layer of PS as clearly seen from the FESEM images in fig. 1.9 (g-h). Figure 1.9 (a-h) shows the planar and/or cross-sectional/ tilted view FESEM images of ZnO nanostructures developed on Si or PS substrates by different research groups [45,79-82].

For ZnO incorporation in the present dissertation work, cost effective pulsed DC magnetron sputtering [45], has been used which provides uniform, highly adhesive and transparent ZnO thin films on the PS, quartz and glass substrates. Details of the sputtering process involved in the experiment will be briefly discussed in Chapter 2 of the thesis to follow.

Similarly, ZnS thin films can be deposited over silicon or PS substrates by numerous deposition techniques viz., chemical bath deposition, chemical vapour deposition, spray pyrolysis, thermal evaporation, pulsed laser deposition, DC or RF sputtering etc [83-89]. In a recent work, W. Tian et al. [87] fabricated branched nano ZnS-ZnO heterostructure based flexible UV PDs with widerange photo responsivity. These authors first prepared ZnS nanowires on a PET substrate by thermal evaporation method, taking commercial ZnS powder as source material in a horizontal tube furnace. Finally, over this structure ZnO branched ZnS nanowires were coated by hydrothermal method taking equimolar aqueous solution of zinc nitrate and hexamethylene-tetramine



Fig. 1.9 Tilted view FESEM image of (a) Si-NPA and (b) Si-NPA: MAPbI<sub>3</sub>: ZnO heterostructure, (c-d) planar & cross sectional FESEM image of ZnO thin film on glass and (e) n-ZnO: p-Si, planar FESEM image of (f) ZnO NWs-Si and (g-h) PS & ZnO: PS heterostructure (Image courtesy: [45,79-82])



A. K. Katiyar et al. [88] reported fabrication of white LEDs based on vertically aligned ZnS NWs grown on Si-NW template. Vertically ordered Si-NW array template was first prepared by metal assisted chemical etching process taking Au as catalyst from p-type Si wafer. ZnS NWs were further deposited on Si-NW template by pulsed layer deposition (PLD) method using highly pure (99.999%) ZnS target. Device fabrication was completed by depositing a thin layer of transparent and highly conducting Al-doped ZnO (AZO) over the ZnS NW film structure by PLD method and a back contact of thick Al layer deposited by thermal evaporation method. H.J. Xu et al. [89] constructed ZnS: Si-nanoporous pillar array (ZnS: Si-NPA) for study of photoluminescent property for possible application in solid state light emitting devices. The authors first prepared Si-NPA template by hydrothermal etching of p-Si wafer in the solution of HF and ferric nitrate. ZnS nanocrystals were grown over it by heterogeneous reaction process taking zinc acetate and hydrogen sulphide as precursors. Planar and/or cross-sectional/ tilted view FESEM images of some ZnS nanostructures developed on Si, PS or Si-NW substrates by different physical or chemical deposition methods are shown in fig. 1.10 (a-i) as reported elsewhere [87-89].

In the present dissertation work, for fabrication of ZnS: PS: p-Si heterostructure, thermal evaporation of commercial ZnS powder annealed at 200 °C has been carried out over PS:p-Si substrate in a vacuum coating unit. Detailed experimental process and conditions are discussed in the next chapters.

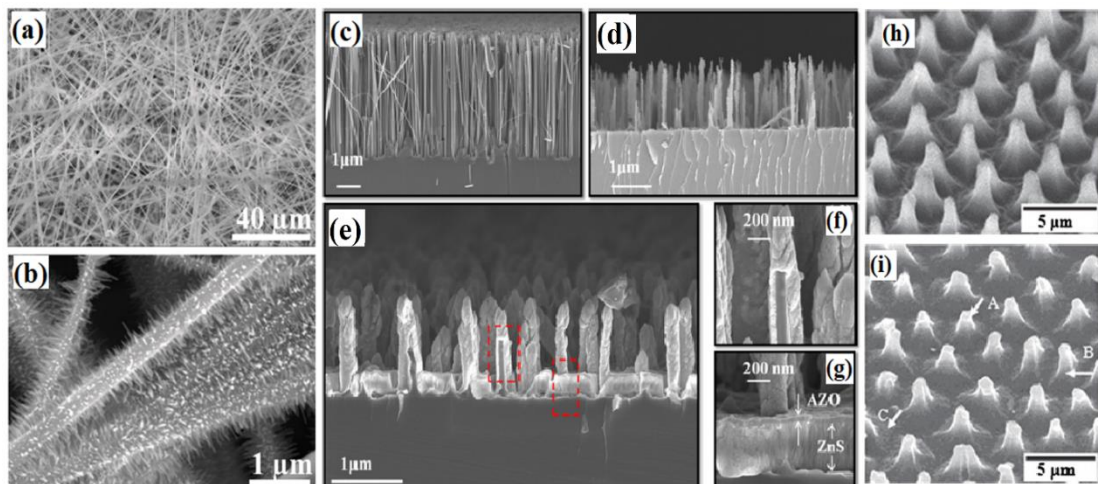


Fig. 1.10 FESEM images of (a) ZnS nanowire and (b) ZnO branched ZnS NWs, (c) Si NWs fabricated by MACE, (d) Si NWs after KOH treatment, (e) fabricated well-separated radial heterojunction arrays by depositing ZnS and AZO, (f) cross sectional image of Si core and ZnS shell, (g) bottom part of AZO:ZnS layer, tilted view FESEM image of (h) Si-NPA, (i) ZnS: Si-NPA (Image courtesy: [87-89])

## 1.4 Objectives of the thesis works

In the last few decades, there are ample developments in exploring key properties and characteristics of PS and its hybrid structures for utilisation in various fields of applications. Nonetheless, some key properties of these heterostructures like optical, electrical and morphological properties are still left to be studied more elaborately for exploring further application potentials of these heterostructures. In the present thesis work, detail study has been carried out on the significant properties of bare PS and its hybrid structures with three inorganic nanostructured materials: CdS, ZnO and ZnS. Metal semiconductor metal (MSM) based photodiodes are also fabricated using these heterostructures for studying photo sensing empolyability in broadband UV-visible range of electromagnetic spectrum.

## 1.5 Outline of the thesis

The whole thesis work is composed of the following 7 chapters:

In **Chapter 1**, the background of the research works related to PS and its hybrid heterostructures that motivated the author to study and explore related important characteristics are included. Various methods used in synthesis of these heterostructures are also briefly discussed.

In **Chapter 2**, discussion about the materials and methods used to carry out the experimetal works of the thesis have been made. The different methods used for basic characterisations of PS and its hybrid structures are also briefly illustrated.

In **Chapter 3**, synthesis of nanostructured CdS powder and CdS-PS: p-Si heterostructure for study of their optical, morphological and electrical properties have been reported.

In **Chapter 4**, fabrication of ZnS-PS: p-Si heterostructure using thermal evaporation method for study of its morphological, optical and electrical properties are briefly discussed.

In **Chapter 5**, effect on morphological, optical and electrical properties of as-prepared and annealed ZnO-PS: p-Si heterostructure fabricated by pulsed DC sputtering method is presented.

In **Chapter 6**, effect of auto-ageing and annealing temperature on optical, morphological and electrical properties of PS:p-Si heterostructure have been investigated.

**Chapter 7** presents the overall summary of the entire thesis work and the future research prospects on the basis of present work.

Finally, in the **Appendix** section, the research publications of the author in referred journals and conference proceedings resulted out from the present thesis work has been listed. It also includes the list of national and international conferences/workshops attended with full paper presentation in poster and oral mode.



# Chapter 2

## **Materials and methods**

## 2

## Materials and methods

### 2.1 Materials used

Materials used in the present work are: p-type silicon (p-Si), hydrofluoric acid, cadmium chloride, sodium sulphide, zinc sulphide and zinc oxide. Other reagents used for synthesis and cleaning are: acetone, chloroform, ammonium hydroxide, hydrogen peroxide, ethanol, hydrochloric acid, isopropyl alcohol, sodium hydroxide, polyethylene glycol, deionized water etc.

p-type silicon wafer purchased from Macwin, India, is used for preparation of porous silicon (PS). This p-Si wafer is boron doped, (100) oriented, single side polished and it has diameter of 7.62 cm, thickness of 375 ( $\pm$  25)  $\mu\text{m}$  and resistivity of (1-10)  $\Omega$  cm. Other chemicals used for RCA cleaning [65] of the wafer are deionized water, acetone, chloroform, ammonium hydroxide, hydrogen peroxide, hydrochloric acid, isopropyl alcohol and sodium hydroxide. Electrochemical etching of p-Si wafer is performed using 48% hydrofluoric acid and ethanol (99.99% pure) as electrolytes in an electrochemical cell made of Teflon. For synthesis of cadmium sulphide (CdS) nanoparticles, polyethylene glycol, cadmium chloride and sodium sulphide are used. Zinc sulphide (ZnS) bulk powder of 99.99% purity is used for fabrication of ZnS-PS: p-Si heterostructure. Zinc oxide (ZnO) nanoparticles are coated by sputter deposition on glass and porous silicon substrates using previously prepared ZnO target [90] and argon gas (99.999% pure). The chemicals and reagents are purchased from Merck

Emplura/Emparta ACS and Sigma-Aldrich, are of high purity (>90%) and are used without any further purification.

One can distinguish between various orientation of p and n-type silicon wafers by mere inspecting them. Fig. 2.1 shows the location of (110) natural cleavage planes in (100) oriented p and n-type silicon wafers with dashed lines and wafers will easily break along these planes. For (100) p-type wafer, there is one major flat parallel to the (110) cleavage plane, it also has a minor flat at 90° clockwise from the major flat. But, (111) p-type wafer has only one major flat as shown in figure. For (100) n-type wafer, there is a major flat parallel to the (110) cleavage plane and parallel to this flat there is a minor flat on the other side of the wafer. (111) n-type wafer has a major flat parallel to the cleavage plane and it also has a minor flat at 45° clockwise from the major flat.

Although the conductivity type (p or n) of the purchased wafers are specified by the manufacturer, these are also verified in the laboratory by the author. Among the methods to verify this, the hot-probe method [66] is a simpler one to differentiate between p and n type semiconductors. The method is shown in fig. 2.2. Two probes of a digital multimeter (DMM) are placed over the wafer, positive terminal of the DMM

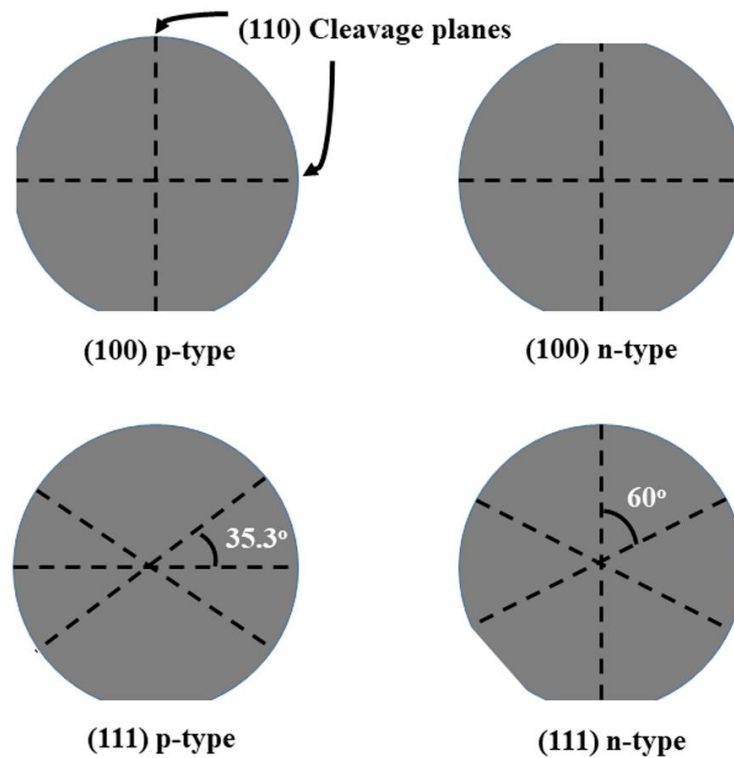


Fig. 2.1 Schematic of [(100), (111)] oriented p-type and n-type Si-wafers

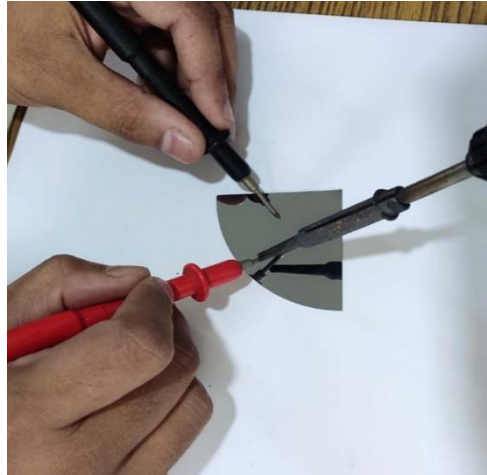


Fig. 2.2 Hot probe measurement of conductivity type

is heated with a soldering iron and the negative one is connected to the ground. The sign of the voltage difference between the probes indicated in the DMM identifies whether the wafer is p or n type. Negative sign indicates a p-type wafer and positive one ascertains n-type.

## 2.2 Methods of preparations

### 2.2.1 Cutting, cleaning and anodization of silicon wafers

In order to break the (100) p-type wafer in four equal quadrants of ~2.4 cm dia, first the wafer is placed on top of a tissue on a flat hard surface. Using a sharp needle, firm pressure is applied to the edge of the (110) cleavage plane on the major flat of the wafer and the needle is pulled off until it snaps the wafer into two semi-circular portions. Now, these two portions are cut into four quadrants using the similar process along the line parallel to the minor flat of the cleavage plane.

For atomically smooth cleaning and removing the native oxide layer of the p-Si wafer RCA (Radio Corporation of America) treatment [65] is adopted. The RCA cleaning process performed using the following steps:

- 1) The wafer is first boiled in ethanol for 30 min.
- 2) Successively sonicated in chloroform, acetone and ethanol for 10 min in each.
- 3) Soaked for 15 min at 75° C in RCA-1 solution ( $\text{H}_2\text{O}:\text{NH}_4\text{OH}:\text{H}_2\text{O}_2::5:1:1$ )
- 4) Soaked for 15 min at 75° C in RCA-2 solution ( $\text{H}_2\text{O}:\text{HCl}:\text{H}_2\text{O}_2::5:1:1$ )
- 5) Finally rinsed with deionized water and ethanol, then kept in vacuum desiccator for further use.



Among numerous processes for preparation of porous silicon as mentioned in Chapter 1, electrochemical etching process is adopted in the present study. The setup is shown in fig. 2.3. The electrochemical cell is made up of Teflon and the electrolytes used are hydrofluoric acid and ethanol. Before proceeding to preparation of PS for further study, to get thoroughly cleaned and reproducible surfaces, sacrificial porous layer developed on RCA cleaned p-Si wafer is removed using the following steps:

- 1) The RCA cleaned wafer is sonicated in isopropyl alcohol for 10 min.
- 2) The sample is etched in 3: 1 solution of HF and ethanol at current density of  $200 \text{ mA cm}^{-2}$  for 30 s.
- 3) Etched wafer is then soaked in 1 M aqueous strong base solution of NaOH for 5 min, in this solution PS layer get easily dissolved.

After this process, the wafer and the Teflon cell are rinsed with ethanol and the electrolyte solution of HF and ethanol in the ratio of 1: 1 is added to the cell for PS etch process. As shown in fig. 2.3, platinum (Pt) wire dipped into the electrolyte solution acts as the counter electrode (cathode) and thick aluminium (Al) sheet at the back of the Si wafer acts as the working electrode (anode). The reason for use of Pt electrode is that it's very less reactive to aqueous hydrofluoric acid. The effective etching surface area of the Si wafer is  $\sim 4.53 \text{ cm}^2$ . The wafer is etched for a total time 202 s by varying the current density in the range of  $17.2\text{-}22.1 \text{ mAcm}^{-2}$ . The current density is manually controlled by the single-output Agilent 6634B 100 watt DC power supply.

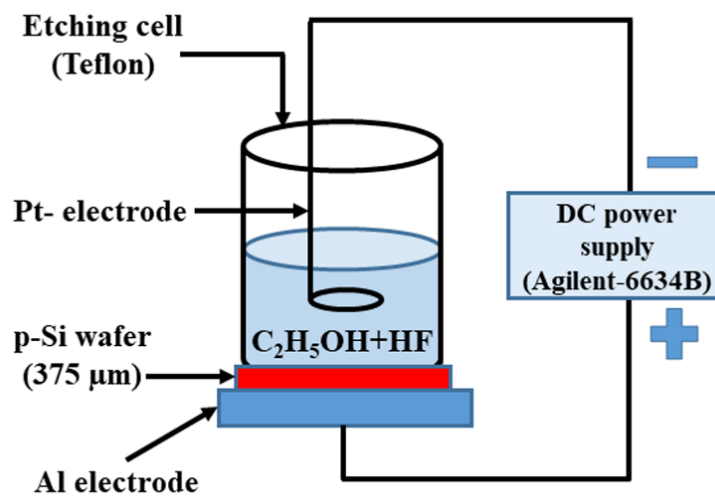


Fig. 2.3 Experimental setup for electrochemical etching

Some of the specifications of this power supply are given below:

- 1) Operates very fast (response time  $\sim 400 \mu\text{s}$ ) and has very low-noise outputs.
- 2) Provides maximum output power upto 100 W, with  $V_{\text{max}} = 100 \text{ V}$  and  $I_{\text{max}} = 1 \text{ A}$ .
- 3) Has DC measuring accuracy upto  $V \sim 12 \text{ mV}$  and  $I \sim 2.5 \mu\text{A}$  at room temperature.
- 4) Has protection features to ensure DUT (device under test) safety, also it is portable to carry.

### 2.2.2 Deposition of CdS and ZnS powders and metal electrodes

Planar and sandwich electrode configurations of different metals i.e. aluminium (Al), gold (Au) on PS or PS based heterostructures are deposited by thermal evaporation method using vacuum coating unit (HIND, Model: 12A4D) at our own laboratory. The schematic of this setup is shown in fig. 2.4. CdS nano powder and annealed bulk ZnS powder are also deposited on glass along with PS:p-Si substrates using this setup at chamber pressure of  $\sim 10^{-5}$ - $10^{-6}$  mbar. For deposition of these materials by adopting resistive heating method, Al wire is taken on tungsten coil, whereas Au foil, CdS and ZnS powders are taken on molybdenum boats.

### 2.2.3 Preparation of CdS nanoparticles

Synthesis of cadmium sulphide (CdS) nanoparticles is carried out by wet chemical method. The synthesis process is schematically shown in fig. 2.5. Among various techniques used for CdS synthesis [91-93], this one is much simpler and cost effective, it also provides high reproducibility. In this process, cadmium chloride and sodium sulphide are used as cadmium and sulphide source precursors respectively. Whereas,

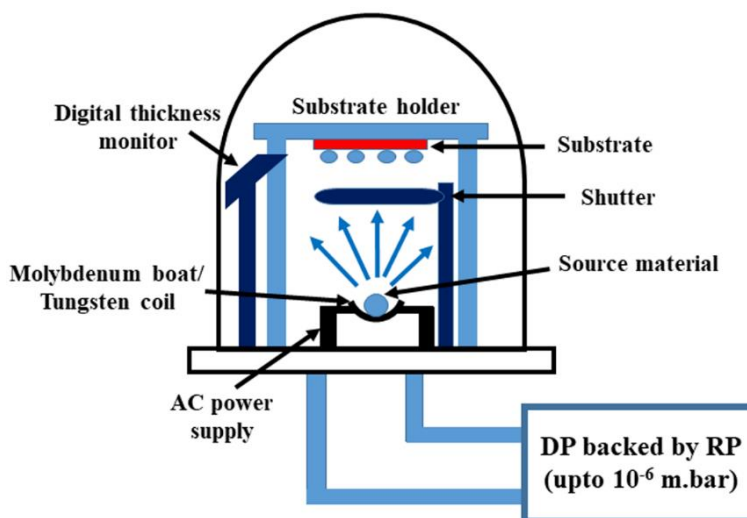


Fig. 2.4 Schematic for thermal evaporation method using vacuum coating unit

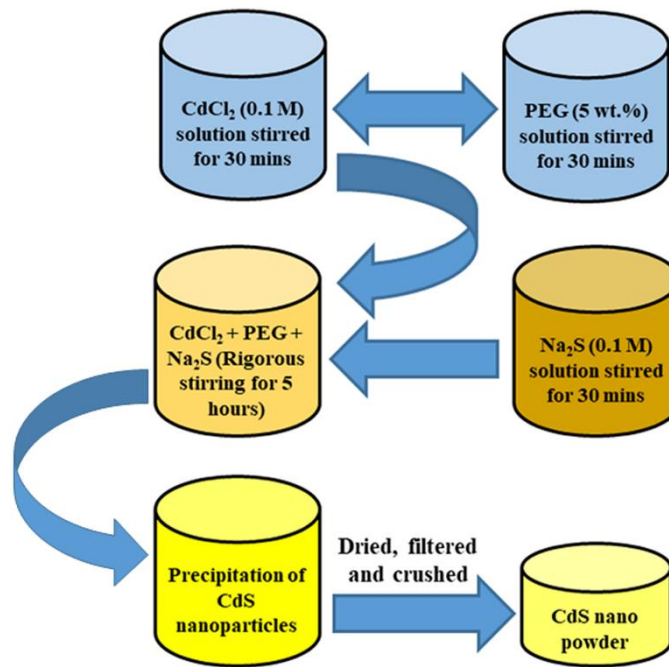


Fig. 2.5 Schematic for wet chemical synthesis of CdS nanopowder

polyethylene glycol (PEG) is used as capping agent which offer colloidal stability to prevent agglomeration of the nanoparticles.

#### 2.2.4 Deposition of nanostructured ZnO

Nanostructured ZnO is deposited on glass, Si and PS substrates by pulsed DC magnetron sputtering process. The schematic of the whole sputtering setup is shown in fig. 2.6. It is a physical vapour deposition technique particularly effective for the sputtering of metals and insulating non-conducting materials which can acquire charges. Its primary advantage over conventional DC sputtering is that, it reduces formation of arcs which occur when the target material used for coating takes on a charge [94]. The sputtering system is equipped with three numbers of water-cooled planar magnetrons and a rotatable substrate holder. A ZnO sputtering target, prepared from high purity (99.99%) ZnO powder as described by Sarma et al. [95], is placed in one of the magnetrons at a distance of 45 mm from glass and PS:p-Si substrate. Prior to deposition, the chamber is evacuated up to a base pressure of  $\sim 2 \times 10^{-5}$  mbar. Ar (99.999% purity) is used as the sputtering gas at a gas pressure of  $\sim 2 \times 10^{-2}$  mbar. A pulsed DC of few hundreds of volts is applied to the target material, which acts as cathode and the substrate to be coated acts the anode. The gas in the vacuum chamber

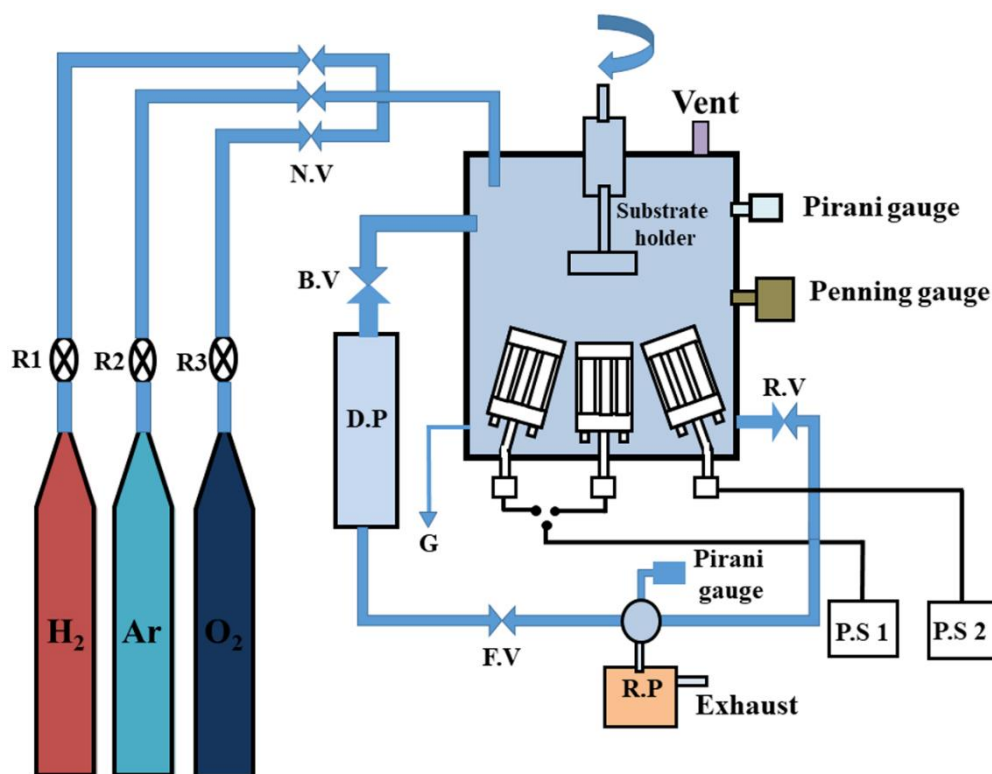


Fig. 2.6 Schematic for pulsed DC magnetron sputtering of ZnO nanoparticles

gets ionized, move towards the target and collides with the target surface to sputter off atoms to get deposited on the substrate. Magnetic field around the target material holds the bombarding gas ions nearer to it for maximum sputtering yield from the target. ZnO film deposition is carried out by rotating the substrate holder for 20 min while maintaining the sputtering power at 70 W with 100 kHz pulse frequency and 70% duty cycle to achieve uniform coating. The setup used is from other laboratory of our department.

### 2.2.5 Annealing of bulk ZnS powder and Schottky devices

Bulk ZnS powder (99.99% pure) is annealed at 200 °C for 2 hrs in a high temperature horizontal tube furnace (Electroheat, NASKAR). The schematic block diagram of the setup is shown in fig. 2.7. The annealed powder is deposited on PS: p-Si substrate by thermal evaporation method to get ZnS-PS:p-Si heterostructure. Annealing of the powder makes it contamination free and increases crystallinity. PS and its hybrid heterostructure based Schottky devices are also annealed at different temperatures (200-500 °C) using the same furnace to study effect on their optical and electrical properties.

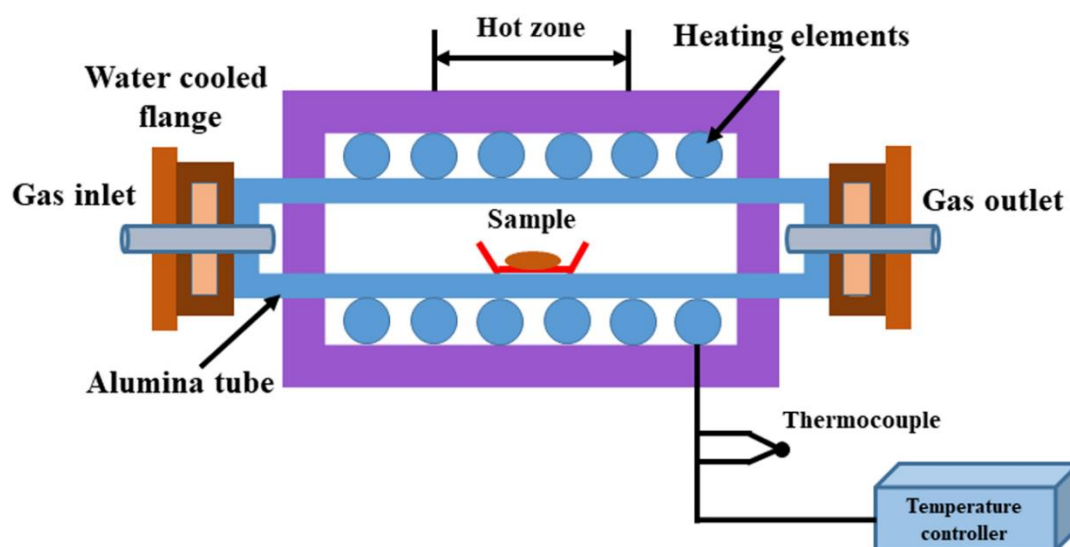


Fig. 2.7 Schematic diagram of high temperature horizontal tube furnace

The tube furnace can provide maximum working temperature upto  $1400^{\circ}\text{C}$  at the central zone, using silicon carbide as heating elements. The working temperature of the furnace is controlled by a digital PID temperature controller (Maxthermo) and an alumina sintered S-type thermocouple. A digital safety controller trips the furnace in case of over-heating. The samples to be annealed are kept in an alumina boat placed near the hot central zone of the horizontal alumina tube.

## 2.3 Characterisation techniques

### 2.3.1 Field emission scanning electron microscopy (FESEM)

An electron microscope has the capability to provide detailed surface morphology of a sample, it produces magnified image of a sample using a focussed beam of high energy electrons getting incident and scattered from the sample. Based on electron emission sources, electron microscopes can be of two types- scanning electron microscope (SEM) and field emission scanning electron microscope (FESEM). In SEM, thermionically emitted electrons from an electrically heated up tungsten (W) or lanthanum hexaboride (LaB6) filaments act as high energy electron sources, whereas, in FESEM a field emitter cathode with a narrow tungsten tip acts as an electron gun to provide high energy electron beams. FESEM provides much brighter and spatially resolved images with minimised charging of the samples as compared to that of SEM images. The accelerating voltage applied to generate high energy electron beam varies in the range of 0.02 KV- 30 KV. In order to avoid contamination and oxidation of the

sample, a high vacuum of  $\sim 10^{-5}$  mbar is required within the sample chamber and  $\sim 10^{-10}$  mbar is required in the gun chamber. The high energy electron beams are narrowly focussed by electromagnetic lenses. Interaction with the sample can be either elastic or inelastic giving rise to various types of signals, which includes secondary electrons (SEs), back-scattered electrons (BSEs) and characteristic X-rays. The secondary electrons give morphological information of the sample with high resolution, as they are originated from a few nanometers below the sample surface. Due to inelastic interactions with incident high energy electron beam, these have very low energy ( $< 50\text{eV}$ ) [96].

In the present dissertation, the FESEM instrument ZEISS Sigma 300 (Gemini) of Central Instrumentation Facility (CIF), Gauhati University, is used for study of in-plane and cross-sectional morphology of PS and its hybrid structures. As the samples used in the present investigation are semiconducting in nature, a thin gold layer ( $\sim 2$  nm) is sputter deposited on the samples to make them electrically conducting before analysing. This setup can provide magnification in the range of  $\sim 10 \times$  -  $1 \text{ MX}$  with resolution of  $\sim 1$  nm. The schematic of the FESEM setup is shown in fig. 2.8.

### 2.3.2 Energy dispersive X-ray spectroscopy (EDX)

Energy dispersive X-ray spectroscopy is a technique that uses X-ray emitted by a sample when interacting with a focussed high energy electron beam to provide elemental or chemical composition of the sample. Its principle is based on the fact that each element present in a sample emits unique characteristic X-ray on electron transition from higher to lower energy state. The incident high energy electron beam excite and eject an electron of an atom from innermost shell, resulting a vacancy of electron which is filled up by an electron from higher energy shell. The energy difference between these two shells is released in the form of X-ray, giving unique identity of the atom present in the sample. An EDX spectra normally exhibits peaks corresponding to different elements present in the sample with different intensities depending upon concentrations of the elements present in the sample [97].

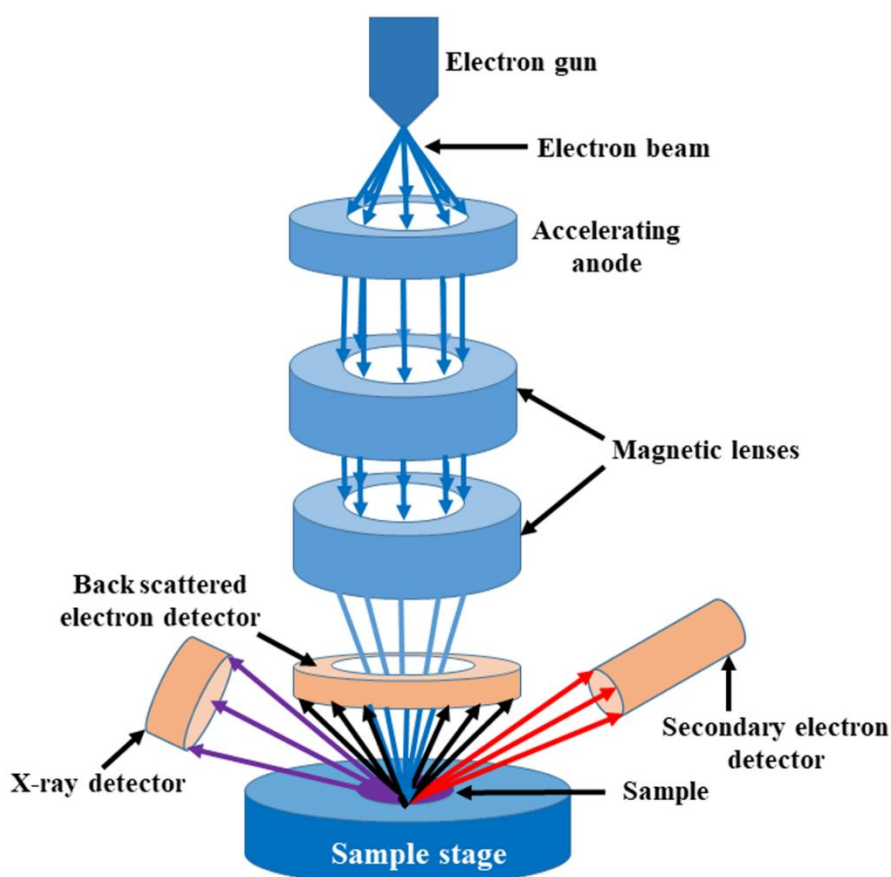


Fig. 2.8 Schematic for FESEM imaging and EDX analysis

This equipment along with the X-ray detector is attached to the FESEM unit as shown in the fig. 2.8. In the present work, planar and selected area cross sectional EDX spectra of PS and its heterostructures are analysed to investigate their elemental contents.

### 2.3.3 Field emission transmission electron microscopy (FETEM)

The field emission transmission electron microscopy (FETEM) is an effective technique for characterizing nano materials. The schematic diagram for working of FETEM setup is shown in fig. 2.9. It is basically used for determining microstructural details of nano materials such as particle or grain size, shape, crystallization etc. with high magnification and resolution. Working principle of the microscope is same as that of optical microscope but it uses electron beams instead of light. Moreover, it gives higher resolution images compared to an optical microscope, as wavelength of electron beam is much smaller ( $\sim 0.25$  nm) than that of light. FETEM setup includes electron gun, electromagnetic lenses, sample holder and imaging system. A tungsten filament

cathode acts as electron gun to generate high energy electron beam which are then guided by electromagnetic lenses through vacuum environment within the microscope. The condenser electromagnetic lens concentrates the accelerated electron beam and the condenser aperture focuses this beam onto a certain part of the ultra-thin (<100 nm) specimen. It is operated in two basic modes- imaging and diffraction modes. In imaging mode of operation, the objective aperture is adjusted to be placed in back focal plane of the objective lens. When objective aperture allows to transmit only central beam, then bright field images are produced. If the diffracted beam is allowed and primary beam is blocked, then dark field image is obtained. Finally, with the help of projector lenses magnified image of the sample is obtained on a fluorescent screen. In diffraction mode of operation, a selected area objective aperture placed in image plane of objective lens exactly determines the specimen area from which the signal will be displayed. Diffraction pattern is recorded on the screen by changing the strength of electron beam

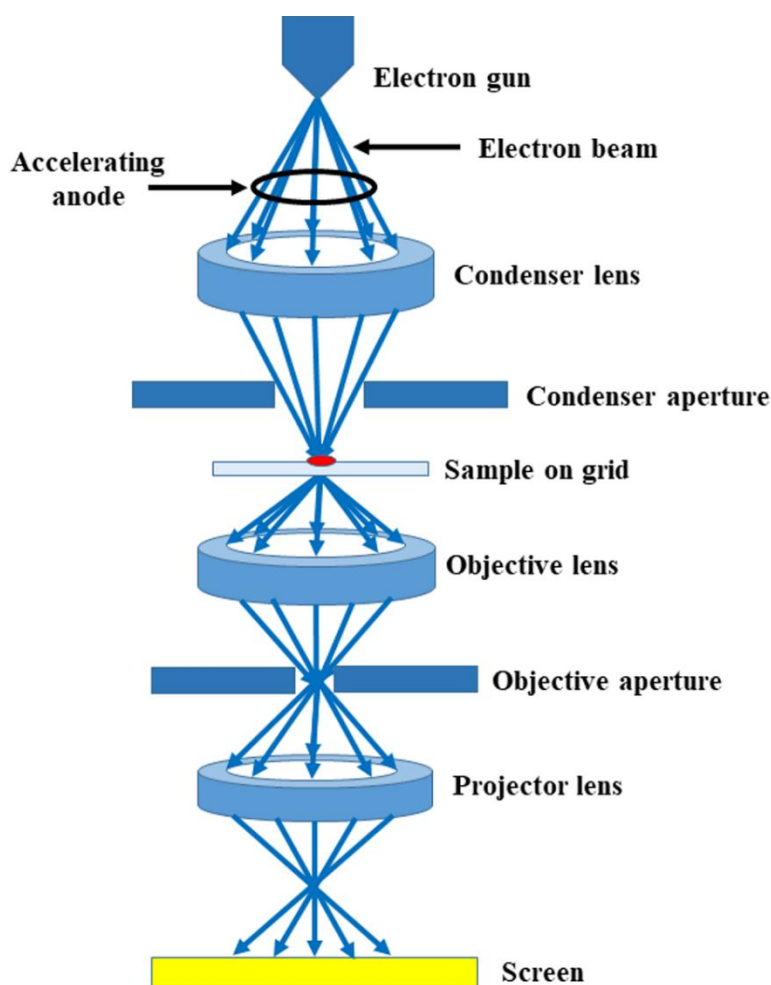


Fig. 2.9 Schematic for FETEM imaging process



through the projector and intermediate lenses. Diffraction pattern provides details of crystal planes present in the nano-material sample [98].

In the present work, the FETEM images of some prepared nanoparticles are recorded by using JEOL-2100F setup of IIT Guwahati. In this setup, accelerating voltage of ~200 kV is applied for high energy electron beam emission and this beam is guided through the chamber at a pressure of  $\sim 10^{-9}$  mbar. It can provide point resolution upto ~0.2 nm and maximum magnification of images upto 1.5 MX. For FETEM analysis, the powder sample is first dispersed in ethanol using an ultrasonicator and the sample solution is drop cast on a 300 mesh carbon coated copper grid and dried in room temperature in a clean environment. Finally, the dry grid on the grid holder is taken inside the chamber for FETEM image analysis.

### 2.3.4 X-ray diffraction (XRD)

X-ray diffraction is one of the basic characterisation techniques for determining various crystalline properties of any material. The basic working principle of this technique is that, X-ray has wavelength of around  $\sim 1\text{\AA}$ , of the order of the interatomic spacing of crystals, enables it to produce diffraction pattern due to scattering from crystal planes. Diffraction pattern of a crystal is unique finger print for it, as no two different crystalline materials can have the same diffraction patterns. The condition to be satisfied for diffraction of X-ray is given by the Bragg's diffraction law given by the equation,

$$2d_{hkl} \sin\theta = n\lambda \quad (2.1)$$

Where  $d_{hkl}$  is inter-planar spacing,  $\theta$  is Bragg's angle,  $\lambda$  is the incident X-ray wavelength and  $h, k, l$  are the miller indices. For a set of parallel planes of a crystal, we get diffraction pattern only if the values of  $d_{hkl}$ ,  $\theta$  and  $\lambda$  satisfy the Bragg's law as shown in fig. 2.10(a). The working of X-ray powder diffractometer can be described by Bragg-Brentano geometry [99] as shown in fig. 2.10(b). X-ray source and the detector lie on the circumference of the goniometer circle and the sample is placed at its centre. The analysis process can be carried out in two basic modes of operation-  $\theta:\theta$  and  $\theta:2\theta$  modes. In  $\theta:\theta$  geometry mode of operation, sample at the centre is kept fixed and the X-ray source and the detector is rotated to get the diffraction pattern. On the other hand, in  $\theta:2\theta$  mode, the X-ray source tube is fixed and sample and the detector are rotated.

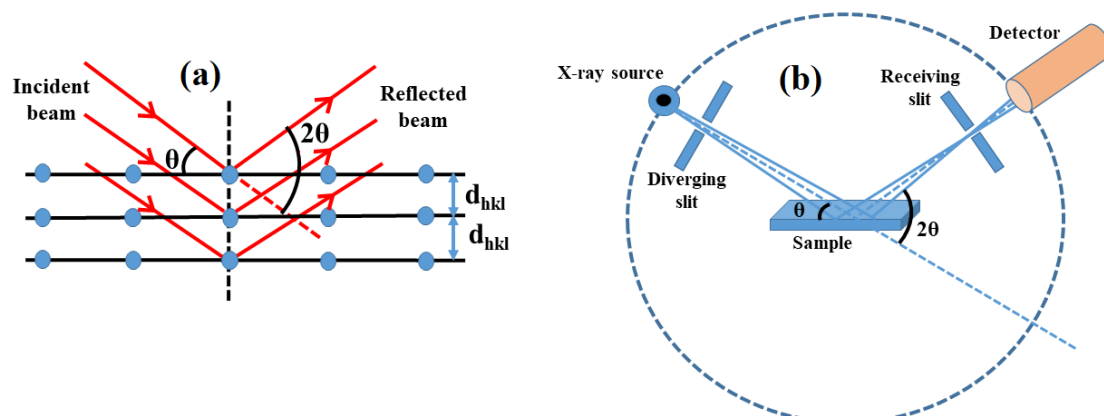


Fig. 2.10 Schematic for (a) Bragg's diffraction law and (b) X-ray diffractometer setup

Crystallite size ( $L$ ) of a material can be calculated from its diffraction pattern using the Scherrer equation [100], given by,

$$L = \frac{k\lambda}{\beta \cos\theta} \quad (2.2)$$

Here,  $k$  ( $\sim 0.9$ ) is Scherrer const.,  $\beta$  (radian) is the FWHM value of the diffraction peak,  $\theta$  is the diffraction angle and  $\lambda$  is the wavelength of X-ray source. For nanocrystalline materials, a broad diffraction peak results in smaller crystallite sizes as calculated from the above equation. This diffraction peak broadening can be ascribed to the presence of less number of lattice planes in the crystal, here all incoherent scatterings do not cancel each other at angles close to the Bragg angle. But, in case of bulk materials we get strong coherent scattering and the incoherent scatterings also cancel out each other, resulting sharp diffraction peaks. However, some other sources like strain in the crystal, thermal vibrations of atoms and intrinsic diffractometer broadening may also be the reasons for XRD peak broadening.

In the present study, Phillips X'Pert Pro PW 3040/60 diffractometer, of Sophisticated Analytical Instrumentation Facility (SAIF), Gauhati University is used. CuK-alpha1 and 2 lines with wavelengths of 1.5406 and 1.5444 Å respectively act as X-ray source. Diffraction angle ( $2\theta$ ) is scanned from  $10^0$  to  $90^0$  in steps of  $0.001^0$ .

### 2.3.5 Raman spectroscopy

Raman spectroscopy is a tool for demonstrating microstructural features of materials. This is based on the principle of inelastic scattering of incident photons by atomic vibration in the lattice. In materials science, this technique is basically used for

determining crystallinity and identification of constituent elements etc. in a material. Schematic of Raman spectrometer is illustrated in fig. 2.11(a). When the sample is irradiated with a monochromatic laser source, light photons interact with the vibrating molecules present in the sample. This interaction may be elastic or inelastic, giving rise to Rayleigh or Raman scattering respectively. If the frequency of absorbed photon is higher than the frequency of emitted photon, then Stokes line appears, whereas, if the frequency of emitted photon is higher than the absorbed one, then anti-Stokes line appears. Energy level diagram for relevant transition is shown in fig. 2.11(b). The monochromatic light from laser source, when incident on beam splitter, gets separated into two beams of equal wavelengths. The part of beam incident on the sample gives rise to Rayleigh and Raman scattering. The notch filter present in the setup allows only Raman scattered beam, which is then passed through a grating and an etalon to increase its intensity. Finally, high intensity beam get incident on a charge-coupled device (CCD), which detect the change of polarizability as a function of beam intensity and wave number and displays on a computer screen [101].

In the present work, Raman spectra of PS samples are studied by using micro-Raman spectrometer (LabRam HR800, Horiba Jobin Vyon) setup of IIT Guwahati, using the laser excitation wavelength of 633 nm.

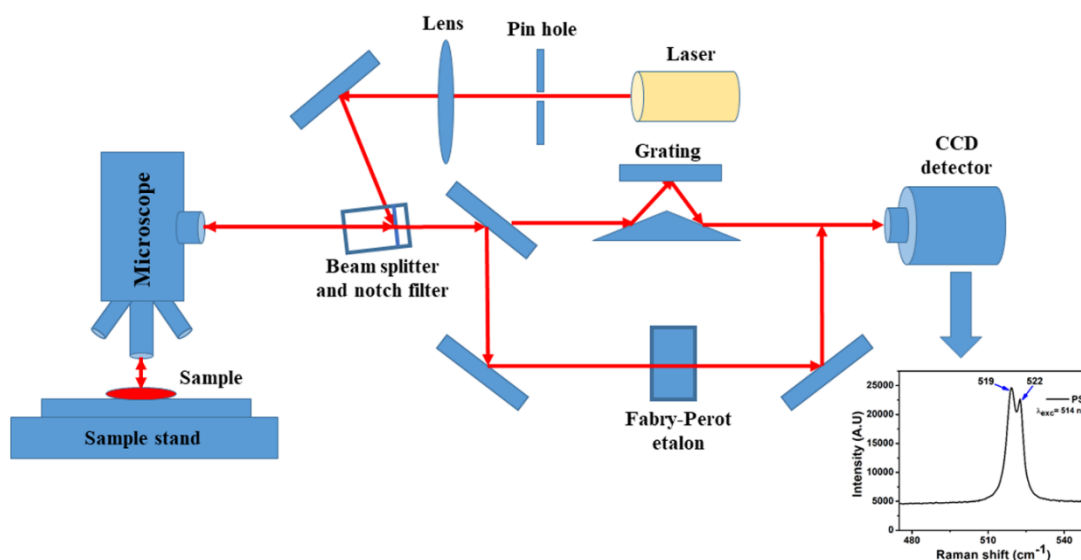


Fig. 2.11(a) Schematic for Raman spectroscopy analysis

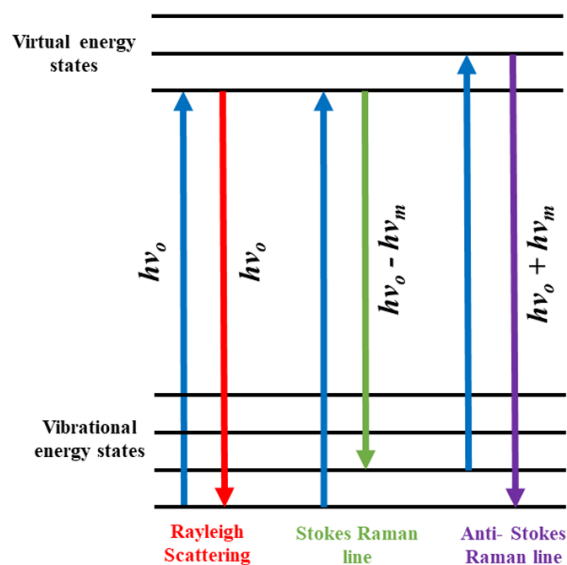


Fig. 2.11(b) Energy level diagram of Raman spectroscopy

### 2.3.6 UV-Visible spectroscopy

Ultraviolet-visible spectroscopy is one of the basic characterization techniques to analyse various optical properties of materials. The schematic of basic working of a spectrophotometer is presented in fig. 2.12. When a light photon is incident on the surface of a material, it can get absorbed, reflected or transmitted. In absorption spectroscopy, an electron in a lower electronic state jumps to higher state due to absorption of high energy photons by a molecule present in the material. An absorption band edge position determines the required radiation wavelength for an electronic transition and band edge intensity defines the interaction probability of radiation energy with electronic system. Reflectance spectra provides measurement about the portion of light incident on a material get reflected back from its surface. Whereas, transmittance spectra provides measure about the transmission of incident light through the material [102]. The basic components of a UV-vis spectrophotometer unit are: UV-visible light source, monochromator, a signal processor with detector, a sample and a reference with holder. The monochromatic light beam is first divided into two beams of equal intensity using a half silvered mirror. One beam is transmitted through the sample, while the other beam is allowed to transmit through the reference material. The intensity difference between these two final beams is recorded and compared by detectors to display as output in the computer screen.

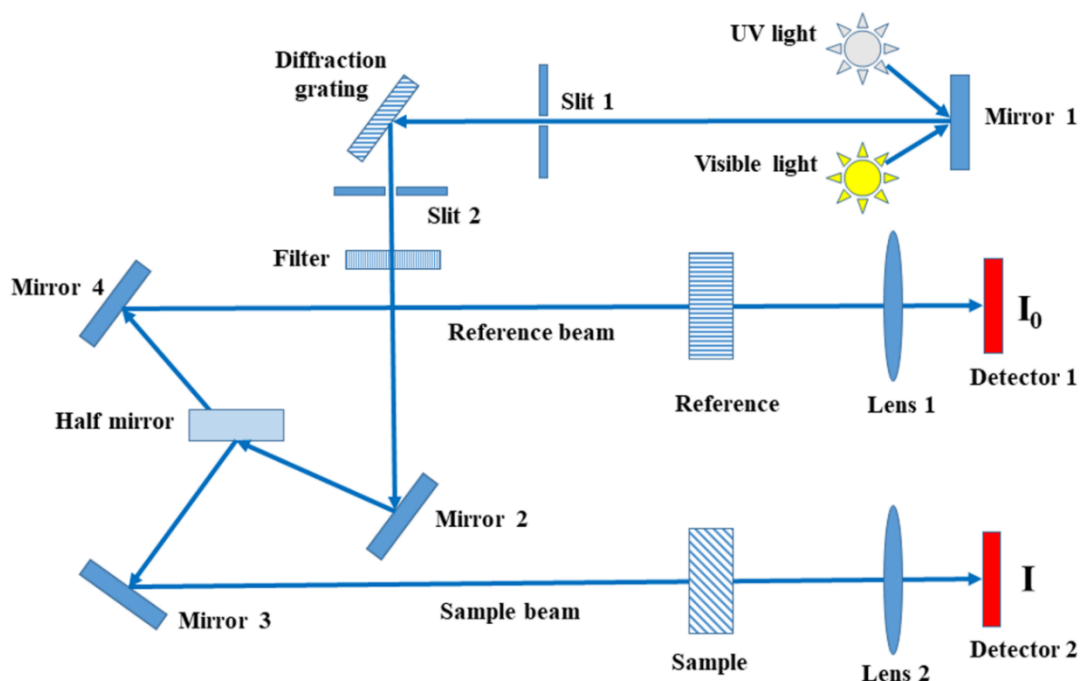


Fig. 2.12 Schematic for UV-visible spectrophotometer

In the present work, Varian-Carry 300 UV-vis spectrophotometer, housed in our laboratory itself is used to analyse the absorbance, transmittance and reflectance properties of bare CdS, ZnO, ZnS and their hybrid structures with PS in the wavelength range of 300- 800 nm.

### 2.3.7 Photoluminescence spectroscopy (PL)

Photoluminescence (PL) is a process of photon emission from any material after absorption of photon of definite energy. It is a proficient tool for determination of optical band gap, presence of impurities and defect levels within semiconductor materials. The schematic of brief working principle and energy level diagram of the PL process is illustrated in fig. 2.13 (a-b) respectively. When a semiconductor is excited with laser light having higher or equal energy of the optical band gap of the material, electron-hole pairs are generated in the valence and conduction band of the material, which may also get trapped by defect states present in the semiconductor. Electrons in the higher excited states of conduction band come to the lower edge of the band by non-radiative relaxation process. Further, these electrons get de-excited and recombine with valence band holes by emitting photon at the band gap energy of the material. These radiative transitions in some semiconductors may also include transitions from shallow or deep trap levels present in them. Detail analysis of these spectra can lead to the

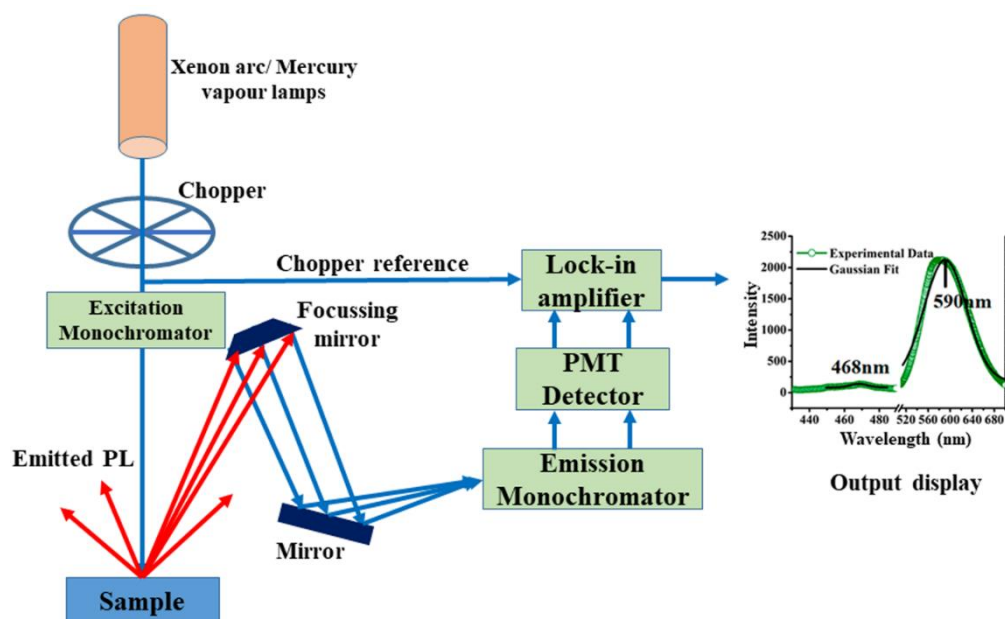


Fig. 2.13 (a) Schematic for photoluminescence process using spectro fluorometer setup

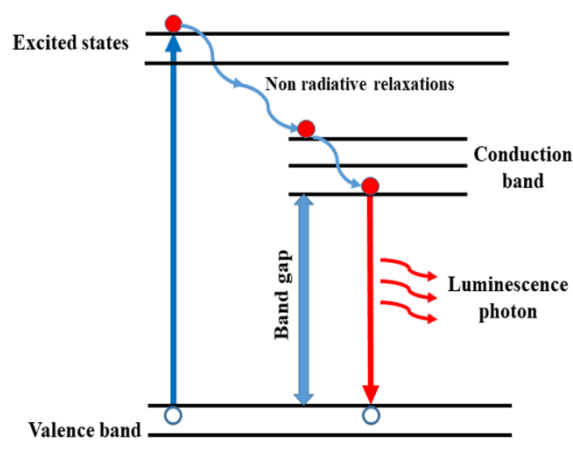


Fig. 2.13 (b) Schematic for energy level diagram of photoluminescence process

identification of origin of these trap levels [103]. The basic components of a PL setup are: a monochromatic light source, focussing mirror, collecting mirror, emission monochromator and detector. Excitation monochromatic light is focussed on the sample and the radiated photons are collected by focussing mirrors and transmitted towards the emission monochromator and finally detected by highly sensitive photomultiplier tube (PMT) detectors.

In this thesis work, Jasco (FP-8300) spectro fluorometer of another laboratory of the department is used for PL study of PS and its hybrid structures. In this equipment, xenon arc and mercury vapour lamps are used as excitation light sources. This setup

can be used in the excitation and emission wavelength range of ~200- 750 nm. It has high rms sensitivity (S/N ratio) of ~2800 and resolution of ~1 nm.

### 2.3.8 Dark and photo current measurement

The schematic of the set up for dark and photo I-V measurement of PS and PS based heterostructure MSM devices assembled in our laboratory is shown in fig. 2.14. This setup consists of a mercury arc lamp with a power supply, a monochromator, a dark chamber to avoid outside light to the device, a computer interfaced source meter. The device is loaded in the dark chamber to analyse the dark and photo I-V characteristics and on- off switching kinetics of the device at room temperature for different voltage biasing and illumination conditions. For demonstrating electrical properties of PS and its heterostructures, both planar and sandwich electrode configurations are devised using thermal evaporation method as discussed in subsection 2.2.2 of this chapter. The mercury arc lamp (Newport-Oriel, 6283 NS) is used as light source, it has wide UV to IR (200-2500 nm) usable spectral range with maximum output power of 155 watt. The Newport-69907 power supply provides precise monitoring and adjustability of output voltage, current and power of the lamp source. This power supply can be operated in constant current and constant power modes, with loaded DC output voltage range of 0-70 V and 1.5-12 A output current range. The monochromator (Oriel, Cornerstone-260) provides usable wavelength range of 180-2500 nm with the help of diffraction gratings inside it with a resolution of ~0.1 nm. Desired wavelength can be selected to get

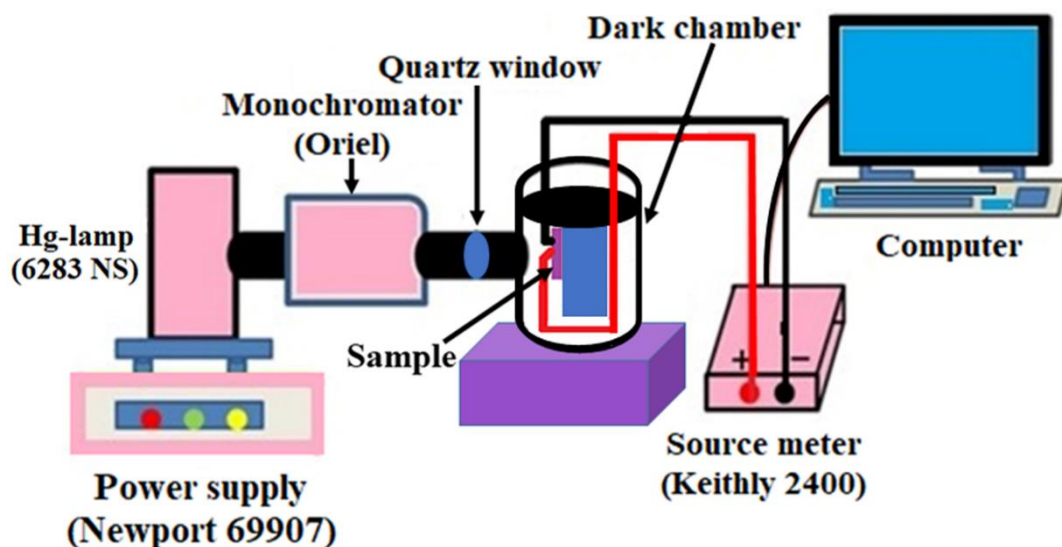


Fig. 2.14 Schematic for experimental setup for device dark and photo current analysis

incident on the device using a mechanical screw and a mechanical shutter attached with it helps controlling the light illumination to the device placed inside the dark chamber. Electrical measurements are recorded using computer interfaced Keithley-2400 source meter. This source meter consists of a highly stable, precise and low-noise DC power supply and a high-impedance, stable multi-meter. The unit has source and measurement specifications as shown below:

- 1) Source voltage range is upto 200 V with resolution of 500  $\mu$ V
- 2) Measure voltage range is upto 200 V with resolution of 100  $\mu$ V.
- 3) Source current range is upto 1 A with resolution of 50 pA.
- 4) Measure current range is upto 1 A with resolution of 10 pA.
- 5) Maximum output power is 22 W.
- 6) Minimum transient response time for an output to recover is 30  $\mu$ s.

In the present work for study of electrical properties of the samples, two probe method has been adopted, which is suitable for a sample having resistance much greater than the lead resistance. However, if the sample resistance is much closer to the lead resistance, then for accurate measurements four probe method is to be adopted.



# Chapter 3

## **Optical and electrical properties of nanostructured CdS-PS: p-Si heterostructure**

[M. Das, S. Sarmah and D. Sarkar, J. Mater. Sci.: Mater.  
Electron. **30**, 11239 (2019)]



## Optical and electrical properties of nanostructured CdS-PS: p-Si heterostructure

### 3.1 Introduction

Photoconductivity is a well-known phenomenon in semiconductor physics, which indulges conversion of light energy into electrical signal [104]. Photodetectors (PDs) and photovoltaic devices (PVs) rely on this basic principle. These devices have found many important applications in radiation detection and solar cell industries [105-107]. Furthermore, extensive research has been under way for developing heterostructure based PDs and PVs in the field of material science in recent years [108-111]. However, one of the biggest challenges for configuration of such heterostructure is the choice of appropriate material. Porous silicon (PS) is one of such material which attracts great interest due to its fascinating electrical and optoelectronic properties [112, 113]. PS can be fabricated by methods like electrochemical anodization [4], metal assisted chemical etching [114] etc. PS fabricated on p-type Si (p-Si) wafer acts as active hole transport layer, thus by deposition of electron rich material on PS: p-Si substrate p-n type heterojunction can be developed. There are various electron transport materials such as ZnO, ZnS, TiO<sub>2</sub>, CdS etc. [115, 116], which can be employed for devising UV-vis PDs. However, processing and deposition of such materials are quite complex as well as expensive [117]. Metal sulphides, in particular nano structured CdS is easy to process and can be grown on large scale. Also, as reported in literature, higher electron mobility

of CdS ( $\sim 350 \text{ cm}^2 \text{ V}^{-1} \text{ s}^{-1}$ ) as compared to some other metal oxides [118], makes it a good candidate for heterostructure configuration in device application. In a recent work by Ismail et al. [119], the reported parameters of the CdS-PS based PDs do not show much promising result. This is possibly because of the fact that in their method they adopted CdS deposition by drop casting on PS wafer. There is another work by Manna et al. [78] on CdS deposited Si nanowire made by anodization of Si wafer. Their method of sample preparation involves complex and expensive techniques. Present chapter aims at fabrication of nanostructured CdS-PS:p-Si MSM heterostructure by simpler method yet attaining much better result in terms of photoresponsivity.

## 3.2 Experimental

### 3.2.1 Preparation of Al/nano CdS-PS:p-Si MSM heterostructure

The preparation of PS:p-Si structure and CdS nanoparticles have already been described in detail in Chapter 2, under subsection 2.2.1 and 2.2.3 respectively. Synthesized CdS nano powder weighing 0.15 g is deposited simultaneously on PS:p-Si as well as on glass substrate using Hind high vacuum coating unit by thermal evaporation method in a vacuum condition of  $\sim 10^{-5}$  mbar. The thickness of the deposited CdS nanoparticle layer is maintained at  $\sim 170$  nm by quartz crystal digital thickness monitor (DTM) attached to the chamber. Further construction of metal semiconductor metal (MSM) heterostructure is carried out in the same coating unit under the same condition. For this highly pure (99.99%) Al metal electrode of  $\sim 20$  nm thickness is coated on CdS-PS:p-Si heterostructure and bare PS:p-Si (for comparison) structure using interdigitated shadow mask of dimension  $6 \text{ mm} \times 6 \text{ mm}$ . Schematic of the heterostructure is depicted in fig. 3.1. Thin n-CdS layer is preferred, so that equal number of charge carriers could be collected at the Al electrodes in equal time without

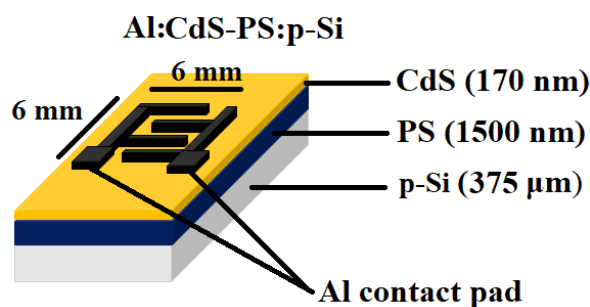


Fig. 3.1 Schematic of Al: CdS-PS: p-Si MSM heterostructured PD

recombination as  $e^-$  mobility at room temperature is reported to be greater (3 times) than  $h^+$  mobility [120], which will consequently increase the photocurrent of the heterostructure.

### 3.3 Results and discussion (M. Das et al., [121])

#### 3.3.1 Morphological analysis

Morphology of the prepared CdS nanostructure is observed from FESEM and FETEM analyses, which are shown in fig. 3.2. Fig. 3.2(a) shows planar FESEM micrograph of the prepared nano powder. This micrograph shows that spherical nano CdS particles get agglomerated to form a hierarchical flower like structure. These agglomerations can be further clearly visualized from FETEM micrograph as shown in fig. 3.2(b). The average particle size calculated by sampling 50 number of nanoparticles within the marked circular regions of fig. 3.2(a, b) are found to be 28 and 17 nm respectively. FESEM micrographs of prepared PS:p-Si and CdS-PS:p-Si heterostructure are shown in fig. 3.3. Fig. 3.3(a) shows top view surface morphology of PS layer grown on p-Si substrate. This shows random distribution of mesopores of the PS layer. Fig. 3.3(b) shows the top view of CdS-PS:p-Si heterostructure, showing hierarchical flower like CdS nanostructures grown on PS:p-Si surface. The basic advantage of such hierarchical structure is to increase surface to volume ratio of the heterostructure, which efficiently increases its photo sensing property. To visualize the interface between CdS and PS:p-Si structure, cross sectional view of FESEM micrograph of the heterostructure is observed. This is shown in fig. 3.3(c), which shows uniform growth of CdS layer with thickness of  $\sim 170$  nm on uniformly etched PS layer. To ascertain the presence of CdS

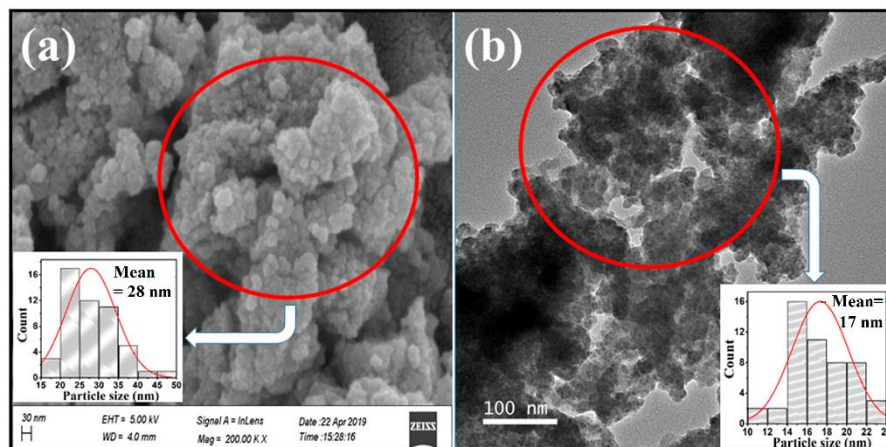


Fig. 3.2 (a) FESEM and (b) FETEM micrographs of CdS nanopowder [insets- particle size histograms]

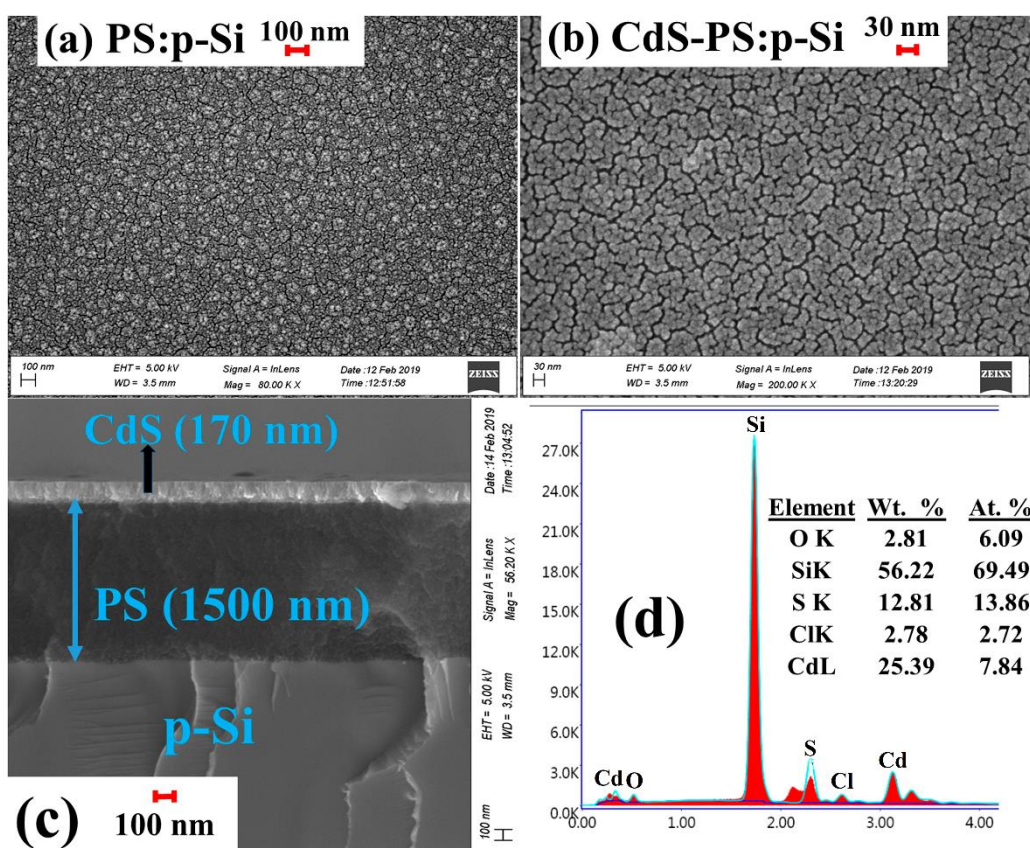


Fig. 3.3 FESEM micrograph of (a) PS surface, (b) CdS-PS surface, (c) CdS-PS:p-Si interface and EDX spectrum of (d) CdS-PS: p-Si heterostructure

on the PS:p-Si heterostructure, EDX analysis is carried out, which is presented in fig. 3.3(d). Presence of Cd is found to be 25.39 weight percent and 7.84 of atomicity percentage and for S it is 12.81% by weight and 13.86% by atomicity. Apart from Cd and S, other elements with atomicity (%) namely Si (69.49%), O (6.09%) and Cl (2.72%) are also present. Atomic weight of Si is maximum which is likely because CdS is deposited on PS:p-Si substrate. Presence of oxygen is attributed to growth of atmospheric oxygen on PS surface. The presence of chlorine (Cl) atom is a consequence of residual ( $\text{CdCl}_2$ ), which is used during chemical synthesis of CdS.

### 3.3.2 Optical studies

Optical analysis of the prepared CdS and the heterostructures are observed via UV-visible absorbance, reflectance spectra and photoluminescence (PL) spectra. Fig. 3.4(a) shows UV-vis absorbance spectra of nanostructured CdS with onset and offset absorption band edge at  $\sim 482$  and  $\sim 440$  nm respectively, which correspond to the bandgap energy of  $\sim 2.6$  eV as calculated using well known Tauc's equation and is

depicted in fig. 3.4(b). Calculated bandgap energy of nanostructured CdS is appreciably larger than its bulk counterpart (2.42 eV). This blue shift of 0.18 eV for CdS nanostructure compared to its bulk one is attributed to the quantum size effect in CdS nanostructure [122]. These facilitate employing such materials for photo detection in the shorter wavelength range of 250-490 nm of the UV-vis spectrum. Fig. 3.4(c) shows normalized UV-vis reflectance spectra of PS:p-Si and CdS-PS:p-Si heterostructure in the wavelength range of 200-800 nm. PS:p-Si structure exhibits multiple interference pattern due to Fabry-Perot interference of light reflected from various interfaces of PS:p-Si heterostructure [123]. However on CdS deposition, i.e. for CdS-PS:p-Si heterostructure there is an increment as well as blue shift of interference patterns as compared to bare PS:p-Si structure. This can be attributed to the change in refractive index of the heterostructure on CdS deposition. Fig. 3.5(a-c) shows PL spectra of the prepared CdS, PS: p-Si and CdS-PS:p-Si heterostructure for excitation wavelength of 250 nm. Bare CdS nanostructure exhibits two broad emission bands within the spectral range of 430-490 nm and 510-600 nm respectively. On deconvoluting the peaks using

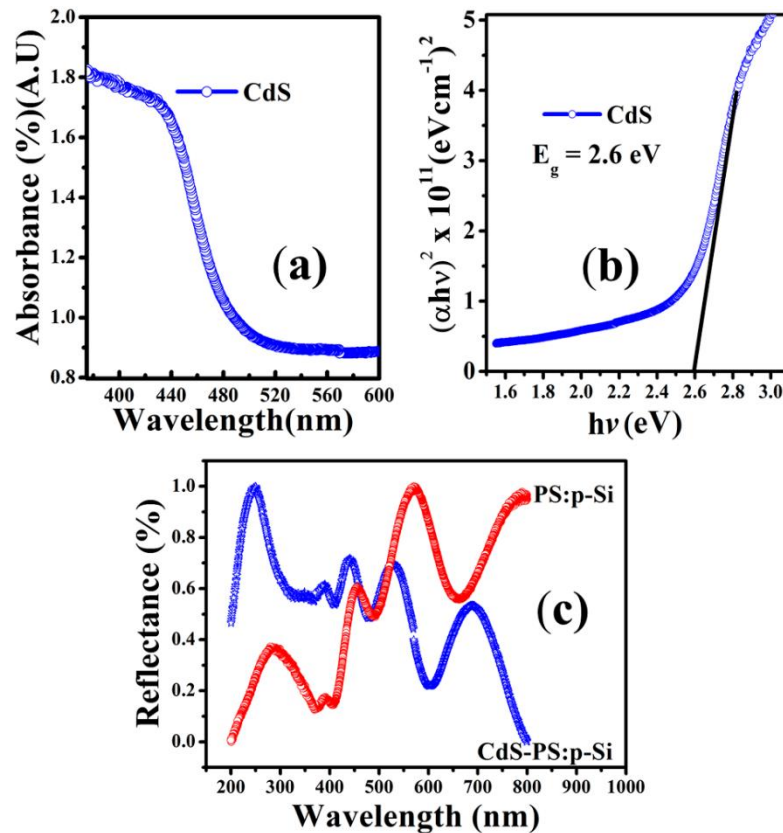


Fig. 3.4 (a) UV-vis absorbance spectra, (b)  $(\alpha h\nu)^2$  vs.  $h\nu$  plot of nanostructured CdS, (c) normalized UV-vis reflectance spectra of PS:p-Si and CdS-PS:p-Si heterostructure

Gaussian fitting analysis, peak positions are found to be at 450, 460, 468, 482 and 533 nm with FWHM of  $\sim 5$ , 23, 10, 8 and 22 nm respectively. The luminescence bands centred at  $\sim 450$ , 460, 468 and 482 nm are due to recombination of excitons or shallow trapped electron-hole pairs and are attributed to band edge emission of CdS nanoparticle [124, 125]. The green emission band centred at  $\sim 533$  nm is a contribution of defect level electronic transition from sulphur vacancy ( $V_s$ ) to the valence band of CdS nanostructure [126]. The luminescence mechanism for CdS nanostructure is shown in band representation in fig. 3.5(d). PS: p-Si heterostructure exhibits two distinct luminescence bands at  $\sim 468$  and  $\sim 590$  nm. The weak luminescence band at  $\sim 468$  nm with FWHM of  $\sim 12$  nm is attributed to  $\text{SiO}_2$  related transition [127]. The strong luminescence band at  $\sim 590$  nm with FWHM of  $\sim 90$  nm is attributed to band to band transition due to quantum confinement effect in Si nanostructure [128]. However, on deposition of CdS on PS: p-Si structure, it is observed that CdS related luminescence bands retain their original peak positions while PS: p-Si related luminescence band shows appreciable peak shifting [fig. 3.5(c)]. On peak deconvolution using similar

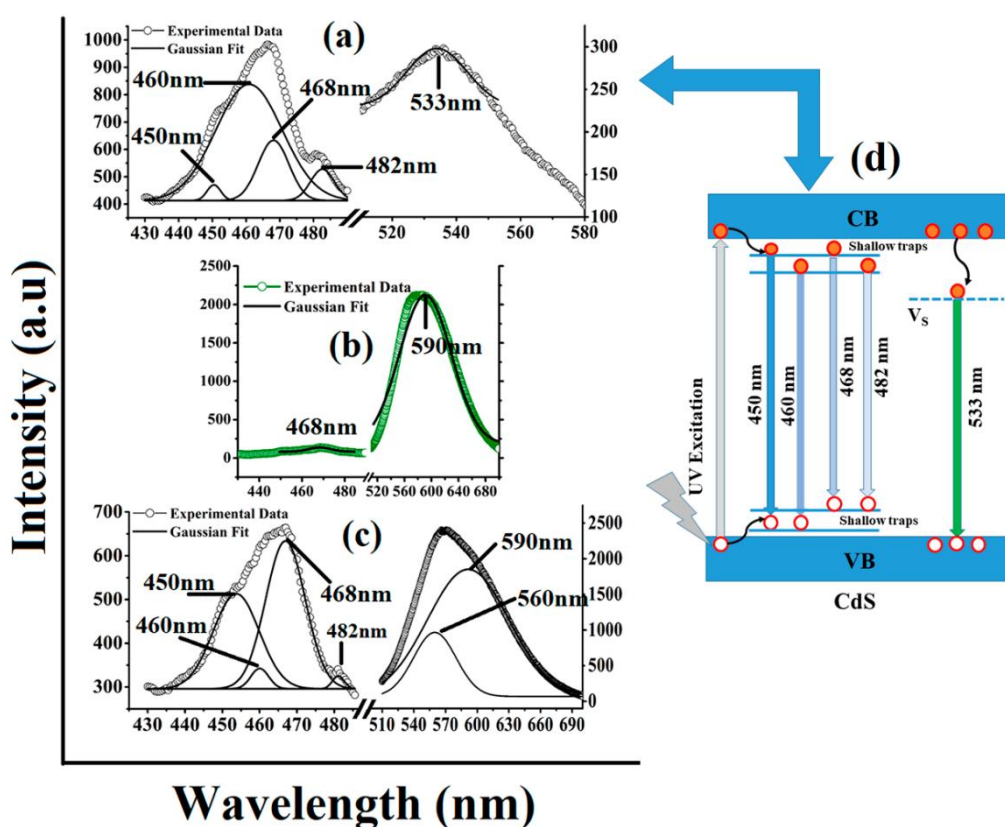


Fig. 3.5 PL spectra of (a) CdS nanostructure, (b) PS:p-Si structure, (c) CdS-PS:p-Si heterostructure and (d) schematic of electronic transitions involved in luminescence of CdS nanostructure



Gaussian fitting for the spectral range of 430-490 nm and 510-700 nm, it has been found that SiO<sub>2</sub> related luminescence band overlapped with 468 nm luminescence peak of CdS. Along with the characteristic PS:p-Si luminescence band at ~590 nm, a new defect related luminescence peak appeared at ~560 nm compensating the 533 nm peak of bare CdS nanostructure. The related 560 nm luminescence band is attributed to the presence of Cl atoms on sulphur vacancy sites of CdS nanostructure in CdS-PS: p-Si heterostructure [129]. Thus from the PL studies it can be stated that in CdS-PS:p-Si heterostructure traps and defect states play crucial role for electron- hole pair recombination, which subsequently have a direct role on its electrical and photo sensing abilities to be discussed in next subsections.

### 3.3.3 Electrical and photo response studies

For efficient performance of any photo sensing device it is highly required that a very low magnitude of dark current ( $I_d$ ) flows through the device. To inspect this, current-voltage ( $I$ - $V$ ) characteristics of both the devices are recorded for a voltage range of -2 V to +2 V under dark and illumination condition at room temperature. Fig. 3.6(a) shows forward biased *semi-log*  $I$ - $V$  plot of dark currents for biasing upto 2V. The inset of the figure shows similar plot under reverse bias condition for voltage range up to -2V. The heterostructures produce low magnitude of reverse leakage current and are found to be ~32 nA at -2V for both the heterostructures. Also, decrease in the  $I_d$  value for CdS-PS: p-Si compared to PS: p-Si structure in low voltage region (-0.2 V to 0.2 V) is observed due to dominance of surface charge recombination in CdS-PS: p-Si junction compared to PS:p-Si junction. To know more about the electrical nature of the prepared heterostructures, forward biased  $I$ - $V$  curve is divided into two regions. In region I (0-0.2V), current is seen to increase linearly up to 0.1V for CdS-PS: p-Si. This linearity is valid up to 0.2V for PS:p-Si structure. Such behaviour can be attributed to thermally generated  $e^-h^+$  pairs at CdS-PS:p-Si and PS:p-Si junctions at room temperature. Applying thermionic emission model in this region, ideality factor ( $n$ ) and saturation current ( $I_s$ ) are calculated. The related equations [130] are mentioned as follows,

$$I = I_s \exp \frac{eV}{nkT} \quad (3.1)$$

$$n = \frac{e}{kT} \frac{dV}{d \ln I} \quad (3.2)$$

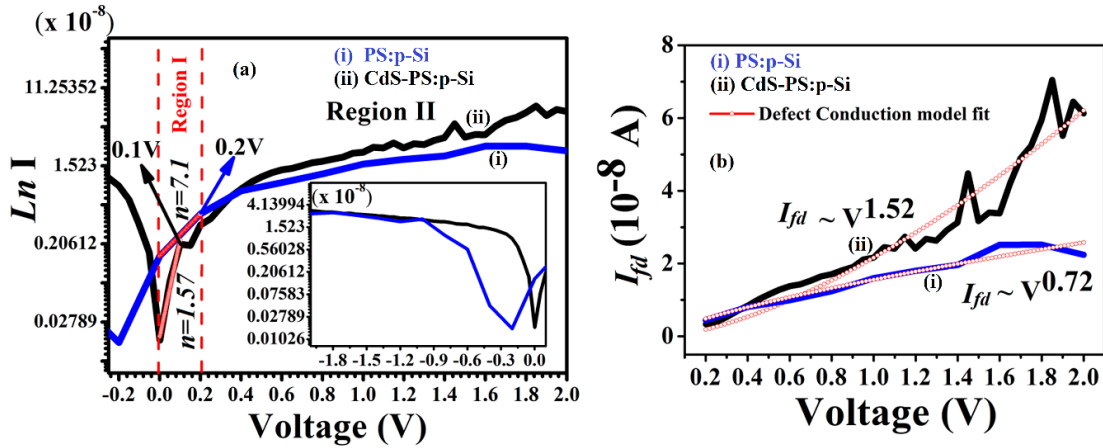


Fig. 3.6 (a) Forward biased semi-log dark  $I$ - $V$  plot, inset shows the plot under reverse bias, (b) plot of defect conduction model fitted forward  $I$ - $V$  curve for PS:p-Si and CdS-PS: p-Si heterostructure

Where  $k$  is Boltzmann constant,  $e$  is electronic charge,  $T$  is room temperature. The values of the ideality factors ( $n$ ) are calculated to be 1.57 and 7.1 and saturation current ( $I_s$ ) as 0.2 and 1.5 nA respectively for the two devices. The values of  $n$  and  $I_s$  for the nanostructured CdS deposited on the heterostructure are seen to decrease suggesting improvement in device quality in comparison to the bare PS:p-Si structure. In region II ( $> 0.2V$ ), forward current is seen to increase exponentially with applied voltage. Basically in this region conduction takes place due to drift motion of charge carriers. To explore more about the conduction mechanism in this regime, defect conduction model is fitted to the forward  $I$ - $V$  curve of both the devices using the equation  $I_{fd} = CV^m$  [fig. 3.6(b)], where  $I_{fd}$  is forward dark current,  $C$  is the proportionality constant,  $V$  is the applied forward voltage and  $m$  is the fitting or scaling parameter. This model fits well for CdS-PS:p-Si device with adjusted  $R$ -square value of 0.94, giving  $m$  values of 1.54. However,  $m$  values for bare PS:p-Si is found to be 0.72. So, it can be asserted that current conduction phenomenon in the former device is controlled by traps and defects present within the heterostructure [131].

To observe photoresponse characteristics, spectral responses of both the devices are recorded in the wavelength ( $\lambda$ ) range of 250-500 nm at -2V bias. Responsivity ( $R_\lambda$ ) and external quantum efficiency ( $EQE$ ) vs.  $\lambda$  plots are shown in fig. 3.7. The equations 3.3 and 3.4 mentioned below are fin use to calculate these parameters.

$$R_\lambda = \frac{I_{ph}}{SP} \quad (3.3)$$

$$EQE = \frac{hc}{e\lambda} R_{\lambda} = \frac{1240 R_{\lambda}}{\lambda (nm)} \quad (3.4)$$

Where,  $I_{ph}$  is the photocurrent in ampere,  $S$  is effective device area in  $cm^2$ ,  $P$  is power density in  $Wcm^{-2}$ ,  $\lambda$  is the wavelength of incident radiation in  $nm$ ,  $e$  is the electronic charge,  $h$  is Planck's constant and  $c$  is the velocity of light. It is evident from fig. 3.7 that CdS deposited heterostructure exhibits enhanced maximum  $R_{\lambda}$  and  $EQE$  at 400 nm with the values of  $\sim 0.6 AW^{-1}$  and  $\sim 180\%$  compared to  $\sim 0.3 AW^{-1}$  and  $\sim 85\%$  for the bare PS: p-Si structure. Along with this, one can notice an additional enhanced  $R_{\lambda}$  peak overlapping the weak PS:p-Si peak at  $\sim 440$  nm. This particular peak coincides with the band edge absorbance peak of nano CdS as shown in the inset of the figure. The high  $EQE$  value ( $> 100\%$ ) is believed to be due to the presence of trapped charge carriers in CdS-PS heterostructure, which upon illumination results in reduction of Schottky barrier height [132, 133]. Since,  $R_{\lambda}$  and  $EQE$  describe the performance figures of merit of any photo sensing heterostructure, 100% enhancement in respective values ensure that CdS-PS:p-Si device performance is far superior as compared to the bare PS:p-Si one. On application of high external bias of  $-2V$  dissociation of photo-generated  $e^{-}h^{+}$  pairs occur and are transported and collected by the Al electrodes before recombination, thereby reducing the charge carrier recombination. Fig. 3.8(a) shows linear  $I-V$  plot of CdS-PS: p-Si heterostructure under incident radiation wavelength of 400 nm. From the plot it is evident that the heterostructure shows almost symmetric enhancement of rectification in forward and reverse bias condition with a photo to dark current ratio ( $I_{ph}/I_d$ ) of 3.15 and 10.26 at  $\pm 2V$  respectively. The symmetrical rectification

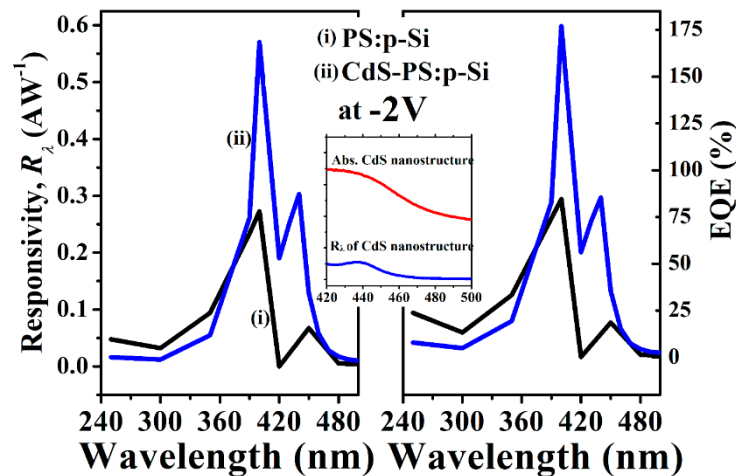


Fig. 3.7 plot of  $R_{\lambda}$  and  $EQE$  vs.  $\lambda$  at  $-2V$  for both the heterostructure PDs, inset shows absorbance and  $R_{\lambda}$  spectra of nanostructured CdS

enhancement under illumination is basically due to the lateral MSM configuration of the device [134]. The photoresponse is also recorded by changing irradiation intensities ( $33\text{-}71\mu\text{W cm}^{-2}$ ) at a fixed 400 nm wavelength radiation of light. The intensity dependent  $I_{ph}$  graph at  $-2\text{V}$  is shown in fig. 3.8(b). This shows power law dependence, i.e.  $I_{ph}$  follows power law equation  $I_{ph} = AP^\alpha$  where  $A$  is proportionality constant,  $P$  is intensity of the irradiating wavelength and  $\alpha$  is scaling parameters whose specific value reveals the type of carrier dynamics present [135].  $\alpha = 1$  implies number density of trapped  $e^-$  ( $N_{trap}$ )  $\gg$  number density of free  $e^-$  ( $N$ ), which is first order carrier dynamics.  $\alpha = 0.5$  implies  $N_{trap} \ll N$ , which is for second order carrier dynamics [136]. In the present work,  $\alpha$  value is 0.8, which suggests carrier transport in CdS-PS:p-Si heterostructure to be governed by the combination of first and second order dynamics. The on-off transient kinetics of the heterostructure under different irradiation intensities at bias voltage of  $-2\text{V}$  with on-off time interval of 10 s is shown in fig. 3.8(c). From the curve it is clear that the heterostructure shows steep rise in current when the incident light is turned on and remain in a stable state until the light is turned off and relaxes to its initial state. Also, with increasing irradiation intensity from 33 to 71  $\mu\text{W cm}^{-2}$ , the on-off ratio increases from 1.32 to 2.92, indicating strong influence of irradiation intensity on its switching behaviour. Since the nature of curve in fig. 3.8(c) represents sigmoidal growth in the 'ON' state and exponential decay in the 'OFF' state, response and recovery times of the heterostructure can be calculated using the following fitting equations.

$$I = \frac{A_1 - A_2}{1 + e^{(t-t_0)/\tau}} + A_2 \quad (3.5)$$

$$I = I_0 + Ae^{-t/\delta} \quad (3.6)$$

Equation (3.5) represents Boltzmann function, where  $A_1$ ,  $A_2$  and  $\tau$  are onset value, offset value and response time constant respectively. Equation (3.6) represents exponential decay function, where  $I_0$ ,  $A$  and  $\delta$  are offset value, amplitude and recovery time constant respectively. From the fitted curve as shown in fig. 3.8(d), the value of  $\tau$  and  $\delta$  are found to be  $0.16 \pm 0.03$  and 0.35 sec respectively. Recovery time is longer than the response time, as thermal relaxation of  $e^-$  is a slower process compared to the photoexcitation of  $e^-$  [137, 138]. The response time is quite high compared to some of the earlier reported high speed PDs [139-141], which can be attributed to the presence of interfacial defects

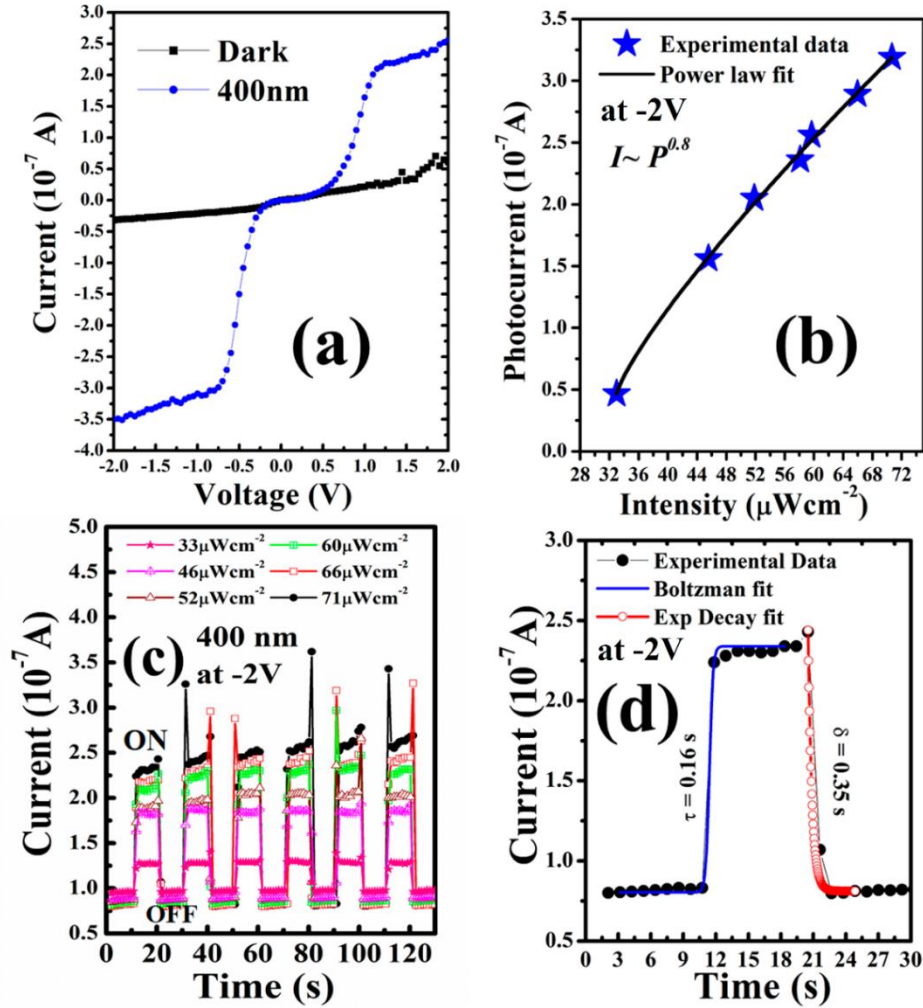


Fig. 3.8 (a) Linear  $I$ - $V$  plot under dark and illumination condition, (b) intensity dependent  $I_{ph}$  plot, (c) On-off kinetics under different intensity of 400 nm and (d) response and recovery time calculation for CdS PS:p-Si heterostructure PD at -2V

within the heterostructure. Further improvement towards the response time can be done by optimizing the thickness of CdS and PS layer and also by annealing the PS prior to electrode deposition. On the basis of performance parameters, Al: CdS-PS: p-Si is compared with some of the best reported silicon based hybrid heterostructure PDs and the results are summarized in Table 3.1. From the table it is evident that performance of the present heterostructure PD is more or less at par with some devices [78, 109, 139-146], whereas in some other cases it's even superior in performance in spite of simpler and less expensive fabrication technique utilised.

### 3.3.4 Conclusion

MSM device based on nanostructured CdS-PS: p-Si heterostructure has been successfully developed with simpler inexpensive technique. Light sensing abilities in a

**Table 3.1** Comparative performance analysis of Al: CdS- PS:p-Si heterostructure PD with some of the best reported Si-based PDs in the literature.

Device	Measurement condition [wavelength ( $\lambda$ ), intensity ( $I$ )]	Reverse saturation current (nA)	Responsivity ( $\text{AW}^{-1}$ )	Response time (ms)		Ref.
				Rise ( $\tau$ )	Decay( $\delta$ )	
CuO: Si (p-n)	$\lambda = 405 \text{ nm}$ $I = 0.48 \text{ Wcm}^{-2}$	–	$3.89 \times 10^{-4}$	0.06	0.08	[139]
Graphene: Si	$\lambda = 488 \text{ nm}$ $I = 0.04 \mu\text{Wcm}^{-2}$	$3 \times 10^2$	0.23	5	5	[141]
MoS <sub>2</sub> : Si heterojunction	$\lambda = 808 \text{ nm}$ $I = 30 \text{ mWcm}^{-2}$	–	0.30	$3 \times 10^{-3}$	$4 \times 10^{-2}$	[140]
MoS <sub>2</sub> : Si heterojunction	$\lambda = 514 \text{ nm}$ $I = 0.8 \text{ mWcm}^{-2}$	10	0.47	10	10	[142]
PS- MSM device	$\lambda = 530 \text{ nm}$ $I = 1.5 \text{ mWcm}^{-2}$	–	0.08	510	450	[145]
n-SiCN/p-PS/p-Si	$\lambda = 254 \text{ nm}$ $I = 0.5 \text{ mWcm}^{-2}$	–	–	$7 \times 10^3$	$1 \times 10^4$	[146]
PS: n-Si MSM device	$\lambda = 450 \text{ nm}$ $I = 259 \mu\text{Wcm}^{-2}$	–	2.00	1000	1000	[144]
	$\lambda = 250 \text{ nm}$ $I = 28.2 \mu\text{Wcm}^{-2}$	95	1.42	700	800	
p-Si/n-CdS core shell nanowire	$\lambda = 700 \text{ nm}$	–	1.37	–	–	[78]
CdS:PS	$\lambda = 577 \text{ nm}$	–	1.7	–	–	[109]
<b>Al: CdS-PS: p-Si</b>	<b><math>\lambda = 400 \text{ nm}</math></b> <b><math>I = 71 \mu\text{Wcm}^{-2}</math></b>	<b>32</b>	<b>0.60</b>	<b>160</b>	<b>350</b>	<b>Present work [121]</b>

UV-vis spectral range between 250 to 500 nm is tested for this device. FESEM and FETEM analyses confirm formation of CdS nanostructure. Cross sectional FESEM view confirms uniform interface between CdS and PS: p-Si structure. EDX analysis confirms presence of Cd and S in the prepared heterostructure which is also supported by UV-vis reflectance measurement showing increment as well as blue-shift of the interference pattern on CdS deposition. PL study reveals trap and defect assisted luminescence bands at 450, 460, 468, 482 and 533 nm for nanostructured CdS along with characteristic band gap emission of PS at ~590 nm. These traps and defects in turn control electrical current conduction phenomena within the heterostructure as confirmed from dark current analysis. The heterostructured PD exhibits low leakage current and under illumination of 400 nm radiation shows high responsivity, high EQE and fast response time of ~160 ms at -2V. All these facts assure the device to be applicable as an eligible candidate for UV-vis photodetector and switching device.

# Chapter 4

## **Optical and electrical properties of nanostructured ZnS-PS: p-Si heterostructure**

[M. Das, S. Sarmah and D. Sarkar, in *Materials Today:  
Proceedings* (2020)]





## Optical and electrical properties of nanostructured ZnS-PS: p-Si heterostructure

### 4.1 Introduction

Photodetectors (PDs) based on silicon have attracted great interest due its broad visible to NIR photodetection ability [147-150]. However, Si faces disadvantage due to its low and indirect bandgap which creates obstacle particularly in efficient detection of UV-visible radiation. Porous silicon (PS) on the other hand is well known for its visible photo luminescence ascribed to confinement effect in nano silicon region [112]. PS is also known to increase the visible light sensing efficiency. However, for UV detection PS faces some limitations. To minimize these drawbacks wide bandgap materials like ZnS, ZnO, CuO, NiO etc., which are well known for their specific UV responses, can be coupled with PS:p-Si structure for fabricating efficient UV to visible radiation sensing devices. However, there have been various reported works on UV and visible range PDs [151-155]. To name a few, Uday et al. [56] reported improved Al/ZnS/PS/c-Si/Al device with responsivity of  $0.06 \text{ AW}^{-1}$  and  $0.03 \text{ AW}^{-1}$  at UV and visible region respectively. There is also a report on wide range photoresponse UV-A PD based on ZnS/ZnO biaxial nanobelt [156]. Another group of authors reported ZnS quantum dot based UV PDs with maximum responsivity of  $0.3 \text{ AW}^{-1}$  at 390 nm [157]. But reports on specific band UV to visible radiation sensing PDs with high responsivity are not many. In this chapter, particularly fabrication and characterization of distinct and

enhanced UV to visible photo sensing device based on ZnS-PS:p-Si heterostructure has been reported. Different work function metal electrodes have been combined to achieve Schottky contacts from ZnS and PS:p-Si structure.

## 4.2 Experimental

### 4.2.1 Preparation of Al + Au/ZnS-PS: p-Si MSM heterostructure

Preparation of PS:p-Si structure and annealing of bulk ZnS powder has been already described in the Chapter 2, subsection 2.2.1 and 2.2.5 respectively. For preparation of ZnS-PS:p-Si heterostructure, bulk ZnS powder (99.99% pure) annealed at 200 °C for 2 hrs is deposited on PS:p-Si and RCA cleaned glass substrates (for optical analysis) using thermal evaporation method in a chamber pressure of  $\sim 10^{-5}$  mbar. Thickness of the deposited ZnS powder is maintained at  $\sim 110$  nm using digital thickness monitor attached to the chamber. For construction of MSM heterostructure, high purity (99.99%) Au and Al electrode of thickness 8 nm and 22 nm are thermally evaporated on ZnS-PS:p-Si surface using a shadow mask of dimension 6 mm  $\times$  6 mm in a vacuum pressure of  $\sim 10^{-5}$ . Here Au and Al electrodes are used for providing Schottky contact to n-ZnS and p-type PS:p-Si surface respectively. Also, for comparison another MSM structure is fabricated on bare PS:p-Si using Al as contact electrode.

## 4.3 Results and discussion (M. Das et al., [158])

### 4.3.1 Morphological analysis

Morphological and elemental features of the prepared heterostructure are analysed using FESEM and cross sectional EDX analysis. These are shown in fig. 4.1(a-d) and fig. 4.2(a-d) respectively. Fig. 4.1(a) and (c) show planar view FESEM micrograph of PS:p-Si structure and ZnS-PS:p-Si heterostructures respectively. Spherical shaped ZnS particles are clearly visible in the micrograph with mean diameter of  $\sim 115$  nm as calculated from the particle size histogram plot. The particles are seen to be uniformly distributed on the surface of PS:p-Si structure. Fig. 4.1(b) and (d) show their cross sectional FESEM views. These show uniform interface of PS (540 nm thick) and ZnS (110 nm thick) layers with p-Si and PS layers respectively. To confirm elemental composition, EDX spectra are recorded. Fig. 4.2(a-d) shows selected area cross sectional EDX spectra of the heterostructure, Area 1 is selected for ZnS region, which

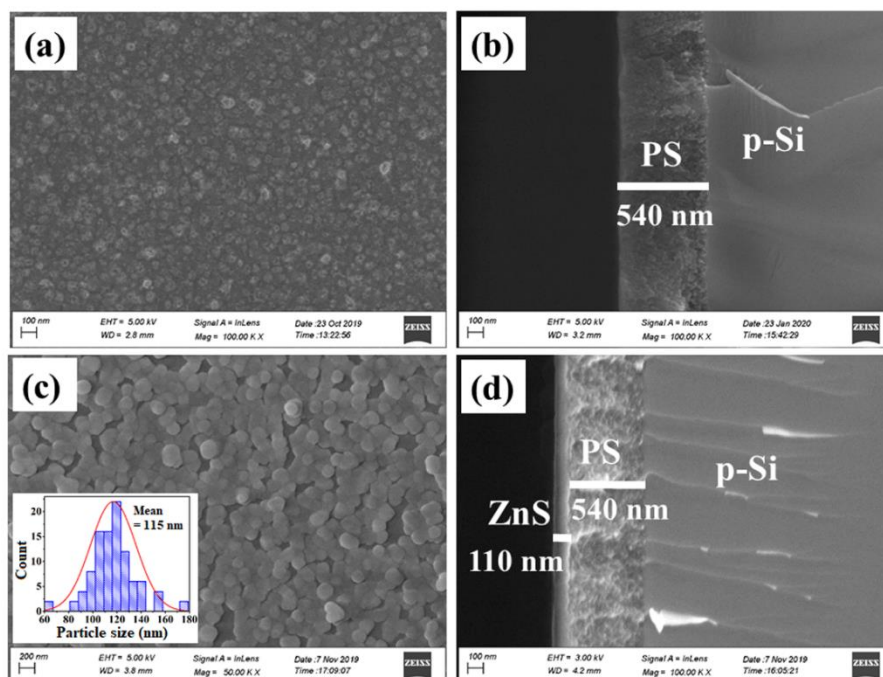


Fig. 4.1 FESEM view of (a) PS:p-Si surface, (b) PS:p-Si interface, (c) ZnS-PS:p-Si surface (inset shows particle size histogram), (d) ZnS-PS:p-Si interfaces.

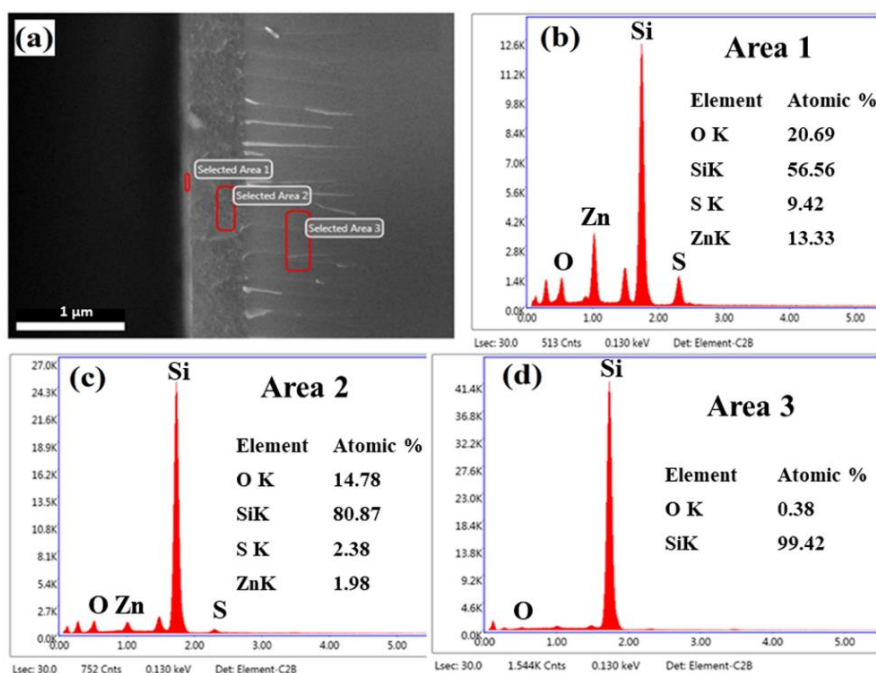


Fig. 4.2 (a) Selected areas for EDX analysis, EDX spectra for (b) ZnS region, (c) PS region and (d) p-Si region.

shows presence of Zn (13.33%), S (9.42%), Si (56%) and O (20%) by atomicity respectively [fig. 4.2(b)]. Si and O contribution is arising due to the fact that area selected is very near to the PS interface. Area 2 is selected for PS region, which shows

atomic presence of Si (80.87%), O (14.78%), Zn (1.98%), and S (2.38%) respectively as shown in fig. 4.2(c). Presence of Zn and S suggests diffusion of some percentage of ZnS particles into the porous layer of PS making it more ZnS rich which would consequently enhance photoresponsivity of the layer to be discussed later in the coming subsection. Area 3 selected is for p-Si region and is shown in fig. 4.2(d), which shows maximum elemental presence of Si upto 99.6% by atomicity as expected.

### 4.3.2 Optical analysis

Optical analysis of the bare ZnS sample coated on glass substrate and the prepared heterostructure are carried out using UV visible absorbance and reflectance spectra and photoluminescence (PL) spectra which are shown in fig. 4.3(a-d). Fig. 4.3(a) shows UV visible absorbance spectra of ZnS-Glass and inset showing its transmittance spectra. This shows onset of absorption band edge at  $\sim 380$  nm at UV region, with transmittance of 70-95 % of electromagnetic radiation in near UV to visible region, thus making it eligible candidate for visible blind photodetectors and solar cells. Bandgap energy of bare ZnS is calculated using Tauc plot, which is shown in fig. 4.3(b). The band gap energy is found to be 3.4 eV. Fig. 4.3(c) shows UV-vis reflectance spectra of p-Si (black line) along with that of bare ZnS (red line), PS:p-Si (blue line) and ZnS-PS:p-Si (pink line) structures for the wavelength range of 300-800 nm. ZnS-PS:p-Si is seen to exhibit low reflectance of EM radiation in the wavelength range of  $\sim 390$ -800 nm. This is 10-20 % less than that of bare ZnS and PS:p-Si structure respectively which are also  $\sim 15$ -20 % less compared to bare p-Si which seen to reflect about 35-45 % of radiation within this wavelength range. These observations indicate that the prepared heterostructure can exhibit minimum light energy loss compared to bare p-Si and PS:p-Si. Fig. 4.3(d) shows the PL spectra for bare PS, bare ZnS and ZnS: PS heterostructure for excitation of 300 nm radiation. The spectra is fitted for Gaussian curve to deconvolute the prominent PL emission peaks of the three spectra. Bare PS shows broad characteristic emission peak at 597 nm with full width half maxima (FWHM) of  $\sim 130$  nm arising due to quantum confinement of Si nanostructures. For bare ZnS, emission peaks at 384, 415 and 467 are observed. The most intense emission peak at 384 nm can be ascribed to radiative recombination between defect states near to the valence and conduction bands

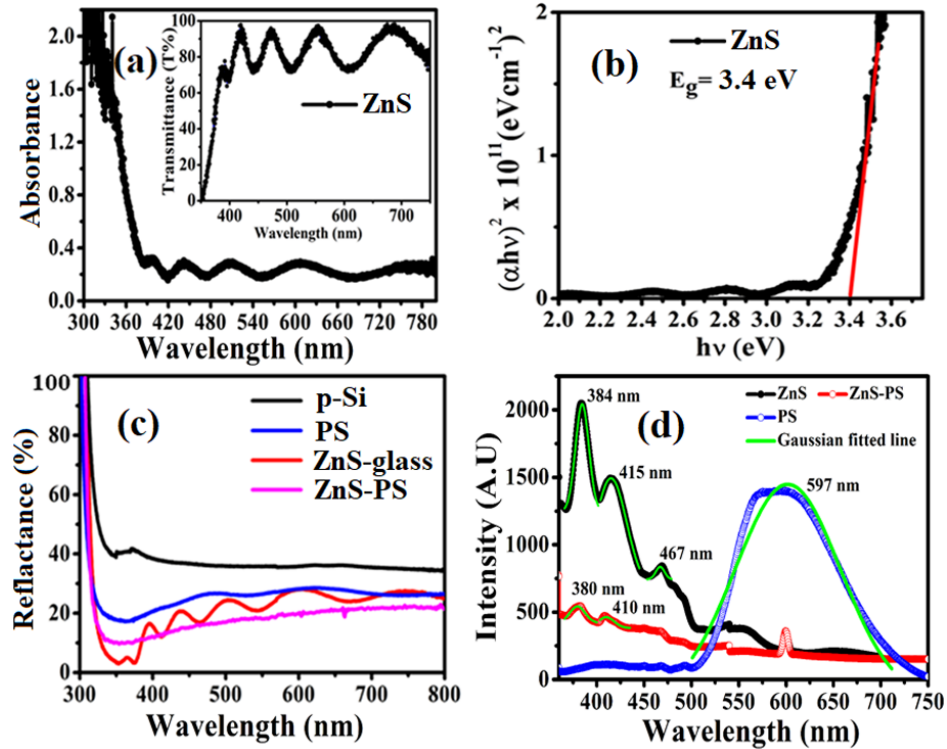


Fig. 4.3 (a) absorbance spectra of bare ZnS (inset shows transmittance spectra), (b) Tauc plot for ZnS, (c) UV-vis reflectance spectra of p-Si, bare ZnS, PS and ZnS-PS, (d) PL spectra of bare ZnS, PS and ZnS:PS heterostructure

of ZnS [159]. The emission peak centred at 415 nm is associated with the recombination of  $e^-h^+$  pairs between conduction band and shallow state for the sulphur vacancy near the valence band [159,160]. However, for ZnS: PS heterostructure, these two peaks are marginally quenched and red shifted to 380 and 410 nm. The particle size of ZnS changes in the heterostructure due to its diffusion into the porous layer, which may lead to PL quenching and red shift. Moreover, for the same fact of ZnS diffusion into PS layer, PS characteristic peak also disappears for ZnS: PS heterostructure. The emission peak at 467 nm observed for bare ZnS is related to recombination of  $e^-h^+$  pairs at sulphur vacancy near the conduction band and zinc vacancy near the valence band. This emission peak is not prominent in case of ZnS: PS heterostructure. To observe the effects of vacancy or defect states on photo sensing ability of the heterostructure, further studies have been carried out and discussed in the following section.

### 4.3.3 Electrical and photo response analysis

To observe the electrical property of the heterostructure it is recommended to analyse the leakage current flowing through it. To analyse this, current-voltage ( $I$ - $V$ )

characteristic of the heterostructure has been recorded under dark condition for the voltage range of -5V to +5 V. Fig. 4.4(a) shows forward region semi log  $I$ - $V$  plot of Al+Au/ZnS-PS:p-Si and Al/PS:p-Si devices with inset showing similar plot for reverse bias region. Reverse leakage currents for the devices are calculated to be  $1.94 \times 10^{-7}$  A and  $5.52 \times 10^{-8}$  A at -5V respectively, which are quite low values. This establishes the fact that both the devices produces very low magnitude of leakage current. Also, from the figure it can be seen that dark current ( $I_d$ ) values for Al + Au/ZnS-PS:p-Si is lower compared to that of Al/PS:p-Si in the voltage region of -0.2 V to -1.2 V. This decrease in current is attributed to the surface charge recombination within the space charge region due to formation of p-n junction between n-type ZnS and p-type PS:p-Si structure. To analyse the quality of the prepared devices, thermionic emission model is applied to the low voltage regions i.e. -0.5 to -0.2V for Al+Au/ZnS-PS:p-Si and -0.2 to 0.5V for Al/PS:p-Si. In these regions  $I_d$  is seen to be linearly dependent on applied voltage giving ideality factor ( $n$ ) of 1.5 and 7 for the two devices with reverse saturation current ( $I_s$ ) values of  $7.4 \times 10^{-6}$  A and  $1.5 \times 10^{-9}$  A respectively. One can say that the device quality is improved for Al+Au/ZnS-PS:p-Si, due to its low ideality factor value. In the voltage region  $>-0.2$ V for Al+Au/ZnS-PS:p-Si and  $>0.2$ V for Al/PS:p-Si, current is seen to increase non-linearly with increasing applied voltage, which is attributed to the effect of series resistance arising due to drift motion of the charge carriers and also due to recombination of charge carriers within the interface states. To observe more in-depth, forward  $I$ - $V$  region is analysed using defect conduction model fitting equation  $I_{fd} = CV^m$  [131], the plot is shown in fig. 4.4(b). From the fit, the scaling parameter  $m$  is found to be 1.0 and 1.06 for Al+Au/ZnS-PS:p-Si and Al/PS:p-Si respectively. These

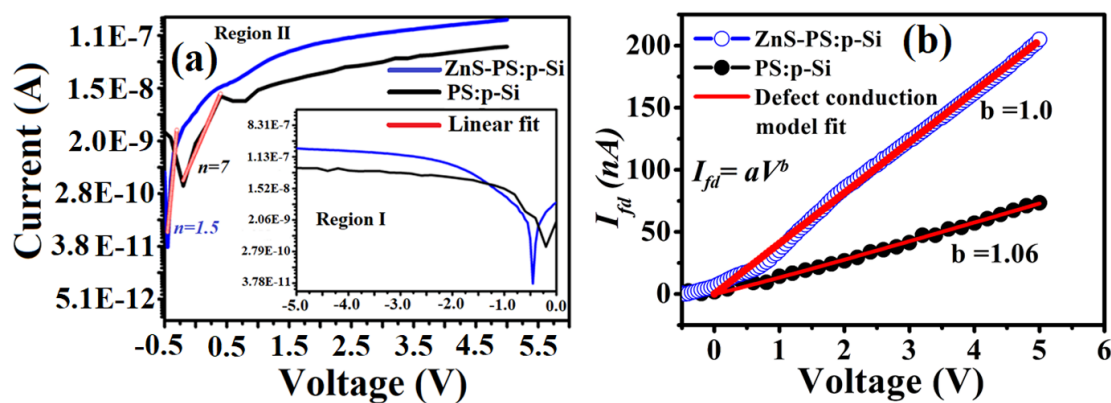


Fig. 4.4 (a) Forward biased semi-log dark  $I$ - $V$  plot (inset shows the plot for reverse bias) and (b) plot of defect conduction model fitted  $I$ - $V$  curve for PS and ZnS: PS devices

ascertain that defects and traps play no significant role in current conduction phenomenon for these devices. To analyse the photoconduction phenomenon, semi log photo  $I$ - $V$  for both the devices are plotted in the voltage range of -5V to +5V. Fig. 4.5(b) shows the plot for PS under illumination of 400 nm, also for ZnS: PS under illumination of 365 and 400 nm along with their dark currents. Both the devices show almost symmetric rectification enhancement under +ve and -ve biasing condition. This symmetric enhancement is quite likely because of their lateral electrode configuration [fig. 4.5(a)]. Spectral response for the devices are recorded for the wavelength range of 200-500 nm under bias voltage of -4V and their corresponding responsivity ( $R_\lambda$ ) vs. wavelength ( $\lambda$ ) plots are shown in fig. 4.5(c). Here it can be seen that Al+Au/ZnS-PS:p-Si device shows enhanced and distinct responsivity peaks at 365 and 400 nm with values of 0.95 and 1.13  $\text{AW}^{-1}$  respectively compared to 0.59  $\text{AW}^{-1}$  for Al/PS:p-Si device at 400 nm. The peak at 365 nm for the former device is attributed to band to band absorption in ZnS as can be seen from the absorption spectra shown in fig. 4.3(a). Whereas the peak observed at 400 nm for the devices is attributed to maximum absorption of photons in PS:p-Si structure. The enhancement of the responsivity peaks for Al+Au/ZnS-PS:p-Si can be attributed to the photo generated charge carriers within the depletion region or the active region of the heterostructure due to p-n junction formation. Fig. 4.5(d) shows the  $R_\lambda$  vs.  $\lambda$  plots for Al+Au/ZnS-PS:p-Si device under different biasing of -3, -4 and -5V in the wavelength of 200-500 nm. The  $R_\lambda$  value increases from 0.5 to 1.1  $\text{AW}^{-1}$  and 0.3 to 1.4  $\text{AW}^{-1}$  for illumination of 365 and 400 nm, when bias value increases from -3 to -5V. Here,  $R_\lambda$  value shows saturation due to constancy of photo current for higher biasing conditions. Intensity dependent photocurrent ( $I_{ph}$ ) for the devices are recorded under illumination of 400 nm in the light intensity range of 11-45  $\mu\text{Wcm}^{-2}$  at -4V biasing [fig. 4.6(a)].  $I_{ph}$  follows the power law equation,  $I_{ph} = aP^b$ , where,  $a$  is const. of proportionality,  $b$  is the scaling parameter. Photo current conduction in both the devices are controlled by trap or defect states, as the value of  $b$  lies in the range of ~0.97-0.98 [161]. To know more about the switching dynamics of the Al+Au/ZnS-PS:p-Si device, on-off transient kinetics are recorded for bias voltage range of 0 and -4V, which are shown in fig. 4.6(b,c). Here, it can be seen that the device shows stable switching dynamics for UV-visible light illumination with on-off ratio of 2.18 for 400 nm irradiation and 2.34 for 365 nm at -4V bias. However,

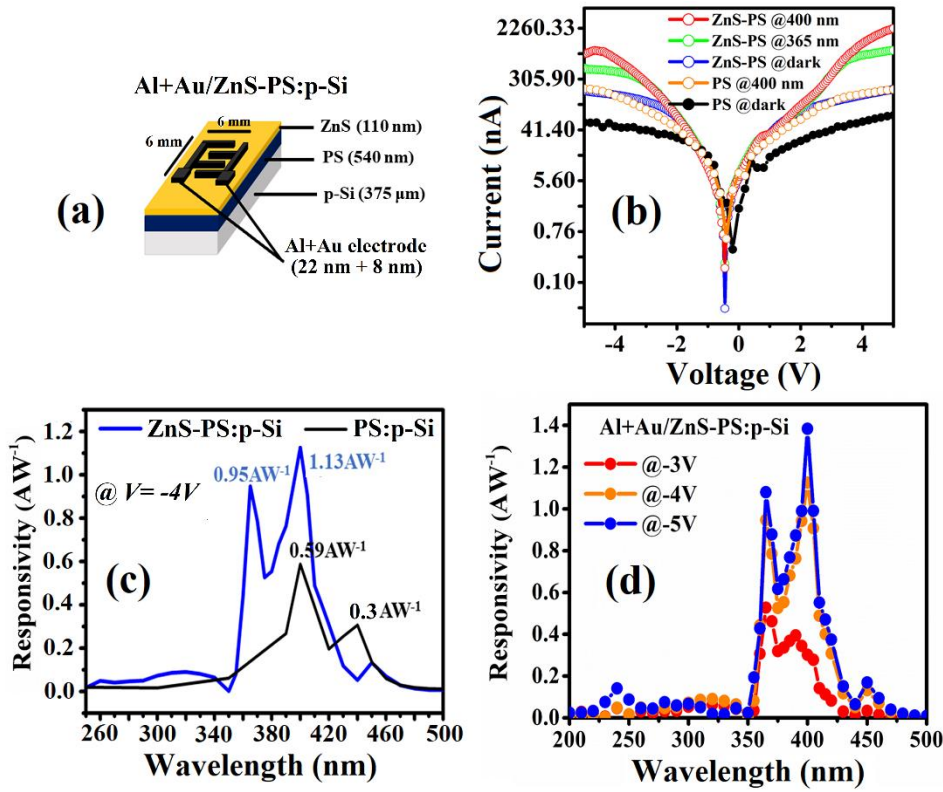


Fig. 4.5 (a) Schematic of ZnS-PS device, plot of (b) semi-log  $I$ - $V$  under dark and illumination condition,  $R_2$  vs.  $\lambda$  (c) at  $-4V$  for ZnS-PS and PS devices, (d) at  $-3$ ,  $-4$  and  $-5V$  for ZnS-PS device

for zero bias ( $0V$ ), the switching dynamics are less stable with average on-off ratio of  $\sim 6.5$ . To calculate the response and recovery times effectively, the transient kinetics under UV and visible irradiations are fitted using exponential fitting functions given by the equations,

$$I = Ae^{t/\tau} + I_0 \quad (4.1)$$

$$I = Ae^{-t/\delta} + I_0 \quad (4.2)$$

Eq. (4.1) represents exponential growth function, where  $A$ ,  $\tau$  and  $I_0$  are amplitude, growth constant (response time) and onset value respectively. Eq. (4.2) represents similar decay function, where  $\delta$  and  $I_0$  are decay constant (recovery time) and offset value respectively. From the fitted curves shown in fig. 4.6(d), for 365 nm radiation, response and recovery times are calculated to be  $0.54 \pm (4.3 \times 10^{-4})$  s and  $0.38 \pm 9.5 \times 10^{-5}$  s. Whereas for 400 nm radiation these are found to be  $0.50 \pm 2.8 \times 10^{-4}$  s and  $0.35 \pm 6.5 \times 10^{-5}$  s respectively. Here it can be seen that response time of the device for constant irradiation wave length is slow compared to its recovery time, which can be



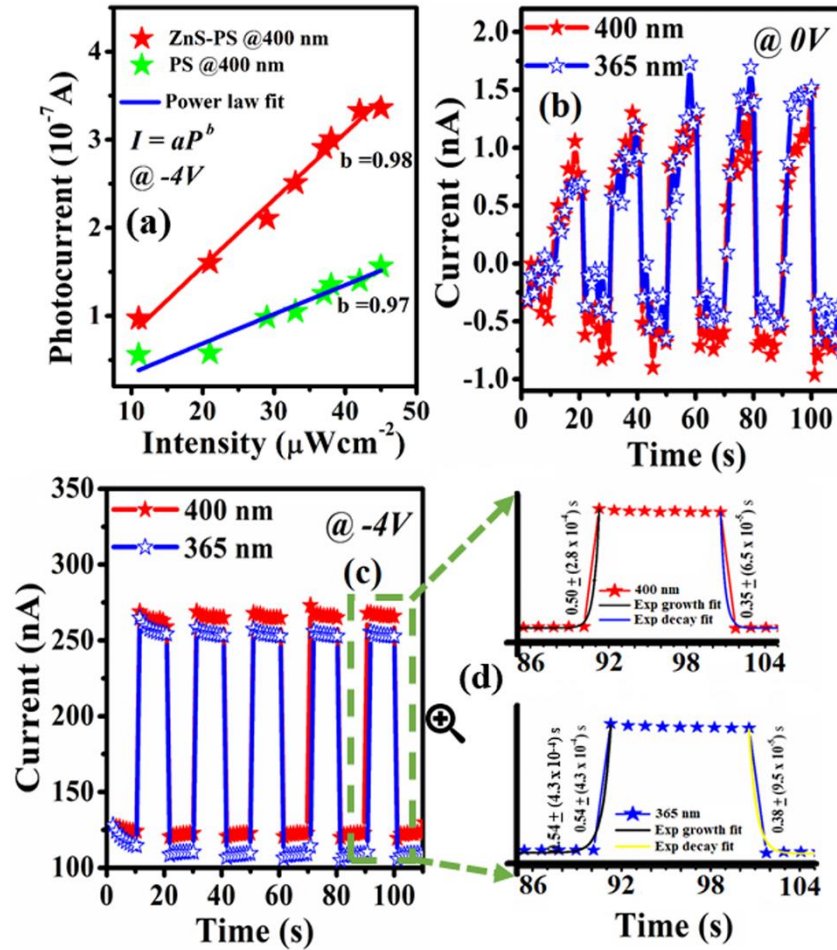


Fig. 4.6 (a) Intensity dependent  $I_{ph}$  plot, time response kinetics of ZnS-PS device under irradiation wavelengths of 365 and 400 nm at (b) 0V, (c) -4V, (d) response time calculations

attributed to trapping and de trapping of charge carriers within the interface states due to inhomogeneity in the heterostructure.

#### 4.4 Conclusion

Photodetector (PD) with distinct and enhanced responsivity from ZnS-PS: p-Si heterostructure has been successfully developed. FESEM micrograph shows uniform interface between ZnS and PS:p-Si structure. Cross section EDX analysis reveals diffusion of some ZnS particles into PS layer. UV-visible spectra of bare ZnS reveals maximum light absorption in UV region and transmit maximum radiation in near UV to visible region. Reflectance spectra shows that ZnS-PS:p-Si heterostructure exhibits low reflectivity compared to bare ZnS and PS:p-Si. ZnS-PS shows ZnS related band edge luminescence at  $\sim 380$  nm with some defect dominated luminescence bands in the visible range. Dark current analysis shows low leakage current of  $\sim 10^{-7}$  and  $10^{-8}$  A for

Al+Au/ZnS-PS: p-Si and Al/PS:p-Si devices respectively. Al+Au/ZnS-PS: p-Si exhibits distinct and enhanced responsivity ( $R_\lambda$ ) values of 0.95 and 1.13  $\text{AW}^{-1}$  respectively at 365 nm and 400 nm radiations compared to 0.59  $\text{AW}^{-1}$  for Al/PS:p-Si structure at 400 nm. These distinctness are mainly attributed to maximum band to band absorption of photons in ZnS and PS:p-Si structure. Response and recovery times of the device are fast enough for potential application as UV visible photodetector and switching devices.

# Chapter 5

## **Optical and electrical properties of as-prepared and annealed ZnO- PS: p-Si heterostructure**

[M. Das, S. Sarmah, D. Barman, B.K. Sarma and D. Sarkar,  
Mater. Sci. Semicond. Process. **118**, 105188 (2020)]



## Optical and electrical properties of as-prepared and annealed ZnO-PS: p-Si heterostructure

### 5.1 Introduction

High speed UV photodetectors (PDs) with high spectral response are the basic needs for applications in solar astronomy, optoelectronics, ecological monitoring etc. Although it has been observed from literature survey that reports on such PD's are not many. For this purpose, metal oxides, mainly ZnO has been explored widely in last few decades due to its exceptional UV sensing ability [162-165]. However, PDs which can cover the wavelength range from UV to visible would be of much advantage. Devising PDs with high responsivity and fast response in UV-visible range is still a challenge for researchers [166-169]. Porous silicon is known to sense the visible range. So, porous silicon based PDs which have high spectral response in visible spectral range, but have limitations in UV light sensing can be coupled with the nanostructured ZnO having wide electronic band gap for better photo sensing in UV-visible range of the electromagnetic spectrum [170,171]. Many growth methods viz., pulsed laser deposition, hydrothermal, spray pyrolysis, sol-gel process, RF or DC sputtering etc. are used for deposition of ZnO nanostructures on PS substrates [172-177]. In the present work, pulsed DC magnetron sputtering is used for growth of highly adhesive good quality nanostructured ZnO films on PS:p-Si and glass substrates. Several groups have reported fabrication of ZnO-PS based Schottky PDs using electrodes of Al, Ag, Au and

Pt metals [178-181]. To achieve distinct band UV-visible PDs from ZnO-PS:p-Si heterostructure, gold (Au) and aluminium (Al) metal electrodes are used. Moreover, the effects of post annealing treatment on photo sensing properties of ZnO-PS based Schottky PDs are also not much reported till date. However, to name a few, A.A. Thahe [182], recently reported Pt/n-PS/ZnO based PDs with maximum responsivity of  $5.99 \text{ AW}^{-1}$  when annealed at  $700 \text{ }^\circ\text{C}$  under illumination of 380 nm. But, the device fails to sense visible light, possibly due to lack of novelty in the sample preparation and improper selection of the electrode metals. Keeping these in mind, the prepared Al+Au/ZnO-PS:p-Si Schottky device has been annealed in the range of  $200\text{-}500 \text{ }^\circ\text{C}$  to study the annealing effects on its photo sensing performances. Morphological and optical properties of the as-prepared and annealed ZnO-PS:p-Si heterostructure also have been studied to examine these effects on the UV-visible light sensing performances.

## 5.2 Experimental

### 5.2.1 Preparation of ZnO-PS:p-Si heterostructure

PS:p-Si structure has been prepared using anodization method. Nanostructured ZnO with thickness of  $\sim 160 \text{ nm}$  is sputter deposited on glass and PS:p-Si substrates using pulsed DC magnetron sputtering for a deposition time of 20 min under Ar atmosphere. The details of PS preparation and ZnO sputtering process have been already described in Chapter 2 under subsection 2.2.1 and 2.2.4 respectively.

### 5.2.2 Preparation of MSM hybrid structures

Construction of MSM devices are carried out in vacuum coating unit. Two types of MSM devices are constructed, viz., planar Al+Au/ZnO-PS:p-Si (PD1) configuration and sandwich Al+Au/ZnO-PS: p-Si/Al (PD2) configuration. Along with these, a planar electrode of Al+Au/ZnO: Glass configuration is also constructed to examine the contribution of bare ZnO in photo sensing. Schematic of the respective PDs are shown in fig. 5.1(a-c). Highly pure Au (99.99%) and Al (99.99 %) metal electrodes of thickness 7 nm and 23 nm respectively are successively coated on ZnO-PS:p-Si and ZnO-glass substrates using interdigitated shadow mask of dimension  $6 \text{ mm} \times 6 \text{ mm}$  to achieve lateral MSM device configuration. To achieve the sandwich MSM device

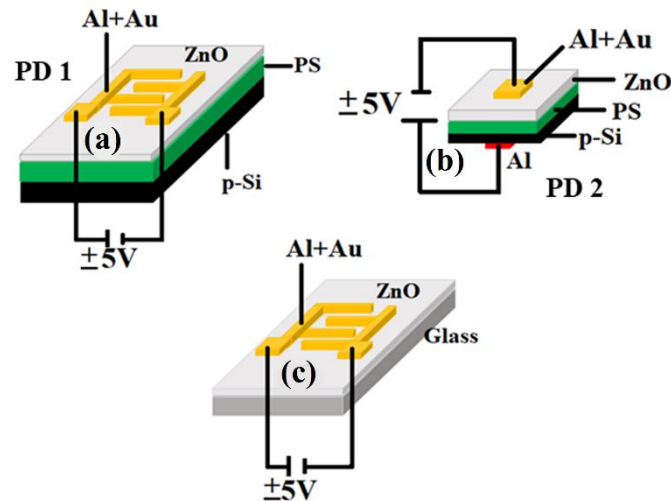


Fig. 5.1 Schematic of the devices (a) PD1, (b) PD2 (c) and bare ZnO

configuration, Al+Au (30 nm) and Al (30 nm) electrodes of effective area  $0.04 \text{ cm}^2$  are deposited on front and back side of ZnO-PS:p-Si heterostructure respectively in a base pressure of  $\sim 10^{-5}$  mbar. Au being a high work function metal (5.30 eV), makes rectifying Schottky contact with n-type ZnO (4.71 eV) [183], while Al metal with lower work function of  $\sim 4.26$  eV provides good adherence to the Au electrode and makes rectifying Schottky contact with PS:p-Si structure. PD1 as well as the ZnO-PS:p-Si heterostructure are annealed in the temperature range of 200-500  $^{\circ}\text{C}$  in a horizontal tube furnace. The details of the annealing method have been described in details in subsection 2.2.5 of Chapter 2.

### 5.3 Results and discussion: Part A: Optical and electrical properties of the as-prepared ZnO-PS:p-Si heterostructure (M. Das et al., S. Sarmah et al. and S. Sarmah et al. [184-186])

#### 5.3.1 Morphological analysis

Morphological and elemental properties of the prepared heterostructures are studied using FESEM and EDX techniques which are shown in fig. 5.2, 5.3 respectively. Fig. 5.2(a, d) shows planar and cross sectional view of PS:p-Si structure. These show randomly distributed silicon mesopores with uniform PS layer thickness of  $\sim 540$  nm. Fig. 5.2(b) shows in-plane FESEM micrograph of the ZnO thin film deposited on glass

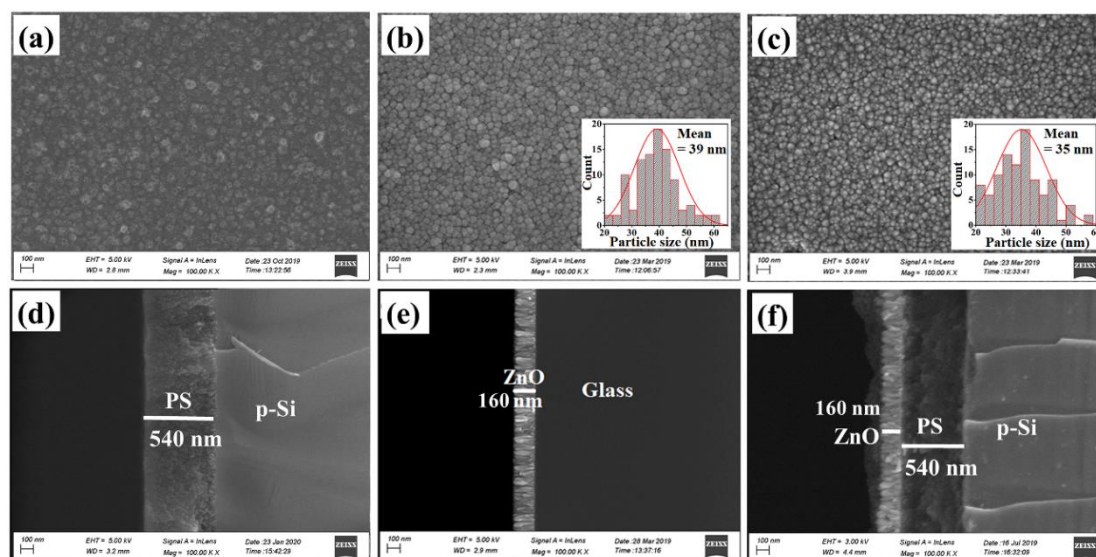


Fig. 5.2 Planar FESEM images of (a) PS:p-Si, (b) bare ZnO on glass, (c) ZnO-PS:p-Si, (insets-particle size histograms), Cross sectional FESEM images of (d) PS:p-Si, (e) ZnO:glass and (f) ZnO-PS:p-Si interfaces.

substrate, which shows uniformly grown spherical shaped ZnO nanoparticles with mean diameter of 39 nm calculated from the particle size histogram [inset of fig. 5.2(b)]. The thickness of the ZnO layer as observed from cross section FESEM view shown in fig. 5.2(e) is calculated to be ~160 nm. Fig. 5.2(c) shows planar view of ZnO-PS:p-Si heterostructure, which shows growth of ZnO nanoparticles with slightly reduced mean particle size of 35 nm as calculated from the histogram [inset of fig. 5.2(c)]. Slight reduction in ZnO particle size might arise from the diffusion of the nanoparticles into the pores of PS layer. The combined thickness of ZnO-PS layer is calculated to be ~700 nm as shown in the cross-sectional view of fig. 5.2(f). Fig. 5.3(a-d) shows cross sectional EDX analysis of ZnO-PS:p-Si heterostructure for different regions. Fig. 5.3(a) shows the regions selected for the analysis. For area 1 comprising of p-Si only, as expected, elemental presence of Si is 100% by atomicity [fig. 5.3(b)]. For area 2 in the PS region, elements present are Si (78.88%), Zn (12.49%) and O (8.64%) by atomicity, these are shown in fig. 5.3(c). Thus, it is evident that some percentage of ZnO particles gets penetrated through the porous structure of the PS layer making the layer more ZnO rich, which may consequently effect the conductivity of the PS layer. From fig. 5.3(d), for selected area 3 in ZnO layer, it is seen that along with the presence of Zn (28.52%) and O (37.97%), Si (33.50%) is also present and is attributed to the portion of thin ZnO layer selected very near to the PS interface. These confirm formation of p-n junction between p-type PS:p-Si and n-type ZnO layer.



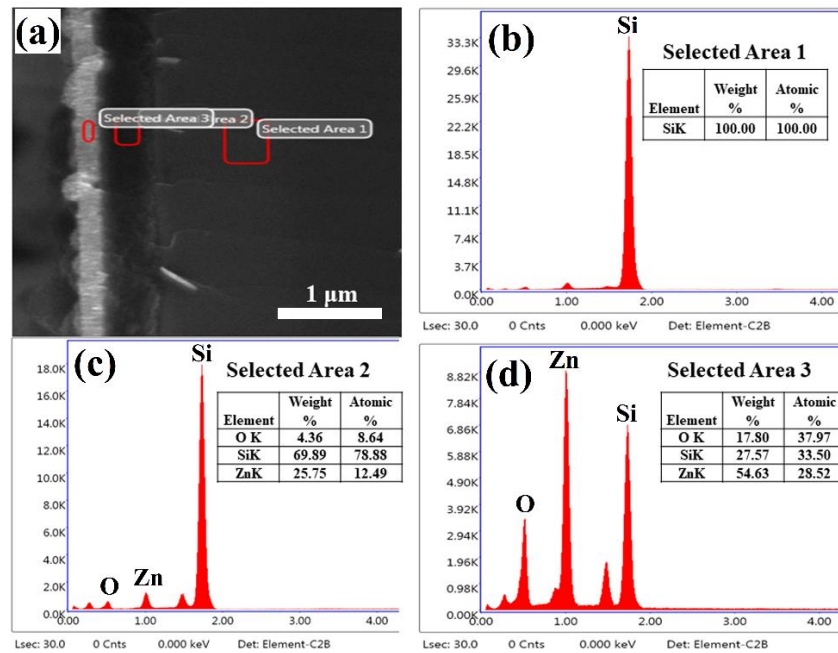


Fig. 5.3 (a) Selected areas for EDX analysis of ZnO-PS:p-Si interfaces, EDX spectra of (b) p-Si region, (c) PS region and (d) ZnO region.

### 5.3.2 Optical analysis

Optical properties of the sputtered ZnO and the heterostructures are studied through UV-visible and photoluminescence (PL) spectra. Fig. 5.4(a) shows UV-visible absorbance spectra of sputtered ZnO along with the inset showing its transmittance spectra. ZnO shows onset and offset absorption band edge at  $\sim 390$  and  $\sim 350$  nm respectively in the UV region and transmitting 80-90% of the visible light in the region 400-700 nm, thereby making it one of the best transparent material for visible radiation of the electromagnetic spectrum. Band gap energy of the sputtered ZnO is calculated using the conventional Tauc plot as shown in fig. 5.4(b). This gives band gap of the material to be 3.3 eV, making it suitable for UV light sensing. Fig. 5.4(c) shows absolute UV-visible (200-800 nm) reflectance spectra of the p-Si wafer along with bare ZnO, PS:p-Si and ZnO-PS:p-Si heterostructure. These show 35-45% reflectivity of p-Si, whereas bare ZnO, PS:p-Si and ZnO-PS:p-Si show decreased reflectivity upto 10-20%. This decrease in reflectivity is attributed to the increased surface roughness and decreased refractive index of the heterostructures. Also, some percentage of radiation get trapped within the textured surface of PS:p-Si and ZnO:PS interfaces. Thus, the heterostructures can reduce energy loss as compared to that of bulk c-Si. Also, there is

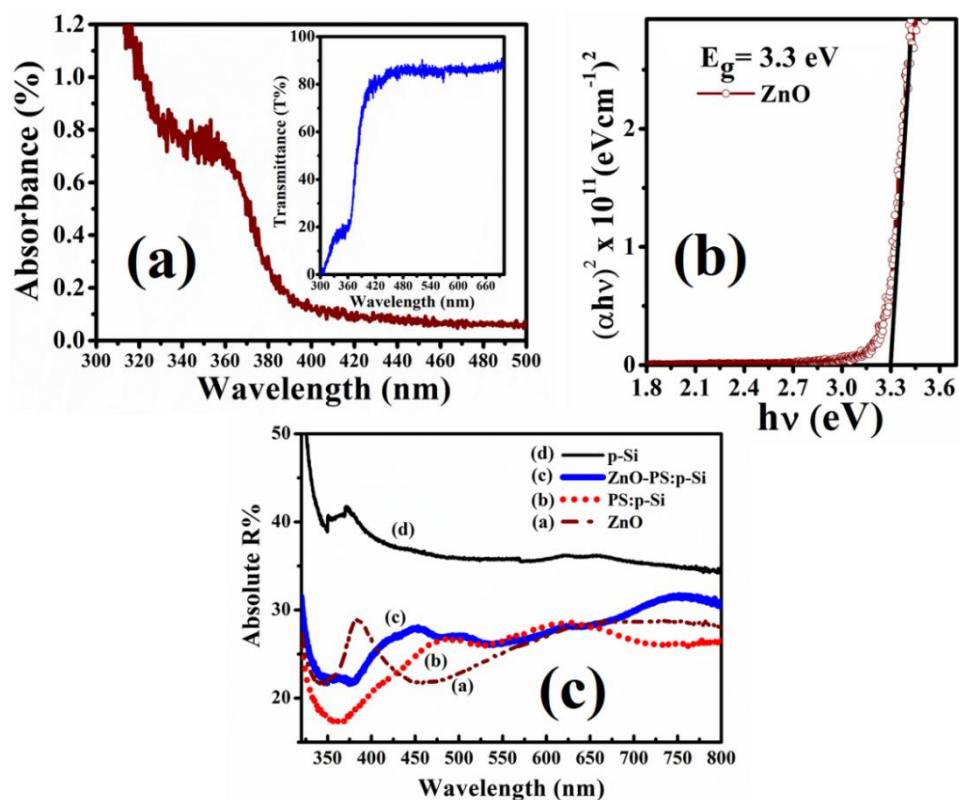


Fig. 5.4 (a) Absorbance spectra of bare ZnO inset shows its transmittance spectra, (b) Tauc plot for bare ZnO, (c) reflectance spectra of p-Si, bare ZnO, PS:p-Si, ZnO-PS:p-Si.

an increment of interference patterns for ZnO-PS:p-Si heterostructure, which is attributed to increased effective thickness and change in refractive index on ZnO incorporation. To observe the spectral analysis of the prepared ZnO-PS:p-Si heterostructure, PL spectra are recorded for an excitation wavelength ( $\lambda_{exc.}$ ) of 340 nm which is shown in fig. 5.5(a). Fig. 5.5(b) shows that for bare ZnO for comparison. The band at 378 nm (3.28 eV) may be assigned to band-to-band transitions of ZnO nanoparticles [fig. 5.4(b)]. Bands at ~388 and 398 nm corresponding to energy values of 3.19 eV and 3.12 eV are attributed to transitions from slightly lower excitonic states near conduction band (CB) to the valence band (VB). Along with these two bands, bands at 410, 420, 433, 450, 467, 482 and 492 nm in the visible range are also observed. The visible violet luminescence band at ~410 nm (3.02 eV) is attributed to electronic transition from bottom of the CB to the Zn vacancy ( $V_{Zn}$ ) level and it matches with the energy interval (3.06 eV) between CB and Zn vacancy level [187]. The blue luminescence band at ~420 nm (2.95 eV) can be ascribed to the electronic transition from CB edge to the oxygen interstitial ( $O_i$ ) site [188]. The bluish violet band at ~433 nm (2.86 eV) is due to the transition from  $Zn_i$  site lying 0.34 eV below the CB edge to

the top of the VB [189]. The luminescence bands appearing in the wavelength range of 450-468 nm are ascribed to doubly ionized Zn vacancies ( $V_{Zn}^{2-}$ ) [81,190]. Luminescence band at ~482 and 492 nm are ascribed to the transition from  $Zn_i^+$  to  $V_{Zn}$  and CB to the neutral oxygen vacancy ( $V_o$ ) level [81, 191]. It is evident from the PL spectra that the peak resolution for ZnO-PS:p-Si structure is better than that of bare ZnO, which may be attributed to diffusion of good quality ZnO nanoparticles into the PS layer as confirmed from EDX analyses [45]. The heterostructure shows broad luminescence band covering the range of 500-700 nm. On deconvoluting this band using Gaussian fitting, the peak is found to be at ~597 nm which is ascribed to confinement of electron in nano silicon region within the PS layer [128]. Thus, from the PL spectra it can be said that the heterostructure exhibits various defect/traps dominated luminescence bands in the UV-visible region of the radiation spectrum. The PL mechanism is described schematically in fig. 5.5(c). One can presume that these defects and traps would consequently have effect in light sensing property of the heterostructure, which are discussed in the following section.

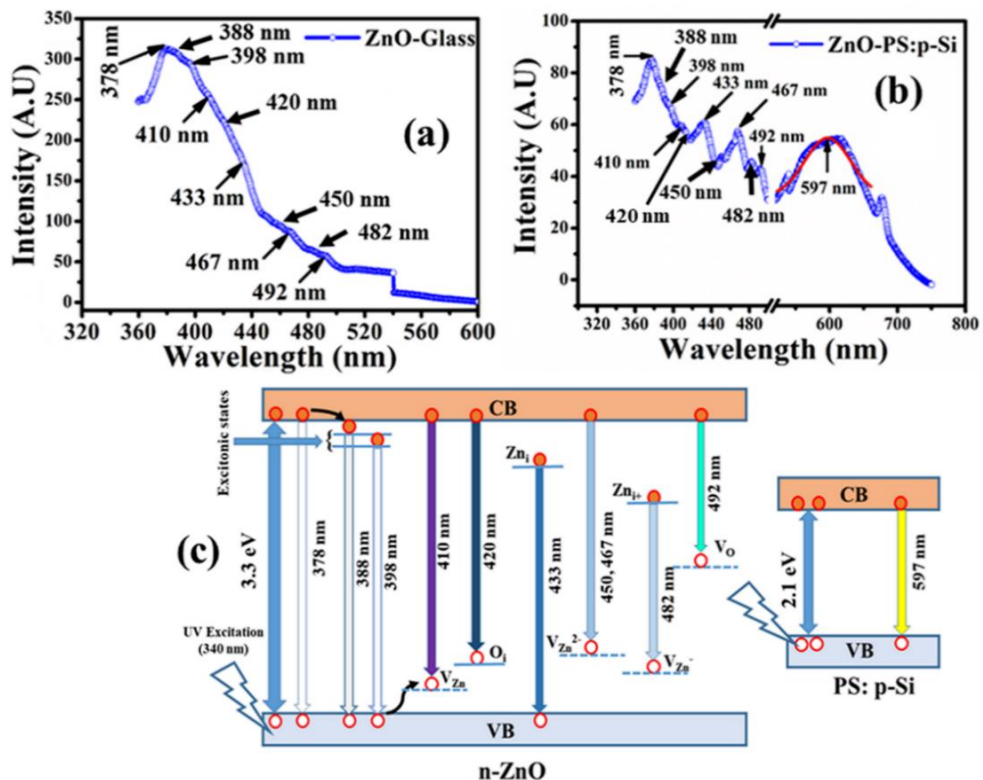


Fig. 5.5 PL spectra of (a) ZnO-PS:p-Si, (b) bare ZnO and (c) schematic of PL mechanism.

### 5.3.3 Electrical and photo response analysis

To know better about the junction properties of the prepared MSM heterostructures, it is recommended to analyse the dark current ( $I_d$ ) that flows through the heterostructures. Semi-logarithmic current-voltage ( $I$ - $V$ ) characteristics under dark condition for the applied bias range of -5V to +5V are recorded for both planar and sandwich electrode configurations (PD1 and PD2). The data for ZnO device with planar electrode configuration are shown to visualize the contribution of ZnO. These results are shown in fig. 5.6(a). The  $I$ - $V$  curves are divided into three regions; namely region I (-5 to 0V), region II (0 to 0.2V) and region III (0.2 to 5V). Region I is the reverse bias region which gives reverse leakage current ( $I_R$ ) of  $6.6 \times 10^{-8}$  A and  $7.5 \times 10^{-7}$  A for PD1 and PD2 respectively, whereas the device with bare ZnO shows lower value of  $6 \times 10^{-9}$  A at -5V. Increased  $I_R$  value of PD1 and PD2 compared to ZnO device is possibly due to increase of minority carrier density, as PD1 and PD2 are architect using n-type ZnO and p-type PS:p-Si. Also, PD2 contributes more current compared to PD1 due to sandwich electrode configuration. In region II, for the low forward bias (0 to 0.2V), the current is seen to increase linearly with applied voltage and can be explained from thermionic emission model of carrier generation. Applying this model, saturation current ( $I_s$ ), ideality factor ( $n$ ) and barrier height ( $\phi_b$ ) are calculated using following equations (5.1)-(5.3) [192] at ambient temperature, i.e.,  $T= 300$  K.

$$I = I_s \exp \frac{eV}{nkT} \quad (5.1)$$

$$n = \frac{e}{kT} \frac{dV}{d \ln I} \quad (5.2)$$

$$\Phi_b = -\frac{kT}{e} \ln \frac{I_s}{AA^*T^2} \quad (5.3)$$

Where  $k$  is Boltzmann constant,  $e$  is electronic charge,  $T$  is temperature,  $A$  is the effective area of the diode ( $0.36 \text{ cm}^2$  for PD1 and  $0.04 \text{ cm}^2$  for PD2) and  $A^*$  is Richardson constant ( $32 \text{ A/cm}^2 \text{ K}^2$  for the system) [130]. Calculated  $I_s$ ,  $n$  and  $\phi_b$  values for PD1 and PD2 are 0.4 nA, 3.8 and 0.92 eV; 3.2 nA, 1.7 and 0.81 eV respectively. The corresponding values for bare ZnO device are 36.3 pA, 2.4 and 0.98 eV. The deviation of ideality factor and barrier height from theoretical values [193, 194] is attributed to surface defects within the metal-semiconductor interface of the devices.

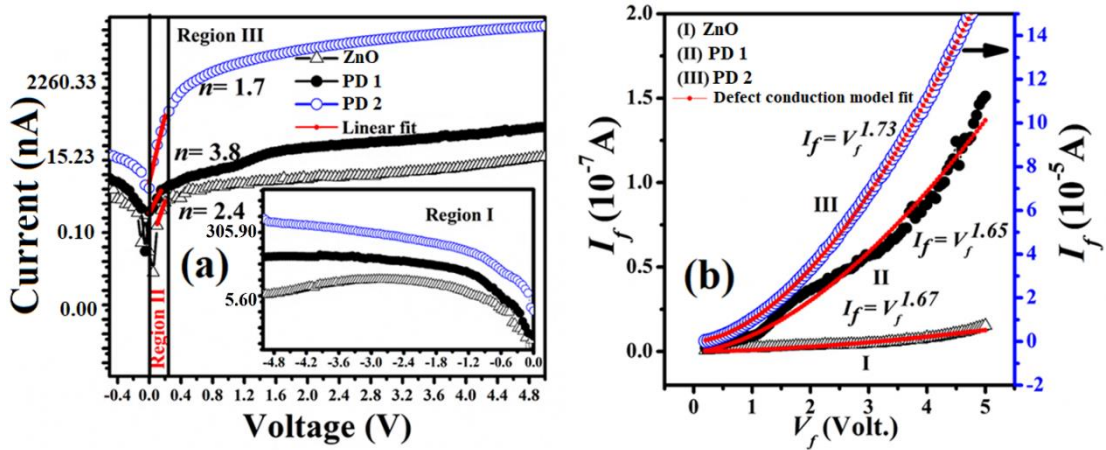


Fig. 5.6 (a) Forward bias semi-log dark  $I$ - $V$  plot (inset shows the plot under reverse bias condition), (b) plot of defect conduction model fitted  $I$ - $V$  curve for PD1, PD2 and bare ZnO

Also, from the ideality factor ( $n$ ) values it can be said that the device quality of PD2 is better compared to that of PD1 and bare ZnO. Region III of the  $I$ - $V$  curve (0.2-5V) shows power law dependence of current on voltage due to effect the of series resistance arising from charge recombination at traps or defect states. To know more about the current conduction phenomenon, this region is analysed with defect conduction model with power law fitting equation,  $I_f = V_f^m$ , where  $I_f$  is forward dark current,  $V_f$  is forward voltage and  $m$  is the scaling parameter which determines the defect dominated carrier dynamics. Plots of  $I_f$  vs.  $V_f$  are shown in fig. 5.6(b) which yield  $m$  values for PD1 and PD2 as 1.65 and 1.73 respectively and that of ZnO device as 1.67 with adjusted *R-squared* values of 0.98238, 0.99991 and 0.92588 respectively, indicating good fit of the model. These confirm defect dominated current conduction phenomenon in the PDs [131]. To observe the effects of native defects on light sensing properties of PDs', spectral responses are recorded for the UV-visible spectrum (200-500 nm). Responsivity ( $R_\lambda$ ) and external quantum efficiency (EQE) are determined using the equations 3.3 and 3.4 as mentioned in Chapter 3, subsection 3.3.3. Fig. 5.7(a, b) show plots of calculated  $R_\lambda$  and EQE vs.  $\lambda$  at -2V bias value for PD1 and PD2, whereas fig. 5.7(c) gives the plot for the bare ZnO device. The insets of these figures show similar plots for -0.5V bias. Fig. 5.7(a, b) indicate that PD1 and PD2 exhibit two distinct  $R_\lambda$  and EQE peaks at 375 and 400 nm. Here  $R_\lambda$  and EQE values of PD1 are  $\sim 1.87 \text{ AW}^{-1}$ ,  $2.6 \text{ AW}^{-1}$  and  $\sim 600, 800\%$  respectively, whereas for PD2 these values are  $\sim 55 \text{ AW}^{-1}$ ,  $68 \text{ AW}^{-1}$  and 20,000, 22,000%. This massive difference in the values of PD1 and PD2 is due to low effective device area ( $S$ ) of PD2 compared to that of PD1. This also

indicates that these devices to be responsive in both UV and visible region of the radiation spectra. However, on application of low bias voltage i.e.  $-0.5V$ , these PDs show single peak for  $R_\lambda$  and EQE at  $\sim 375$  nm confirming dominant contribution from ZnO. These can be confirmed from such plots of device with bare ZnO on glass substrate (fig. 5.7(c)). Bare ZnO device shows maximum  $R_\lambda$  and EQE of  $1.7 \text{ AW}^{-1}$  and  $550\%$  at  $375$  nm ( $3.3$  eV), and is attributed to maximum band edge absorption of electromagnetic radiation incident on the surface of ZnO film. This indicates that bare ZnO is only responsive in the UV region of the spectra. These two distinct peaks at  $375$  and  $400$  nm are attributed to maximum absorption of photon in ZnO and PS:p-Si structures. Obtained EQE value  $>100\%$  can be ascribed to trap assisted charge carrier multiplication [171]. To explore more in-depth, the  $I$ - $V$  characteristics under irradiating wavelength of  $375$  and  $400$  nm for bias voltage in the range of  $-5$  to  $+5V$  are studied. These results are shown in fig. 5.8(a, b) for PD1 and PD2, whereas fig. 5.8(c) shows these results for bare ZnO. Bare ZnO and PD1 show symmetric rectification enhancement in the forward and reverse bias direction. This is due to the lateral MSM electrode configuration, as this type of arrangement gives scope for double Schottky contact formation between Au metal and n-type ZnO and Al metal and p-type PS:p-Si respectively in the forward and reverse biases, as clarified from the energy level

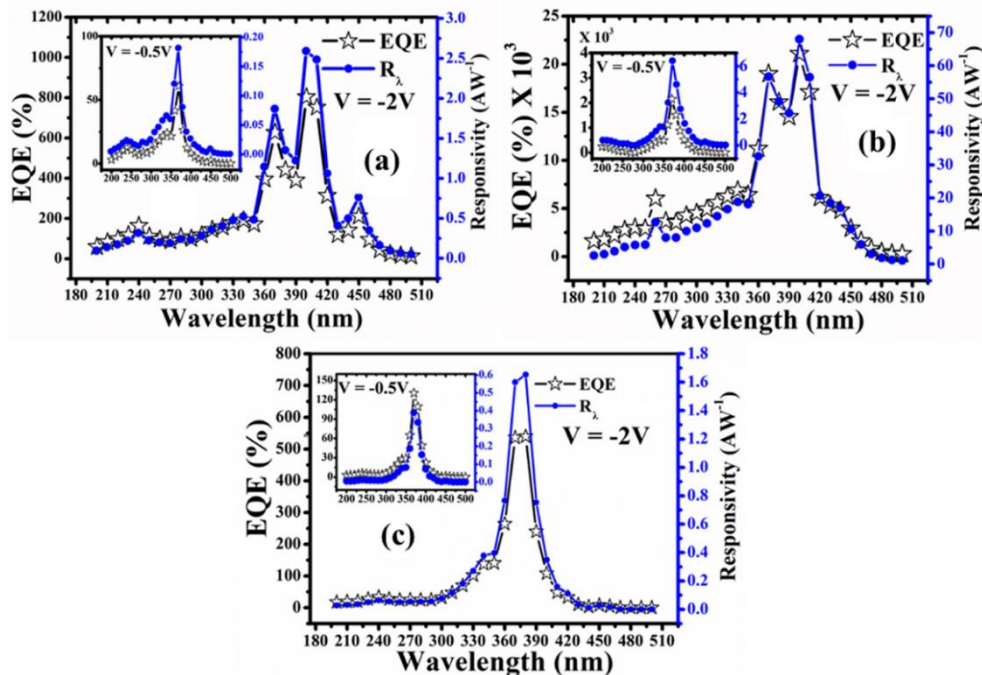


Fig. 5.7 Plot of EQE and  $R_\lambda$  vs.  $\lambda$  for (a) PD1, (b) PD2 and (c) bare ZnO at  $-2V$ , inset shows similar plots at  $-0.5V$

diagram presented in fig. 5.8(d, e). For PD1 and ZnO on illumination of 400 nm (PD1) and 375 nm (PD1 and ZnO) radiation maximum band to band absorption occur. Photo-generated  $e^-h^+$  pairs, confined within the quantum well at the PS: p-Si and PS:ZnO interfaces could tunnel through the barrier and contribute towards  $I_{ph}$ . Additionally, charge carriers are also produced within the space charge regions D1 and D2 along with the trap assisted ones. These  $e^-h^+$  pairs are collected by the coplanar Al+Au electrodes i.e.  $e^-$  are collected by the positively biased electrode and  $h^+$  are collected by the negative one before recombination, thereby decreasing the Schottky barrier height which subsequently increases the gain in EQE of the heterostructures. Thus, due to the band alignment as there is no restriction in the movement of these charge carriers from metal surface to the PS:p-Si heterostructure or ZnO surface and vice versa, results symmetric enhancement with photo to dark current ratio (PDCR) of 13 and 29 under 375 and 400 nm illumination for PD1 and 54 under 375 nm illumination for ZnO at -2V. However, in case of PD2, asymmetric rectification enhancement is observed (fig. 5.8 b) under illumination condition, i.e., there is an increment in  $I_{ph}$  only in reverse region. So, it can be said that PD2 is operational only in the reverse bias condition with PDCR of 10 and 21 for the respective irradiating wavelengths at -2V. The asymmetric nature in PD2 is due to discontinuity within the interfaces of the heterostructure. There is an upward bending of the conduction band in PS and p-Si structure compared to ZnO on application of forward bias. So, photo generated  $e^-h^+$  pairs along with the trap assisted ones induced in ZnO under irradiation of 375 nm and 400 nm light, cannot propagate toward PS and p-Si due to the potential barrier hindrance. This gives rise to charge carrier recombination resulting in no change in  $I_{ph}$  upon illumination. However, on similar condition, upon application of reverse bias, the motion of the induced charge carriers is not hindered due to band bending geometry, increasing the built-in electric field of the active regions (D1 and D2 respectively) and hence, effective separation of photo generated charge carriers take place, which are then collected by the top and bottom contact electrodes resulting in significant increase in  $I_{ph}$ . The change in  $I_{ph}$  is more in PD2 compared to that of PD1 and also that of bare ZnO. Further, the  $I$ - $V$  plots at -1.2 to +1.8V for PD1 and -1.2 to 0V for PD3 [inset of fig. 5.8 (a, b)] suggests that  $I_{ph}$  is more under illumination of 375 nm radiation, confirming dominant contribution of photo-generated carriers from ZnO in low voltage region. To know more about their

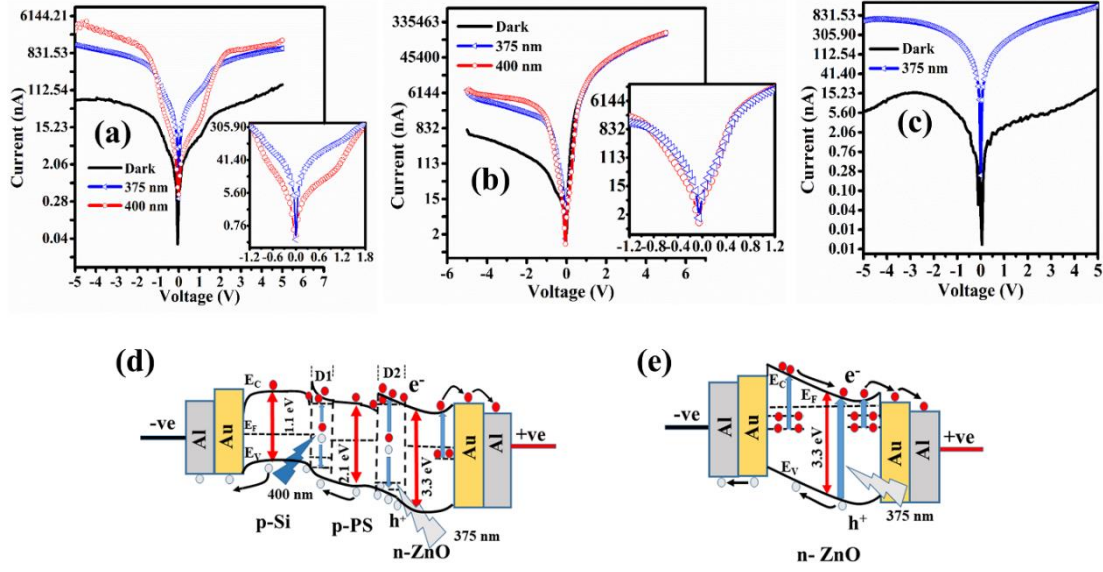


Fig. 5.8 Semi-log  $I$ - $V$  plot under dark and illumination condition for (a) PD1, (b) PD2 and (c) bare ZnO, (d, e) energy band diagram for the respective PDs under reverse bias conditions.

photo conduction carrier dynamics time response kinetics are recorded for bias voltage of -2V which are shown in fig. 5.9(a-c). For PD1 and PD2 the transient kinetics are more stable compared to that of bare ZnO.  $I_{ph}$  growth and decay can be represented as a function of time ( $t$ ) by the following equations.

$$I_{ph} = I_0 + A \exp\left(\frac{t}{\tau}\right) \quad (5.4)$$

$$I_{ph} = I_\alpha + A \exp\left(-\frac{t}{\delta}\right) \quad (5.5)$$

Here  $I_0$ ,  $I_\alpha$  are offset values for growth and decay constant,  $A$  is the amplitude,  $\tau$  and  $\delta$  are the growth and decay time constants respectively.  $\tau$  and  $\delta$  values for PD1 are 2.1 s and 0.7 s for 375 nm and 1.12 s and 0.3 s for 400 nm respectively, whereas for PD2 these values are 2.4 s, and 0.7 s and 1 s. The pattern for bare ZnO can be fitted with biexponential fitting as shown in fig. 5.9(c). The growth and decay of  $I_{ph}$  as functions of time ( $t$ ) can be represented by the following equations.

$$I_{ph} = A_1 \exp\left(\frac{t}{\tau_1}\right) + A_2 \exp\left(\frac{t}{\tau_2}\right) + I_0 \quad (5.6)$$

$$I_{ph} = A_1 \exp\left(-\frac{t}{\delta_1}\right) + A_2 \exp\left(-\frac{t}{\delta_2}\right) + I_\alpha \quad (5.7)$$

Where  $A_1$  and  $A_2$  are the amplitudes. The calculated values of  $\tau_1$ ,  $\tau_2$  and  $\delta_1$ ,  $\delta_2$  are found to be 3.6 s, 0.5 s and 3.6 s respectively. This indicates that growth time under UV (375



nm) illumination is slow, while the decay time is combination of both fast and slow photo relaxation process due to electron trapping and de-trapping in the defect levels. Response times are large compared with commercially available PDs due to native defects present in the material as also confirmed from the PL analysis. However, the prepared PDs exhibit moderately fast response compared to some of the ZnO based reported works [164-166]. This type of slow response indicates optical communication application is still a challenging task for ZnO based UV-visible PDs. For better efficiency towards light detection the intrinsic properties of ZnO have to be optimized by minimizing native defects. The performance parameters of the prepared PDs are compared with some of the best reported ZnO/silicon based PDs in literatures, which are listed in Table 5.1. It is evident from the results that the PDs reported in the present dissertation exhibit fair enough distinct band spectral responsivity in UV-vis spectrum.

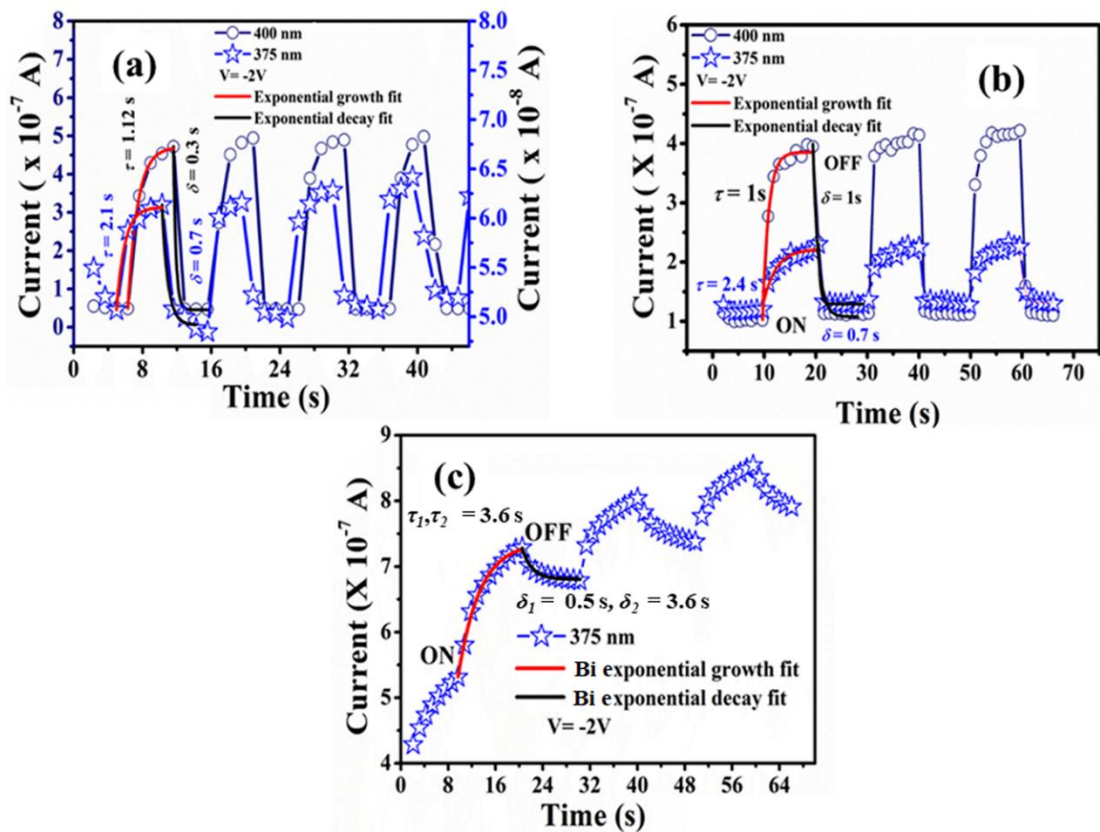


Fig. 5.9 On-off transient kinetics of (a) PD1, (b) PD2 and bare (c) ZnO at -2V bias condition.

**Table 5.1** Comparative performance analysis of PD 1, 2 with some of the best reported ZnO and Si-based PDs in literature.

Device	Measurement condition [wavelength ( $\lambda$ ), intensity ( $I$ )]	Specific detectivity (Jones)	Responsivity ( $\text{AW}^{-1}$ )	Response time (s)		Ref.
				Rise ( $\tau$ )	Decay ( $\delta$ )	
CuI/ZnO	$\lambda = 350 \text{ nm}$ $I = 0.62 \text{ mWcm}^{-2}$	$6.0 \times 10^{10}$	0.0015	15	2.7	[164]
FTO-NiO-ZnO- Ti-Au	$\lambda = 325 \text{ nm}$ $I = 4.1 \text{ mWcm}^{-2}$	$6.3 \times 10^{11}$	0.28	0.28	5.4	[166]
Pt/n-PSi/ZnO NCs/Pt	$\lambda = 380 \text{ nm}$ $I = 1.55 \text{ mWcm}^{-2}$	–	5.99	0.34	0.22	[182]
ZnO-Spiro- MeOTAD	$\lambda = 380 \text{ nm}$ $I = 1.55 \text{ mWcm}^{-2}$	–	0.017	$2.5 \times 10^{-4}$	$9.5 \times 10^{-4}$	[167]
ZnO NWs/CdS	$\lambda = 350 \text{ nm}$	–	12.86	62	45	[165]
ZnO/Cu <sub>2</sub> O nanowire/ electrolyte	$\lambda = 355 \text{ nm}$ $I = 6.0 \text{ mWcm}^{-2}$	–	0.008	0.14	0.36	[168]
p-ZnO/n-Si nanowire heterojunctions	$\lambda = 442 \text{ nm}$ $I = 1.2 \text{ mWcm}^{-2}$	–	1.02	0.01	0.01	[169]
CdS: PS heterostructure	$\lambda = 400 \text{ nm}$ $I = 71 \mu\text{Wcm}^{-2}$	$3.4 \times 10^{13}$	0.60	0.16	0.35	[121]
<b>Al+Au/ZnO-PS: p-Si/Al (PD 1)</b>	$\lambda = 375 \text{ nm}$ $I = 27.2 \mu\text{Wcm}^{-2}$	$9.7 \times 10^{12}$	<b>1.87</b>	<b>2.1</b>	<b>0.7</b>	<b>Present work [184]</b>
	$\lambda = 400 \text{ nm}$ $I = 71 \mu\text{Wcm}^{-2}$	$1.3 \times 10^{13}$	<b>2.6</b>	<b>1.1</b>	<b>0.3</b>	
<b>Al+Au/ZnO-PS: p-Si/Al +Au (PD 2)</b>	$\lambda = 375 \text{ nm}$ $I = 245 \mu\text{Wcm}^{-2}$	$4.9 \times 10^{13}$	<b>55</b>	<b>2.4</b>	<b>0.7</b>	
	$\lambda = 400 \text{ nm}$ $I = 443 \mu\text{Wcm}^{-2}$	$5.8 \times 10^{13}$	<b>68</b>	<b>1</b>	<b>1</b>	

## 5.4 Results and discussion: Part B: Optical and electrical properties of annealed ZnO-PS: p-Si heterostructure

### 5.4.1 Microstructural and optical studies

Morphology of the annealed ZnO-PS:p-Si heterostructure is analysed by FESEM and EDX, these results are shown in fig. 5.10-5.12. Fig. 5.10(a-d) shows FESEM micrographs of the ZnO-PS:p-Si heterostructure annealed at 200, 300, 400 and 500 °C. Mean grain size of uniformly grown ZnO globular nano seed layer over PS:p-Si heterostructure calculated from histogram plot are found to be increasing from 35 to 50 nm, when annealing temperature increased from 200 to 500 °C [fig. 5.10(e-h)]. With rise of annealing temperature after 400 °C, along with regular globular one, some bigger grains appear in the morphology due to agglomeration, which results in low grain boundary density. Inset of fig. 5.10(a-d) shows cross-sectional FESEM images of the ZnO-PS:p-Si heterostructure interfaces for annealed samples at 200-500 °C. The thickness of the uniform PS and ZnO layers are found to be 540 and 160 nm respectively, which does not change much with annealing temperature. To investigate the elemental changes due to annealing, EDX analyses are performed, which are shown in fig. 5.11(a-f) and 5.12(a-h). Fig. 5.11(a) shows the selected area for planar EDX analysis. There is clear evidence of presence of ZnO nanostructure over PS substrate with zinc (Zn), oxygen (O) and silicon (Si) atomicity of 15.43 %, 25.07 % and 59.50 %

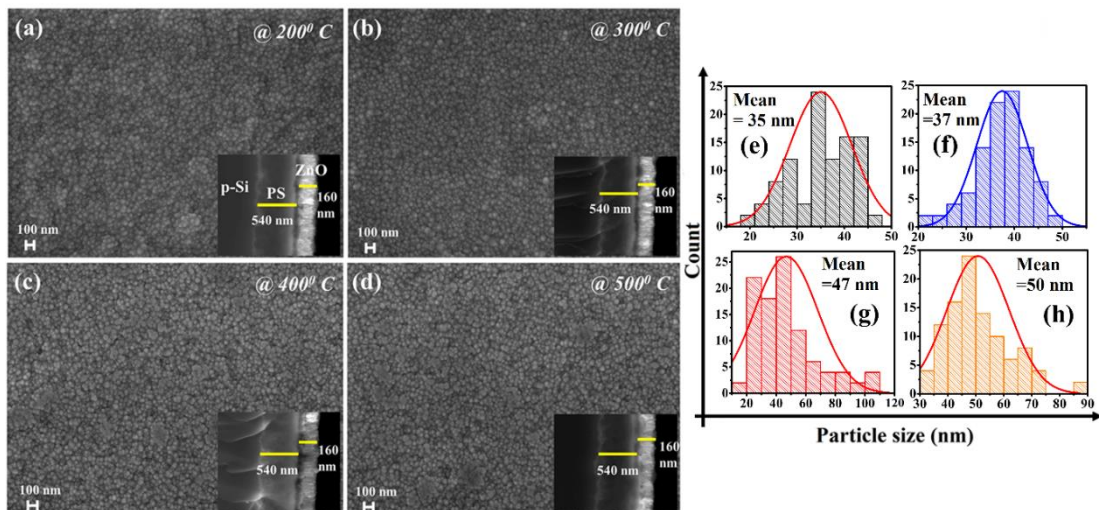


Fig. 5.10 Planar FESEM images of ZnO-PS:p-Si annealed at (a) 200 °C, (b) 300 °C, (c) 400 °C and (d) 500 °C, (Insets show cross sectional FESEM images), (e-h) particle size histograms for annealed samples (i) change of thickness with annealing conditions.

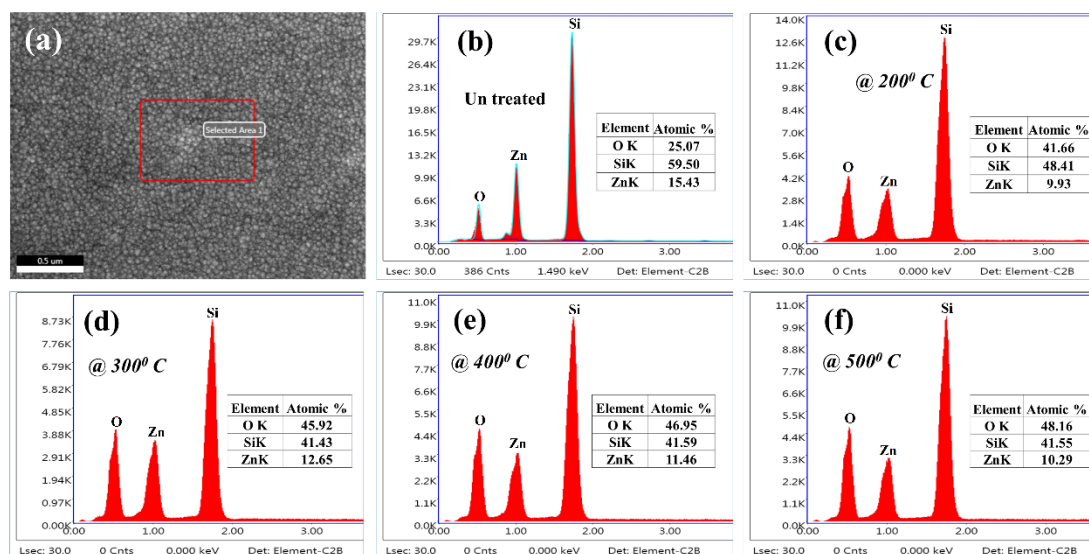


Fig. 5.11 (a) Selected area for EDX analysis of ZnO-PS:p-Si, EDX spectra of ZnO-PS:p-Si (b) untreated, annealed at (c) 200 °C, (d) 300 °C, (e) 400 °C and (f) 500 °C (Insets show elemental contents)

respectively for the untreated sample (fig. 5.11(b)). Whereas, for annealed one in the range of 200-500 °C, there is gradual increase in oxygen content from 25.07 to 48.16 % as confirmed from fig. 5.11(c-f), which may be attributed to the formation of silicon suboxide ( $\text{SiO}_x$ ) interlayer within the heterostructure due to annealing of the sample in presence of air. For confirmation of ZnO nanostructure diffusion into PS layer, cross-sectional EDX analysis is performed for untreated and annealed one at 500 °C, which are shown in fig. 5.12(a-h). The heterostructure is scanned for 3 different regions at selected areas 1, 2 and 3 for p-Si, PS and ZnO respectively as presented in fig. 5.12(a) and (e). Selected area 1 for untreated sample shows 100 % presence of Si by atomicity, whereas, for annealed one, additionally 24.5 % O is present. In the selected area 2, 12.49 % of Zn, 8.64 % of O and 78.88 % of Si are present by atomicity for untreated one, whereas, for the annealed one, O content significantly increases to 54.01 %. These also evidently confirm penetration of n-type ZnO nanostructure into the pores of p-type PS layer of the heterostructure, which may subsequently enhance its electrical conductivity. In selected area 3, along with the presence of Zn and O by atomicity of 28.52 % and 37.97 %, Si (33.50 %) is also present, as this scan area is very nearer to PS interface, it may further endorse diffusion of ZnO into the PS layer. In the EDX spectra of selected area 3, for both untreated and annealed heterostructure, a strong elemental peak related to aluminium (Al) metal to the left of Si peak is seen coming from alloy of the sample holder due to transparency of the thin ZnO layer grown over

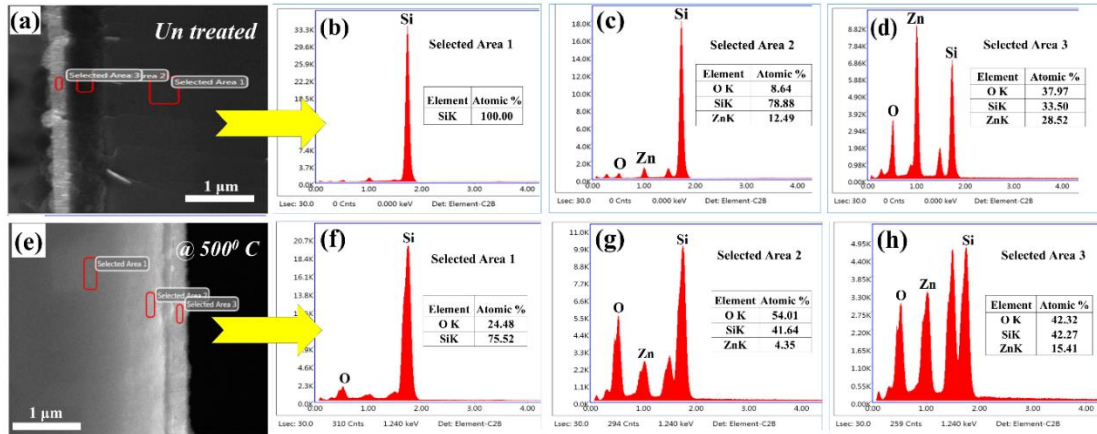


Fig. 5.12 Selected area for EDX analysis of ZnO-PS:p-Si (a) untreated, (e) annealed at 500 °C, EDX spectra for untreated ZnO-PS:p-Si (b) p-Si region (c) PS region (d) ZnO region, annealed ZnO-PS:p-Si at 500 °C (f) p-Si region (g) PS region (h) ZnO region

PS substrate. UV-visible absorbance spectra of bare ZnO nanostructure sputter deposited on quartz glass and annealed in the temperature range of 200-500 °C is presented in fig. 5.13(a). The absorbance band edge onset of ZnO: quartz starts at ~390 nm for all annealing temperature, having peak value in the range of ~353-358 nm with FWHM value of ~21-48 nm. Optical band gaps for nanostructured ZnO annealed at different temperatures are determined from Tauc plots as shown in fig. 5.13(b). From these plots the optical band gap energies of annealed ZnO thin films are found to be decreasing from 3.27 to 3.23 eV for increasing annealing temperature from 200 to 500 °C, which are narrower than that of bulk ZnO. This result is much interesting for material science researchers, as one can observe tuning or modulation of optical band gap energy by annealing treatment. The reduction in the energy band gap of nanostructured ZnO can be ascribed to the modification of electronic structure due to change in density of native defect states upon annealing treatment [195]. The transmittance spectra of the annealed ZnO: quartz thin film is shown in fig. 5.13(c). The films for all the annealing temperatures remain highly transparent in the visible and a part of NIR region (400-800 nm) with transmittance in the range of 65-78 %. The sharp fall of optical transmittance below 400 nm suggests excellent UV light shielding and visible light absorbing capacity of ZnO thin film. Taking advantage of this property, ZnO thin films are incorporated with PS substrates to convert the heterostructure to have application possibility in solar cells, UV-NIR wide range photodetectors etc. Fig. 5.13(d) shows the absolute reflectance spectra in the wavelength range of 350-800 nm for ZnO-PS:p-Si heterostructure annealed at 200-500 °C. Absolute reflectance for the

sample is seen to increase with increase of annealing temperature from 200 to 500 °C. This can be ascribed to lowering of surface roughness of the heterostructure, confirming formation of relatively smooth surface with rise in annealing temperature due to lowering in grain boundary density of deposited ZnO nanostructures on the PS surface. However, there is lowering of absolute reflectance for the annealed ZnO-PS: p-Si heterostructure as compared to that of bare p-Si, which can be attributed to increased surface roughness after sputter deposition of ZnO nanostructure seed layer on PS:p-Si substrate. This result suggests more trapping of incident UV-visible light for implementing the heterostructure in photo sensing applications. Fig. 5.14(a) shows the photoluminescence (PL) spectra for untreated and annealed ZnO-PS:p-Si heterostructure for excitation of 340 nm radiation. The luminescence peak at 376 nm (FWHM ~30 nm), which is related to band edge recombination in ZnO and a broad PS characteristic peak at 600 nm (FWHM ~120 nm) are observed as prominent peaks for the untreated heterostructure. However, upon annealing, the ZnO related PL peak (376 nm) gets significantly quenched due to low recombination of photo induced band edge  $e^-h^+$  pairs in the heterostructure [45]. This peak also get red shifted in the range of 377-

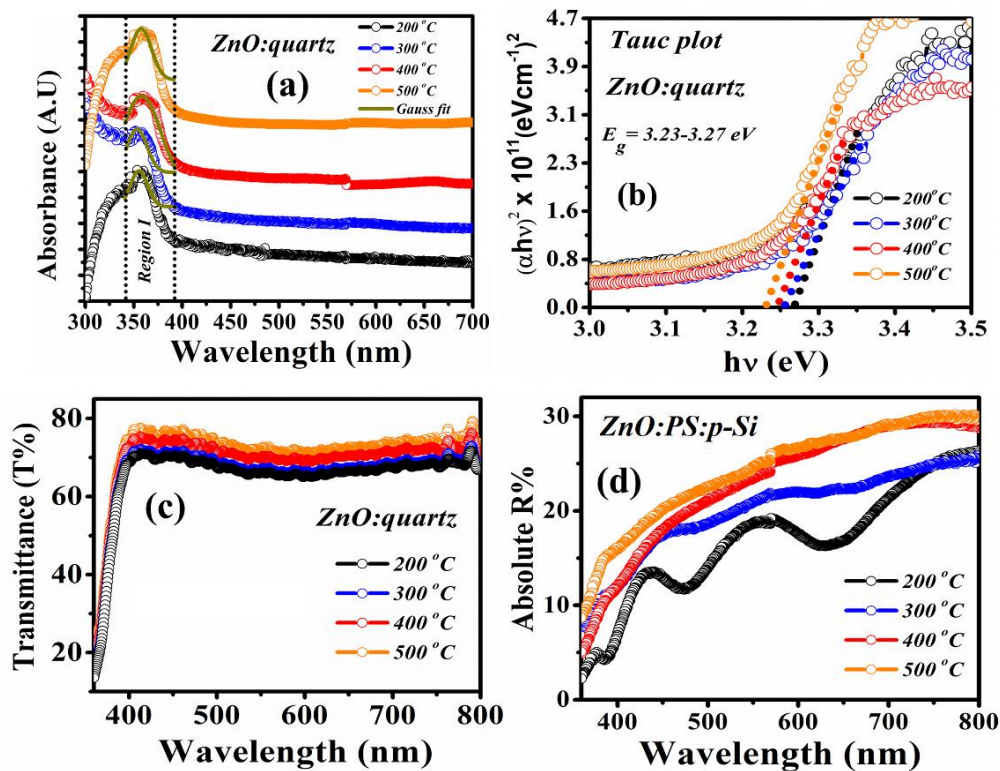


Fig. 5.13 (a) Absorbance spectra, (b) Tauc plot and (c) transmittance spectra for annealed bare ZnO, (d) reflectance spectra for annealed ZnO-PS:p-Si heterostructure

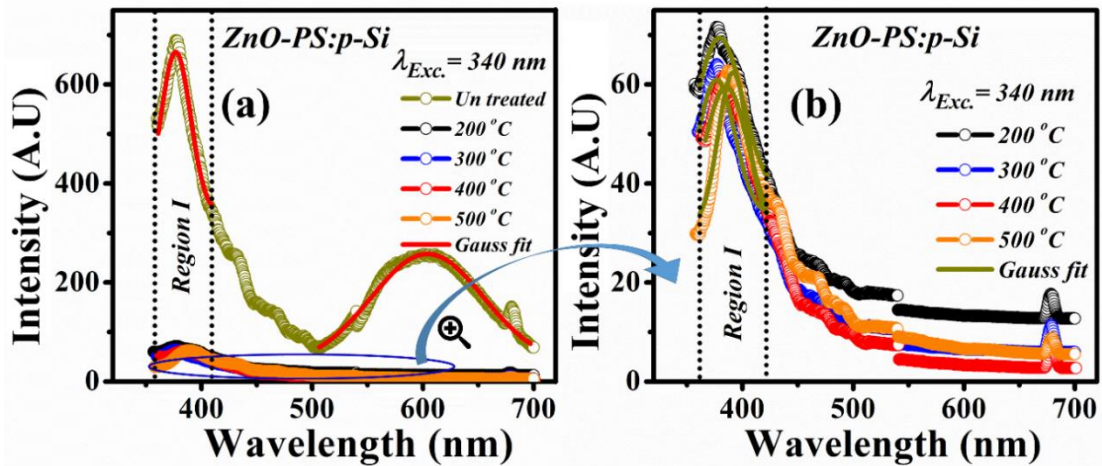


Fig. 5.14 (a) PL spectra for untreated and annealed ZnO-PS:p-Si heterostructure, (b) zoomed view of PL spectra for annealed ZnO-PS:p-Si heterostructure

391 nm, which may be attributed to increased mean grain size of ZnO seed layer with annealing as confirmed from the FESEM analyses. The PS characteristic peak (600 nm) disappears completely for all annealing conditions. Upon annealing, the modification of ZnO seed layer over PS layer totally suppresses the contribution from PS layer. The zoomed view of the PL spectra for annealed heterostructure are shown in fig. 5.14(b).

#### 5.4.2 Electrical and photo sensing studies

To investigate the device performances of ZnO-PS:p-Si heterostructure, its dark currents for different annealing temperatures are analysed as depicted in fig. 5.15(a, b). Fig. 5.15(a) shows the *semi log I-V* plots for the device annealed in the range of 200-500 °C for 1 hour for -5 to 5V biasing. It can be seen that the device annealed at 200 °C shows almost symmetric rectification with minimum current of 3 nA at zero bias. However, the *I-V* curves for the device annealed at 300-500 °C deviate from zero slope regime and shift towards negative quadrant with minimum current values of 0.2 nA at -0.9 V, 0.3 nA at -0.5 V and 2 nA at -1.4 V for annealing temperature of 300, 400 and 500 °C respectively. The gradual growth of SiO<sub>x</sub> layer within the heterostructure with increasing annealing temperature may originate negative built-in potential across the junction, which further result in shift of the device dark *I-V* curve. These can also be attributed to the fact that with rise of annealing temperature, there is Schottky barrier height (SBH) mismatch between the electrodes and the ZnO-PS:p-Si heterostructure for forward and reverse bias conditions. Thus, to confirm change of SBH for different

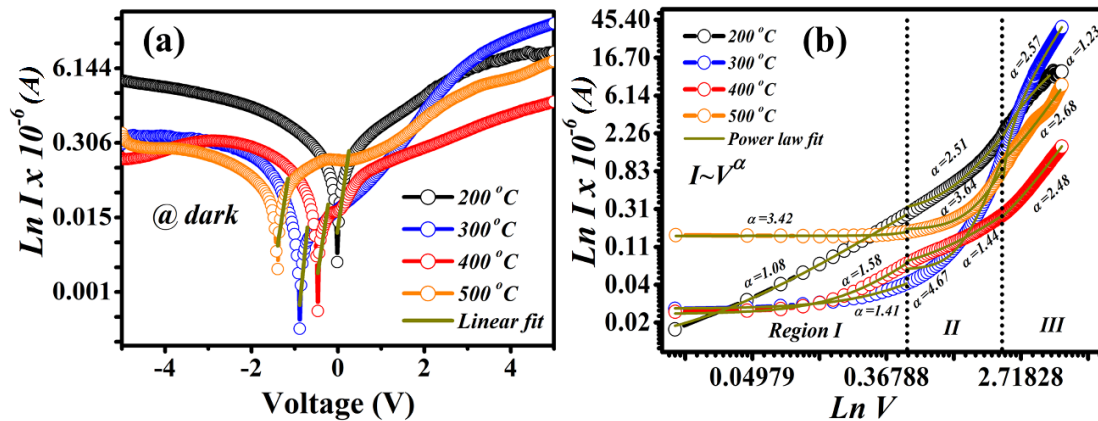


Fig. 5.15 (a) semi log dark  $I$ - $V$  curve and (b)  $\ln I$ - $\ln V$  plot of forward dark current for annealed ZnO-PS:p-Si heterostructure device

annealing temperatures, ideality factor ( $n$ ) and barrier height ( $\Phi_b$ ) are determined using thermionic emission (TE) model in the low voltage region as shown in fig. 5.15(a). The calculated values of the effective barrier heights ( $\Phi_b$ ) are found to vary in the range of 0.52 to 0.84 eV, whereas, the  $n$  values are found to be increasing from 2.22 to 3.45 with rise of annealing temperature from 200 to 500 °C. The device shows deviation from ideal diode characteristics upon annealing at temperature higher than 200 °C. To know about the device conduction phenomenon, the forward  $\ln I$ - $\ln V$  curves under dark condition for different annealing temperatures are plotted as shown in fig. 5.15 (b). The curves are divided into three regimes viz., region I (0-0.5 V), II (0.5-2 V) and III (2-5 V), where curves in each region are fitted with the power law equation given by,  $I \propto V^\alpha$  as shown in the figure. In region I, for low biasing voltage, the scaling parameter  $\alpha$  for annealing conditions 200-400 °C are found to be approximately unity, indicating domination of ohmic conduction mechanism. However,  $\alpha$  value for 500 °C is found to be  $\sim 3.42$ , signifying non-ohmic  $I$ - $V$  characteristics of the device due to degradation. In region II and III,  $\alpha$  values are found to be in the range of 1.44 - 4.67 and 1.23 - 2.68 respectively for the annealing temperatures of 200-500 °C. This further suggests dominance of space charge limited conduction (SCLC) mechanism in these two regimes [196]. Thus, the annealed device shows cross-overs between two charge transport mechanisms viz., ohmic and SCLC mechanisms for different annealing temperatures at the three biasing regimes. To explore about the photo sensing performances of the annealed device, its figure of merit parameter, responsivity ( $R_\lambda$ ) for biasing of -2 and 0 V are determined. The plots of  $R_\lambda$  vs. wavelength ( $\lambda$ ) for the device annealed in the range of 200-500 °C under illumination of 200-600 nm are depicted in



fig. 5.16 (a-d). The device annealed at 200 °C, shows maximum  $R_\lambda$  values of 51 and 0.4  $\text{AW}^{-1}$  for illumination of 375 nm under biasing of -2 and 0 V respectively, which is quite high as compared to that of the untreated one ( $1.87 \text{ AW}^{-1}$  at -2 V). The reduction in defect density upon annealing as confirmed from PL spectra, reduces trapping of photo generated charge carriers, which subsequently make enhancement in responsivity of the device. However, for the device annealed at 300-500 °C, there is gradual decrement in maximum  $R_\lambda$  values in the range of 0.5-6  $\text{AW}^{-1}$  for -2 V and 0.1- 0.4  $\text{AW}^{-1}$  for 0 V biasing. These decrement of the figure of merit parameter of the device can be attributed to the development of negative built-in potential and its continuing increment with increase of annealing temperature. The negative built-in potential causes shift of dark and photo  $I$ - $V$  curves to negative voltage regime, which can be visualised from the semi log dark and photo  $I$ - $V$  plots as shown in fig. 5.17 (a-d) and consequently the device responsivity reduces. The device annealed at 500 °C, is found to be the most deteriorated one with ideality factors of 4.4 and 4.3 and Schottky barrier heights of 0.5 and 0.4 eV under illumination of 375 and 400 nm respectively as calculated using the TE model. Another figure of merit parameter, photo to dark current ratio (PDCR) of the device annealed at 200-500 °C for illumination of 375 and 400 nm are plotted against reverse bias condition (-5 to 0 V) as shown in fig. 5.16 (e, f). One can observe that for the device annealed in the range of 200-500 °C, PDCR values show sharp peaks for low reverse bias below -1.5 V. The peak PDCR values are found to be 21 at 0 V, 808 at -0.9 V, 225 at -0.5 V and 22 at -1.4 V for different annealing

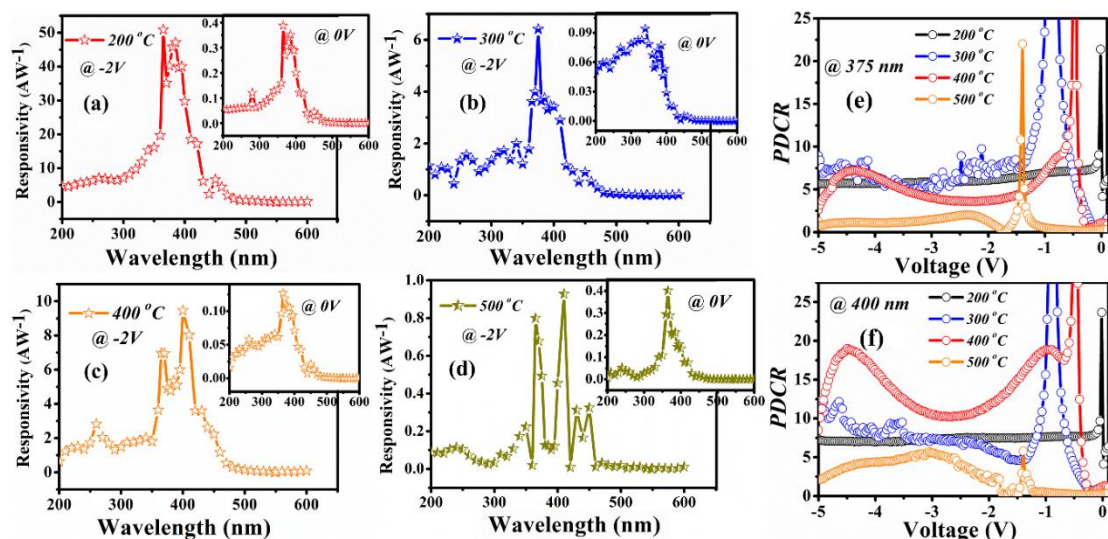


Fig. 5.16 (a-d) Responsivity plot at -2 V (Insets show plots at 0 V), PDCR plot under illumination of (e) 375 nm and (f) 400 nm for annealed ZnO-PS:p-Si heterostructure device.

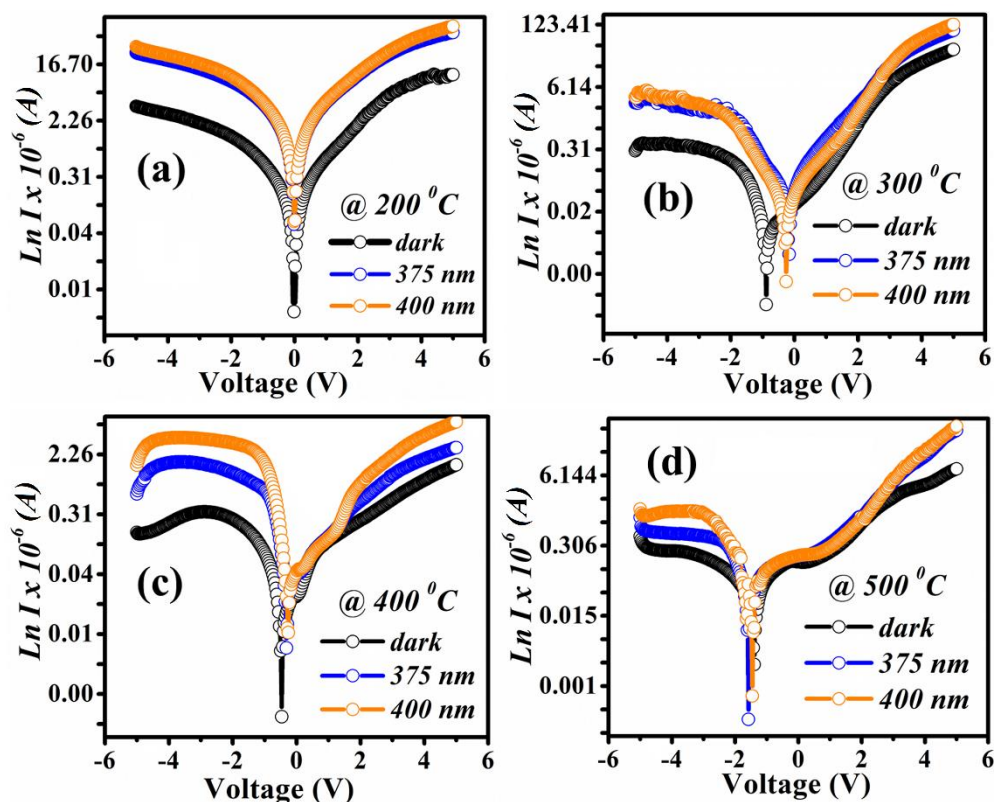


Fig. 5.17 Semi- log dark and photo  $I$ - $V$  plots for ZnO-PS:p-Si heterostructure device annealed at (a) 200 °C, (b) 300 °C, (c) 400 °C and (d) 500 °C

temperatures of 200, 300, 400 and 500 °C respectively. These peak positions exactly coincide with the negative potential values with minimum dark currents as determined earlier. However, the device annealed at 500 °C, under illumination of 375 and 400 nm exhibit lowest PDCR values in comparison to the other annealing conditions due to device degradation. Time response kinetics of the annealed device under illumination of 375 and 400 nm radiation at biasing of -2 V and 0 V for the on/off time interval of 10 s are analysed as shown in fig. 5.18(a-h). The device annealed at 200-400 °C under -2 V bias, shows good switching behaviour with on/off ratio in the range of 1.10 - 7.89. The response and recovery times are found to be in the range of 0.6 to 2.2 s and 0.6 to 1.5 s respectively. Response times for the device annealed at 200 °C under illumination of 375 and 400 nm are found to be relatively fast (0.6, 0.8 s) as compared to that of the untreated one (2.1, 1.1 s). This may be attributed to the fast photo generation process and declined rate of charge carrier trapping at defect states upon annealing treatment [197]. However, the device annealed at 500 °C for -2 V bias, shows some spikes at the edges of on and off illumination cycles with on/off ratio of 2.0 and 2.1. These spikes are also seen for the device at zero bias for all annealing conditions, where one can

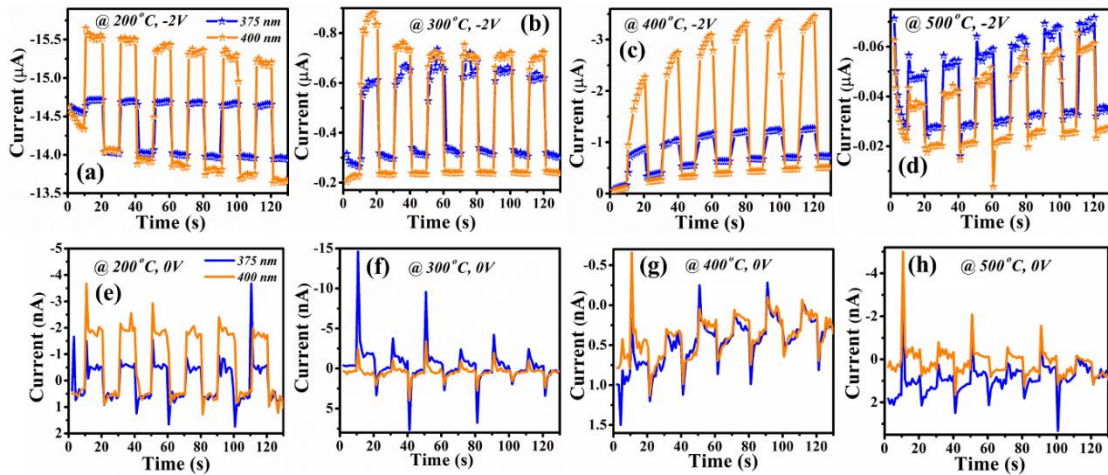


Fig. 5.18 Time response kinetics for ZnO-PS:p-Si heterostructure device annealed at 200 °C, 300 °C, 400 °C and 500 °C for biasing of (a-d) -2V and (e-h) 0V

notice very negligible on/off ratio. These spikes are originated from pyroelectric potential due to light induced instantaneous change of temperature. It can be inferred that pyroelectric effect is more dominating over photo sensing performance of the device for low bias conditions. Hence, one can observe deterioration of the device photo sensing ability with increase of annealing temperature to 500 °C. However, when annealed at 600 °C, the Al electrodes get diffused into the PS layer due to its low melting point, breaking the device continuity to hinder the test further.

## 5.5 Conclusion

Distinct band UV to visible MSM photodetector from ZnO-PS:p-Si heterostructure has been successfully developed. Light sensing property of these PDs have been tested by spectral response in the range of 200-500 nm, these give distinct  $R_\lambda$  and EQE values at 375 and 400 nm respectively. Cross sectional FESEM confirms uniform interface between ZnO and PS:p-Si structure. Planar FESEM analyses indicate increase of mean grain size of ZnO nanoparticles, when the heterostructure is annealed at 400 and 500 °C. EDX analyses confirm diffusion of ZnO nanostructures into pores of PS layer and oxygen content in the heterostructure rises with annealing. Optical band gap energy of nanostructured ZnO changes from 3.30 to 3.23 eV upon annealing, due to change in the density of defect states. The film remains highly transparent (65-78 %) in vis-NIR region even after annealing treatment. PL spectra reveals various traps and defect assisted luminescence bands along with characteristic band to band emission peaks of ZnO and PS:p-Si structures. ZnO band edge luminescence peak significantly quenches

and PS characteristic peak disappears completely upon annealing. PD1 and PD2 show distinct band UV-visible photo response with slow UV response and fast visible response time. Bare ZnO on the other hand is sensitive to UV range only and has slower response. Slower response in UV region for the PDs is due to oxygen related vacancies present in ZnO. PD1 when annealed at 200 °C, exhibits rise in responsivity value up to 30 AW<sup>-1</sup> as compared to that of untreated one (2.6 AW<sup>-1</sup>) for illumination of 400 nm. However, upon further annealing in the range of 300-500 °C, due to development of negative built-in potential device responsivity decreases. Response times for the device annealed at 200 °C are found to be relatively faster as compared to that of the untreated one. For the annealed device at lower bias, pyroelectric effect is more dominating over its photo sensing performance.

# Chapter 6

## **Optical and electrical properties of aged and annealed PS: p-Si structure**

[S. Sarmah, M. Das and D. Sarkar, Mater. Lett. **297**, 129972  
(2021)]



## Optical and electrical properties of aged and annealed PS: p-Si structure

### 6.1 Introduction

To overcome the limitation of low response for UV light of Si based PDs, many researchers have devised PDs based on porous silicon (PS) structures [198, 42]. PS has optical luminescence in visible region and electronic band gap of  $\sim 2.1$  eV as reported by Chen et al. [18]. Nayef et al. [20] recently reported PS based PDs which has photo sensing ability in the UV-visible range of  $\sim 200$ - $900$  nm, but with very low responsivity of  $\sim 0.045$   $\text{AW}^{-1}$ . However, some researchers revealed that defect levels present on silicon suboxide ( $\text{SiO}_x$ ,  $x \leq 2$ ) enriched silicon or porous silicon based devices such as light emitting diodes, solar cells and PDs [199-201] strongly affect their optical properties, band structure and electrical performances to subsequently enhance spectral responsivities [202-206]. In this context, some researchers developed natively grown  $\text{SiO}_x$  based high responsive Si PDs [207,208]. In a recent study, Ling et al. [209] reported native  $\text{SiO}_2$  based UV-NIR range SnSe:  $\text{SiO}_2$ : Si PDs with responsivity of  $\sim 0.25$   $\text{AW}^{-1}$  at  $\sim 500$  nm with response time of  $\sim 29$   $\mu\text{s}$ . Saglam et al. [210] reported the effects of native  $\text{SiO}_2$  layer on dark currents of p-Si based heterostructure, though photo sensing of the device was not studied. However, the  $\text{SiO}_x$  layer grown on PS due to long period auto-ageing, inevitably quenches its spectral responsivities. Many researchers reported that post thermal annealing treatment on MSM based PDs can

significantly improve crystallinity of microstructures and reduce their defect states, which subsequently enforce positive effect on their photo sensing performances. To name a few, Lee et al. [211] reported Al/PS/Si/Al visible-IR PDs, whose characteristics are improved by rapid thermal oxidation and annealing at 850 °C for 90 s and 15 s in O<sub>2</sub> and N<sub>2</sub> atmosphere respectively. Liu et al. [212] reported enhanced photoelectric property of amorphous GaN/p-Si heterojunction using thermal annealing in NH<sub>3</sub> atmosphere. Chang et al. [213] reported Ir/Pt: GaN Schottky diode with low leakage current and high Schottky barrier heights (SBHs) by thermal annealing, which is more suitable for optoelectronic applications over untreated one. One can conclude from literature that detailed study of conduction mechanisms and reasons behind enhancement of photo sensing performances of aged Si or PS based devices upon thermal annealing are scarce. In this chapter, it is thus thought worthwhile to investigate the effects of native grown silicon suboxide over PS due to ageing on its photo sensing property. Moreover, post annealing treatment has also been followed to improve the photo sensing performances of the aged PS based Schottky PD. The dependence of microstructural and optical properties of PS on its ageing time and annealing treatment are also studied for possible correlation among these properties with photo sensing.

## **6.2 Experimental details**

### **6.2.1 Preparation of Al/PS: p-Si MSM structure and its annealing**

Details of PS:p-Si structure preparation by electrochemical anodization is already mentioned in Chapter 2 under subsection 2.2.1. Planar configured Al/PS: p-Si MSM structure is fabricated by depositing Al on top of freshly synthesized PS: p-Si substrate using a Hind high vacuum coating unit. Highly pure (99.99 %) aluminium (Al) is deposited with the help of a 6 mm × 6 mm interdigitated shadow mask by thermal evaporation method at chamber pressure of 10<sup>-5</sup> mbar. The thickness of the electrode is maintained at 30 nm using the digital thickness monitor attached to the coating unit. However, PS surface as well as the Al metal electrode upon ageing readily form silicon and aluminium surface oxides respectively. In this study, only effects of silicon oxide layer on photo sensing performances of PS: p-Si structure have been taken into consideration, as effect of aluminium oxide is insignificant due to low effective surface area of the Al electrode. Also, the aged Schottky device has been annealed at four



different temperatures: 200, 300, 400 and 500 °C for 1 hour. The details of the annealing process have been already discussed in Chapter 2 under subsection 2.2.5.

### 6.3 Results and discussion: Part A: Optical and electrical properties of aged PS: p-Si structure

#### 6.3.1 Microstructural and optical studies

Morphology of the prepared PS: p-Si structure is analysed using FESEM and EDX techniques, which are shown in fig. 6.1-6.3. Planar FESEM micrographs of the as-prepared PS: p-Si structure and the ones aged for 18, 36 and 60 days respectively are shown in fig. 6.1(a-d). Mean pore sizes of the uniformly distributed mesopores on the silicon surface calculated from pore size histograms are found to be in the range of 28-30 nm [fig. 6.1(e-h)]. Inset of fig. 6.1(a-d) show cross-sectional view FESEM images of the as-prepared and aged PS: p-Si structure. The porous layer displays uniform interface with p-Si with constant thickness of 540 nm, with almost no change with ageing, suggesting ageing not to have adverse effect on pore size and thickness of the PS layer. However, EDX spectra confirm formation of oxide layer as shown in fig. 6.2 and 6.3. Fig. 6.2(b-c) shows EDX spectra for cross-section of the as-prepared PS: p-Si

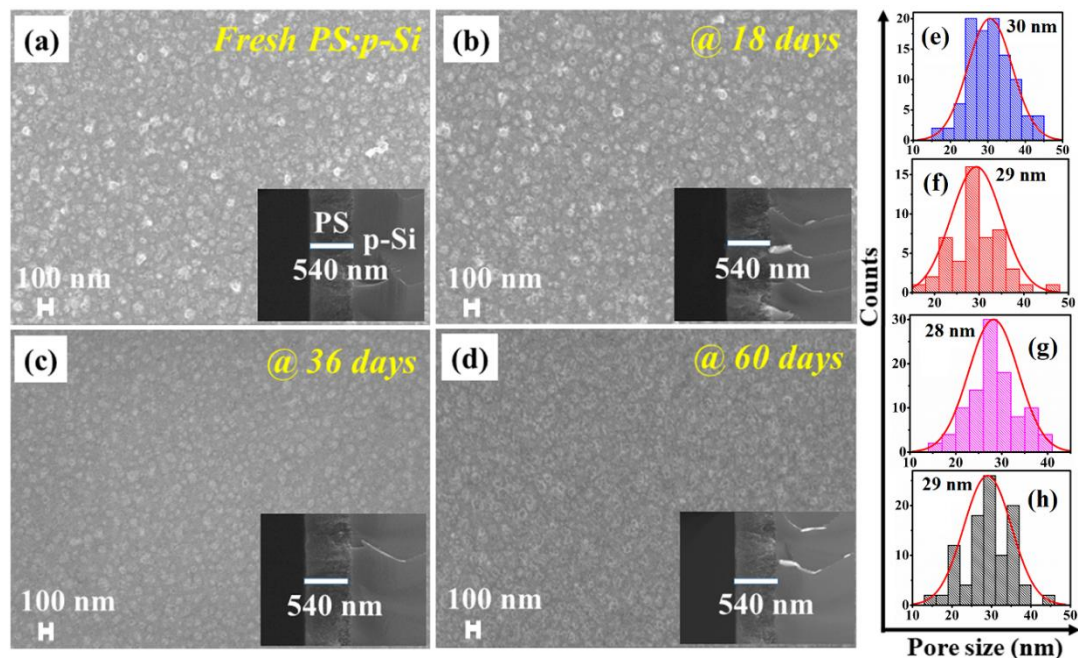


Fig. 6.1 Planar FESEM micrographs of PS:p-Si (a) as-prepared, aged for (b) 18 days, (c) 36 days and (d) 60 days, [insets show cross-sectional FESEM micrographs], (e-h) pore size histograms.

structure. Area 1 and 2 represented in fig. 6.2(a) are the selected scan regions of PS and p-Si layers respectively. EDX of area 1 shows 95.57 % of Si and 4.43 % of O by atomicity, but area 2 shows 100 % of Si [fig. 6.2(b, c)]. These confirm the possibility of SiO<sub>x</sub> layer formation on top of PS: p-Si surface. This can be further ascertained from fig. 6.2(d), where the bare p-Si wafer shows 100% of Si. Thus, one can conclude that PS layer on p-Si substrate is more vulnerable to get attacked by atmospheric oxygen compared to that of bare p-Si. Fig. 6.3(a) shows selected area for planar EDX analyses of the as-prepared and aged PS surface. As-prepared PS sample [fig. 6.3(b)] shows 93.89 % of Si and 6.11 % of O by atomicity. Fig. 6.3(c-e) shows the EDX spectra of the structure with ageing durations for 18, 36 and 60 days respectively. These show increase in elemental content of O from atomicity value of 13.97 % to 37.21 % with increase of ageing time. Fig. 6.3(f) shows the dependence of oxygen content on increase of ageing, which shows near saturation of the oxygen content for ageing to 60 days. It can be inferred that though ageing does not change the physical nature of the structure, as evident from the FESEM micrographs, some elemental changes occur as are evident from the EDX analyses due to formation of silicon suboxide layers in the PS: p-Si

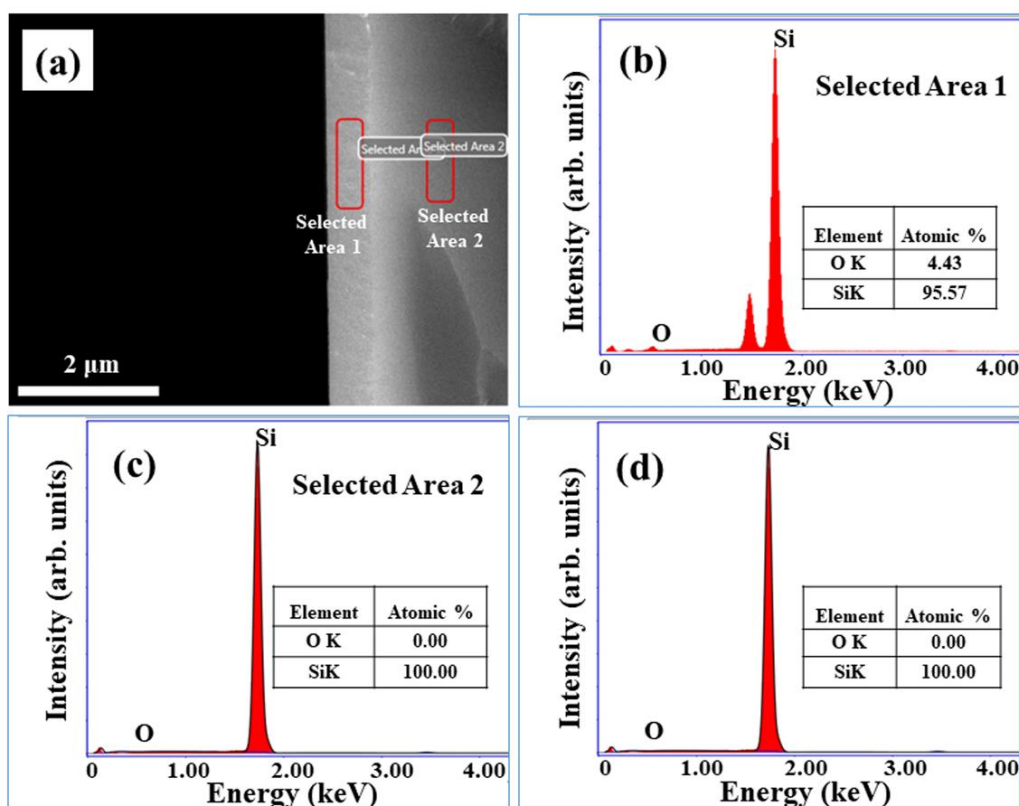


Fig. 6.2 (a) Cross- sectional selected areas for EDX analysis, EDX spectra of (b) PS region (area 1), (c) p-Si region (area 2) and (d) RCA treated bare p-Si surface.

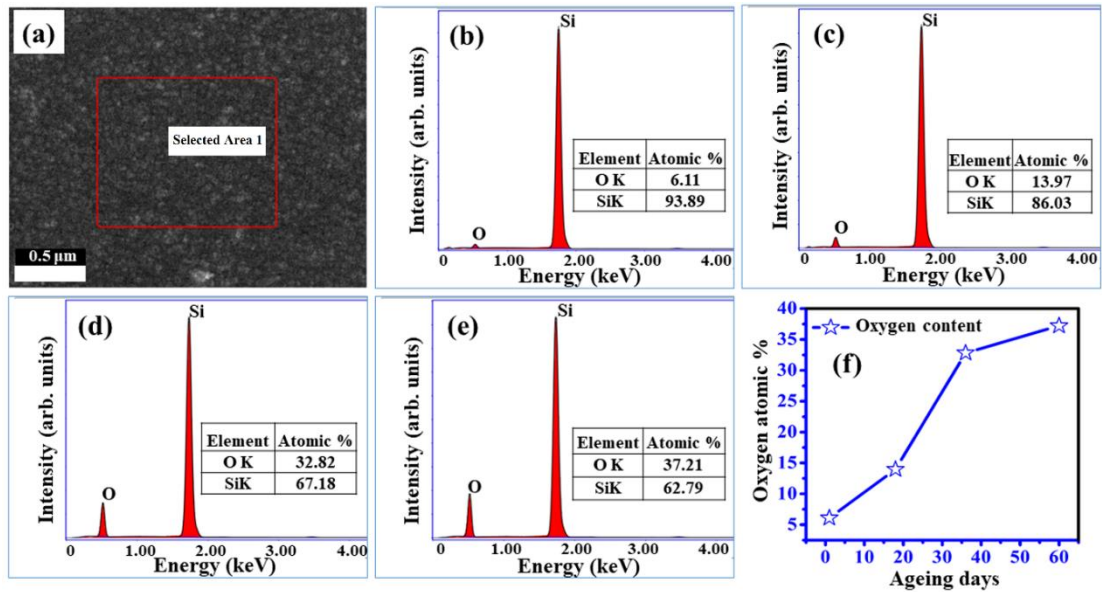


Fig. 6.3 (a) Planar selected area for EDX analysis, EDX spectra of PS:p-Si (b) as-prepared, (c) aged for 18 days, (d) 36 days, (e) 60 days and (f) plot of atomic percentage of O with ageing.

structure [210]. Further microstructural analyses are carried out through XRD study of the as-prepared and aged PS: p-Si structure along with the bare p-Si, the results of which are shown in fig. 6.4(a). For crystalline p-Si, the peaks at  $2\theta = 33^\circ$  and  $2\theta = 69.1^\circ$  correspond to (200) and (400) reflection plane of c-Si respectively as clearly visible in the zoomed view shown in the inset of fig. 6.4(a) [214]. As-prepared and aged PS: p-Si structure show similar peaks at the same  $2\theta$  position as that of the crystalline p-Si. On fitting the strong (400) reflection peaks using Lorentz curve as shown in fig. 6.4(a), give full width half maxima (FWHM) value of  $0.23^\circ$ . The crystallite size of the structure calculated using Scherrer eqn. [215] are found to be 45 nm. Due to PS formation, the p-Si (400) reflection peak (FWHM  $\sim 0.22^\circ$ ) gets slightly broadened (by  $0.01^\circ$ ), which can be attributed to nanocrystalline size effect [216]. PS being a surface modified thin layer on single crystalline p-Si, gives diffraction peaks as sharp as bare p-Si [217]. Also, formation of homogeneous layer of  $\text{SiO}_x$  on PS might have led to these sharp peaks [218]. To investigate more about the microstructural details, Raman spectra of PS: p-Si structure along with bare crystalline p-Si are studied. The spectra recorded using the laser excitation line of 633 nm are shown in fig. 6.4(b). The allowed LO phonon mode of c-Si at  $522 \text{ cm}^{-1}$  is observed for p-Si (FWHM of  $3.8 \text{ cm}^{-1}$ ), which is symmetric in nature. As-prepared and aged PS: p-Si structure show more broad and asymmetric spectra peaked at  $519 \text{ cm}^{-1}$  along with the peak related to c-Si ( $522 \text{ cm}^{-1}$ ) with an effective FWHM value of  $9 \text{ cm}^{-1}$ . This broadening and asymmetric nature of the spectra

is ascribed to phonon confinement effect [219] due to nanocrystalline nature of the PS layer. Since as-prepared and aged PS: p-Si sample exhibit same Raman spectra, only 60 days aged PS: p-Si sample is compared with as-prepared one. Here, the increased Raman intensity ( $\sim 4$  times) in the as-prepared and aged PS: p-Si sample compared to that of bare p-Si can be attributed to trapping and successive scattering of incident light within the pores of PS: p-Si structure [220]. Optical properties of the prepared structure are studied with the help of PL spectra, which are shown in fig. 6.4(c,d). Fig. 6.4(c) shows PL spectra of the as-prepared PS: p-Si structure for four different excitation wavelengths ( $\lambda_{Exc.}$ ) of 275, 300, 350 and 400 nm. These give broad emission bands in the region of 500-700 nm. On analysing these emission spectra by Gaussian fitting, characteristic PS: p-Si strong emission peak at 590 nm is estimated [128], which show gradual broadening (FWHM value 92.6-99.4 nm) and decrease in emission intensity with increasing  $\lambda_{Exc.}$ . This can be attributed to the deviation of  $\lambda_{Exc.}$  value from maximum one at 275 nm as presented in photoluminescence excitation (PLE) spectra for fixed

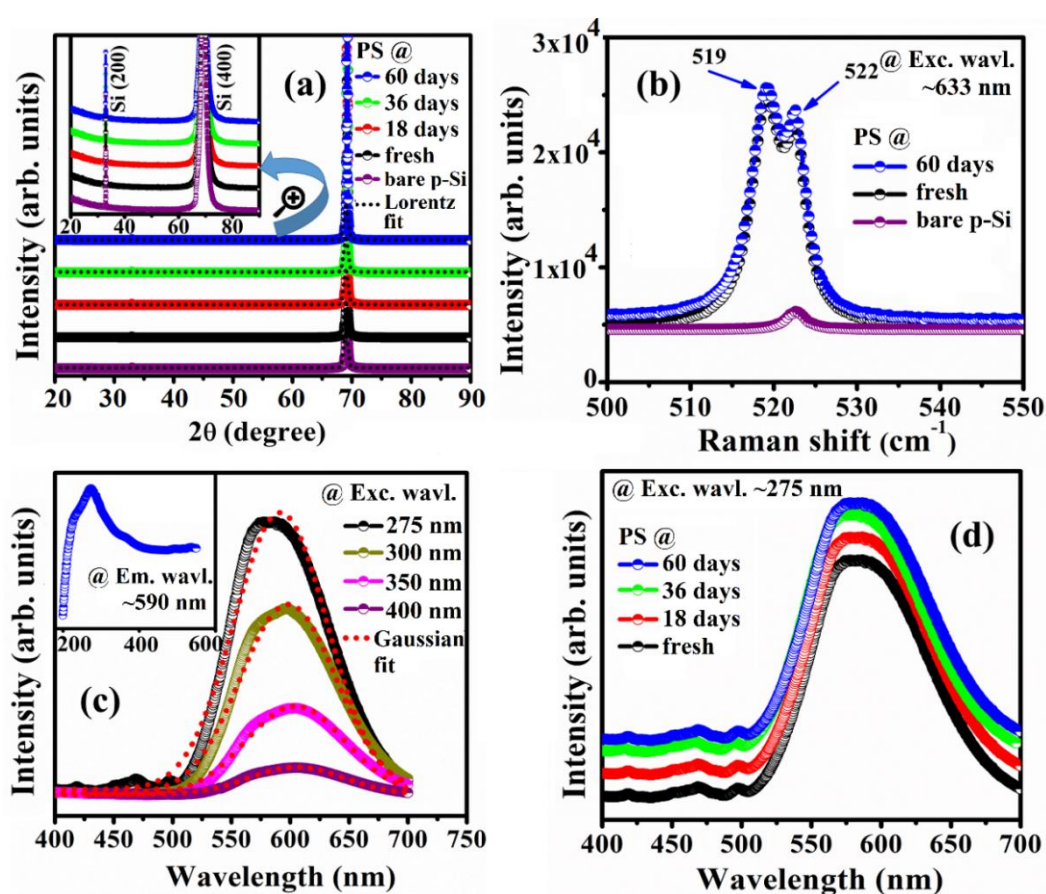


Fig. 6.4 (a) XRD patterns [inset shows enlarged view] and (b) Raman spectra of p-Si, as-prepared and aged PS:p-Si heterostructure, PL spectra of (c) as-prepared PS:p-Si for different  $\lambda_{Exc.}$  and (d) as-prepared and aged PS:p-Si for  $\lambda_{Exc.}$  of 275 nm [inset of (c) shows PLE spectra of as-prepared PS:p-Si].

$\lambda_{Em}$  at 590 nm, shown in the inset of the figure. The characteristic PS emission peak at 590 nm shows slight red-shift of 15 nm with increasing  $\lambda_{Exc}$ . This follows that emission wavelength is almost independent of excitation wavelengths and obeys Kasha's rule [221]. PL spectra of the as-prepared and aged PS: p-Si structure for a fixed excitation wavelength of 275 nm is shown in fig. 6.4(d), which exhibits strong visible light emission band peaked in the range of 590-592 nm with FWHM value of 92.6-93 nm. This characteristic emission peak at 590 nm is assigned to band to band transition of electrons confined in the PS: p-Si structure [128]. PL spectra does not show appreciable change with ageing. Here, no significant quenching and red shift of the characteristic PL peak is observed due to constancy of Si crystallite sizes with oxidation, as confirmed from the XRD analyses also. The weak emission bands peaked at 470 and 500 nm observed for as-prepared and aged sample can be attributed to electronic transitions from defect levels present in SiO<sub>x</sub> layer developed on PS: p-Si surface [222], which further confirms the growth of silicon suboxide layers assigned from elemental study of the EDX analyses. One can anticipate from the PL analyses that ageing time can have stranded effect on the UV-visible photo sensing property of the structure. Microstructural and optical analyses data beyond ageing time of 60 days are excluded in the present work, as the structure shows degradation in photo sensing performances beyond 60 days.

### **6.3.2 Electrical and photo response studies**

The current-voltage (*I-V*) characteristic for a bias voltage range of -5 to +5V in dark are recorded for as-prepared as well as aged Al/PS: p-Si devices and the plots are shown in fig. 6.5(a). Inset shows the zoomed view of the dark *I-V* curves under reverse bias condition. The *I-V* plots are non-linear in nature and with ageing the  $I_d$  value of the device increases for higher voltage region ( $> \pm 1V$ ). This fact can be attributed to collection of more charge carriers at the electrodes contributed from silicon suboxide layers developed on PS: p-Si surface with ageing [223,224]. The non-linear *semi log I-V* curve can be divided into two regions as shown in fig. 6.5(b). The region I is the low voltage regime (0-0.4 V), where the curve is linear and region II, the high voltage one (0.4-5.0 V) is the non-linear regime. The region I of *semi log I-V* plot is analysed by thermionic emission model [225] to calculate the ideality factor (*n*) and barrier height ( $\phi_b$ ) of the device. Ideality factors and barrier heights are found to vary in the range of

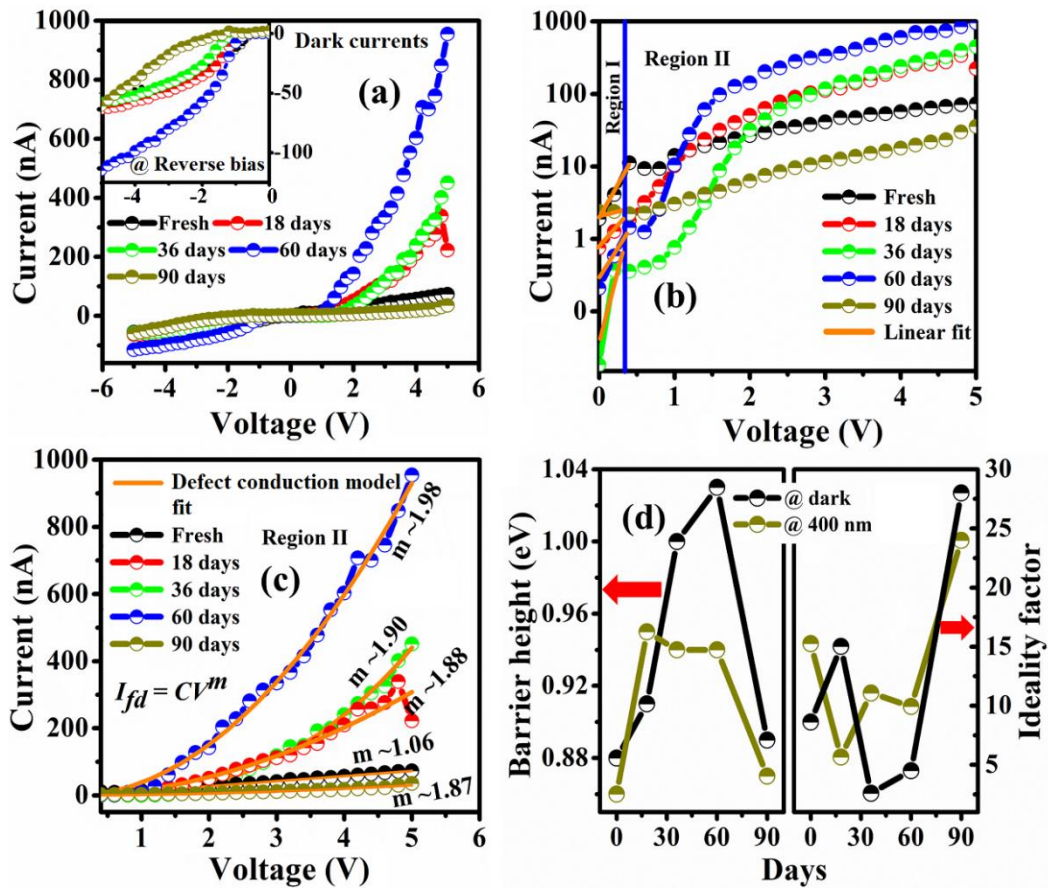


Fig. 6.5 (a) Linear dark  $I$ - $V$  plot, [inset shows plot at reverse bias], (b) forward biased semi-log dark  $I$ - $V$  plot (c) defect conduction model fitted forward  $I$ - $V$  plot and (d) plot of variation of  $\phi_b$  and  $n$  with device ageing under dark and illumination condition.

2.6 to 15.0 and 0.88 to 1.03 eV respectively with ageing. The plots of  $n$  and  $\phi_b$  vs. ageing days are shown in fig. 6.5(d). With ageing upto 60 days, both these parameters show trend of saturation. However, after 90 days, dark current decreases with  $n$  and  $\phi_b$  values of 28 and 0.89 eV respectively, suggesting possible device degradation. Inherently grown dangling bonds on the PS with ageing provide surface states, defect or trap centres etc. causing unstable device dark current. Further, the higher values of  $n$  and  $\phi_b$  compared to the ideal Si based MSM diodes, can be attributed to unavoidably formed thin native oxide layer on PS: p-Si surface and interfacial defect states causing more recombination of  $e^-$ - $h^+$  pairs in the device [226]. Some earlier works [227,228] also reported Si based diodes with higher ( $\gg 1$ )  $n$  values. The presence of defect states in native oxide layer and interfaces of the as-prepared and aged structure can be further investigated by defect conduction model analyses carried out in region II (0.4-5V) of the forward  $I$ - $V$  plot using the power law equation  $I_{fd} = CV^m$ . In this equation,  $I_{fd}$  is

forward dark current,  $C$  is a constant,  $V$  is the applied voltage and  $m$  is the scaling parameter for defect dominated conduction.  $I_{fd}$  vs.  $V$  plots for as-prepared and aged device are shown in fig. 6.5(c). The scaling parameter ( $m$ ), obtained from these plots is seen to increase from 1.06 to 1.98 with ageing, which possibly endorses the fact that with increase in native oxide formation within the PS layer, the current conduction in the structure is dominantly controlled by defects [131]. To explore more about the defect dominated conduction, photo currents of the as-prepared and aged samples are analysed by plotting the photo  $I$ - $V$  characteristics for irradiation wavelength in the range of 250-450 nm along with dark current for bias voltage of -5 to +5 V. These plots under irradiation of 250 and 400 nm are shown in fig. 6.6(a-e). Interdigitated planar configuration of the electrodes [fig. 6.7(a)] allow maximum photons to be incident on the PS: p-Si structure. The as-prepared and aged device show almost symmetric enhancement of rectification for +ve and -ve bias with maximum photo-to-dark current ratio  $[(I_{ph} - I_d)/I_d]$  of 2.2-7.0 for 400 nm illumination at  $\pm 3V$  bias. However, with ageing beyond 90 days, the device shows asymmetry with very low PDCR of 1 and 1.8 under the same illumination and biasing conditions due to degradation [fig. 6.6(e)]. Symmetric rectification enhancement can be attributed to planar MSM device

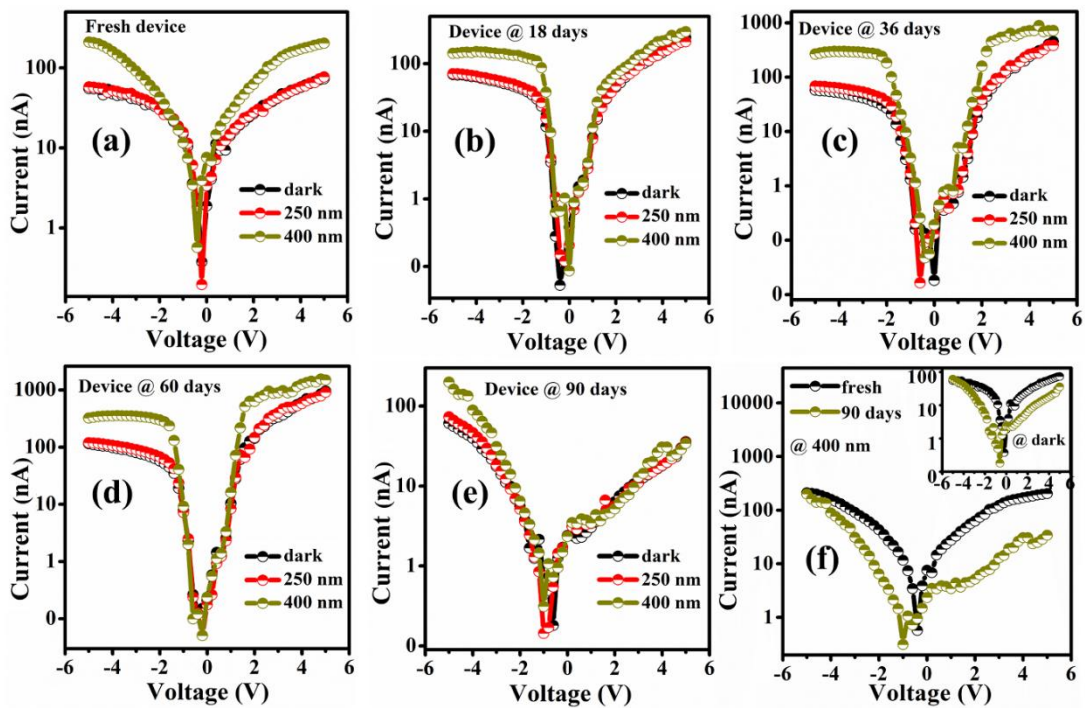


Fig. 6.6 *Semi-log I-V* plot under dark and illumination condition for (a) as-prepared and (b-e) aged device and (f) comparative plots of *semi-log photo I-V* for fresh and 90 days aged device [inset shows plot under dark condition].

configuration, where the two Al metal electrodes make almost identical Schottky barriers ( $\phi_b$ ) with PS: p-Si structure [229] and for forward and reverse bias the photo generated  $e^-h^+$  pairs suffer similar restriction in movement from metal to PS: p-Si and vice versa. The band schemes for such contacts are displayed in fig. 6.7(b, c). These diagrams give the idea about photo conduction mechanism for the as-prepared and aged device under biased condition, taking electronic band gap ( $E_g$ ) of 2.1 eV for PS: p-Si structure [18]. In case of the as-prepared device, as it is illuminated under biased condition, the absorbed photons create additional  $e^-h^+$  pairs within the PS: p-Si depletion region and subsequently get separated and collected by the two Al electrodes depending upon the polarity of the electrodes. There is also accumulation of charge carriers at the trap states of two Schottky barriers ( $D_1, D_2$ ) as shown in the figure. The process further reduces the barrier heights for higher bias conditions [230,231] and facilitate significant increase in photo current ( $I_{ph}$ ) of the device. This reduction of Schottky barrier heights (SBHs) for the as-prepared and the aged device under illumination condition compared to that of the dark one (0.88- 1.03 eV) are found to be in the range of 0.86- 0.94 eV calculated using thermionic emission model for the photo  $\ln I$ - $V$  characteristics and are plotted with device ageing as shown in fig. 6.5(d). The  $\text{SiO}_x$  layer developed on PS surface for the aged device may further increase the SBHs ( $D'_1, D'_2$ ) compared with that of the as-prepared one and attain saturation value, which can be easily visualised from energy band diagram depicted in fig. 6.7(c).  $\text{SiO}_x$  layer provides more defect states for accumulation of photo generated charge carriers within the Schottky barriers and subsequently increases the photocurrent ( $I_{ph}$ ) of the device for higher applied voltages. Similar enhancement of photocurrent due to native oxide layer has been reported for ZnO and  $\text{TiO}_2$  based planar MSM PDs [210,230]. Responsivity ( $R_\lambda$ ) and external quantum efficiency (EQE %) are considered as the figure of merit parameters for the photo sensing ability of a PD. Fig. 6.7(d) shows the spectral response of the as-prepared and aged device, where  $R_\lambda$  and EQE are plotted for UV-visible wavelength range of 250-500 nm at -3V bias. The equations used for calculating  $R_\lambda$  and EQE for as-prepared and aged device are already mentioned in Chapter 3 under subsection 3.3.3. Calculated maximum values of  $R_\lambda$  and EQE of the as-prepared device at a biasing of -3V are obtained for irradiation of 400 nm and are found to be  $0.09 \text{ AW}^{-1}$  and 28 % respectively. The photocurrent ( $I_{ph}$ ) of the device increases with ageing and



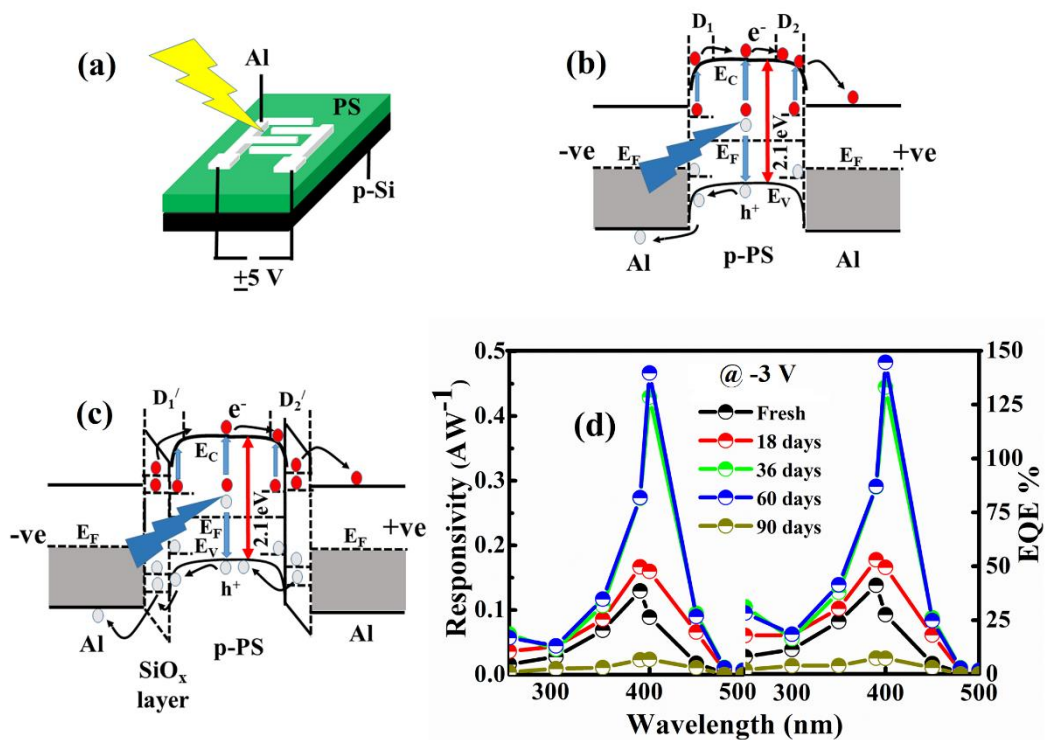


Fig. 6.7 (a) Schematic of the prepared MSM device, energy band diagram for (b) as-prepared and (c) aged device under illumination, (d) plot of  $R_\lambda$  and EQE vs.  $\lambda$ .

it consequently increases the  $R_\lambda$  and EQE values for fixed irradiation wavelength ( $\lambda$ ) and optical power density.  $R_\lambda$  and EQE are seen to attain the saturation values of  $0.47 \text{ AW}^{-1}$  and 145 % respectively after 60 days of ageing of the device. Increase of  $R_\lambda$  and EQE values for aged device (upto 60 days) compared to that of the as-prepared one can be attributed to the development of silicon suboxide layers on PS: p-Si surface. The saturation values in the parameters are due to complete filling of the dangling bonds of Si surface atoms by atmospheric oxygen atoms [210,232]. Also, higher values ( $>100\%$ ) of EQE can be ascribed to dominance of defect assisted conduction mechanism in the device with ageing. However, on further ageing upto 90 days,  $R_\lambda$  and EQE values ( $0.02 \text{ AW}^{-1}$  and  $0.07 \%$ ) are found to be even lower than that of the as-prepared device due to degradation. This  $\sim 20$ -fold decrease in responsivity compared to that of fresh device is ascribed to the development of high interfacial defects due to formation of  $\text{SiO}_x$  layer, which is evident from the shift observed in both dark and photo  $I$ - $V$  curves from zero slope regime towards the negative voltage regime with asymmetric nature [fig. 6.6(f)]. In comparison to this result, we have report of Vivanco et al. [233] on near UV-visible PS:p-Si: $\text{SiO}_2$  based MSM PD with  $R_\lambda$  value of  $\sim 8.0 \times 10^{-5} \text{ AW}^{-1}$  for illumination of  $\sim 400 \text{ nm}$ . Responsivity of this PD appears to be less ( $\sim 2$  order) even compared to that

of the degraded device reported in the present work. Planar MSM PD used here also shows superiority in terms of higher values of responsivity among some other MSM PDs based on p-Si:SiO<sub>2</sub> and graphene:p-Si:SiO<sub>2</sub> heterostructures reported in the literature [206, 234]. Fig. 6.8(a) shows the photocurrent dependence of the as-prepared and aged device under different illumination intensities (11-45 μWcm<sup>-2</sup>) for 400 nm wavelength irradiation at -3V bias. The device shows significant response down to a very low incident light intensity of 11 μWcm<sup>-2</sup>.  $I_{ph}$  of the as-prepared and the aged device follows power law dependence ( $I_{ph} = aP^b$ ) with illumination light intensity ( $P$ ), where  $a$  is a constant and  $b$  is a scaling parameter. Scaling parameters ( $b$ ) for the as-prepared and aged device are found to be in the range of 0.68-1.03. Whereas, for the degraded device after 90 days,  $b$  value is found to be 1.30. Value of  $b$  approaching unity for the aged device suggests photo current conduction mechanism to be dominantly controlled by trap or defect states [161]. Time response on-off kinetics for the as-prepared and aged device are recorded under illuminating wavelengths in the range of 250-450 nm at -3V bias with time intervals of 10 s [Fig. 6.8(b-d)]. It is evident from the figure that the as-prepared as well as the 60 days aged device show good stability with gradual rise in  $I_{ph}$  and constancy of  $I_d$  values during each on-off cycle. The fresh and 60 days aged device show maximum on-off ratio of 5.2 and 4.5 respectively for 400 nm illumination, signifying worthy influence of UV-visible light illumination on its switching performances. Though, the 90 days aged device shows unstable on-off cycles with low on-off ratio of 1.6 as shown in fig. 6.8(d). Fig. 6.8(e) shows similar plot for fresh as well as aged (upto 90 days) device under illumination of 400 nm at a biasing of -3V.  $I_{ph}$  and  $I_d$  are seen to increase with ageing of the device during on and off cycles respectively and maximum on-off ratio of 6.3 is obtained for the 36 days aged device. However, after 90 days,  $I_{ph}$  and  $I_d$  values decrease as compared to that of fresh one, which are in consistency with our earlier findings. To determine response ( $\tau$ ) and recovery times ( $\sigma$ ) of the device, best fitted Boltzmann and exponential decay equations are used, which are already mentioned in Chapter 3 under subsection 3.3.3. For ready reference of the device response time determination, the calculation for the as-prepared one is displayed in fig. 6.8(f). Response and recovery times of the as-prepared device are found to be  $0.16 \pm 0.03$  and 0.24 s respectively. No remarkable change of  $\tau$  and  $\sigma$  values with ageing is observed. The device has moderately slow response and recovery

times compared to some of the earlier reported silicon based high speed PDs [235-237], but shows faster response compared to some others [161, 238]. Slow response of the device might originate due to the presence of trap or defect states in PS: p-Si interfaces and within the Schottky barriers, the fact is in correlation with the results detailed earlier. These defect states improve the device responsivities and also act as recombination sites leading to slow response, this is also witnessed in some of the best silicon based PDs reported in literature as displayed in Table 6.1. Thus, the device has good stability and reproducibility in photo sensing features upto a limited period of time, the period may be further enhanced by following some passivation strategies. One can follow PS surface passivation strategies such as atmospheric thermal oxidation, hydrofluoric acid or alcoholic sulphide treatment etc. to optimise and stabilize the PS based devices against degradation [239, 240]. In part B of this chapter, the effects of thermal annealing treatment on aged PS:p-Si Schottky PD have been investigated in order to improve its photo sensing performances.

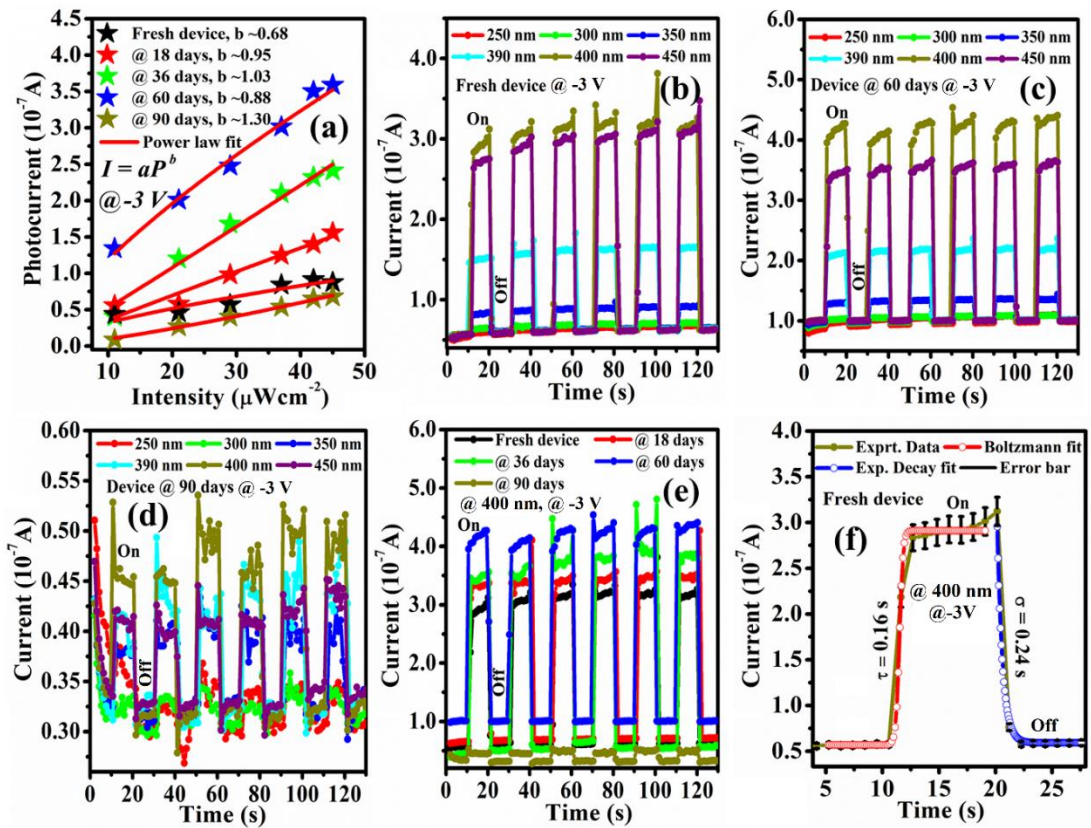


Fig. 6.8 (a) light intensity dependent  $I_{ph}$ , on-off kinetics for (b) as-prepared, (c) 60 days and (d) 90 days aged device for different illumination wavelengths, (e) as-prepared and aged device plotted together and (f) calculation of response time for illumination of 400 nm at -3 V bias.

## Chapter 6 Optical and electrical properties of aged and annealed PS: p-Si...

**Table 6.1** Comparative performance analysis of Al/PS: p-Si structure PD with some of the best reported Si-based PDs in the literature.

Device	Measurement condition [wavelength ( $\lambda$ )]	Responsivity ( $\text{AW}^{-1}$ )	Response time (m Sec)		Ref.
			Rise ( $\tau$ )	Decay ( $\sigma$ )	
<b>N-doped TiO<sub>2</sub>/n-Si</b>	$\lambda = 365$ nm	0.053			[236]
	$\lambda = 565$ nm	1.1	50	50	
<b>MoS<sub>2</sub>/Si PD</b>	$\lambda = 400$ nm	0.15			[237]
	$\lambda = 550$ nm	0.21	0.3	0.3	
<b>MoS<sub>2</sub>/p-Si PD</b>	$\lambda = 400$ nm	0.23			[161]
	$\lambda = 665$ nm	0.75	~1000	~1000	
<b>Ni:SiC:PS MSM PD</b>	$\lambda = 340$ nm	0.04	$8.2 \times 10^3$	$16 \times 10^3$	[238]
<b>MoS<sub>2</sub>/SiO<sub>2</sub>/p-Si PD</b>	$\lambda = 400$ nm	0.15			[235]
	$\lambda = 808$ nm	9.10	$56 \times 10^{-6}$	$83 \times 10^{-5}$	
<b>MoS<sub>2</sub>/SiO<sub>2</sub>/Si nanocone PD</b>	$\lambda = 405$ nm	0.03			[234]
	$\lambda = 650$ nm	0.06	-	-	
<b>Graphene/SiO<sub>2</sub>/Si PD</b>	$\lambda = 400$ nm	0.30			[236]
	$\lambda = 1100$ nm	0.10	-	-	
<b>PS/SiO<sub>2</sub>/p-Si PD</b>	$\lambda = 400$ nm	$8.0 \times 10^{-5}$			[233]
	$\lambda = 430$ nm	$1.0 \times 10^{-4}$	-	-	
<b>Al:PS:p-Si MSM PD</b>	$\lambda = 400$ nm	0.47	160	240	<b>Present work</b>

## 6.4 Results and discussion: Part B: Optical and electrical properties of annealed PS: p-Si structure (S. Sarmah et al., [241])

### 6.4.1 Morphological and optical analysis

Morphological analysis of the PS: p-Si sample at four different annealing temperatures (200 to 500 °C) are carried out through FESEM imaging and EDX spectra, which are shown in fig. 6.9 and fig. 6.10 respectively. Fig. 6.9(a-d) show planar view of the FESEM micrograph with insets showing the cross-sectional views of PS: p-Si sample annealed at 200, 300, 400 and 500 °C for 1 hour. These indicate that there is no visual change in pore morphology and thickness of the PS layer with increasing annealing temperature. The pore size (30 nm) calculated from the histogram plot [fig. 6.9(e)] and thickness of PS layer (540 nm) is unchanged with annealing. To observe quantitative change in  $\text{SiO}_x$  composition on PS surface, EDX spectra are recorded, the results are shown in fig. 6.10(a-f). Fig. 6.10(a) shows the scanned region selected for analysis. Fig. 6.10(b) shows EDX spectra of the untreated sample, which shows elemental composition of Si and O by their atomic percentages are 93.89 and 6.11 % respectively. However, with annealing at different temperatures, the atomic percentage of oxygen is seen to increase, which is evident from fig. 6.10(c-f). The percentages of Si and O for PS: p-Si sample annealed at 200, 300, 400 and 500 °C for 1 hour are found to be 64.57,

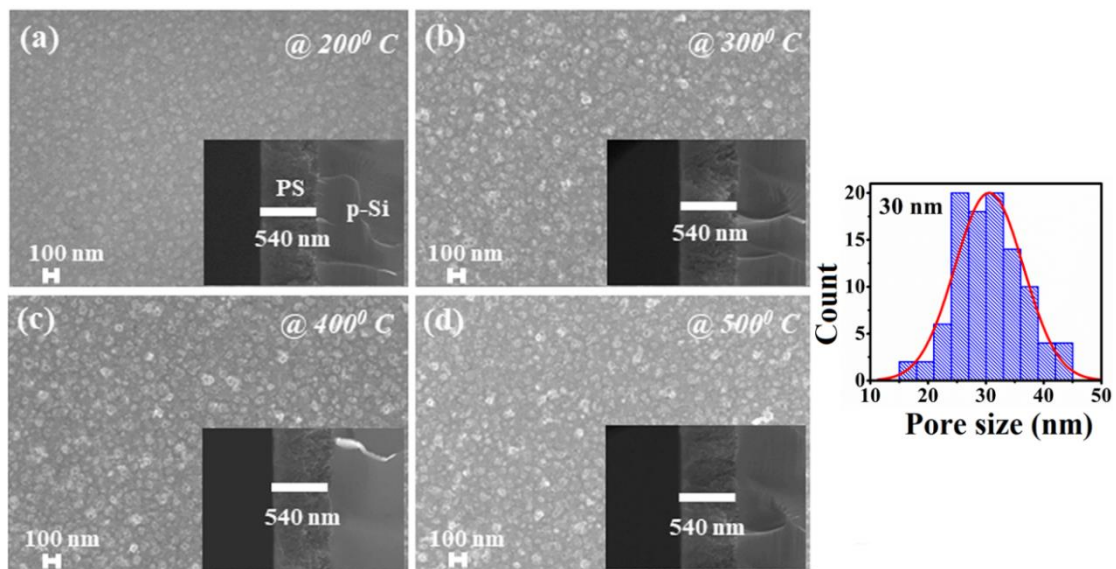


Fig. 6.9 Planar FESEM micrographs of PS:p-Si annealed at (a) 200 °C (b) 300 °C, (c) 400 °C and (d) 500 °C, [insets show cross-sectional views], (e) pore size histogram, (f) change of pore size/thickness with annealing

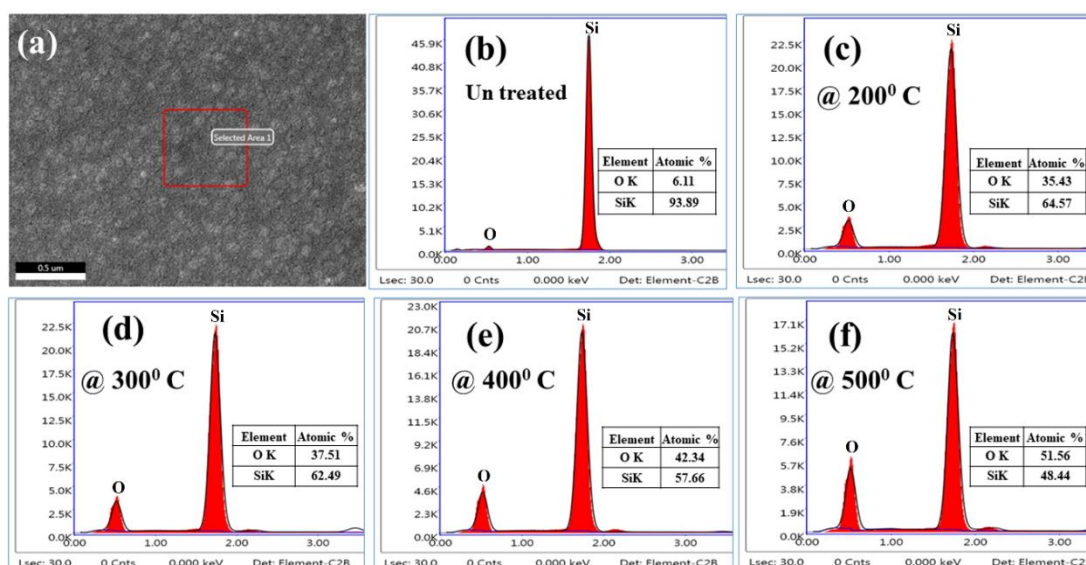


Fig. 6.10 Selected area of annealed PS:p-Si for EDX analysis, EDX spectra of (b) untreated and annealed PS:p-Si at (c) 200 °C (d) 300 °C, (e) 400 °C and (f) 500 °C

62.49, 57.66 and 48.44 % and 35.43, 37.51, 42.34 and 51.56 % respectively. These confirm that with increasing annealing temperature, oxygen content in the PS surface increases and subsequently a layer of  $\text{SiO}_x$  is formed. Fig. 6.11(a) shows the UV-vis absolute reflectance spectra for annealed PS:p-Si structure along with the bare p-Si one in the wavelength range of 350-800 nm. Annealed PS:p-Si samples show lower reflectance (10-30 %) in UV-vis range as compared to that of bare p-Si (35-40 %), confirming more light absorption in the range. Fig. 6.11(b) shows photoluminescence (PL) spectra for untreated as well as annealed PS:p-Si for an excitation wavelength of 275 nm. Untreated PS show broad characteristic luminescence peak at 600 nm with FWHM value of 140 nm. This characteristic peak is attributed to band to band recombination of charge carriers confined in the PS: p-Si nanostructure [128]. However, upon annealing this peak is significantly quenched and after 300 °C of annealing, it disappears completely as evident from zoomed view in fig. 6.11(c). With annealing treatment, the peaks at 420 and 470 nm related to silicon suboxide grown over PS gradually dominate and suppress the PS characteristic peak. As will be discussed in the subsection to follow, thermal annealing would affect electrical and photo sensing property of PS.

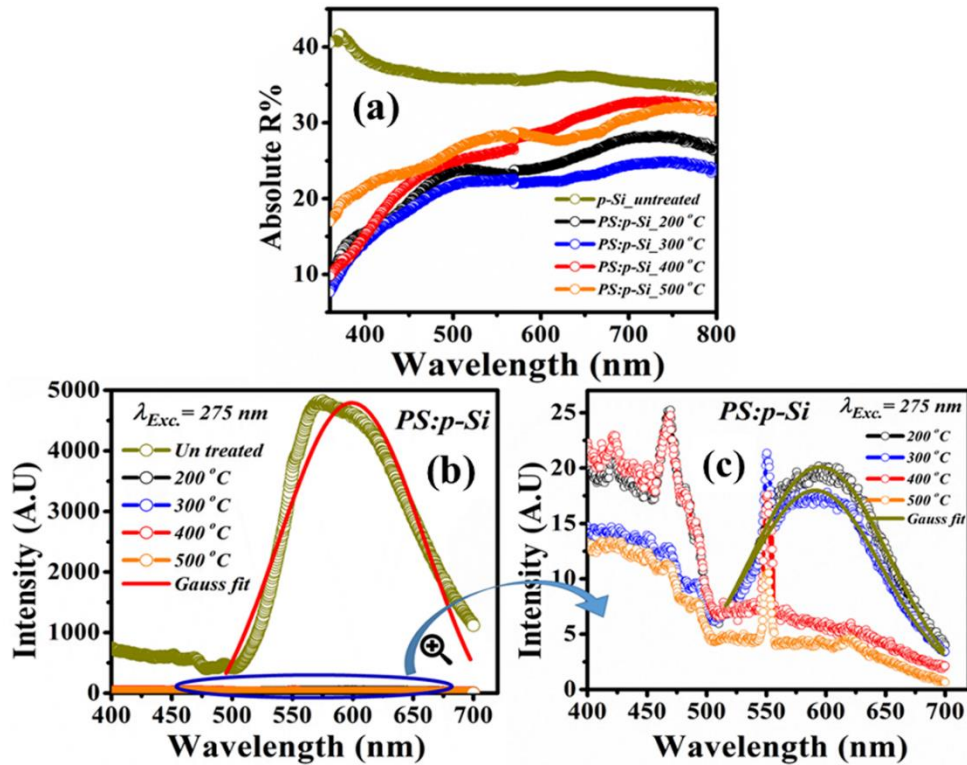


Fig. 6.11 (a) Reflectance spectra of bare p-Si and annealed PS:p-Si, (b) PL spectra of untreated and annealed PS:p-Si, (c) zoomed view of PL spectra for annealed PS:p-Si

### 6.4.2 Electrical and photo response analysis

To observe the electrical conduction phenomenon in the annealed Al/PS: p-Si, it is recommended to analyse the dark current ( $I$ )-voltage ( $V$ ) characteristics, these plots are shown in fig. 6.12(a, b). Fig. 6.12(a) shows its *semi-log I-V* plot under dark condition for the voltage range of -5 to 5V when annealed at different temperatures 200, 300, 400 and 500 °C respectively for 1 hour. It can be seen that for the device annealed at 200 °C, the  $I-V$  curve deviates from zero slope and shift towards negative quadrant showing minimum current value  $\sim 0.4 \text{ nA}$  at -2 V compared to  $\sim 1.3 \text{ nA}$  at -0.5 V,  $\sim 0.09 \text{ nA}$  at -0.07 V and  $\sim 5.20 \mu\text{A}$  at -0.02 V for device annealed at 300, 400 and 500 °C respectively. This deviation from zero slope regime and shifting of current minima towards the negative quadrant with increasing annealing temperature may be attributed to development of negative built-in potential due to gradual growth of  $\text{SiO}_x$  layer on PS:p-Si surface. Moreover, it can be observed that unlike untreated fresh PS:p-Si planar MSM devices, the  $I-V$  characteristics are not symmetric even at low annealing temperature of 200 °C. Thus the effective Schottky barrier height is different for forward and reverse direction and is dependent on the annealing temperature. To

investigate further in detail, the important parameters like ideality factor ( $n$ ) and Schottky barrier height ( $\phi_B$ ) are calculated using thermionic emission (TE) model for both forward and reverse directions. For this device, the region where current is seen to be increasing linearly with applied voltage before attaining a saturation value in both the directions are fitted with the TE model, as discussed earlier and the plots are shown in fig. 6.12(a). The variations of ( $n$ ) and ( $\phi_B$ ) as function of annealing temperature are shown in fig. 6.12(c, d) and their calculated values are listed in Table 6.2. It can be seen that  $n$  values of the device approaches unity for both forward and reverse direction when annealed at 400 °C, while the effective barrier height shows increasing trend in the forward direction and decreasing trend in the reverse direction with increasing annealing temperature. So, it can be found that diode quality of the device enhances when annealed at 400 °C for 1 hour. To know more about the current conduction phenomenon, forward biased  $\ln I$ - $\ln V$  curve is divided into three voltage regimes and each regime has been fitted to a power law equation expressed as  $I_f \propto V_f^\alpha$  as shown in fig. 6.12(b). Here,  $I_f$  is the forward dark current,  $V_f$  is forward voltage and  $\alpha$  is the

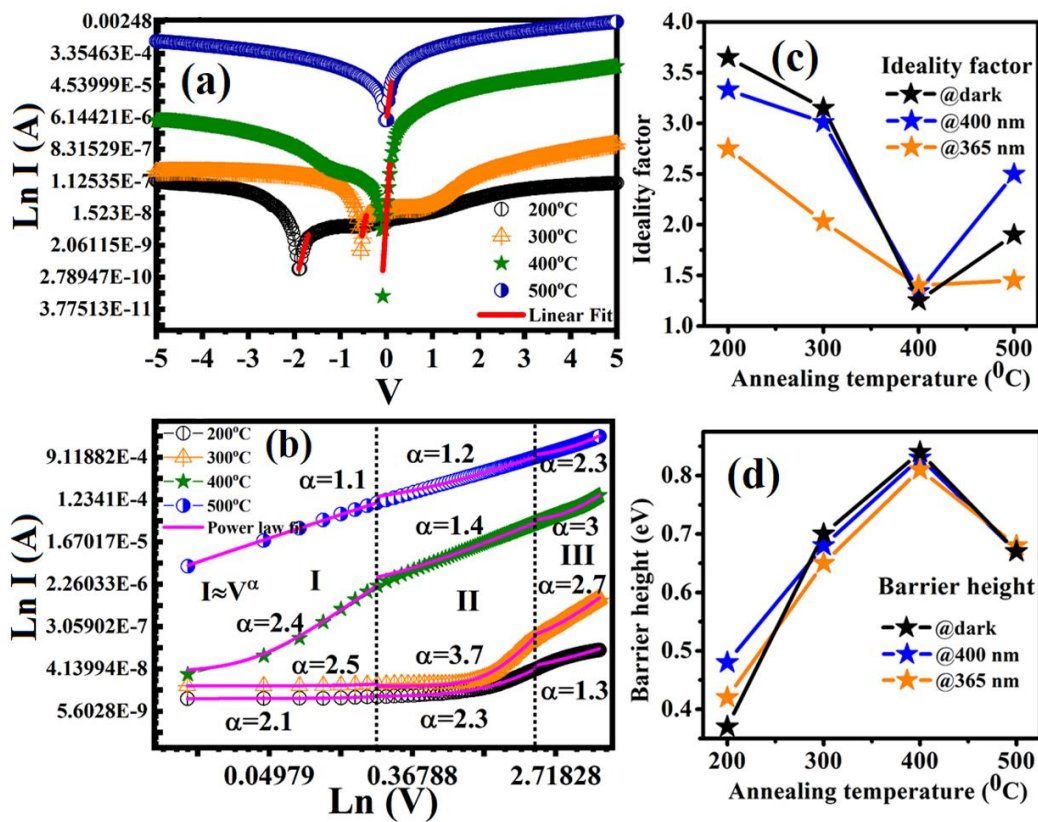


Fig. 6.12 (a) Semi log dark  $I$ - $V$  plot, (b) forward dark  $\ln I$ - $\ln V$  plot, (c) variation of ideality factor and (d) barrier height for annealed PS:p-Si



fitting parameter. For region I ( $V_f = 0.0 - 0.2V$ ), it can be seen that  $\alpha$  value lies in the range of 2.1-2.5 for the device treated at 200-400 °C and in this region current conduction in the device is mostly dominated by traps or defect states [131]. However, on further increasing the annealing temperature to 500 °C,  $\alpha$  becomes approximately unity and so it can be suggested that the conduction becomes trap independent and follows ohmic conduction mechanism. Similarly, for region II ( $0.2 < V_f < 2V$ ),  $\alpha$  values are 2.3, 3.7, 1.4 and 1.2 for the device annealed at 200-500 °C respectively. In this voltage region, the current increases super linearly for the device when annealed at 200 and 300 °C and starts to show ohmic behaviour with increased annealing temperature. Further, for region III ( $V_f > 2V$ ),  $\alpha$  values are found to be 1.3, 2.7, 3 and 2.4 respectively. Thus, the annealed device shows mix conduction phenomenon with cross-overs between ohmic and space charge limited conduction (SCLC) mechanisms for different annealing temperatures. To observe further, photo sensing property of the device at different annealing temperatures are studied. Fig. 6.13(a-d) shows the plots of responsivity ( $R_\lambda$ ) vs. wavelength ( $\lambda$ ) at bias voltage of -2V, inset showing similar plot at 0 V under illuminating wavelength in the range of 200-600 nm for the device annealed at 200-500 °C. From the figure it can be seen that with increasing annealing temperature, device shows enhanced  $R_\lambda$  value and shows distinct multi-bands when treated at 300 and 400 °C. The device annealed at 200 °C [fig. 6.13(a)], shows maximum  $R_\lambda$  value of  $0.08 \text{ AW}^{-1}$  for illumination of 365 nm at -2V, though it does not exhibit appreciable response on application of bias voltage of 0V. Although, it shows negative responsivity, which can be attributed to the negative built-in potential at the junction. Similarly, device treated at 300 °C [fig. 6.13(b)], exhibits multiband  $R_\lambda$  values of  $25 \text{ AW}^{-1}$ ,  $15 \text{ AW}^{-1}$  and  $20 \text{ AW}^{-1}$  at 365, 400 and 440 nm respectively at biasing of -2 V. However, on application of 0 V bias, it shows very low responsivity. The device shows multi-band maximum  $R_\lambda$  values of 50, 25, 15 and  $16 \text{ AW}^{-1}$  at 365, 400, 440 and 450 nm respectively when treated at 400 °C for -2V biasing. Conversely, the same device when further annealed to 500 °C show a broad spectrum in wavelength range of 350-440 nm with maximum  $R_\lambda$  value of  $100 \text{ AW}^{-1}$  at 365 nm and a weak peak at 440 nm with  $R_\lambda$  value of  $30 \text{ AW}^{-1}$ . This broad spectrum is observed mainly due to ohmic behaviour of the annealed device at this temperature. On application of 0 V for the device annealed at 400 and 500 °C, it again shows some positive and negative spikes due negative built-

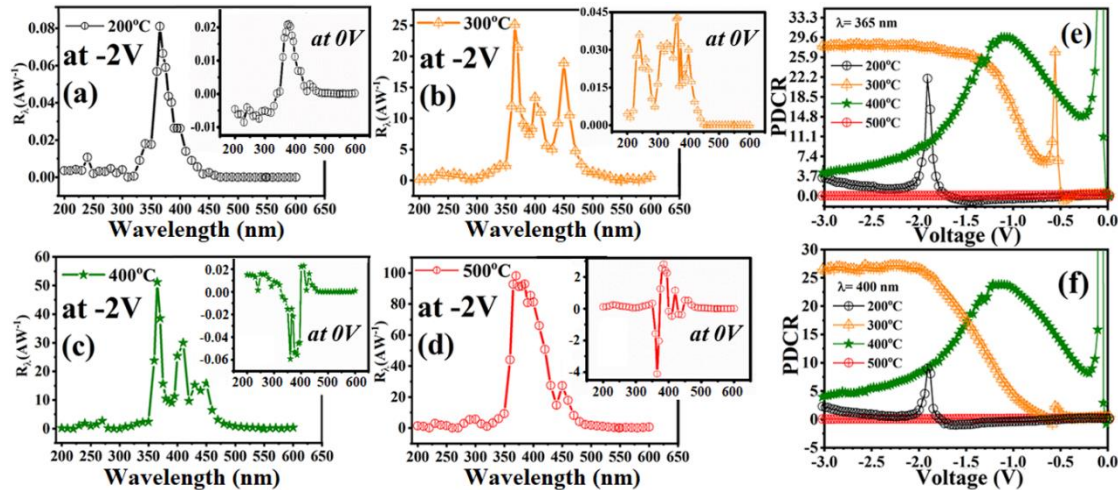


Fig. 6.13 Responsivity plot for PS:p-Si annealed at (a) 200 °C, (b) 300 °C, (c) 400 °C and (d) 500 °C at -2V [insets show plots at 0V], PDCR plots for annealed PS:p-Si under illumination of (e) 365 nm and (f) 400 nm

-in potential. The interesting feature is that with increase of annealing temperature, responsivity of the device enhances, which basically happens due to increase in the device current with annealing temperature as is evident from semi-log photo  $I$ - $V$  plot [fig. 6.14(a-d)]. To know more about the photoconduction phenomenon, plots of photo to dark current ratio (PDCR) vs. applied reverse bias ( $V_{ra}$ ) are shown in fig. 6.13(e, f). From the figure it is clear that PDCR value is maximum for the device annealed at 300 °C for illumination of 365 nm at  $V_{ra} > -1.5V$  and gradually decreases on lowering the bias voltage. However, at  $V_{ra} = -0.5V$ , PDCR attains a sharp peak of 29, similar peak with a lower value of 22 is observed at  $V_{ra} = -2V$  for the device annealed at 200 °C. These peak positions exactly coincide with the negative potential values for minimum dark currents. On further treating the device to 400 °C, sharp increase of PDCR value is seen for low voltage region (0 to  $-1.5V$ ) and tends to decrease towards high reverse voltage region, suggesting low power operation suitability of the device. However, for the same device when treated at 500 °C, PDCR drops to minimum value and is mainly attributed to decrease in active region which is evident from linear dependence of current on applied voltage in both directions [inset of fig. 6.14(d)]. These patterns of PDCR can also be observed for the device under illumination of 400 nm radiation [fig. 6.13(f)], though with appreciably lower values. The possible reason for such lower PDCR values could be the energy difference in the illuminating radiations. Time dependent switching dynamics of the annealed device under illumination of 365 and 400 nm radiation for the bias voltage of -1V and 0V are analysed, these results are

shown in fig. 6.15(a-h). Fig. 6.15(a, b) shows time response kinetics of the device annealed at 200 °C with on-off time interval of 10 seconds. From these curves it is evident that under illumination of 365 and 400 nm radiation, the device shows positive and negative spikes at the edges of the transient kinetics as soon as the illumination is turned on and off respectively. Fig. 6.15(c, d) shows similar curve for the device annealed at 300 °C under biasing of -1 and 0V respectively. These spikes generally appear due to mis-alignment of the centre of electric charges across the junctions of Al-SiO<sub>x</sub>: PS:p-Si due to anisotropy. This can be clearer from zoomed view in fig. 6.15(i). On illumination under zero bias condition, current initially shoots to a certain negative value (stage I) due to light induced pyroelectric potential with instantaneous change in temperature [242]. In stage II, the saturation region is attained due to lack of photo induced temperature variation i.e., pyroelectric potential disappears and the output current equals the device dark current. As the illumination is turned off (stage III), variation of photo induced temperature occurs, which tends to raise the pyroelectric potential in reverse direction to that in stage I, thereby enhancing the current to certain positive value and thus degrade photo sensing stability of the device. In stage IV, pyroelectric potential disappears and current saturation is attained as in case of stage II.

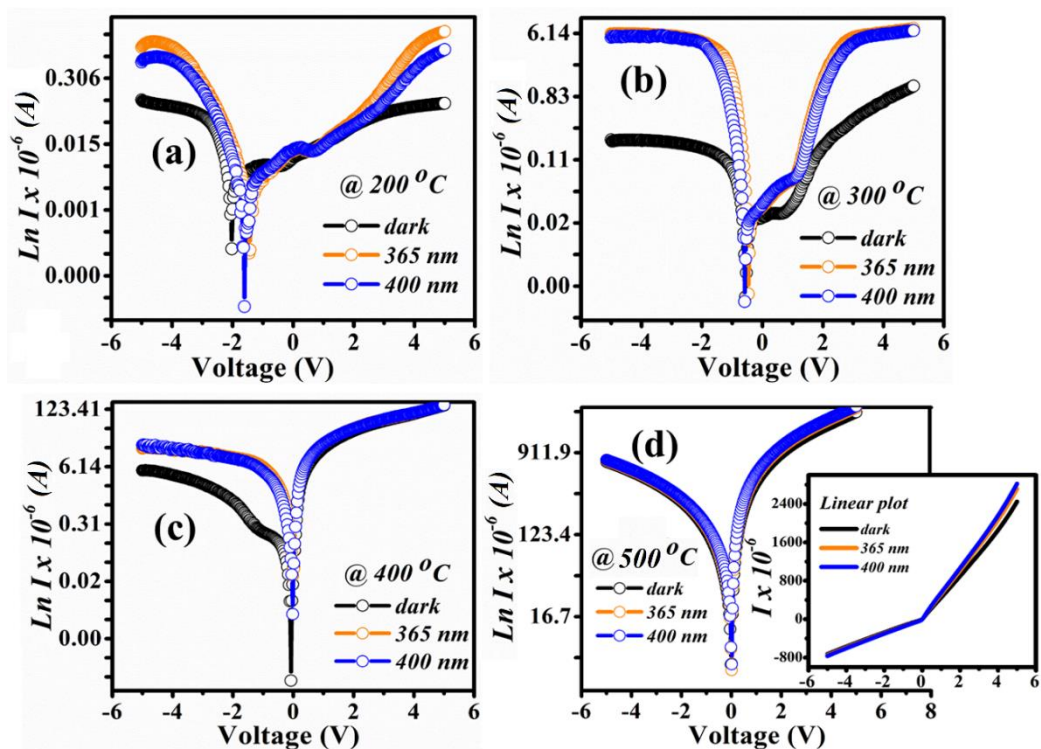


Fig. 6.14 Dark and photo semi log  $I$ - $V$  plot for annealed PS:p-Si at (a) 200 °C, (b) 300 °C, (c) 400 °C and (d) 500 °C [inset of (d) show linear  $I$ - $V$  plot]

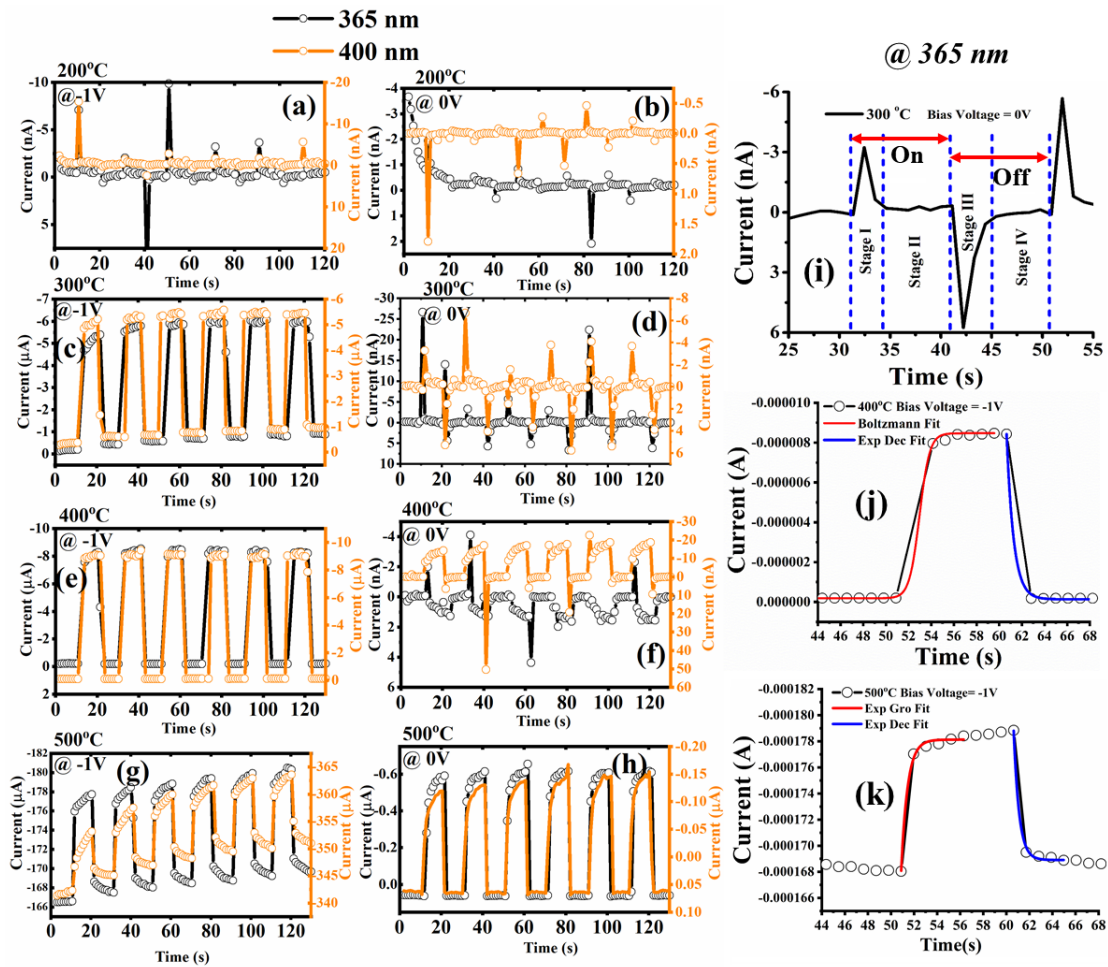


Fig. 6.15 (a-h) Time response plots for annealed PS:p-Si at 0V and -1V bias under illumination of 365 and 400 nm, (i) different stages of pyroelectric effect, (j,k) fitted curves for calculation of response times

However, for annealing temperature of 300 °C under -1V bias, the spikes are eliminated. The growth and decay times are found to be  $0.31 \pm 0.1$  s,  $0.12 \pm 0.04$  s and  $0.69 \pm 10^{-4}$  s,  $0.24 \pm (2 \times 10^{-6})$  s under 365 and 400 nm radiations respectively. The pyro-spikes are further eliminated when annealed at 400 °C, with growth and decay times of  $0.45 \pm 0.07$  s,  $0.35 \pm 0.1$  s and  $0.62 \pm (8.6 \times 10^{-5})$  s,  $0.32 \pm (1.6 \times 10^{-6})$  s at -1V under illumination of 365 and 400 nm radiations respectively [fig. 6.15(j)]. Light induced pyroelectric potential completely disappears for the device annealed at 500 °C with growth and decay times of  $0.56 \pm 2.1 \times 10^{-4}$  s,  $0.88 \pm 9.02 \times 10^{-4}$  s and  $0.47 \pm 1.16 \times 10^{-4}$  s,  $0.82 \pm 9.3 \times 10^{-4}$  s at -1V for 365 and 400 nm respectively [fig. 6.15(k)], signifying dominance of photo effect over pyroelectric effect. This fact can be attributed to the decrease in built-in potential as discussed earlier. Also, due to ohmic  $I$ - $V$  behaviour, the device shows photo

**Table 6.2** Performance analysis of annealed Al/PS:p-Si MSM Schottky device.

Annealing temperature (°C)	Illumination conditions	Ideality factor ( <i>n</i> )		Schottky barrier height ( $\phi_B$ ) eV		Responsivity ( <i>R</i> ) AW <sup>-1</sup>		Response time (s)	
		Forward bias	Reverse bias	Forward bias	Reverse bias	-2V biasing	-0.25V biasing	Rise time ( $\sigma$ )	Decay time ( $\tau$ )
200	dark	3.65	2.23	0.37	1.83	-	-	-	-
	365 nm	2.75	2.82	0.42	1.46	0.08	-0.01	-	-
	400 nm	3.33	1.62	0.48	1.97	0.03	0.01	-	-
300	dark	3.15	2.71	0.70	1.07	-	-	-	-
	365 nm	2.03	2.35	0.65	1.06	25.16	0.01	0.31	0.69
	400 nm	3.01	1.82	0.68	1.19	15.00	0.01		
400	dark	1.25	1.33	0.84	0.97	-	-	-	-
	365 nm	1.40	3.17	0.81	0.80	50.23	4.5	0.45	0.35
	400 nm	1.34	2.02	0.83	0.85	25.44	1.5	0.62	0.32
500	dark	1.90	4.70	0.67	0.67	-	-	-	-
	365 nm	1.45	4.70	0.68	0.66	92.82	50.0	0.56	0.88
	400 nm	2.50	3.80	0.67	0.66	81.26	38.0	0.47	0.82

response even at 0V with response times of  $1.21 \pm 0.002$  s and  $1.79 \pm 0.005$  s under UV (365 nm) and visible (400 nm) illuminations respectively.

### 6.5 Conclusion

Al/PS: p-Si planar Schottky UV-vis photodetector has been successfully designed. The photoresponsivity of the aged device shows enhancement upon thermal annealing. FESEM analyses confirm formation of mesopores on p-Si surface with uniform PS: p-Si interface. Elemental EDX analyses endorse development of silicon suboxide layers on PS: p-Si surface for aged and annealed structure. Photoluminescence spectra of the as-prepared and aged structure for excitation wavelength of 275 nm show strong characteristic peak at 590 nm along with some weak emission peaks at 470 and 500 nm related to the defect levels of SiO<sub>x</sub> layers developed on the PS surface. Upon annealing, the silicon suboxide related peaks gradually dominate over PS characteristic peak and suppress this peak completely when annealed at 400 °C. Defect enriched aged device show increase of  $I_{ph}$  for higher voltage region, subsequently increasing responsivity and EQE values upto 0.47 AW<sup>-1</sup> and 145 % respectively. However,  $R_l$  and EQE values drop by 20-fold after ageing for 90 days, due to device degradation with the growth of high

interfacial defects. The device exhibits best multiband UV-visible photo-response when annealed at 400 °C. However, on annealing to higher temperature, i.e., at 500 °C, the device exhibits ohmic behaviour and consequently broad responsivity spectra is observed. Response and recovery times of the as-prepared device are found to be 0.16 and 0.24 s respectively, which remain constant with ageing of the device. However, some pyro-spikes are observed when the device is annealed between 200 to 400 °C. These spikes are completely eliminated when annealed at 500 °C. Annealing of the naturally oxidized Al/PS: p-Si Schottky device at an appropriate temperature (400 °C) minimizes interfacial defects, which consequently enhances its UV-visible photoresponse.

# Chapter 7

## **Overall summary and future prospects**





## 7

## Overall summary and future prospects

This chapter gives overall compilation of the entire work that has been carried out under Chapters 3-6. This will provide a concise view of the present work. This chapter also contains future prospects of work based on the present dissertation. The following two sections deal with these matters.

### 7.1 Overall summary

Present dissertation work reports the study of optical, morphological and electrical properties of porous silicon and its hybrid heterostructures. The simple, cost effective and highly reproducible electrochemical etching method for preparation of porous silicon has been used. Porous silicon based hybrid structures are fabricated by some physical deposition methods viz., thermal evaporation and pulsed DC sputtering. UV-visible photo sensing performances of the bare porous silicon and its heterostructures viz., CdS-PS:p-Si, ZnS-PS:p-Si, ZnO-PS:p-Si are studied in details in four chapters (3-6) of the thesis.

The methods used in the present thesis work are facile, cost effective and highly reproducible, which emphasize novelty of the work. The improvised optical responsivity and response time of the fabricated devices in comparison to some previous works from the literature also administrate great novelty of the results.

To start with metal semiconductor metal device based on nanostructured CdS-PS:p-Si heterostructure has been successfully developed with simpler inexpensive techniques. Light sensing abilities in UV-vis spectral range of 250 to 500 nm is tested for this device. FESEM and FETEM analyses confirm formation of CdS nanostructure. Cross sectional FESEM view confirms growth of uniform interface between CdS and

PS: p-Si structure. PL study reveals trap and defect assisted luminescence bands at 450, 460, 468, 482 and 533 nm for nanostructured CdS along with characteristic PL peak of PS at 590 nm. These traps and defects in turn control electrical current conduction phenomena within the heterostructure as confirmed from dark current analyses. The heterostructured photodetector (PD) exhibits high responsivity, high EQE and quite fast response time of ~160 ms under illumination of 400 nm radiation at bias voltage of -2V. All these facts assure the device to be applicable as UV-vis photodetector and switching device.

In the next work, PD with distinct and enhanced responsivity from ZnS-PS: p-Si heterostructure has been developed. FESEM micrograph shows uniform interface between ZnS and PS:p-Si structure. Cross sectional EDX analyses reveal diffusion of some ZnS particles into PS layer. UV-visible spectra of bare ZnS reveals maximum light absorption in UV region and maximum transmittance in the visible region. Reflectance spectra shows that ZnS-PS:p-Si heterostructure exhibits low reflectivity compared to bare ZnS and PS:p-Si. ZnS-PS shows ZnS related band edge luminescence at ~380 nm with some defect dominated luminescence bands in visible range. Al+Au/ZnS-PS: p-Si exhibits distinct and enhanced responsivity ( $R_\lambda$ ) values of 0.95 and 1.13  $\text{AW}^{-1}$  respectively at 365 nm and 400 nm radiation compared to 0.59  $\text{AW}^{-1}$  for Al/PS:p-Si structure at 400 nm illumination. This distinctness is mainly attributed to maximum band to band absorption of photons in ZnS and PS:p-Si structure.

Next to follow, distinct band UV to visible MSM photodetector from ZnO-PS:p-Si heterostructure has been developed. Light sensing property of these PDs have been tested by spectral response in the range of 200-500 nm, these give distinct  $R_\lambda$  and EQE values at 375 and 400 nm respectively. Cross sectional FESEM confirms uniform interface between ZnO and PS:p-Si structure. Planar FESEM analyses indicate increase of mean grain size of ZnO nanoparticles, when the heterostructure is annealed at 400 and 500 °C. EDX analyses confirm diffusion of ZnO nanostructures into pores of PS layer and oxygen content in the heterostructure rises with increase of annealing temperature. Optical band gap energy of nanostructured ZnO changes from 3.30 to 3.23 eV upon annealing, due to change in the density of defect states. The film remains highly transparent (65-78 %) in vis-NIR region even after annealing treatment. PL spectra reveals various traps and defect assisted luminescence bands along with

characteristic band to band emission peaks of ZnO and PS:p-Si structures. ZnO band edge luminescence peak significantly quenches and PS characteristic peak disappears completely upon annealing. PD1 and PD2 show distinct band UV-visible photo response with slow UV response and fast visible response time. Bare ZnO on the other hand is sensitive to UV range only and has slower response. Slower response in UV region for the PDs is due to oxygen related vacancies present in ZnO. PD1 when annealed at 200 °C, exhibits rise in responsivity value upto 30 AW<sup>-1</sup> as compared to that of untreated one (2.6 AW<sup>-1</sup>) for illumination of 400 nm. However, upon further annealing in the range of 300-500 °C, due to development of negative built-in potential device responsivity decreases. Response times for the device annealed at 200 °C are found to be relatively faster as compared to that of the untreated one. For the annealed device at lower bias, pyroelectric effect is more dominating over its photo sensing performance.

Lastly, Al/PS: p-Si planar Schottky UV-vis photodetector has been designed and studied the effect of ageing and annealing on this. The photoresponsivity of the aged device shows enhancement upon thermal annealing treatment. FESEM analyses confirm formation of mesopores on p-Si surface with uniform PS: p-Si interface. Elemental EDX analyses endorse development of silicon suboxide layers on PS: p-Si surface for aged and annealed structure. Photoluminescence spectra of as-prepared and aged structure for fixed excitation wavelength of 275 nm show strong characteristic peak at 590 nm along with some weak emission peaks at 470 and 500 nm related to defect levels of SiO<sub>x</sub> layers developed on PS surface. Upon annealing, the silicon suboxide related peaks gradually dominate over PS characteristic peak and suppress this peak completely when annealed at 400 °C. Defect enriched aged device show increase of  $I_{ph}$  for higher voltage region, subsequently increase responsivity and EQE values upto 0.47 AW<sup>-1</sup> and 145 % respectively. However,  $R_{\lambda}$  and EQE values drop by 20-fold after 90 days, due to device degradation with grow of high interfacial defects. The device exhibits best multiband UV-visible photo-response when annealed at 400 °C. However, on annealing to higher temperature, i.e., at 500 °C, the device exhibits ohmic behaviour and consequently broad responsivity spectra is observed. Response and recovery times of the as-prepared device are found to be 0.16 and 0.24 s respectively, which remain constant with ageing of the device. However, some pyro-

spikes are observed when the device is annealed between 200 to 400 °C. These spikes are completely eliminated when annealed at 500 °C. So as to say, annealing of the naturally oxidized Al/PS: p-Si Schottky device at an appropriate temperature (400 °C) minimizes interfacial defects, which consequently enhances its UV-visible photoresponse.

The summarized results of the whole dissertation study are in tabulated in **Table 7.1** for ready view of the entire work.

## 7.2 Future prospects

There is ample scope for future studies based on the works reported in this dissertation. One can study different properties of porous silicon or silicon based nanostructures for exploring their application potential. Some specific prospect studies are mentioned below:

- 1) Silicon based nanostructures or silicon nanowires (Si-NWs) can be synthesized by various chemical methods such as electrochemical etching or metal assisted chemical etching etc.
- 2) Different heterostructures of silicon nanostructures with nanostructured zinc oxide (ZnO), aluminium doped ZnO (AZO), nanostructured zinc sulphide (ZnS) etc. can also be developed using various physical methods such as thermal evaporation, magnetron sputtering etc.
- 3) Silicon nanostructure and its heterostructure based metal semiconductor devices can be designed for application in photodiodes (PDs) and solar cells.
- 4) Such PDs and solar cells can be optimized and stabilized by following various passivation strategies such as thermal annealing treatment, acidic or alcoholic treatment etc.

Table 7.1 Summarised results of the whole dissertation

Chapter No	Sample	Sample Preparation Condition	Pore Size (nm)	Particle Size (nm)	Thickness (nm)	Optical Band-gap (eV)	PL Peak (nm)	Electrical and Photo Sensing Parameters						
								Device Configuration	$n$	$\phi_b$ (eV)	Illumination Condition	$R_s$ (AW <sup>-1</sup> )	$\tau$ (s)	$\delta$ (s)
3	CdS	-	28	-	170	2.6	450-482	-	-	-	-	-	-	
	CdS-PS:p-Si	-	-	-	170+1500=1670	-	450-482, 590	Lateral	1.57	-	400	0.60	0.16	0.35
4	ZnS	-	115	-	110	3.4	384, 415, 467	-	-	-	-	-	-	
	ZnS-PS:p-Si	-	-	-	110+540=650	-	380, 410	Lateral	1.5	-	400	1.13	0.50	0.35
5A	ZnO	-	39	-	160	3.3	378, 433, 467, 482, 492	Lateral	2.4	0.98	375	1.70	3.6	0.5, 3.6
	ZnO-PS:p-Si	-	-	-	160+540=700	-	378, 433, 467, 482, 492, 597	Lateral	3.8	0.92	375	1.87	2.1	0.7
5B	Annealed ZnO-PS:p-Si	200	35	-	327	3.27	380	Sandwich	1.7	0.81	400	68	1.0	1.0
		300	38	-	326	3.26	377				375	6.0	0.6	0.7
6A	Aged PS:p-Si	fresh	30	-	323	3.23	391				400	9.5	2.2	1.5
		18	29	-	325	3.25	385	Lateral	3.33	0.75	375	5.0	2.1	1.5
6B	Annealed PS:p-Si	300	30	-	540	-	590-592	Lateral	3.45	0.45	400	0.5	-	-
		36	28	-	540	-	590-592	Lateral	3.45	0.45	400	0.5	-	-
6B	Annealed PS:p-Si	60	29	-	595	-	595				365	0.08	-	-
		200	30	-	591	-	591				400	0.03	-	-
6B	Annealed PS:p-Si	300	30	-	540	-	591	Lateral	3.15	0.70	365	25.16	0.31	0.69
		400	400	-	-	-	-				400	15.00	0.12	0.24
6B	Annealed PS:p-Si	500	500	-	-	-	-				365	50.23	0.45	0.35
		500	500	-	-	-	-				400	25.44	0.62	0.32
6B	Annealed PS:p-Si	500	500	-	-	-	-				365	92.82	0.56	0.88
		500	500	-	-	-	-				400	81.26	0.47	0.82

---

## References

- [1] N.N. Greenwood and A. Earnshaw, *Chemistry of the Elements*, 2<sup>nd</sup> edition (Elsevier, Butterworth-Heinemann, 1997).
- [2] A. Uhlir and I. Uhlir, *Phys. Status Solidi C Conf.* **2**, 3185-3187 (2005).
- [3] M. Voos et al., *Appl. Phys. Lett.* **61**, 1213 (1992).
- [4] L.T. Canham, *Appl. Phys. Lett.* **57**, 1046 (1990).
- [5] H. Pan, Y.P. Feng, *ACS Nano* **2**, 2410 (2008).
- [6] U.R. Virgili, *Porous Silicon Multilayer Opt. Devices*. (2007), Chapter 2, pp.5-26.
- [7] A.E. Pap et al., *Opt. Mater.* **28**, 506 (2006).
- [8] K. Kulathuraan et al., *Spectrochim. Acta - Mol. Biomol. Spectr.* **152**, 51 (2016).
- [9] A.G. Roman and D.H. Cuate-Gomez, *Sensors Actuators A Phys.* **292**, 121 (2019).
- [10] N. Naderi, S. Rasi and M. Moradi, *Optik* **172**, 57 (2018).
- [11] J.M.M. Duart and R.J.M. Palma, *Phys. Status Solidi Basic Res.* **232**, 81 (2002).
- [12] R.J. Martín-Palma et al., *Mater. Sci. Eng. C.* **19**, 359 (2002).
- [13] J. Han et al., *Chemistry Select.* **3**, 7385 (2018).
- [14] A.A. Hussain, A.R. Pal and D.S. Patil, *Org. Electron.* **15**, 2107 (2014).
- [15] Y. Zou, Y. Zhang and Y. Hu, H. Gu, *Sensors* **18**, 2072 (2018).
- [16] T. Yang et al., *ACS Nano.* **12**, 1611 (2018).
- [17] J.H. Zhao et al., *IEEE Trans. Electron Devices.* **65**, 4905 (2018).
- [18] Z. Chen, T.Y. Lee and G. Bosman, *Appl. Phys. Lett.* **64**, 3446 (1994).
- [19] Y. Cheng et al., *Sol. Energy Mater. Sol. Cells.* **204**, 110230 (2020).
- [20] U.M. Nayef, K.A. Hubeatir and Z.J. Abdulkareem, *Optik* **127**, 2806 (2016).
- [21] U.M. Nayef and R.I. Kamel, *Optik* **207**, 163847 (2020).
- [22] N. Naderi and M. Moghaddam, *Ceram. Int.* **46**, 13821 (2020).
- [23] N.A.A Khaleq, U.M. Nayef and A.K.H. Albarazanchi, *Optik* **212**, 164793 (2020).
- [24] K.H. Wu and C.W. Li, *Materials* **8**, 5922 (2015).
- [25] S. Mahmoudi et al., *J. Alloys Compd.* **803**, 231 (2019).
- [26] D.H. Shin et al., *J. Alloys Compd.* **715**, 291 (2017).
- [27] H. Fang et al., *Nanotechnology.* **19**, 255703 (2008).
- [28] S. Ozdemir and J. Gole, *Curr. Opin. Solid State Mater. Sci.* **11**, 92 (2007).
- [29] M. Husairi et al., *Semicond. Sci. Technol.* **29**, 075015 (2014).

- [30] F.A. Harraz, *Sensors Actuators B Chem.* **202**, 897 (2014).
- [31] M. Li et al., *Electrochim. Acta.* **108**, 167 (2013).
- [32] A.M. Alwan, D.A. Hashim and M.F. Jawad, *Solid. State. Electron.* **153**, 37 (2019).
- [33] S. Patra, P. Mitra and S.K. Pradhan, *Mater. Res.* **14**, 1 (2011).
- [34] H.M. Pathan and C.D. Lokhande, *Bull. Mater. Sci.* **27**, 85 (2004).
- [35] L.K. Dhandole et al., *Ind. Eng. Chem. Res.* **59**, 9488 (2020).
- [36] V.B. Sanap and B.H. Pawar, *Chalcogenide Lett.* **6**, 415 (2009).
- [37] R.A. Ismail, A.M.E. Al-Samarai and A.Y. Ali, *Optik* **168**, 302 (2018).
- [38] M. Moghaddam et al., *Ceram. Int.* **46**, 7388 (2020).
- [39] J. Theerthagiri et al., *Nanotechnology.* **30**, 392001 (2019).
- [40] R. Yousefi and A.K. Zak, *Mater. Sci. Semicond. Process.* **14**, 170 (2011).
- [41] J.-J. Chen et al., *ECS Trans.* **2**, 153 (2006).
- [42] M.M.H. Shahkarami, J. Koohsorkhi and H.G. Fard, *Nano.* **12**, 1750044 (2017).
- [43] P. Rong, S. Ren and Q. Yu, *Crit. Rev. Anal. Chem.* **49**, 336 (2019).
- [44] A. Janotti and C.G. Van De Walle, *Reports Prog. Phys.* **72**, 126501 (2009).
- [45] S.Y. Ma et al., *J. Alloys Compd.* **566**, 9 (2013).
- [46] L. Luo et al., *Sensors Actuators, A Phys.* **127**, 201 (2006).
- [47] A.S. Ibraheam et al., *Mater. Res. Express.* **6**, 055916 (2019).
- [48] L. Schmidt Mende and J.L. MacManus Driscoll, *Mater. Today.* **10**, 40 (2007).
- [49] M. Taherkhani et al., *J. Electron. Mater.* **48**, 6647 (2019).
- [50] T.V.K. Karthik, L. Martinez and V. Agarwal, *J. Alloys Compd.* **731**, 853 (2018).
- [51] F.S. Husairi et al., *Sensors Actuators, A Phys.* **236**, 11 (2015).
- [52] L. Haji et al., *Appl. Phys. Lett.* **100**, 111102 (2012).
- [53] L. Martínez et al., *Nanoscale Res. Lett.* **9**, 437 (2014).
- [54] F. Miao et al., *Microelectron. Eng.* **149**, 153 (2016).
- [55] X. Fang et al., *Prog. Mater. Sci.* **56**, 175 (2011).
- [56] U.M. Nayef, *Optik* **130**, 441 (2017).
- [57] K. Zhang et al., *Nanoscale.* **9**, 15416 (2017).
- [58] V. Parkhutik, *Solid. State. Electron.* **43**, 1121 (1999).
- [59] A. Loni et al., *Thin Solid Films.* **276**, 143 (1996).
- [60] M.K. Lee and K.R. Peng, *Appl. Phys. Lett.* **62**, 3159 (1993).

- 
- [61] L.A. Golovan and V.Y. Timoshenko, *J. Nanoelectron. Optoelectron.* **8**, 223 (2013).
- [62] P. Menna, G. D. Francia and V. L. Ferrara, *Sol. Energy Mater. Sol. Cells.* **37**, 13 (1995).
- [63] G. Marsh, *Mater. Today.* **5**, 36 (2002).
- [64] M.K. Sahoo and P. Kale, *Microporous Mesoporous Mater.* **289**, 109619 (2019).
- [65] M. J. Sailor, *Porous Silicon in Practice: Preparation, Characterization and Applications* (Wiley, 2012).
- [66] M.J. Sailor, *Fundamentals of Porous Silicon Preparation*, Chapter 1 (Wiley, 2012).
- [67] C.M.A. Ashruf et al., *Sensors Actuators, A Phys.* **74**, 118 (1999).
- [68] K. Peng et al., *Chemie - Int. Ed.* **44**, 2737 (2005).
- [69] X. Li and P.W. Bonn, *Appl. Phys. Lett.* **77**, 2572 (2000).
- [70] K. Peng et al., *Appl. Phys. Lett.* **90**, 163123 (2007).
- [71] B. Moumni and A. Ben Jaballah, *Appl. Surf. Sci.* **425**, 1 (2017).
- [72] J.M. Chen et al., *Appl. Surf. Sci.* **392**, 498 (2017).
- [73] H. Lin et al., *J. Mater. Chem. A.* **1**, 9942 (2013).
- [74] A. Esmanski and G.A. Ozin, *Adv. Funct. Mater.* **19**, 1999 (2009).
- [75] Z. Bao et al., *Nature.* **446**, 172 (2007).
- [76] H. Jia et al., *Adv. Energy Mater.* **1**, 1036 (2011).
- [77] S.H. Lee, J.S. Kang and D. Kim, *Materials* **11**, 2557 (2018).
- [78] S. Manna et al., *J. Phys. Chem. C.* **116**, 7126 (2012).
- [79] T. Yen et al., *Electrochem. Solid-State Lett.* **14**, H415 (2011).
- [80] N.H. Al-Hardan et al., *Sensors Actuators, A Phys.* **207**, 61 (2014).
- [81] R.K. Biroju and P.K. Giri, *J. Appl. Phys.* **122**, 044302 (2017).
- [82] S. Sampath et al., *RSC Adv.* **6**, 25173 (2016).
- [83] X. Wu et al., *Appl. Surf. Sci.* **254**, 6455 (2008).
- [84] Z.Z. Zhang et al., *Thin Solid Films* **513**, 114 (2006).
- [85] L.X. Shao, K.H. Chang and H.L. Hwang, *Appl. Surf. Sci.*, **212**, 305 (2003).
- [86] K.T. Hillie and H.C. Swart, *Appl. Surf. Sci.* **253**, 8513 (2007).
- [87] W. Tian et al., *Adv. Mater.* **26**, 3088 (2014).
- [88] A.K. Katiyar et al., *ACS Appl. Mater. Interfaces.* **6**, 15007 (2014).



- [89] H.J. Xu and X.J. Li, *Semicond. Sci. Technol.* **24**, 075008 (2009).
- [90] P. Rajkumar and B.K. Sarma, *Appl. Surf. Sci.* **509**, 144798 (2020).
- [91] W.W. Yu and X. Peng, *Angew. Chemie - Int. Ed.* **41**, 2368 (2002).
- [92] I. Mekis et al., *J. Phys. Chem. B.* **107**, 7454 (2003).
- [93] L. Qi, H. Cölfen and M. Antonietti, *Nano Lett.* **1**, 61 (2001).
- [94] A.V. Rane, *Synthesis of Inorganic Nanomaterials*, Chapter 5 (Woodhead Publishing, 2018), pp 121-139.
- [95] B. Sarma, P. Rajkumar and B.K. Sarma, *Mater. Res. Express.* **6**, 016420 (2019).
- [96] J.I. Goldstein et al., *Scanning Electron Microscopy and X-ray Microanalysis: a text for Biologists, Materials Scientists, and Geologist* (Springer, 1981).
- [97] J.I. Goldstein et al., *Scanning Electron Microscopy and X-ray Microanalysis* (Springer, 2003).
- [98] L. Reimer and H. Kohl, *Elements of a transmission electron microscope* (Springer, 2008).
- [99] M. Birkholz, *Thin Film Analysis by X-Ray Scattering* (Wiley, 2006).
- [100] A.L. Patterson, *Phys. Rev.* **56**, 978 (1939).
- [101] H. Kasani, A.K. Jameil and M.T. Ahmadi, *Diyala Journal of Engg.* **8**, 606 (2015).
- [102] D.A. Skoog, F.J. Holler and S.R. Crouch, *Principles of Instrumental Analysis, 7<sup>th</sup> edition* (Cengage Learning, 2007).
- [103] H. Haug and S.W. Koch, *Quantum theory of the optical and electronic properties of semiconductors, 5<sup>th</sup> edition* (World Scientific, 2009).
- [104] X. Wang et al., *Adv. Funct. Mater.* **23**, 1202 (2013).
- [105] F. Sarubbi et al., in *Proceedings of 38<sup>th</sup> European Solid-State Device Research Conference* (2008), pp. 278-281.
- [106] G.F. Knoll, *Radiation detection and measurement, 4<sup>th</sup> edition* (Wiley, 2010), pp. 265-302.
- [107] H.A. Atwater and A. Polman, *Nat. Mater.* **9**, 205 (2010).
- [108] H. Chen et al., *Mater. Today* **18**, 493 (2015).
- [109] T. Zhou et al., *Nano Energy* **50**, 118-125 (2018).
- [110] C. Li et al., *Solar Energy Mater. Solar Cells* **172**, 341 (2017).
- [111] J. Wei et al., *Opt. Lett.* **42**, 911 (2017).
- [112] L.T. Canham et al., *Appl. Surf. Sci.* **102**, 436 (1996).

- [113] Y. Qu et al., *Nano Lett.* **9**, 4539 (2009).
- [114] X. Li and P.W. Bohn, *Appl. Phys. Lett.* **77**, 2572 (2000).
- [115] L. U. Khan and M.J.M. Jaffar, *J. Mater. Sci.: Mater. Electron.* **28**, 7677 (2017).
- [116] D. Max Roundhill and J.P. Fackler Jr., *Optoelectronic Properties of Inorganic Compounds* (Springer, 2013).
- [117] F. Meng and Z. Sun, *Appl. Surf. Sci.* **255**, 6715 (2009).
- [118] E.M. Kaidashev et al., *Appl. Phys. Lett.* **82**, 3901 (2003).
- [119] R.A. Ismail, K.S. Khashan and A.M. Alwan, *Silicon* **9**, 321 (2017).
- [120] N.D. Arora, J.R. Hauser and D.J. Roulston, *IEEE Trans. Electron Dev.* **29**, 292 (1982)
- [121] M. Das, S. Sarmah and D. Sarkar, *J. Mater. Sci.: Mater. Electron.* **30**, 11239 (2019).
- [122] A.I. Olivaa et al., *Thin Solid Films* **391**, 28 (2001).
- [123] C. Pacholski et al., *J. Am. Chem. Soc.* **127**, 11636 (2005).
- [124] L. Spanhel and M.A. Anderson, *J. Am. Chem. Soc.* **112**, 2278 (1990).
- [125] Q. Wang et al., *Sci. Rep.* **5**, 13593 (2015).
- [126] R.M. Nirmal, K. Pandian and K. Sivakumar, *Appl. Surf. Sci.* **257**, 2745 (2011).
- [127] H.Z. Song and X.M. Bao, *Phys. Rev. B* **55**, 6988 (1997).
- [128] J.L. Gole et al., *Phys. Rev. B* **56**, 2137 (1997).
- [129] N. Maticiu et al., *Thin Solid Films* **535**, 184 (2013).
- [130] S.M. Sze, *Physics of Semiconductor Devices, 2<sup>nd</sup> edition* (Wiley, 1981) pp. 849.
- [131] A. Chouket, et al., *J. Appl. Phys.* **114**, 243105 (2013).
- [132] A.A. Hussain et al., *Appl. Mater. Interfaces* **8**, 4258 (2016).
- [133] D.S. Tsai et al., *ACS Nano* **7**, 3905 (2013).
- [134] P.R. Berger, in *Proceedings of SPIE* (2001), Vol. 4285.
- [135] L.J. Willis et al., *Nano Lett.* **9**, 4191 (2009).
- [136] R.H. Bube, *Photoconductivity of Solids* (Wiley, 1960).
- [137] E. Baek et al., *Nano Res.* **8**, 1229 (2015).
- [138] G.W. Robinson and R.P. Frosch, *J. Chem. Phys.* **38**, 1187 (1963).
- [139] Q. Hong et al., *Appl. Mater. Interfaces* **6**, 20887 (2014).
- [140] L. Wang et al., *Adv. Funct. Mater.* **25**, 2910 (2015).
- [141] X. An et al., *Nano Lett.* **13**, 909 (2013).

- [142] S. Mukherjee et al., *Nanotechnology* **28**, 135203 (2017).
- [143] C.D. Wessendorf et al., *Sol. RRL* **2**, 1800056 (2018).
- [144] M. Das, S. Sarmah and D. Sarkar, *Superlatt. Microstruct.* **101**, 228 (2017).
- [145] A.A. Thahe et al., *Optik* **168**, 424 (2018).
- [146] T.H. Chou et al., *Sensors Actuators, A Phys.* **279**, 462 (2018).
- [147] A. Zhang et al., *Nano Lett.* **10**, 2117 (2010).
- [148] S.W. Jee et al., *Nano Convergence* **1**, 29 (2014).
- [149] M. Fernandes et al., *Thin Solid Films* **364**, 204 (2000).
- [150] A. Chatterjee and S.K. Selvaraja, in *Proceedings of SPIE* (2018), Vol. 10528.
- [151] Y.Y. Qiang et al., *Cryst. Eng. Commun.* **15**, 1635 (2013).
- [152] S.C. Rai et al., *ACS Nano* **9**, 6419 (2015).
- [153] W. Yang et al., *Nano Lett.* **18**, 4697 (2018).
- [154] X.J. Huang and Y.K. Choi, *Sens. Actuators B.* **122**, 659 (2007).
- [155] H. Li, D. Yang and T. Zhang, *J. Mater. Sci.* **54**, 11556 (2019).
- [156] Hu. Linfeng et al., *Adv. Mater.* **24**, 2305 (2012).
- [157] S. Premkumar et al., *Scientific Rep.* **9**, 18704 (2019).
- [158] M. Das, S. Sarmah and D. Sarkar, in *Materials Today: Proceedings* (2020).
- [159] M. Kiani, A. Haghghatzadeh, *J Inorg. Organomet Polym* **31**, 229 (2021).
- [160] B.L. Devi et al., *Appl. Phys. A* **124**, 767 (2018).
- [161] A. Sarkar et al., *Nanotechnology* **30**, 485202 (2019).
- [162] G. Chai et al., *Sensors Actuators, A Phys.* **150**, 184 (2009).
- [163] K.J. Chen et al., *J. Alloys Compd.* **479**, 674 (2009).
- [164] Siyuan Li, *Adv. Mater. Interfaces* **6**, 1900669 (2019).
- [165] K.T Lam et al., *Nanoscale Res. Lett.* **12**, 31 (2017).
- [166] R. Debnath et al., *RSC Adv.* **5**, 14646 (2015).
- [167] O. Game, *Nanoscale* **6**, 503 (2014).
- [168] Z. Bai and Y. Zhang, *J. Alloys Compd.* **675**, 325 (2016).
- [169] K.C. Pradel, *Chem. Phys. Lett.* **658**, 158 (2016).
- [170] L. Shi and S. Nihtianov, *IEEE Sensor. J.* **12**, 2453 (2012).
- [171] P. Sharma, *J. Phys. D Appl. Phys.* **51**, 015103 (2018).
- [172] V.R. Shinde et al., *Appl. Surf. Sci.* **245**, 407 (2005).
- [173] H. Kim et al., *Thin Solid Films* **377-378**, 798 (2000).

- [174] P. Nunes, *Thin Solid Films* **337**, 176 (1999).
- [175] J.A. Jeong et al., *J. Phys. D Appl. Phys.* **43**, 465403 (2010).
- [176] S. Baruah and J. Dutta, *Sci. Technol. Adv. Mater.* **10**, 013001 (2009).
- [177] M.N. Razaie, *Appl. Surf. Sci.* **392**, 549 (2017).
- [178] C.A. Mead, *Phys. Lett.* **18**, 218 (1965).
- [179] R.C. Neville and C.A. Mead, *J. Appl. Phys.* **41**, 3795 (1970).
- [180] J.C. Simpson and F. Cordaro, *J. Appl. Phys.* **63**, 1781 (1988).
- [181] N. Ohashi et al., *J. Mater. Res.* **17**, 1529 (2002).
- [182] A.A. Thahe et al., *Opt. Mater.* **84**, 830 (2018).
- [183] W. Min et al., *Energy Procedia* **16**, 76 (2012).
- [184] M. Das et al., *Mater. Sci. Semicond. Process.* **118**, 105188 (2020).
- [185] S. Sarmah, M. Das and D. Sarkar, *AIP Conf. Proc.* **2265**, 030246 (2020).
- [186] S. Sarmah, M. Das and D. Sarkar, in *Materials Today: Proceedings* (2020).
- [187] B. Lin, Z. Fu and Y. Jia, *Appl. Phys. Lett.* **79**, 943 (2001).
- [188] S. Vempati, J. Mitra and P. Dawson, *Nanoscale Res. Lett.* **7**, 470 (2012).
- [189] Q.H. Li et al., *Appl. Phys. Lett.* **86**, 123117 (2005).
- [190] A. Janotti and C.G.V. Walle, *J. Cryst. Growth* **287**, 58 (2006).
- [191] R. Khokhra et al., *Sci. Rep.* **7**, 15032 (2017).
- [192] C.R. Crowell, *Solid-State Electron.* **8**, 395 (1965).
- [193] M.A. Yeganeh and S.H. Rahmatollahpur, *J. Semiconduct.* **31**, 074001 (2010).
- [194] W.C. Huang et al., *Microelectron. Eng.* **107**, 200 (2013).
- [195] B. Sarma and B.K. Sarma, *Appl. Surf. Sci.* **410**, 557 (2017).
- [196] X. Chen, G. Wu, and D. Bao, *Appl. Phys. Lett.* **93**, 093501 (2008).
- [197] S. Dhara and P.K. Giri, *Thin Solid Films* **520**, 5000 (2012).
- [198] M. Moun and R. Singh, *J. Appl. Phys.* **127**, 135702 (2020).
- [199] D.A. Muller et al., *Nature* **399**, 758 (1999).
- [200] X.Y. Chen et al., *J. Appl. Phys.* **97**, 014913 (2005).
- [201] A.L. López, M.A. Mijares and O. Malik, *Sensors Actuators, A Phys.* **132**, 278 (2006).
- [202] X. Zhang et al., *Appl. Surf. Sci.* **504**, 144437 (2020).
- [203] B. H. Kim et al., *J. Appl. Phys.* **113**, 073705 (2013).
- [204] J.A.L. López et al., *Sensors Actuators, A Phys.* **233**, 83 (2015).

- [205] G.R. Lin et al., J. Appl. Phys. **97**, 094306 (2005).
- [206] S. Riazimehr et al., ACS Photonics **6**, 107 (2019).
- [207] R. Peng, Thin Solid Films **629**, 55 (2017).
- [208] C.Y. Huang et al., Nanotechnology, **29**, 505202 (2018).
- [209] C. Ling et al., Ceram. Int. **45**, 13275 (2019).
- [210] M. Sağlam et al., Appl. Surf. Sci. **230**, 404 (2004).
- [211] M.K. Lee, Y.H. Wang and C.H. Chu, IEEE J. Quantum Electron. **33**, 2199 (1997).
- [212] Y. Liu et al., Mater. Res. Express. **6**, 085904 (2019).
- [213] P.C. Chang et al., Phys. Status Solidi Curr. Top. Solid State Phys. **4**, 1625 (2007).
- [214] M. Das, P. Nath and D. Sarkar, Superlatt. Microstruct. **90**, 77 (2016).
- [215] S. Calvin et al., Appl. Phys. Lett. **87**, 233102 (2005).
- [216] Z.X. Zhao et al., Mater. Lett. **58**, 3963 (2004).
- [217] K. Barla et al., J. Cryst. Growth **68**, 721 (1984).
- [218] D. Bellet and G. Dolino, Thin Solid Films **276**, 1 (1996).
- [219] M. Yang et al., J. Appl. Phys. **75**, 651 (1994).
- [220] M. Ramesh, H.S. Nagaraja, Mater. Today Chem. **3**, 10 (2017).
- [221] A.D.M. Naught and A. Wilkinson, *Compendium of Chemical Terminology*, 2<sup>nd</sup> edition (IUPAC Gold Book, 1997).
- [222] Y. Kanemitsu et al., Phys. Rev. B - Condens. Matter Phys. **55**, R7375(R) (1997).
- [223] S. Arulkumaran et al., Appl. Phys. Lett. **84**, 613 (2004).
- [224] F. Amy et al., Phys. Rev. B-Condens. Matter Phys. **65**, 165323 (2002).
- [225] K. Horio and H. Yanai, IEEE Trans. Electron Devices **37**, 1093 (1990).
- [226] W.C. Huang et al., Microelectron. Eng. **107**, 200 (2013).
- [227] R.K. Gupta, K. Ghosh and P.K. Kahol, Curr. Appl. Phys. **9**, 933 (2009).
- [228] R.K. Gupta, K. Ghosh and P.K. Kahol, Phys. E: Low Dim. Syst. Nanostructures **42**, 1509 (2010).
- [229] J.S. Liu et al., Appl. Phys. Lett. **97**, 251102 (2010).
- [230] R. Gegevičius et al., Adv. Electron. Mater. **4**, 1800114 (2018).
- [231] H.K. Park and J. Choi, Adv. Electron. Mater. **4**, 1700317 (2018).
- [232] K.K. Liu et al., Nano Lett. **12**, 1538 (2012).
- [233] M.R.J. Vivanco et al., Nanomaterials. **10**, 222 (2020).
- [234] Y. Cho et al., ACS Appl. Mater. Interfaces. **9**, 6314 (2017).

- [235] S. Qiao et al., *J. Mater. Chem. C.* **6**, 3233 (2018).
- [236] T. Ji et al., *J. Mater. Chem. C.* **5**, 12848 (2017).
- [237] M.R.E. Rad and S. Salahuddin, *Sci. Rep.* **3**, 2345 (2013).
- [238] N. Naderi and M.R. Hashim, *J. Alloys Compd.* **552**, 356 (2013).
- [239] A.S. Mayet et al., *J. Opt. Soc. Am. B.* **35**, 1059 (2018).
- [240] M.V. Lebedev et al., *Semiconductors* **45**, 526 (2011).
- [241] S. Sarmah, M. Das and D. Sarkar, *Mater. Lett.* **297**, 129972 (2021).
- [242] B. Basumatary et al., *J. Electron. Mater.* **49**, 5467 (2020).

---

## Appendix

### [A] List of publications in referred journals

1. **S. Sarmah**, M. Das and D. Sarkar, *Enhanced UV-visible photo responsivity of annealed Al/porous silicon (PS): p-Si Schottky device*, **Materials Letters** **297**, 129972 (2021).
2. M. Das, **S. Sarmah** and D. Sarkar, *Distinct band UV-visible photo sensing property of ZnO-porous silicon (PS): p-Si hybrid MSM structure*, **Materials Science in Semiconductor Processing** **118**, 105188 (2020).
3. M. Das, **S. Sarmah** and D. Sarkar, *Photo sensing property of nanostructured CdS-porous silicon (PS): p-Si based MSM heterostructure*, **Journal of Materials Science: Materials in Electronics** **30**, 11239 (2019).
4. **S. Sarmah**, M. Das and D. Sarkar, *Ageing mediated silicon suboxide interlayer growth in porous silicon: p-Si heterostructured metal-semiconductor-metal device for enhanced UV-visible photodetection*, (Second Revision Submitted, **Thin Solid Films**).

### [B] Conference proceedings

1. **S. Sarmah**, M. Das and D. Sarkar, *Photo sensing properties of porous silicon (PS): p-Si and ZnO-PS: p-Si -MSM devices: A comparative analysis*, **AIP Conference Proceedings** **2265**, 030246 (2020).
2. **S. Sarmah**, M. Das and D. Sarkar, *UV-visible photo sensing properties of CdS-porous silicon (PS): p-Si and ZnO-PS: p-Si heterostructures metal-semiconductor-metal (MSM) based devices*, **Materials Today: Proceedings**, Article in Press (Accepted, 27<sup>th</sup> April 2020), <https://doi.org/10.1016/j.matpr.2020.04.773>
3. M. Das, **S. Sarmah** and D. Sarkar, *Distinct and enhanced ultraviolet to visible ZnS-porous silicon (PS): p-Si hybrid metal-semiconductor-metal (MSM) photodetector*, **Materials Today: Proceedings**, Article in Press (Accepted, 27<sup>th</sup> April 2020), <https://doi.org/10.1016/j.matpr.2020.04.779>

---

**[C] National/international conferences/workshops attended**

1. “*Effects of auto-ageing on optical and electrical properties of porous silicon (PS): p-Si heterostructure*” (Online mode), **3<sup>rd</sup> National Conference on Recent Advances in Science and Technology (NCRAS-2020)**, Assam Science and Technology University, Guwahati, 17-19 August, 2020.
2. “*UV-visible photo sensing properties of CdS-porous silicon (PS): p-Si and ZnO-PS: p-Si heterostructures metal-semiconductor-metal (MSM) based devices*”, **3<sup>rd</sup> International Conference on Material Science (ICMS)**, Tripura University, Agartala, 04-06 March, 2020. [**Best Oral Presentation Award**].
3. “*Photo sensing properties of porous silicon (PS): p-Si and ZnO-PS: p-Si MSM devices: A comparative analysis*”, **64<sup>th</sup> DAE Solid State Physics Symposium**, IIT Jodhpur, 18-22 December, 2019.
4. “*Comparative study of optical & electrical properties of p-PS and nano-CdS-p-PS heterostructures*”, **Research Conclave-19**, IIT Guwahati, 14-17 March, 2019. [**2<sup>nd</sup> Best Poster Award**].
5. “*Fabrication of porous silicon (PS) and ageing effect on photo-detection of Al: porous silicon (PS):p-Si MSM device*”, **UGC- SAP (DRS II) 2<sup>nd</sup> National Conference on Hard and Soft Condensed Matter Physics-NCHSCMP (2019)**, Dept. of Physics, Tezpur University, 04-06 March, 2019.
6. “*Photo sensing by MSM heterostructure constructed from CdS nanoparticle passivated porous silicon (PS)*”, **A Silver Jubilee National Conference on Condensed Matter Physics (CMDAYS-17)**, Dept. of Physics, Tezpur University, 29-31 August, 2017.
7. “*Influence of S<sup>2-</sup> ion concentration on optical band gap of CdS nanoparticle*”, **UGC- SAP (DRS III) National Seminar on Advances in Material Science**, Dept. of Physics, Gauhati University, 24-25 March, 2017.





# Enhanced UV-visible photo responsivity of annealed Al/porous silicon (PS): p-Si Schottky device



S. Sarmah, M. Das, D. Sarkar \*

Condensed Matter Physics Research Laboratory, Department of Physics, Gauhati University, Guwahati 781014, India

## ARTICLE INFO

### Article history:

Received 2 April 2021

Received in revised form 25 April 2021

Accepted 27 April 2021

Available online 30 April 2021

### Keywords:

Porous materials

Surfaces

Interfaces

Optical materials and properties

Sensors

## ABSTRACT

Present article reports improvement of UV-visible photo sensing property of porous silicon (PS): p-Si Schottky device by thermal annealing of the electrochemically etched PS: p-Si structure aged for a month. This structure is provided with a rectifying Schottky contact of vacuum coated aluminum (Al) metal. The annealed device at 400 °C shows better diode quality and exhibits multi-band UV-visible photo response with maximum photo- to dark current ratio (PDCR) in low applied bias range of -1.8 to 0 V, suggesting low power operation feasibility of the device. For comparison, the results on the device annealed at 200 °C are also presented.

© 2021 Elsevier B.V. All rights reserved.

## 1. Introduction

Porous silicon (PS), a porous layer over silicon (Si) [1,2], is viable for fabricating various optoelectronic devices [3]. In addition, porous materials are also utilized in making various energy conversion and storage devices [4–6]. However, in recent years, most works report UV-visible-NIR range photodiodes (PDs) from PS based heterostructures [7,8] due to its high surface to volume ratio and direct bandgap nature. Among various techniques for synthesis of ordered nanostructures viz., electrodeposition, chemical vapor deposition technique etc. [9,10], silicon nanostructures are typically synthesized using electrochemical etching method, which is known to be cost effective and highly reproducible. The spectral responsivity of UV-visible PDs are reported to be strongly reliant on crystallinity and defect states present in the material. This value can be significantly enhanced by incorporating higher crystalline epilayer [11]. Moreover, due to long auto-ageing period of PS, a silicon suboxide ( $\text{SiO}_x$ ) layer may grow on its surface, which inevitably can quench spectral responsivity. Post thermal annealing of PDs can significantly enhance its crystallinity and consequently can improve the photo sensing performance [12–16]. The present letter reports post annealing effects on photo sensing performance of PS based Schottky PD.

## 2. Experimental details

### 2.1. Materials and methods

PS is prepared from (100) oriented p-type Si wafer as described in authors' earlier work [17]. After PS formation the sample is kept for one month for natural growth of  $\text{SiO}_x$  ( $x \leq 2$ ) on its surface. The Schottky device is prepared by depositing high purity Al (99.99%) metal by vacuum coating. The interdigitated electrode structure is prepared using indigenously built shadow mask of dimension  $6 \text{ mm} \times 6 \text{ mm}$  with spacing and width of 1 mm. The thickness of the electrode is maintained at 30 nm using digital thickness monitor attached to the coating unit. The fabricated Al/ $\text{SiO}_x$ /PS: p-Si device is then annealed at four different temperatures: 200, 300, 400 and 500 °C for 1 h to test photosensitivity performance. The results on the device annealed at 200 and 400 °C are reported in the following sections.

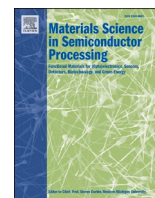
## 3. Results and discussions

### 3.1. Morphological analysis

Fig. 1(a, b) show in-plane FESEM micrographs with insets showing its cross-sectional views. The figures indicate no visual change of PS layer on annealing. The thickness of 540 nm obtained from cross-sectional view is seen to remain unchanged with annealing. EDX spectra shown in Fig. 1(c, d) present the quantitative percentages of Si and O for PS: p-Si sample annealed at 200 and 400 °C and

\* Corresponding author.

E-mail address: [sarkardeepali@gmail.com](mailto:sarkardeepali@gmail.com) (D. Sarkar).



## Distinct band UV–Visible photo sensing property of ZnO-Porous silicon (PS):p-Si hybrid MSM heterostructure

M. Das<sup>a</sup>, S. Sarmah<sup>a</sup>, D. Barman<sup>b</sup>, B.K. Sarma<sup>b</sup>, D. Sarkar<sup>a,\*</sup>

<sup>a</sup> Condensed Matter Physics Research Laboratory, Department of Physics, Gauhati University, Guwahati, 781014, Assam, India

<sup>b</sup> Nanophysics Laboratory, Department of Physics, Gauhati University, Guwahati, 781014, Assam, India

### ARTICLE INFO

#### Keywords:

Photodetector  
Porous silicon  
Zinc oxide  
MSM device  
Heterostructure

### ABSTRACT

Present article deals with fabrication of UV–Visible radiation sensing photodetector (PD) by architecting planar and sandwiched (PD1 and PD2) electrode configurations on ZnO-PS:p-Si heterostructure. PS:p-Si structure is prepared by electrochemical anodization method. Thin ZnO layer of  $\sim 162$  nm is deposited on PS:p-Si substrate using pulsed DC magnetron sputtering technique. Gold (Au) is combined with Aluminium (Al) to provide rectifying Schottky contacts to the devices. Prior to device testing it is tested for various conventional characterizations. FESEM studies confirm uniform deposition of nanocrystalline ZnO thin film with mean particle size of  $\sim 35$  nm, whereas its cross section shows uniform interface between ZnO and PS with combined thickness of  $\sim 700$  nm. Cross sectional EDX analysis confirms diffusion of ZnO particles into PS layer. UV–vis absorption spectrum gives bandgap of ZnO as  $\sim 3.3$  eV. Reflectance measurement of the heterostructure shows decrease in reflectivity compared to bulk c-Si with ZnO-PS:p-Si showing multiple interference pattern compared to bare ZnO coated on glass within the spectral range 200 nm–800 nm. The pattern is remarkably increased compared to that of PS:p-Si. Photoluminescence study reveals various luminescence bands peaked at  $\sim 378$  nm, 388 nm, 398 nm, 410 nm, 420 nm, 433 nm, 450 nm, 467 nm, 482 nm 492 nm and 597 nm. Current–Voltage (I–V) measurement for dark current ( $I_d$ ) gives low leakage current of the devices PD1 and PD2 respectively as  $6.6 \times 10^{-8}$  A and  $7.5 \times 10^{-7}$  A at  $-5$  V, which is however an order of magnitude more than the ZnO coated one on glass. Both the devices PD1 and PD2 show UV–Visible photoresponse, whereas the ZnO device on glass shows response to UV (375 nm) only. Both the devices show response time  $\sim 1$  s in visible range which is nearly half the value in UV range.

### 1. Introduction

Radiation sensors or photodetectors (PDs) have the ability to detect specific set of wavelengths from UV to visible range. These have attracted huge attention from various researchers' [1–4] in research and development, along with some other fields like solar astronomy, ecological monitoring, control system etc. [5,6]. However, for such applications high speed PDs are the basic need. Although it has been observed from literature survey that high speed along with high spectral response PD's are very few. In a way one can say that PDs with high responsivity value are mostly slow detectors basically in detection of UV radiation [7–9]. For the purpose metal oxides mainly ZnO has been explored widely in the last decade due to its exceptional UV sensing ability. To name a few, Siyuan Li et al. [7] reported ZnO based PDs with responsivity of  $0.52 \text{ mA W}^{-1}$  and response time of  $\sim 16$  s under 250–370 nm UV light illumination and improved its responsivity up to  $1.53$

$\text{mA W}^{-1}$  for CuI/ZnO. However, these PDs fail grossly in visible light detection. K. T Lam and his group [8], succeeded in fabricating high response PD based on ZnO NWs/CdS with responsivity of  $12.86 \text{ AW}^{-1}$ , but these also have very slow response time of  $\sim 62$  s and constrained to only UV light detection. To the best of authors' knowledge reports on PDs with high response and distinct band UV to visible photo sensing is rare. So, PDs which can sense both UV and visible light would be of much advantages and our investigation aims for fabrication of such device. Devising PDs with high responsivity and fast response in UV–visible range is still a challenge for researchers. It is seen from some earlier reported works [10–12] that increment in photo responsivity directly results in slow response time and vice versa, which may be attributed to trap assisted photo conduction process. In this context, silicon (Si) based PDs which have high spectral response in visible spectral range, but have limitations in UV light sensing can be coupled with wide band gap (WBG) semiconductors such as ZnO, ZnS etc. (which

\* Corresponding author.

E-mail address: [sarkardeepali@gmail.com](mailto:sarkardeepali@gmail.com) (D. Sarkar).



# Photo sensing property of nanostructured CdS-porous silicon (PS):p-Si based MSM hetero-structure

M. Das<sup>1</sup> · S. Sarmah<sup>1</sup> · D. Sarkar<sup>1</sup>

Received: 25 February 2019 / Accepted: 3 May 2019 / Published online: 7 May 2019  
© Springer Science+Business Media, LLC, part of Springer Nature 2019

## Abstract

Present work reports light sensing property of metal–semiconductor–metal device based on nanostructured CdS-PS:p-Si hetero-structure. PS with thickness of ~ 1500 nm is prepared on p-Si (100) oriented wafer using electrochemical anodization method. Thin nanostructured n-CdS layer of ~ 170 nm is deposited on PS:p-Si substrate by vacuum evaporation. FESEM observation confirms growth of hierarchical flower like CdS nanostructure on PS:p-Si substrate. UV–Vis absorption spectrum gives bandgap of CdS nanostructure to be 2.6 eV. Reflectance measurement of CdS-PS:p-Si hetero-structure shows multiple interference pattern within the spectral range of 200–800 nm, with remarkable blue shift of the pattern compared to that of PS:p-Si structure. Photoluminescence study of the hetero-structure reveals presence of various luminescence bands peaked at ~ 450, 460, 468, 482, 560, and 590 nm. Dark current ( $I_d$ ) analysis shows low leakage current ~ 32 nA at – 2 V with ideality factor ( $n$ ) and reverse saturation current ( $I_s$ ) values of 1.57 and 0.2 nA respectively. Spectral response of the hetero-structure at a bias voltage of – 2 V and irradiation wavelength of 400 nm shows maximum responsivity ( $R_\lambda$ ) value of ~ 0.6 AW<sup>-1</sup> and external quantum efficiency of ~ 180%. Response and recovery times of the device are ~ 160 and ~ 350 ms respectively. The prepared hetero-structure has been compared with other silicon based optoelectronic switching devices to find suitability of an alternate choice.

## 1 Introduction

In semiconductor physics, photoconductivity is well known phenomenon which indulge into conversion of light energy to electrical signal [1]. Photodetectors (PDs) and Photovoltaic devices (PVs) rely on this basic principle. PDs and PVs have found many important applications in radiation detection and solar cell industries respectively [2–4]. Research interest in PDs and PVs in the field of material physics is increasing at high rate, which leads to the development of various types of such devices [5–8]. There is an excellent review article based on ultraviolet PDs made out of large number of materials [9], to name a few Wang et al. [10] reported Graphene-Si hetero-structure PD with responsivity ( $R_\lambda$ ) as high as 0.13 AW<sup>-1</sup> at – 1.5 V for 2.75 μm at room temperature. Hong et al. [11] reports p-CuO-n-Si ultra-fast broadband PD with peak  $R_\lambda$  of  $3.89 \times 10^{-4}$  at 405 nm.

Dhyani et al. [12] reported Vis–NIR MoS<sub>2</sub>-PS based Si heterojunction broadband PD for high speed optical switching, similarly several MoS<sub>2</sub>:Si heterojunction Vis–NIR PDs are also reported [13, 14] while some authors reported large area broadband UV–Vis PDs based on 1D Se–n–Si heterojunctions [15]. Thus extensive research has been under way for developing light sensing devices based on different hetero-structure configuration [16–19], one of the biggest challenge for configuration of such hetero-structure is the choice of appropriate material, PS one of such material which attract great interest due to its fascinating electrical and optoelectronics property [20, 21]. The basic advantage of PS is its interesting fabrication methods like electrochemical anodization [22], metal assisted chemical etching [23]. PS fabricated on p-type Si (p-Si) wafer acts as active hole transport layer, thus by deposition of electron rich material on PS:p-Si substrate P–N type hetero-junction can be developed. There are various electron transport materials such as ZnO, ZnS, TiO<sub>2</sub>, CdS [24, 25] which can be employed for the configuration of PDs to detect specific range of wavelength. Basically nanostructured metal oxides like ZnO, TiO<sub>2</sub> have been explored for UV–Vis light sensing. Shahabina et al. [26] reported ZnO-PS UV PD for irradiation wavelength of

✉ D. Sarkar  
sarkardeepali@gmail.com

<sup>1</sup> Condensed Matter Physics Research Laboratory, Department of Physics, Gauhati University, Guwahati, Assam 781014, India

# Photo Sensing Properties of Porous Silicon (PS): p-Si and ZnO-PS: p-Si -MSM Devices: A Comparative Analysis

S. Sarmah<sup>1,a)</sup>, M. Das<sup>1</sup>, D. Sarkar<sup>1</sup>

<sup>1</sup>Condensed Matter Physics Research Laboratory, Department of Physics, Gauhati University, Guwahati, Assam 781014, India

<sup>a)</sup>Corresponding author: samarjtsarmah59@gmail.com

**Abstract.** Present study reports fabrication and photo sensing property of metal-semiconductor-metal (MSM) devices based on Al/PS: p-Si and Al+Au/ZnO-PS:p-Si heterostructures. FESEM analysis confirms growth of spherical shaped nanostructured ZnO layer of thickness ~160 nm on ~370 nm thick PS: p-Si structure. Dark current analysis of the heterostructures gives ideality factor ( $n$ ) of 7.1 and 4.36 respectively. Electrical properties explored for heterostructures under illumination condition (250-500 nm) reveal superiority of ZnO-PS:p-Si heterostructure in terms of high responsivity  $\sim 2.6 \text{ AW}^{-1}$ , high EQE  $\sim 800\%$  and response time of 0.3 sec compared to  $\sim 0.3 \text{ AW}^{-1}$ ,  $\sim 85\%$  and 0.15 sec respectively for PS: p-Si heterostructure.

## INTRODUCTION

Porous silicon (PS):p-Si (p-type Silicon) is a heterostructure material which attracts extensive attentions of researchers for using it in electrical and optoelectronic fields [1]. However, silicon (Si) or PS still have some limitations in photo detection field due to their low spectral response for UV region. Thus, by incorporating wide band-gap (WBG) semiconductors such as ZnO, ZnS, GaN etc. on PS:p-Si substrate motivates researchers to employ these heterostructures for photo sensing in broad UV-Vis range of EM spectrum [2]. In addition to this, such materials also act as active electron transport layer on p-type PS, whereas PS performs as active hole transport layer and forms a PN junction for enhancement of photo sensing performance [3]. In the present work, we investigated the consequences of ZnO incorporation on photo sensing properties of the PS: p-Si heterostructure.

## EXPERIMENTAL

### Preparation of Al: PS: p-Si & Al+Au: ZnO-PS: p-Si MSM Heterostructures

P-type silicon (100) oriented wafer of  $375 (\pm 25) \mu\text{m}$  thickness and  $(1-10) \Omega \text{ cm}$  resistivity is first cleaned using RCA [4] treatment method for removing the native oxide layer from its surface. RCA treated wafer is then sonicated in isopropyl alcohol for 10 min prior to pre-etching of the sample for 30 sec in a 3: 1 aqueous 48% HF: ethanol solution under constant current density of  $J = 22.1 \text{ mAcm}^{-2}$ . The sample is then soaked in 1 M aqueous solution of NaOH for 5 min to remove the pre-etched PS layer. Finally, PS layer is grown on p-Si surface by anodization keeping the etching parameters same as stated in our previous reported work [5].

ZnO thin film on prepared PS: p-Si substrate is deposited by pulsed DC magnetron sputtering system equipped with three cooled planar magnetrons and a rotatable substrate holder. Target of ZnO prepared from high purity (99.99%) ZnO powder is placed in one of the magnetrons at a distance of 45 mm from the PS substrate and pre-sputtered for 5 min. Prior to deposition the chamber is evacuated upto a base pressure of  $\sim 2 \times 10^{-5}$  mbar. During deposition Argon gas (99.999% pure) is used as sputtering gas at chamber pressure of  $\sim 2 \times 10^{-2}$  mbar. Uniform ZnO film deposition is carried out on PS substrate by rotating the substrate holder for 20 min maintaining the sputtering power at 70 W with 100 kHz frequency and 70% duty cycle. Al-Au electrode of  $6 \text{ mm} \times 6 \text{ mm}$  size and  $\sim 50 \text{ nm}$  thickness is deposited laterally on ZnO-PS: p-Si heterostructure using an interdigitated shadow mask in Hind high vacuum coating unit at vacuum pressure of  $\sim 10^{-5}$  mbar by thermal evaporation of highly pure (99.99%) gold (Au) foil and aluminium (Al) wire respectively. Also for comparison, Al-electrode of same size is deposited on PS:p-Si surface under same condition. Schematic of one of the prepared heterostructure is shown in the inset of fig. 3(b).



Contents lists available at ScienceDirect

## Materials Today: Proceedings

journal homepage: [www.elsevier.com/locate/matpr](http://www.elsevier.com/locate/matpr)

# UV-Visible photo sensing properties of CdS-porous silicon (PS): P-Si and ZnO-PS: p-Si heterostructures metal-semiconductor-metal (MSM) based devices

S. Sarmah\*, M. Das, D. Sarkar

Condensed Matter Physics Research Laboratory, Department of Physics, Gauhati University, Guwahati, Assam 781014, India

## ARTICLE INFO

## Article history:

Received 20 March 2020  
 Received in revised form 18 April 2020  
 Accepted 27 April 2020  
 Available online xxx

## Keywords:

CdS  
 ZnO  
 Hetero structure  
 UV-Visible sensing

## ABSTRACT

Present work reports fabrication of metal-semiconductor-metal (MSM) [1] devices based on CdS-PS: p-Si and ZnO-PS: p-Si heterostructures for photo sensing applications. Field Emission Scanning Electron Microscope (FESEM) analyses confirm growth of hierarchical flower like nanostructured CdS and spherical shaped nanostructured ZnO layers of uniform thicknesses  $\sim 170$  and  $160$  nm respectively on PS: p-Si substrate. UV-visible absorbance spectra for CdS and ZnO nanostructures provide optical band gap of  $2.6$  and  $3.3$  eV respectively. Photoluminescence (PL) spectra analyses of the heterostructures show near band edge (NBE) emissions of nanostructured CdS at  $\sim 450$ – $482$  nm for CdS-PS: p-Si and at  $\sim 378$ – $398$  nm of nanostructured ZnO for ZnO-PS: p-Si along with characteristic PL peaks of PS at  $\sim 600$  nm [2] and some trap/defect assisted luminescence bands. Dark current analyses of the heterostructures give values of ideality factors ( $n$ ) of  $3.4$  and  $4.4$  respectively. Heterostructures under increasing illumination intensity ( $17$ – $71 \mu\text{W cm}^{-2}$ ,  $400$  nm) show almost symmetric rectification enhancement for positive and negative bias condition with maximum photo to dark current ratio ( $I_{ph}/I_d$ ) of  $10.3$  and  $34.3$  respectively at  $-2$  V bias. ZnO-PS: p-Si heterostructure shows superiority for UV-Visible photo sensing application in terms of high responsivity  $\sim 2.6 \text{ AW}^{-1}$ , high EQE  $\sim 800\%$  and response time of  $\sim 1.12$  sec compared to  $\sim 0.6 \text{ AW}^{-1}$ ,  $180\%$  and  $0.16$  sec of CdS-PS: p-Si respectively at biasing of  $-2$  V.

© 2020 Elsevier Ltd. All rights reserved.

Selection and Peer-review under responsibility of the scientific committee of the Third International Conference on Materials Science (ICMS2020).

## 1. Introduction

Porous silicon (PS) is a hybrid material which attracts wide-range of attentions to scientists for exploring its uses in optoelectronic and communication fields [3]. Silicon (Si) or PS still has some restrictions in photo detection field due to their low spectral response for ultraviolet (UV) region. Thus, by assimilating wide band-gap (WBG) semiconducting materials such as zinc oxide (ZnO), zinc sulphide (ZnS), gallium nitride (GaN) etc. with PS: p-Si substrate could be explored for improved photo sensing property in broad UV-Vis range of electromagnetic (EM) spectrum [4]. Similarly, metal sulphides such as nanostructured cadmium sulphide (CdS) which performs as a decent visible light sensing material when assimilated with PS: p-Si, can further enhance photoresponse of PS: p-Si substrate as reported in some recent works

[5]. In this work thin layers ( $<200$  nm) of CdS and ZnO nanostructures are deposited on PS:p-Si substrate so that maximum UV-vis light can reach the CdS-PS:p-Si and ZnO-PS:p-Si junctions respectively to generate more  $e^-h^-$  pairs and consequently increase photocurrent of the heterostructures [6]. There are various techniques used by researchers [7–9] for CdS nanostructure preparation. In the present work, CdS nanostructure is prepared by cost effective wet chemical synthesis process and the obtained nano powder is deposited on PS:p-Si structure by thermal evaporation method. To get Schottky MSM (metal semiconductor metal) contact, low work function metal viz., aluminium (Al) electrode is laterally deposited to devise an electrode of Al/CdS-PS:p-Si configuration. Further, out of numerous techniques viz. hydrothermal, spray pyrolysis, pulse laser deposition, sol-gel process, metal-organic chemical vapour deposition (MOCVD), direct current (DC) and radio frequency (RF) sputtering etc. for ZnO nanostructure deposition [10–16], pulsed DC magnetron sputtering process is adopted to grow good quality ZnO-PS:p-Si films with

\* Corresponding author.

E-mail address: [samarjitsarmah59@gmail.com](mailto:samarjitsarmah59@gmail.com) (S. Sarmah).



Contents lists available at ScienceDirect

## Materials Today: Proceedings

journal homepage: [www.elsevier.com/locate/matpr](http://www.elsevier.com/locate/matpr)

# Distinct and enhanced ultraviolet to visible ZnS-porous silicon (PS):p-Si hybrid metal-semiconductor-metal (MSM) photodetector

M. Das, S. Sarmah, D. Sarkar

Condensed Matter Physics Research Laboratory, Department of Physics, Gauhati University, Guwahati 781014, India

## ARTICLE INFO

## Article history:

Received 5 April 2020

Received in revised form 24 April 2020

Accepted 27 April 2020

Available online xxx

## Keywords:

MSM

Heterostructure

Photodetector

Porous silicon

ZnS

## ABSTRACT

Present article reports distinct and enhanced ultraviolet to visible light sensing property of metal-semiconductor-metal (MSM) based ZnS-PS:p-Si hybrid heterostructure. PS:p-Si heterostructure is prepared using electrochemical anodization technique by alternate variation of etching current density within the limit of 17.2–22.1 mA cm<sup>-2</sup>. ZnS (99.99% purity) in powder form is deposited on PS:p-Si surface via thermal evaporation technique under a chamber pressure of 2 × 10<sup>-5</sup> m bar. To achieve MSM configuration Au electrode of ~8 nm and Al electrode of ~22 nm thickness are successively coated on top of ZnS-PS:p-Si surface using a shadow mask with dimension of 6 × 6 mm. Morphological features of the heterostructure are observed and analysed using cross section FESEM. This gives thickness of the deposited ZnS layer as around ~110 nm on ~540 nm thick PS:p-Si structure. These also confirm uniform interface between the two i.e. ZnS and PS:p-Si layers. Cross sectional EDX analysis indicates diffusion of ZnS particles into the PS layer. Optical analysis observed via UV-Visible spectroscopy gives bandgap (obtained through Tauc plot) of the bare ZnS film to be 3.4 eV with 70–90% transparency in the visible region (390–700 nm). Optical reflectance spectrum of the prepared heterostructure shows decreased reflectivity compared to that of the bare PS:p-Si structure which is itself 20–30% less compared to bulk silicon. Spectral response measured for the wavelength range of 200–500 nm gives distinct and enhanced responsivity peak values of ~0.94 and ~1.12 AW<sup>-1</sup> at 365 nm (UV) and 400 nm (visible) compared to ~0.5 AW<sup>-1</sup> (maximum at 400 nm) of bare PS:p-Si MSM structure for bias voltage of -4 V. The response and recovery times of the heterostructure are found to be 0.54 ± (4.3 × 10<sup>-4</sup>) s, 0.38 ± 9.5 × 10<sup>-5</sup> s and 0.50 ± 2.8 × 10<sup>-4</sup> s, 0.35 ± 6.5 × 10<sup>-5</sup> s under UV and visible irradiations.

© 2020 Elsevier Ltd. All rights reserved.

Selection and Peer-review under responsibility of the scientific committee of the Third International Conference on Materials Science (ICMS2020).

## 1. Introduction

Photodetectors (PDs) based on silicon have attracted great interest due its broad visible to NIR photodetection ability [1–4]. However, Si faces disadvantage due to its low and indirect bandgap which creates obstacle particularly in efficient detection of UV-Visible radiation. Porous silicon (PS) on the other hand is well known for its visible photo luminescence ascribed due to confinement effect in nano silicon region [5]. PS is also known to increase the visible light sensing efficiency. However, for UV detection PS also faces some limitations. Thus to minimize these drawbacks wide bandgap materials like ZnS, ZnO, CuO, NiO etc., which are well known for their specific UV responses, can be coupled with PS:p-Si structure for fabricating efficient UV to visible

radiation sensing devices. Although there have been various reported works on UV and Visible range PDs [6–10]. To name a few Uday et al. [11] reported improved Al/ZnS/PS/c-Si/Al device with a responsivity values ~0.06AW<sup>-1</sup> and ~0.03AW<sup>-1</sup> at UV and Visible region respectively. There is also a report on wide range photoresponse UV-A PD based on ZnS/ZnO biaxial nanobelt [12]. Another group of authors reported ZnS quantum dot-based UV PD with maximum responsivity of 0.3AW<sup>-1</sup> at 390 nm [13]. But reports on specific band UV to visible radiation sensing are scarce. In this article, particularly we report fabrication and characterization of distinct and enhanced UV to visible photo sensing device based on ZnS-PS:p-Si heterostructure by combining different work-function metal electrodes to achieve Schottky contacts from ZnS and PS:p-Si structure.

<https://doi.org/10.1016/j.matpr.2020.04.779>

2214-7853/© 2020 Elsevier Ltd. All rights reserved.

Selection and Peer-review under responsibility of the scientific committee of the Third International Conference on Materials Science (ICMS2020).